

UNIVERSITÀ DEGLI STUDI DELL'AQUILA

*Facoltà di Scienze MM. FF. NN.
Scuola di Dottorato di Ricerca in Fisica
- XXIV ciclo -*



A Thesis submitted for the degree of
Dottore di Ricerca in Fisica S.S.D. FIS/04.

*Measurement of the neutrino
charged current interaction rate on ^{13}C
in Borexino*

Advisors

Dr. Aldo Ianni

sezione INFN LNGS

Dr. Francesco L. Villante

Università dell'Aquila e sezione INFN LNGS

Tutor

Prof. Sergio Petrera

Università e gruppo collegato INFN de L'Aquila

Author

Chiara Ghiano

Università dell'Aquila e sezione INFN LNGS

PhD school coordinator

Prof. Michele Nardone

Università e gruppo collegato INFN de L'Aquila

Contents

Abstract	1
Introduction	5
1 Neutrinos and solar physics	11
1.1 Neutrino properties	11
1.1.1 Neutrinos in the Standard Model	12
1.1.2 Beyond the Standard Model	14
1.1.2.1 Neutrino oscillations	14
1.1.2.2 Present experimental status	21
1.2 Neutrinos: messengers from the Sun	21
1.2.1 The Standard Solar Model	23
1.2.2 Nuclear reactions in the Sun	25
1.2.3 Solar neutrino fluxes	29
1.2.4 Solar abundance problem	30
1.2.5 Electron neutrino survival probability	32
2 The Borexino Experiment	35
2.1 Overview	35
2.2 Location: Laboratori Nazionali del Gran Sasso	36
2.3 Conceptual design of the detector	38
2.4 Neutrino detection in Borexino	40
2.4.1 Detection reactions	41
2.5 Main components of the detector	46
2.5.1 Structural components	46
2.5.2 The scintillator and buffer properties	51
2.5.3 Purification plants	54
2.6 Background issues in low energy ν detection	57
2.6.1 Intrinsic radioactive contaminants	58
2.6.2 Muons and cosmogenics isotopes	62
2.7 Borexino physics program, results and outlook	63
2.7.1 Solar neutrinos	63
2.7.2 Antineutrinos	71
2.7.3 The future	73
3 Data acquisition and event reconstruction	75
3.1 The electronic chain	75
3.1.1 Inner detector DAQ	77
3.1.2 Outer detector DAQ	80
3.1.3 Trigger system	80
3.2 Data Acquisition	82
3.3 Software reconstruction	83

3.3.1	Precalibration, clustering and decoding	86
3.3.2	Energy and position reconstruction	88
3.4	Simulation tools	98
3.5	Calibration with sources	99
3.5.1	Internal calibrations	100
3.5.2	External calibration	104
4	CC neutrino interactions on ^{13}C in high purity liquid scintillators	107
4.1	The physics case	108
4.1.1	Neutrinos on Carbon	110
4.1.2	Cross section of $\nu + ^{13}\text{C}$ reactions	111
4.1.3	Neutrino interactions on ^{13}C	117
4.2	The ^8B solar neutrino flux	118
4.2.1	^8B neutrino signal	119
4.2.2	Event rate expected in Borexino and Kamland	121
4.3	The coincidence detection technique	124
4.4	Backgrounds	125
5	Background sources for the ν CC on ^{13}C interactions rate measurement	127
5.1	Muons and cosmogenic isotopes	127
5.1.1	Muons	127
5.1.2	Cosmogenic isotopes	130
5.2	^{238}U - ^{232}Th contamination	137
5.2.1	^{238}U - ^{232}Th internal contamination	137
5.2.2	External ^{208}Tl	141
5.3	Solar neutrinos	144
5.4	Expected Background in prompt and delayed windows	146
6	Measurement of the neutrino CC interactions rate on ^{13}C in Borexino	147
6.1	Outline	147
6.2	Event selection technique	147
6.3	Data set definition and livetime	148
6.3.1	Filter framework and DSTs	149
6.3.2	Water Extraction runs removal	149
6.3.3	Muons and cosmogenics rejection	151
6.4	Target volume selection	153
6.5	MonteCarlo simulation and efficiencies	156
6.6	Expected signal and background rate	161
6.6.1	Expected and effective signal	161
6.7	Data reduction	165
6.8	The space-time coincidence technique	168
6.8.1	Accidental coincidences and multiplicity cut	170
6.8.2	The correlated background from cosmogenic isotopes	171
6.9	Selected candidates over 4 MeV	175
6.9.1	Selected candidates	176
	Conclusions	181
	A Counting Test Facility	183
	B Radiopurity construction requirements	185
	C Pictures of the detector	187

D	The scintillator and buffer properties	191
E	Cuts to generate DSTs	203
F	Muon Flags	205
G	Selected candidates	207
	Bibliografy	220
	Acknowledgements	221

Abstract

In this dissertation we report the results of the measurement of the solar neutrino charged-current (CC) interactions rate on ^{13}C in Borexino in a period of 646.95 days of livetime and in a 3.3 m fiducial volume. Borexino is a real-time large-volume liquid scintillator detector installed in the underground halls of Laboratori Nazionali del Gran Sasso (LNGS). The detection strategy for the CC events is based on a space and time correlated signals tagging, where the prompt event is due to the neutrino interaction on ^{13}C with ^{13}N production, and the delayed event by the β^+ ^{13}N decay. The proposed detection process has a threshold of 2.22 MeV and a large and well-known cross section. This threshold allows to make a direct measurement of electron neutrinos from ^8B in the pp-chain.

The small isotopic abundance of ^{13}C (1.07%) limits the number of predicted events in the fiducial volume of Borexino: in the Solar Standard Model and neutrino oscillation framework (LMA-MSW) 2.38 ± 0.33 events/year/100t due to neutrino CC interactions on ^{13}C are expected. The tagging for interactions on ^{13}C is challenging due to the long correlation time related to the ^{13}N mean-life of 862.6 sec. Moreover, the spectrum of ^{13}N decay overlaps with that of ^{11}C which is a main source of background in Borexino. In the analysis presented in this dissertation it is shown that the background for the neutrino CC detection is dominated by cosmogenic nuclei produced by muon spallation, in particular the data have shown some not expected feature of the ^{11}C cosmogenic background: high multiplicity of muon-induced neutrons with burst production of ^{11}C nuclei. This feature is of particular importance for our study. We show how critical is the radiopurity of the scintillator and the possibility to veto and tag cosmogenic backgrounds. At present our result is limited by the statistic. The present analysis shows the feasibility of such a detection channel in high purity scintillators with kton scale fiducial mass.



And we can take this huge universe and put it inside a very tiny head: you fold it. -Shpingle-



Introduction

The experimental study of solar neutrinos is one of the main areas of research in neutrino physics. The Sun is a powerful source of electron neutrinos with energy of the order of 1 MeV, produced by weak interactions in the thermonuclear fusion reactions in its core.

Thanks to its proximity, our Sun is unique amongst stars for the fact that a large number of its physical properties are known with a high precision. In fact, astronomers have the opportunity to study in detail dynamic processes occurring in the visible outer stellar layers and to record vast spectroscopic data from the solar photosphere. From the astrophysical point of view the Sun is a main-sequence star which is an ideal candidate to prove our ideas of the internal structure of stars. A well understood and tested model can be transferred to other types of stars and to their evolution.

Solar neutrino astronomy is interesting for the same reason it is difficult: since neutrino interactions with matter is extremely weak, they can reach us from otherwise inaccessible region, where the photons are trapped, permitting us to look inside stars and examine the energetic physical processes that occur in their interiors.

In spite of the extremely large flux of solar neutrinos on Earth ($\sim 6 \cdot 10^{10} \nu \text{ cm}^{-2} \text{ s}^{-1}$), the detection of neutrinos is difficult and requires large detectors because of the small neutrino interaction cross-section. These detectors must be placed underground in order to be shielded by rock from cosmic rays whose interactions in the detector would largely overwhelm the rare solar neutrino interactions.

Over the last decades, the detection of solar neutrinos and helioseismological measurements has provided information about the interior of the Sun and several theoretical models of the solar structure were developed. The so-called Standard Solar Model (SSM), the nuclear energy production and the observed chemical abundances in the photosphere, also makes predictions about the solar neutrino fluxes. The SSM is the standard paradigm for solar neutrino flux calculations.

Since the early beginnings, solar neutrino experiments have faced several discrepancies between the SSM predicted and measured solar neutrino fluxes. First of all, the unexpectedly low rate of solar neutrinos measured in terrestrial neutrino detectors, commonly known as the *Solar Neutrino Problem* was finally solved by demonstrating that solar neutrinos oscillate i.e. the flavor content of solar neutrinos detected on Earth is different from their initial ν_e state when produced in the Sun. This provided the first hint of physics beyond the Standard Model of elementary particle physics and led to a rapidly evolving field of neutrino physics which includes elementary particle physics, astrophysics, cosmology and geology. The Borexino experiment fits into this context.

Borexino is a real-time large-volume liquid scintillator detector installed in the underground halls of Laboratori Nazionali del Gran Sasso (LNGS). The detector is filled with 278 tons of organic liquid scintillator of unprecedented radiopurity, which has the unique possibility to probe solar neutrinos in real time and in the sub-MeV region, but also to detect geo-, reactor- and supernova-antineutrinos.

Thanks to the extreme level of radiological purity of its liquid scintillator target, it has recently measured the flux of ${}^7\text{Be}$ solar neutrinos with better than 5% precision thoroughly testing the current understanding of both neutrino oscillations and how the sun burns; it has also measured the ${}^8\text{B}$ neutrino flux with electron recoil energy threshold of 3.0 MeV. Borexino has also very recently observed the much less abundant pep solar neutrinos and set the most stringent experimental limit on the neutrino flux from the CNO fusion cycle in the Sun. The latter measurement was made possible by novel background suppression techniques whose performance has exceeded the original design performance of the detector. Borexino also provided the first clear observation of geo-neutrinos that are the electron anti-neutrinos produced within the Earth by Uranium and Thorium β decays.

In this dissertation it is reported the work I have done during the PhD at *Università de L'Aquila*, conducted with the Borexino experiment. The main activity during my PhD studies concerned the analysis of Borexino data, in particular the identification of the signal from charged-current (CC) interactions of the ${}^8\text{B}$ solar neutrinos on ${}^{13}\text{C}$ nuclei naturally contained in the scintillator.

The extremely low level of the intrinsic radioactivity of Borexino scintillator, together with the high light yield and large target mass, allow a measurement of the neutrino charged-current interaction rate on ${}^{13}\text{C}$ in Borexino. Albeit event rate is low due to the reduced number of target nuclei, for the natural isotopic abundance of ${}^{13}\text{C}$ of 1.07%, both the CC reaction of ν_e and the NC inelastic scattering are interesting as their thresholds are lower than the interactions of neutrinos on ${}^{12}\text{C}$.

In this thesis I have focused on the CC interactions, which has a larger and much better known cross section, and the advantage of the delayed detection tagging with the ${}^{13}\text{N}$ decay.

The technique used to select the events, is the delayed coincidence, that consists in identifying the solar neutrino signal by exploiting the time and space coincidence with the subsequent decay of the produced ${}^{13}\text{N}$ nuclei. In order to study the optimal cuts for minimizing the background and at the same time maximizing the efficiency for detecting the signal, a dedicated simulation with the Geant-4 based Montecarlo code together with the code that simulates the detector electronics was developed. A study on the background in the region of interests both of accidental and correlated was performed. In particular, I studied the the correlated background from the long lived radioactive isotopes produced in the detector by cosmic muons. This isotopes, mainly ${}^{10}\text{C}$ or ${}^{11}\text{Be}$ and ${}^{11}\text{C}$, can mimic the CC neutrino signature and therefore represent a serious source of background for this measurement.

The dissertation is organized as follows:

- Chapter 1 gives an overview of the physics of solar neutrinos, their oscillations, and the mechanisms of neutrino production in the Sun. The chapter concludes with an overview of some of the questions that still remain in the field.
- The Borexino solar neutrino detector is introduced in Chapter 2. An overview on the neutrino detection reactions in Borexino is presented, followed by a description of the detector components and of the scintillation processes which allow particle identification. The different types of background are discussed and the importance of their suppression is underlined. The physics potentials and results of Borexino conclude the chapter.
- In Chapter 3, a general overview of the Borexino electronics and data acquisition system is presented, giving particular care to the software reconstruction code that has the task of transforming the *raw-data* coming from the detector in the variables that are used in the analysis. It is also given a brief description of the calibration campaigns performed in order to have a better knowledge of the detector response function, of the fiducial mass determination and to tune the Montecarlo simulation code.
- The neutrino interactions on Carbon in organic liquid scintillators, together with an overview on the interaction cross sections are discussed in Chapter 4, showing the merits of detecting neutrinos through the CC interaction on ^{13}C naturally contained in the scintillator. Here it is proposed a technique to tag the solar neutrino events as in [71] that consists in identifying the signal by looking at the time and space coincidence with the decay of the produced ^{13}N nuclei.
- In Chapter 5 a study on the background sources for this measurement is performed, showing that they are mostly due to cosmogenic background from muons and muon-induced production of radioactive nuclides such as ^{10}C and ^{11}C , to ^{238}U - ^{232}Th contamination and to elastic ν -e scattering by solar neutrinos. A summary of the expected background both in the prompt and the delayed signal energy window conclude the Chapter.
- The results of the measurement of the neutrinos CC interaction rate on ^{13}C in Borexino is reported in Chapter 6. The expected rate in the Borexino is $\sim 2.38 \pm 0.3$ ev/year/100t, in the the Standard Solar Model and the MSW-LMA oscillation solution. In order to extract the neutrino candidates we have to perform an accurate reduction of all the backgrounds described in Chapter 5.

First of all, the Borexino data set used in the analysis is selected and is calculated the livetime. Then we perform an energy and radial cut, selecting as active target a sphere of 3.3 m radius and an energy threshold for the prompt signal at 3MeV. This latter cut rejects the external background contamination, consisting basically in the 2.61 MeV gammas from ^{208}Tl coming from the Stainless Steel Sphere (the sphere of 6.5 m radius supporting the photomultipliers). The main contaminants surviving above 3 MeV are cosmogenic isotopes. They are produced

via cosmic muon spallation on the ^{12}C nuclei composing the scintillator. We reject the cosmogenic isotopes with a short decay time applying a 5 s veto after a muon crossing the inner part of the detector.

The study on the efficiency of the selection method chosen for this measurement is done by means of the Borexino Geant4 based Montecarlo code together with the code that simulates the detector electronics. I report the steps to select candidates and it is shown the reduction of the candidates through the application of the cuts.

A study on the accidental and correlated background is performed, taking into account the studies carried out in Chapter 5. Finally it is determined the threshold of the measurement fixed at 4 MeV of visible energy. The results are shown at the end of the Chapter and in the Conclusions.

Chapter 1

Neutrinos and solar physics

The story of neutrinos started in 1930 when Pauli first postulated, in order to conserve energy and spin in the β decay of radioactive nuclei [1], the existence of a neutral particle emitted simultaneously with an electron by decaying nuclei. The neutrino, a neutral weakly interaction fermion, was the perfect solution to explain the observed continuous energy spectrum of the electron without breaking the fundamental physics conservation laws. After almost 80 years since the neutrino was proposed, the neutrino physics represents a great field of modern physics and has implications in particle physics, astrophysics and cosmology.

1.1 Neutrino properties

Since the postulation and then detection (1956, Fred Reines and Clyde Cowan, Savannah River experiment [2]), the neutrinos have been associated with the weak interaction, which accounts for their extremely long penetration lengths in matter and complicates their detection. Nuclear fusion also proceeds via the weak interaction but, unlike fission, is a process that is hard to recreate and observe in a laboratory because of the high temperatures, pressures, and energies involved. The Sun, however, shines huge quantities of energy by the means of thermonuclear fusion and is expected to emit a large number of solar neutrinos, that, because of their interaction with matter, should be detectable on Earth. Solar neutrinos have been observed on Earth, establishing a new and very active research area in both astrophysics and particle physics: solar neutrino physics.

The exotic properties of this particle have surprised physicists more than once: first of all, the unexpected low rate of solar neutrinos measured in terrestrial neutrino detectors, commonly known as the Solar Neutrino Problem (SNP). In fact the measurements of the solar neutrino fluxes on Earth were shown to disagree by many standard deviations with the rates predicted by solar models. This SNP was later solved by allowing transitions between neutrino flavors (see Section 1.1.2).

These transitions, which cause the solar neutrinos produced as electron neutrinos (ν_e) to change into the other two flavors (ν_μ and ν_τ), explained the observed deficit. This quantum mechanical phenomenon, called oscillation, can only occur if neutrinos are mixed, and can only be mixed if they have masses. Thus the SNP was solved and opened the door to another branch of research in

particle physics: neutrino oscillation.

But even after the discovery of neutrino oscillations, a significant number of open question remains: the absolute mass scale of the neutrino mass eigenstates, their hierarchy, the size of the small mixing angle θ_{13} , and the size of the CP violating phase δ in the neutrino mixing matrix are up to now undetermined. Most fundamentally, the nature of the neutrino as a Dirac or Majorana particle is still unknown [3,4].

However, our knowledge of neutrino properties is now precise enough to finally exploit neutrinos for the investigation of their emission sources. While the very small interaction of neutrinos with matter is problematic for detection, it offers an important advantage in the observation of astrophysical objects: unlike the charged particles of cosmic radiation, neutrinos are not deflected by galactic and intergalactic magnetic fields, pointing back at their source. Neutrinos are presently a unique way to directly observe fusion processes in the center of the Sun, the formation of a proto-neutron star hidden inside a stellar envelope, or the production of thermal heat in the deep layers of the Earth.

1.1.1 Neutrinos in the Standard Model

The building blocks of nature, or elementary particles, are classified into half-integer and integer spin particles. The half-integer spin particles are called fermions, divided into quarks and leptons, and integer-spin particles are called bosons. The Standard Model (SM) [5] of particle physics describes the interactions of these elementary particles through a set of gauge bosons, the force carriers, each responsible for specific types of interactions. The Standard Model is therefore a gauge theory, formulated in the framework of quantum field theory, that explains the electromagnetic, weak, and strong interactions. The corresponding local symmetry group is $SU(3)_C \times SU(2)_L \times U(1)_Y$, where C, L and Y are quantum numbers called color, chirality, and hypercharge, respectively. Unlike quarks that carry all three quantum numbers of the theory, the interactions of leptons, like neutri-

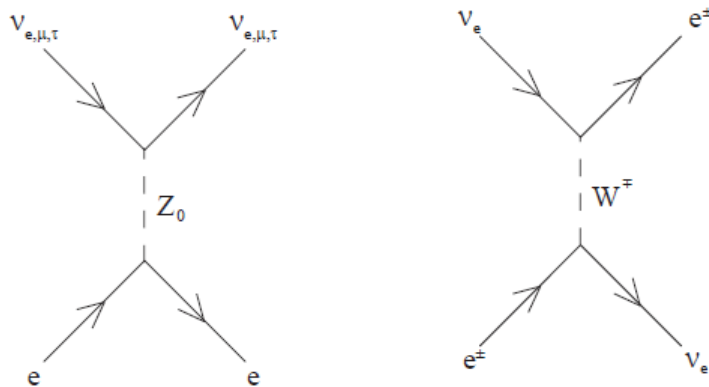


Figure 1.1: First order Feynman diagrams for ν -e scattering. All neutrino flavors scatter via the neutral current reaction (left) while only the electron neutrino can interact through a charged current interaction (right).

neutrinos and electrons, can be described by the electroweak part of the model, $SU(2)_L \times U(1)_Y$, only. The mass of the fermions in the Standard Model are created through the Higgs mechanism, which is the interaction of the fermions with a scalar, spinless, particle, the Higgs boson, that has not been discovered yet in experiments. Neutrinos are chargeless and massless in the minimal Standard Model. Hence in this context the neutrinos neither participate in electromagnetic processes nor interact with the Higgs.

Neutrinos interact through the weak force by coupling to the massive W^\pm and Z_0 bosons. Interactions involving the charged W^\pm bosons are called Charged Current (CC) reactions, and interactions with the neutral Z_0 boson are called Neutral Current (NC) reactions. Experimentally, neutrinos are detected through scattering off electrons or interactions with nuclei. Feynman diagrams for CC electron scattering, NC electron scattering, CC quark (inverse beta decay), and NC quark interactions are shown in Fig. 1.1 and 1.2. Charged current electron scattering can only occur with electron neutrinos. Neutral current scattering involves all three neutrino flavors. Thus an electron neutrino is usually more likely to interact than a muon or tau neutrino.

While the coupling strengths of W^\pm and Z_0 bosons to the weak charge of fermions is comparable to electromagnetic interactions, the fact that the weak exchange bosons are massive ($m_W = 80$ GeV, $m_Z = 92$ GeV) significantly decreases the effective reach and observable strength of the force at low energies: in this regime, neutrino interactions can therefore be described as point-like. The weak interactions responsible for the beta-decay were first introduced by E. Fermi [6]. The Fermi coupling constant $G_F \cong 1.12 \cdot 10^{-5} \text{GeV}^{-2}$ that enters neutrino scattering cross sections quadratically is a rather small quantity: typical cross sections are therefore of the order of 10^{-43} - 10^{-44}cm^2 , see Section 2.4.1. Usually, CC reactions between particles provide larger cross sections than neutral currents (NC).

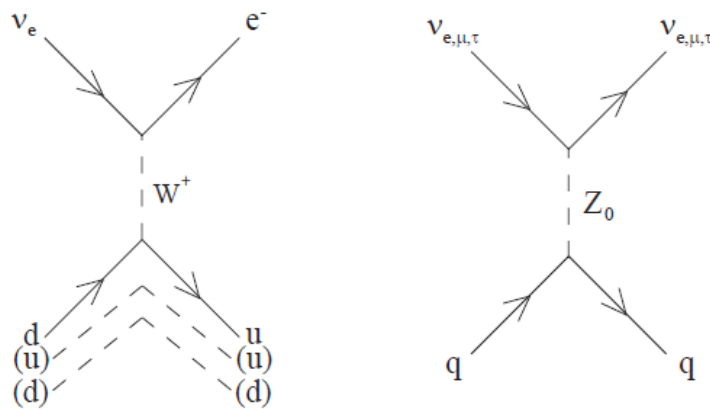


Figure 1.2: First order Feynman diagrams for neutrino nucleon interactions. The interaction on the left shows inverse beta decay $\nu_e + n \rightarrow e^- + p$. The two spectator quarks that do not take place in the interaction are shown in parenthesis. The neutral current interaction on the right applies to all quarks and neutrino flavors.

1.1.2 Beyond the Standard Model

1.1.2.1 Neutrino oscillations

The Standard Model (SM) of particle physics assumes neutrinos to be massless, and therefore, can be described as pure flavor states, that means that an arbitrary neutrino mixture $|\nu\rangle = A_e|\nu_e\rangle + A_\mu|\nu_\mu\rangle + A_\tau|\nu_\tau\rangle$ has only one non-zero A_α coefficient.

However, experimental evidence collected in the last half century, first in the solar physics [7, 8] and then from atmospheric sources [9], revealed a large difference in the neutrino detection rates relative to theoretical calculations, and this difference was irreconcilable with the assumption that the neutrino flavor eigenstates were the eigenstates of their propagation Hamiltonian. The solution to this problem was provided by Pontecorvo in the 1960s [10] postulating the existence of at least one non-zero neutrino mass (and therefore mass eigenstate). The oscillation between weak (flavour) eigenstates was considered by Maki et al.(1962) [11] and Pontecorvo (1967) [12]. If at least one neutrinos is massive, in general the mass eigenstates and the flavour eigenstates may not coincide but they are related by unitary transformation similar to the CKM (Cabibbo-Kobayashi-Maskawa) mixing matrix in the quark sector. If our neutrino detectors on earth are only sensitive to certain neutrino flavors, then this apparent discrepancy can be resolved if the neutrinos have oscillated to a flavor which is undetectable.

In 1978, Wolfenstein observed that *the effect of coherent forward scattering must be taken into account when considering the oscillations of neutrinos traveling through matter* [13]. He discovered that if there exist an interaction through which neutrino can change flavour, the conversion can be enhanced when traveling through matter. In 1985, Mikheyev and Smirnov [14] argued that for specific oscillation and matter density parameters this enhancement could develop a resonance behaviour. This mechanism, known as the Mikheyev-Smirnov-Wolfenstein (MSW) effect, produces large ν_e suppression even with small mixing and in a vast parameter region, and is now widely considered as the most likely solution to the solar neutrino problem.

The phenomenon of the missing solar neutrinos was solved by the SNO experiment after measuring the neutrino flux from the Sun of all flavours of neutrinos [15–17] and comparing it to the other experimental results which only measured the electron flavour neutrino flux. The explanation is the neutrino flavour change on their way from the Sun to the Earth. The experiments that were only sensitive to electron type neutrinos saw less than the predicted flux for all neutrino flavours, whereas the experiment sensitive to all flavours (SNO) was able to measure the complete Standard Solar Model predicted neutrino flux.

The mechanism by which neutrinos oscillate is still an open question in neutrino physics: there are a variety of theories that the available information and measurements support and not enough evidence to determine which model is correct. However, the model that is most widely accepted is the Large Mixing Angle Mikheyev-Smirnov-Wolfenstein (LMA-MSW) model which is supported by solar [18], and reactor [19] neutrino experiments. One of the important predictions of the LMA

MSW model is that the electron neutrino survival probability (the probability that an electron neutrino from the Sun will be detected as an electron neutrino on Earth) will increase at low energies.

Vacuum oscillations

The three neutrino flavor eigenstates $|\nu_\alpha\rangle$ with $\alpha = (e, \mu, \tau)$ are no longer eigenstates of their propagation Hamiltonian, but the propagation is described by an orthogonal basis of mass eigenstates $|\nu_i\rangle$, $i = 1, 2, 3$. The flavor and mass eigenstates can be related by introducing a unitary mixing matrix $U_{\alpha i}$, such that:

$$|\nu_\alpha\rangle = \sum_i U_{\alpha i}^* |\nu_i\rangle \quad |\nu_i\rangle = \sum_\alpha U_{\alpha i} |\nu_\alpha\rangle \quad (1.1)$$

For the three-flavor oscillation a (3x3) rotation matrix known as Maki-Nakagawa-Sakata-Pontecorvo matrix (MNSP matrix) is introduced. Three mixing angles are introduced which are typically denoted by θ_{12} , θ_{23} and θ_{13} . A condition for the observation of neutrino oscillations is that at least one of the angles must be different from $\pi/2$. Moreover, if CP violation occurs one has to introduce a phase δ . In case that the neutrino is its own antiparticle, two additional Majorana phases α and β have to be added:

$$U_{MNSP} = U^{Dirac} e^{i\lambda_M} \quad (1.2)$$

where Majorana part $e^{i\lambda_M}$ is a diagonal matrix with two Majorana phases $\lambda_M = \alpha, \beta$.

$$U_{MNSP} = \begin{pmatrix} c_{12}c_{13} & s_{12}c_{13} & s_{13}e^{-i\delta} \\ -s_{12}c_{23} - c_{12}s_{23}s_{13}e^{i\delta} & c_{12}c_{23} - s_{12}s_{23}s_{13}e^{i\delta} & s_{23}c_{13} \\ s_{12}s_{23} - c_{12}c_{23}s_{13}e^{i\delta} & -c_{12}s_{23} - s_{12}c_{23}s_{13}e^{i\delta} & c_{23}c_{13} \end{pmatrix} \cdot \begin{pmatrix} 1 & 0 & 0 \\ 0 & e^{-i\alpha} & 0 \\ 0 & 0 & e^{-i\beta} \end{pmatrix} \quad (1.3)$$

where $c_{ij} = \cos(\theta_{ij})$ and $s_{ij} = \sin(\theta_{ij})$.

The MNSP-matrix can be expressed in the general form as the product of four separate matrices, to incorporate the unknown Majorana-Dirac nature of neutrinos:

$$U_{MNSP} = \begin{pmatrix} 1 & 0 & 0 \\ 0 & c_{23} & s_{23} \\ 0 & -s_{23} & c_{23} \end{pmatrix} \cdot \begin{pmatrix} c_{13} & 0 & s_{13}e^{-i\delta} \\ 0 & 1 & 0 \\ -s_{13}e^{i\delta} & 0 & c_{13} \end{pmatrix} \cdot \begin{pmatrix} c_{12} & s_{12} & 0 \\ s_{12} & c_{12} & 0 \\ 0 & 0 & 1 \end{pmatrix} \cdot \begin{pmatrix} 1 & 0 & 0 \\ 0 & e^{-i\alpha} & 0 \\ 0 & 0 & e^{-i\beta} \end{pmatrix} \quad (1.4)$$

From equation (1.4) we can clearly see that solar neutrino oscillation is primarily oscillation of ν_e to ν_τ , atmospheric oscillation occurs primarily between ν_μ to ν_τ , and the long baseline experiments primarily observe oscillation from ν_e to ν_τ . In addition to the three mixing angles, the complete neutrino oscillation picture requires knowledge of the Δm^2 , only two of which are independent because $\Delta m_{12}^2 + \Delta m_{23}^2 = \Delta m_{13}^2$. The best-fit values from a global analysis of neutrino data are shown in Table 1.2.

The Majorana phases contribute to an overall phase shift for all neutrino flavors meaning they cannot be measured in oscillation experiments or any experiment involving the kinetic energy of the neutrinos. Therefore in the context of neutrino oscillation, only the Dirac part of the matrix is relevant and the form of the MNSP matrix reduces to $U_{MNSP} = V_{CKM}$.

From standard quantum mechanics, the survival probability for mass state i is given by $|U_{\alpha i}|^2$, and for flavor state α it is $|U_{\alpha i}^*|^2$. In weak interactions, neutrinos are initially produced in a pure flavor state $|\nu_\alpha\rangle$ and we wish to determine the probability that this neutrino changes flavor to state $|\nu_\beta\rangle$ after traveling a distance L .

Expanding the flavour states α, β in their mass eigenstates i , each mass eigenstate contributes its own term, A_i , to the overall probability that is:

$$A_i = U_{\alpha i}^* \Gamma(\nu_i) U_{\beta i} \quad (1.5)$$

$\Gamma(\nu_i)$ is the propagation of the mass eigenstate $|\nu_i\rangle$ traveling at distance L , and is given by the Schrödinger equation and implies that the mass neutrino states evolve in time as plane wave:

$$|\nu_i(t)\rangle = e^{-iE_i t} |\nu_i\rangle \quad (1.6)$$

From calculation in the rest frame of neutrino and then with a Lorentz transformation to the laboratory frame:

$$\Gamma(\nu_i) = e^{-i(E_i t - p_i L)} \quad (1.7)$$

where t and L are the neutrino time-of-flight and the source-detector distance.

At solar neutrino energies E_ν , the neutrinos are ultra-relativistic and the neutrino masses are very small ($m_i \ll E$):

$$\begin{aligned} Et - p_i L &= Et - L\sqrt{E^2 - m_i^2} = Et - L\left(E\sqrt{1 - \frac{m_i^2}{E^2}}\right) \simeq Et - L\left(E - \frac{m_i^2}{2E}\right) \\ &= E(t - L) + \frac{m_i^2 L}{2E} \end{aligned} \quad (1.8)$$

Since the first factor does not affect the overall phase (all of the terms are constant), is possible to neglect it. Inserting the phase into Γ in equation (1.5) we obtain:

$$P(|\nu_\alpha\rangle \rightarrow |\nu_\beta\rangle) = \left| \sum_i U_{\alpha i}^* e^{-i\frac{m_i^2 L}{2E}} U_{\beta i} \right|^2 \quad (1.9)$$

This represent the most general expression of the oscillation probability.

Two-neutrino mixing

The usual treatment of vacuum oscillations is done for the case of just two neutrino species in which we deal with flavor eigenstates ($|\nu_\alpha\rangle, |\nu_\beta\rangle$), mass eigenstates ($|\nu_1\rangle, |\nu_2\rangle$) and the mixing is described by one mixing angle θ .

In many oscillation experiment one of the three mass eigenstate can be neglected because it is slightly coupled to the flavor neutrino produced at the source, due to the mixing angle value. So, only two massive neutrinos and two flavor eigenstates can be considered, well describing the real phenomenon with a useful approximation, as a smaller number of parameters enter the formulas, which become very simple. So, if the two flavors of neutrinos are $|\nu_\alpha\rangle$ and $|\nu_\beta\rangle$, the last one can

coincide with one of the two remaining flavors ($\neq \alpha$) or it can be a linear combination of them. For example, considering solar neutrinos ν_α is the ν_e produced in the Sun and ν_β is a combination of $\nu_\mu - \nu_\tau$, dominated by ν_μ . The two flavor neutrinos are superposition of two mass eigenstates and the mixing matrix in equation (1.3) reduces to:

$$\begin{pmatrix} |\nu_\alpha\rangle \\ |\nu_\beta\rangle \end{pmatrix} = \begin{pmatrix} \cos\theta & \sin\theta \\ -\sin\theta & \cos\theta \end{pmatrix} \cdot \begin{pmatrix} |\nu_1\rangle \\ |\nu_2\rangle \end{pmatrix} \quad (1.10)$$

The propagation of a neutrino born as the eigenstate ν_α can be described by means of the quantum mechanical propagation factor $e^{-i(E_1t - p \cdot x)}$ from the stationary eigenstate solution of the Schrödinger equation, so that

$$|\nu_\alpha(x, t)\rangle = \cos\theta |\nu_1\rangle e^{-i(E_1t - p \cdot x)} + \sin\theta |\nu_2\rangle e^{-i(E_2t - p \cdot x)} \quad (1.11)$$

Assuming the neutrinos to be relativistic and to have small masses, the energy expressed by $E^2 = p_i^2 c^2 + m_i^2 c^4$ can be in most cases Taylor-expanded to $E + m_i^2/2E$. Herein, i stands for $i = 1, 2$. Moreover, the time-dependent probability amplitude for the oscillation of ν_α to ν_β becomes $A(|\nu_\alpha\rangle \rightarrow |\nu_\beta\rangle) = \langle \nu_\beta | \nu_\alpha(t) \rangle$. The oscillation probability $P(|\nu_\alpha\rangle \rightarrow |\nu_\beta\rangle)$ is then defined as

$$P(|\nu_\alpha\rangle \rightarrow |\nu_\beta\rangle) \equiv |A(|\nu_\alpha\rangle \rightarrow |\nu_\beta\rangle)|^2 = |\langle \nu_\beta | \nu_\alpha(t) \rangle|^2 = \sin^2(2\theta) \sin^2 \frac{\Delta m^2 L}{4E} \quad (1.12)$$

with $\Delta m^2 = m_1^2 - m_2^2$ the neutrino mass-squared difference. The probability to observe the ν_α eigenstate is calculated in an analogous way, and turns out to be $1 - |\langle \nu_\beta | \nu_\alpha(t) \rangle|^2$. The equation above depends only on the mixing angle θ , while the second term determines the frequency of the oscillation via a characteristic vacuum oscillation length λ_v , given by

$$\lambda_v = \frac{4\pi E}{\Delta m^2} \quad (1.13)$$

On the other hand, the survival probability is:

$$P(|\nu_\alpha\rangle \rightarrow |\nu_\alpha\rangle) = 1 - P(|\nu_\alpha\rangle \rightarrow |\nu_\beta\rangle) = 1 - \sin^2(2\theta) \sin^2 \frac{\Delta m^2 L}{4E} \quad (1.14)$$

The variable L is the distance between the neutrino source and the detector, commonly referred to as baseline. Equation (1.12) reveals that neutrino oscillations are observable only if at least one neutrino mass m_α is different from zero and simultaneously different from the other mass m_β . This is also true for the three-flavor mixing scenario. It is also possible to note in equation (1.13) that the squared masses Δm^2 are measured by the ratio λ_v/E , this means that oscillation experiments using different neutrino sources and baselines are sensitive to different ranges, as is shown in Table 1.1.

Matter oscillations

The above situation is for vacuum oscillations, but there are also matter oscillations that occur when neutrinos travel through the Earth or Sun on the way to the detector. All flavour types can interact with the Z boson, but only the electron neutrino can interact with the W^\pm boson. The electron type

Source	Energy	Baseline	$\Delta m^2 [\text{eV}^2]$
Sun	0.1-10 MeV	10^{11} m	$10^{-12} - 10^{-10}$
Reactors	1-10 MeV	10 m - 100 Km	10^{-3} -1
Accelerators	0.1-10 GeV	10 m- 10 Km	$10^{-2} - 10^3$
Atmospheric	1-10 GeV	10 - 10^4 Km	10^{-5} -1

Table 1.1: Δm^2 sensitivity for different neutrino sources and indeed for different type of experiments.

neutrino has a larger cross section due to its ability to interact via both the charged current and neutral current interactions. This can significantly change its propagation, resulting in a different probability for flavour changing than in the vacuum. The Mikheyev- Smirnov-Wolfenstein (MSW) effect [20] describes the flavour change that occurs in matter, describing neutrino mass and mixing and neutrino-matter interactions.

This phenomenon was studied for the first time by L. Wolfenstein in 1978 [20], showing that the neutrino flavor oscillation is modified when neutrinos propagate in a medium. The interaction of neutrinos with electrons through coherent forward elastic scattering give rise to a potential that alters the flavor mixing. The oscillation parameters are replaced by effective parameters depending on the medium properties: the effective mixing angle can become large even if the mixing angle in vacuum is small.

In 1985, S.P. Mikheev and A.Yu. Smirnov [14] discovered that the matter effect can lead to a resonant flavor transition, this means that under particular conditions, the effective mixing angle becomes maximal. This effect, known as MSW mechanism, is the key point to explain the solar neutrinos flavor oscillation, in fact, the mixing angle in vacuum relevant for solar neutrinos is large but not maximal, indeed the flavor conversion takes place because of the MSW effect in the interior of the Sun.

If we describe the oscillation in matter in the two-generations approximation, when neutrinos propagate in a medium, they interact with the electrons through the coherent forward elastic weak CC and NC scatterings.

Neutral current interactions (NC) mediated by the Z_0 boson add an additional potential V_{NC} to the existing Hamiltonian H_0 deduced for vacuum oscillations [21]. However, this potential is equal for all three neutrino flavors, and does not change the relative phase difference and the conversion probability of one neutrino flavor into another. Charged current interactions (CC) with electrons in the solar interior, on the other hand, are only possible for ν_e . The potential V_e for ν_e differs from that for the other flavors ν_α , $\alpha = \mu, \tau$, leading to a non-negligible term V_{CC} in the Hamiltonian in matter, $H_m = H_0 + V_{CC}$, where V_{CC} is given by

$$V_{CC} = \sqrt{2}G_F N_e \quad (1.15)$$

where G_F is the Fermi coupling constant and N_e is the electron numerical density.

This potential leads to an extra term in the neutrino oscillation Hamiltonian, whose diagonalization

leads to effective squared mass differences and mixing angles on matter ($\sin^2 2\theta_m, \Delta m_m^2$) which are in general different from the vacuum values ($\sin^2 2\theta, \Delta m^2$).

The vacuum mass matrix used in the basis of $|\nu_e\rangle$ and $|\nu_x\rangle$ is expressed by [22, 23]:

$$M_{vacuum}^2 = \frac{1}{2} \begin{pmatrix} m_1^2 + m_2^2 & 0 \\ 0 & m_1^2 + m_2^2 \end{pmatrix} + \frac{1}{2} \Delta m^2 \begin{pmatrix} \cos 2\theta & \sin 2\theta \\ -\sin 2\theta & \cos 2\theta \end{pmatrix} \quad (1.16)$$

Adding the extra term the Hamiltonian then becomes:

$$i \frac{d}{dt} \begin{pmatrix} |\nu_e\rangle \\ |\nu_x\rangle \end{pmatrix} = -\frac{M_{matter}^2}{2E} \begin{pmatrix} |\nu_e\rangle \\ |\nu_x\rangle \end{pmatrix} \quad (1.17)$$

whit a mass matrix M_m^2 defined as:

$$M_{matter}^2 = \frac{1}{2} \begin{pmatrix} m_1^2 + m_2^2 - \Delta m^2 \cos 2\theta + 4\sqrt{2}G_F N_e E & \Delta m^2 \sin 2\theta \\ \Delta m^2 \sin 2\theta & m_1^2 + m_2^2 + \Delta m^2 \cos 2\theta \end{pmatrix} \quad (1.18)$$

The term $\sqrt{2}G_F N_e E$ is an approximation derived from the relativistic energy-momentum relation $p^2 + m^2 = (E - V_{CC})^2 + V_{CC}^2 \approx E^2 - 2EV_{CC}$ for E^2 much larger then V_{CC}^2 .

After diagonalisation of M_m^2 one obtains two energy eigenvalues, E_1 and E_2 . The related eigenstates $|\nu_{m1}\rangle$ and $|\nu_{m2}\rangle$ are mixtures of $|\nu_e\rangle$ and $|\nu_x\rangle$, which are weighted by coefficients depending on a characteristic mixing angle θ_m , given by

$$\sin^2(2\theta_m) = \frac{\Delta m^2 \sin(2\theta)}{\sqrt{(2\sqrt{2}G_F N_e E - \Delta m^2 \cos(2\theta))^2 + (\Delta m^2 \sin(2\theta))^2}} \quad (1.19)$$

The effective Δm_m^2 turn out to be

$$\Delta m_m^2 = \sqrt{(\Delta m^2 \cos(2\theta) - 2\sqrt{2}G_F N_e E)^2 + (\Delta m^2 \sin(2\theta))^2} \quad (1.20)$$

and the characteristic oscillation lenght in matter becomes $\lambda_m = 4\pi E / \Delta m_m^2$.

The probability to find an electron neutrino $|\nu_e\rangle$ in another flavour state is formally equal to the solution in the vacuum

$$P(|\nu_e\rangle \rightarrow |\nu_\alpha\rangle) = \sin^2(2\theta_m) \cdot \sin^2 \frac{\pi L}{\lambda_m} \quad (1.21)$$

This probability can vary significantly, since a higher electron density N_e and a higher energy E lead to a higher probability. The most interesting implication from equation (1.20) is given by the condition

$$\cos(2\theta) = \frac{2\sqrt{2}G_F N_e E}{\Delta m^2} \quad (1.22)$$

If this case appears, $\sin^2(2\theta_m)$ becomes equal to 1 and it is independent of the value of θ . The mixing angle θ_m must be equal to $\pi/4$, which leads to a maximal mixing of the eigenstates $|\nu_e\rangle$ and $|\nu_x\rangle$. The phenomenon is known as the MSW resonance. This happens if the neutrino energy E is large enough and/or if the electron density in the region that the neutrino passes through is high enough. This energy limit is defined here by E_{min} . Below E_{min} the MSW effect is weak and the

oscillation properties of the neutrinos can be approximated by the vacuum solution.

In the vacuum dominated regime the survival probability P_{ee} is given by

$$P_{ee} = 1 - \frac{1}{2} \sin^2(2\theta) \quad (1.23)$$

while in the matter dominated regime it is

$$P_{ee} = \sin^2(2\theta) \quad (1.24)$$

A transition region around E_{min} between the vacuum and matter enhanced oscillation region is expected.

A further distinction is sometimes required: the electron density N_e might change along the path of the neutrinos, i.e. during their propagation time t . Thus, $N_e = N_e(t)$ and the Hamiltonian becomes time-dependent $H = H(t)$. As a consequence, the mixing angle changes in time and a transition from one eigenstate admixture $|\nu_{m1}\rangle$ to the other $|\nu_{m2}\rangle$ can take place.

Neutrinos from the Sun are ideal probes for the observation of neutrino oscillations in matter (including the MSW effect) and in vacuum. Fig. 1.3 depicts the predicted survival probability of neutrinos of different energies originating from the Sun. In the vacuum dominated regime below 1 MeV one expects $P_{ee} \approx 0.6$, in the matter dominated region above 4 MeV $P_{ee} \approx 0.33$. The values obtained from all solar neutrino experiments so far are also represented. As the potential is a

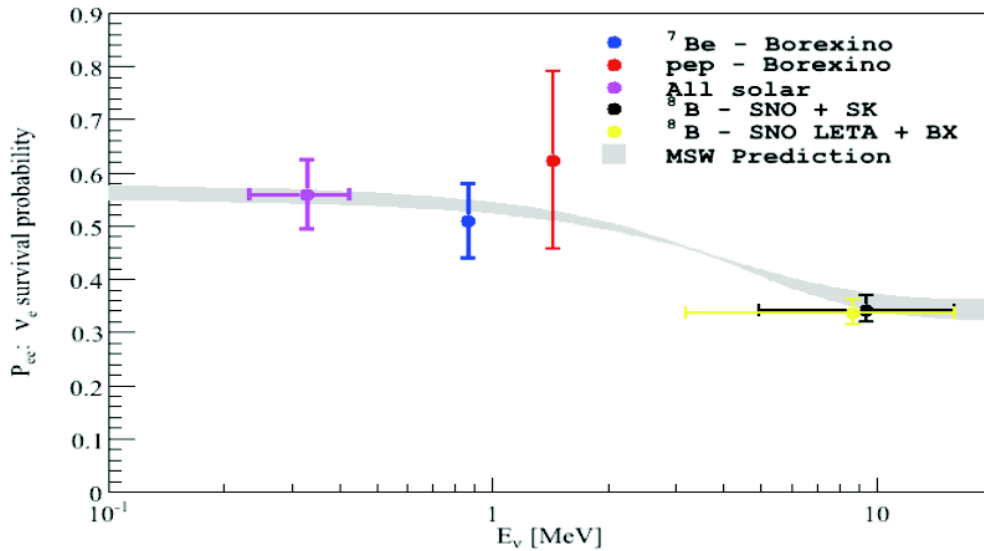


Figure 1.3: Predicted electron neutrino survival probability of solar neutrinos as a function of their energy under the assumption of the standard solar model BPS09(GS98) and the oscillation parameters from the MSW-LMA solution. The predicted curve contains the experimental uncertainty of the oscillations parameters. The results from different solar neutrino experiments are also included showing a good agreement with the predicted curve. In the transition region between matter and vacuum dominated regime a the first measurement is done by Borexino measuring the pep solar neutrino flux (taken from [24]).

function of both the electron density N_e and the neutrino energy E , only part of the solar neutrino

Oscillation parameter	Value
Δm_{21}^2	$7.59 \pm 0.20 \times 10^{-5} \text{eV}^2$
$ \Delta m_{31}^2 $	$2.43 \pm 0.13 \times 10^{-3} \text{eV}^2$
$\sin^2(2\theta_{12})$	0.87 ± 0.03
$\sin^2(2\theta_{23})$	> 0.92
$\sin^2(2\theta_{13})$	< 0.15 CL= 90%

Table 1.2: The current best-fit values of the five neutrino oscillation parameters (neglecting the CP violating phase factor δ). The values are from the recent low energy neutrino analysis [25]. Note the extremely small value for $\sin^2(\theta_{13})$, which makes it possible to neglect $|\nu_e\rangle \rightarrow |\nu_\tau\rangle$ transitions in our discussion of solar neutrino oscillations.

spectrum is undergoing this effect. While both pp and ${}^7\text{Be}$ neutrinos are too low in energy to be affected and undergo only vacuum oscillations, the high-energetic part of the ${}^8\text{B}$ neutrino spectrum is subject to the MSW-effect.

1.1.2.2 Present experimental status

- **The atmospheric evidence.** SuperKamiokande [26] observed disappearance of ν_μ and $\bar{\nu}_\mu$ atmospheric neutrinos, with “infinite” statistical significance ($\sim 17\sigma$). The anomaly is also seen by Macro [27] and other atmospheric experiments. If interpreted as oscillations, one needs $\nu_\mu \rightarrow \nu_\tau$ with quasi-maximal mixing angle. The other possibilities, $\nu_\mu \rightarrow \nu_e$ and $\nu_\mu \rightarrow \nu_s$ cannot explain the anomaly and can only be present as small sub-dominant effects. The SK discovery is confirmed by ν_μ beam experiments as K2K [28]. Table 1.2 reports global fits for oscillation parameters.
- **The solar evidence.** Various experiments [29–32] see a 8σ evidence for a $\sim 50\%$ deficit of solar ν_e . The SNO experiment sees a 5σ evidence for $\nu_e \rightarrow \nu_{\mu,\tau}$ appearance (solar neutrinos have energy much smaller than m_μ and m_τ , so that experiments cannot distinguish ν_μ from ν_τ). The KamLAND experiment [19] sees a 6σ evidence for disappearance of $\bar{\nu}_e$ produced by nuclear reactors. If interpreted as oscillations, one needs a large but not maximal mixing angle, see table 1.1. Other oscillation interpretations in terms of a small mixing angle enhanced by matter effects, or in terms of sterile neutrinos, are excluded.

1.2 Neutrinos: messengers from the Sun

The solution to the question of what powered the Sun was provided in 1930 by Hans Bethe [33]. His theory stated that the only source capable of powering the Sun for the billion years required for our solar system by the age of meteorites and terrestrial rock analysis, are thermonuclear processes occurring in the Sun’s core. In this processes, while most of the energy released is carried by photons, that diffuse to the surface of the Sun and escape in form of sunlight and other radiation, 3% of the energy is emanated in the form of low-energy neutrinos.

The sources of neutrinos are various: ν s are continuously produced through solar fusion reactions, the beta decay of radioactive isotopes, and the interaction of high-energy cosmic rays with the atmosphere. Fusion in the core of the Sun produces neutrinos with a flux at earth of roughly

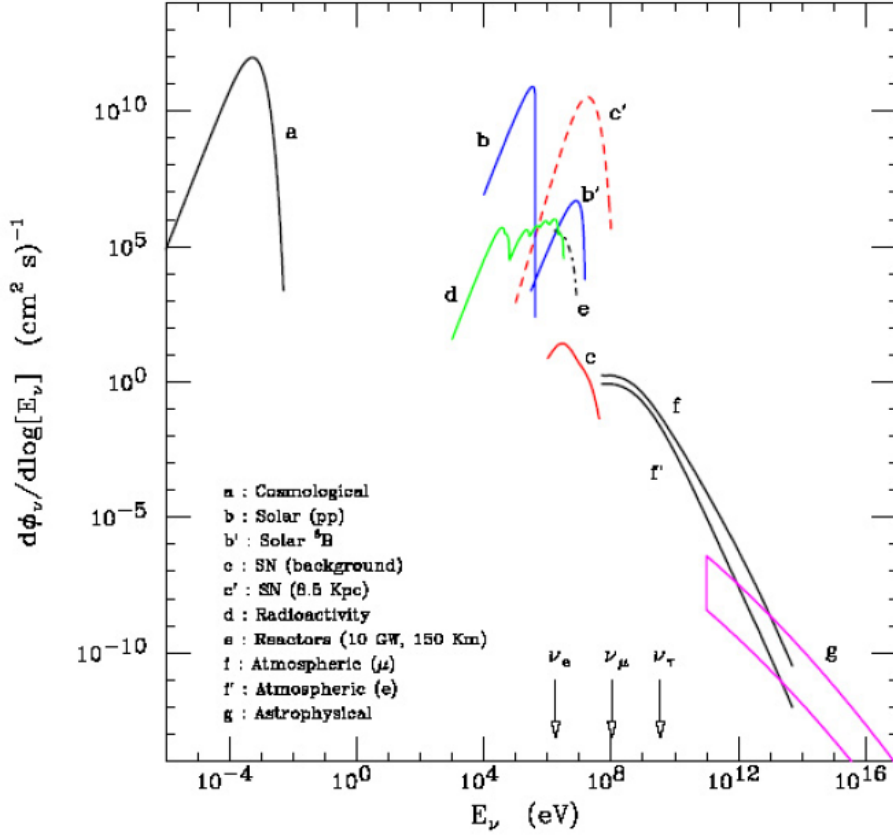
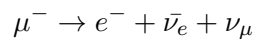
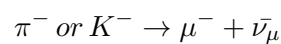
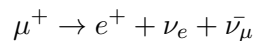
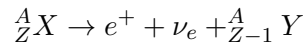


Figure 1.4: The neutrino energy spectra at earth from various sources. From reference [34].

$6 \times 10^{10} \nu/\text{cm}^2/\text{s}$. Terrestrial neutrino sources resulting from weak interactions include natural radioactivity, nuclear reactors whose fission products undergo beta decay, and high energy particle accelerators. Some typical neutrino producing reactions are:



Solar neutrinos in which we are interested, are a result of nuclear reactions in the Sun and are one of the few probes of the solar interior. This is especially interesting as it relates to our Sun and

Source	Type	Average energy	Intensity
Sun	ν_e	0.55 MeV	$10^{38}/\text{s}$ total
Nuclear reactor	$\bar{\nu}_e$	4 MeV	$3 \times 10^{19}/\text{GW}/\text{s}$ [35]
Cosmic rays	ν_e, ν_μ	1 GeV	1 / cm^2/s
Supernova	all	15 MeV	10^{57} collapse
Cosmic ν background	all	164 μeV	$3 \times 10^{12}\text{cm}^2/\text{s}$ [36]
Geoneutrinos	$\bar{\nu}_e$	0.5 MeV	$4 \times 10^6\text{cm}^2/\text{s}$ [37]

Table 1.3: Various sources of neutrinos. The Sun produces neutrinos during nuclear fusion. Fission in nuclear reactors also produces neutrinos. High energy cosmic rays hitting the atmosphere produce a neutrino flux of about 1 / cm^2/s at sea level. Neutrinos produced in the Big Bang that have since cooled now comprise the cosmic neutrino background. Geoneutrinos are produced by the decay of uranium, thorium, and potassium in the ground.

can give very useful information about stellar evolution and stability.

As the Sun produces its energy through thermonuclear reactions, it is a powerful source of electron neutrinos with an averaged energy ~ 0.5 MeV, as shown in Table 1.3 and Fig. 1.4, produced in the thermonuclear fusion reactions in the solar core. Since neutrino interaction with matter is extremely weak, practically all the neutrinos produced in the Sun’s core pass undisturbed through solar interior and flow in space, as J.N.Bachall pointed out: “*Only neutrinos, with their extremely small interaction cross sections, can enable us to see into the interior of a star, and thus verify directly the hypothesis of nuclear energy generation in stars*” [38].

The solar neutrino flux on earth is $\sim 6 \times 10^{10}\text{cm}^{-2}\text{s}^{-1}$, but in spite of this large flux the solar neutrino detection is not easy and requires large detectors because of the small neutrino interaction cross-section. This detectors, as will be explained in the next Chapter, needs to be placed underground in order to be shielded by the rock from cosmic rays whose intersections in the detectors would overwhelm the solar neutrino signal.

The Standard Solar Model (SSM) has been very successful in describing the composition, energy production, and seismology of our Sun and it also gives a detailed description of what the neutrino flux from the Sun should look like, see Fig. 1.7.

Even if solar neutrinos have been studied since many years, there are still some unresolved aspects, some related to the Sun description (see Section 1.2.4) and some related to neutrino oscillations (see Section 1.2.5).

1.2.1 The Standard Solar Model

As described by Bachall in [39], a standard solar model (SSM) is a “*solar model that is constructed with the best available physics and input data*” and is “*required to fit the observed luminosity and radius of the Sun at the present epoch, as well as the observed heavy-element-to-hydrogen ratio at the surface of the Sun*”.

Standard Solar Models (SSMs) are models for Sun-like stars, continuously updated to take in consideration the latest experimental results from every area of physics that is involved in the

modelization. Many SSMs have been constructed by several groups and updated in the course of time as the understanding of the physics of the Sun, the quality and quantity of input data, and computational power have improved. The SSMs that have played the major role in neutrino physics are those developed by Bahcall and collaborators started in 1962 [39–42].

The close distance to the Sun allows a precise measurement of its radius, mass, energy spectrum and luminosity including periodical modulations and its rotation. Moreover, geological surveys of planets and interplanetary material like meteorites have revealed information about the age, stability and composition of the Sun. From the astrophysical point of view the Sun is a main-sequence star which is an ideal candidate to prove our ideas of the internal structure of stars. A well understood and tested model can be transferred to other types of stars and to their evolution. This emphasizes the need to collect information starting from the photosphere and going down to the core of the Sun and to test theoretical predictions.

Recently several experiments have tested the SSM with the helioseismology, that is the science that measures the pressure-mode oscillations of the Sun. From the helioseismological observations is possible to have detailed information on the sound speed and matter density in the interior of the Sun. All this helioseismological data are not used as an input in the construction of the SSMs, therefore there is a beautiful agreement between the SSM predictions and the helioseismological data.

The most commonly accepted solar models (SSMs) [43] are built up according a set of equation of state, on the basis of the following principles:

- **Hydrostatic Equilibrium:** is an assumed condition for the Sun, with the radiative and particle pressures exactly balancing gravity. The gravity force inside the star is supposed to be balanced by the outward pressure of the particle gas. Such an assumption is mandatory in the model, because any deviation from the hydrostatic equilibrium condition would rapidly lead to the collapse or to the explosion of the star.
- **Thermal Equilibrium:** the net energy flux through each layer in the stellar core is balanced by the energy production due to the nuclear reactions; on the contrary of the thermal equilibrium, the hydrostatic one can be violated for long periods during the life of the star: during these phases, energetic equilibrium is granted by the gravitational energy, through contractions and expansions of the star.
- **Radiative Equilibrium:** the total luminosity of the star does not depend on the particular mechanism of energy production, but only on the temperature gradient between the layers of the star; the outward energy flux is mainly due to radiative transport, that is to photons diffusion: for this reason, the opacity of stellar medium is one of the critical parameters of computations.
- **Convective Equilibrium:** whenever the radiative equilibrium is not stable, convective motions are generated inside the star, which allow the reduction of temperature gradients inside the single layers; these convective motions provide, on the other hand, an effective mixing of

the material inside each convective zone: this mechanism produces then a chemical homogeneity on a macroscopic scale.

- **Only nuclear reactions can provide a modification in isotopic abundances:** Energy generation in the Sun is by nuclear fusion, burning hydrogen fuel. The Sun initially was homogeneous in composition; and only over time with nuclear fusion have local abundances of isotopes changed in the solar interior, while the outer layers of the Sun maintain the original composition [44].

The Solar Models are the interactive resolution of a set of state equations, that are the equations describing the above mentioned equilibrium conditions, based on the fundamental assumption that the Sun is a star of the Main Sequence and, spherical and in hydrostatic equilibrium between gravity and the radiative pressure produced by the thermonuclear reactions in its core. The luminosity, the radius, the age and the mass of the Sun are boundary condition, while the input data are provided by the energies and cross sections of the nuclear reactions involved. The system of equation is then solved interactively until there is an agreement between the model and the boundary conditions. The boundary conditions, such as the present mass, total luminosity, radius and age of the Sun are:

- Mass: $M_{\odot} = 1.99 \cdot 10^{33}$ g
- Luminosity: $L_{\odot} = 3.844 \cdot 10^{33}$ erg/sec
- Radius: $R_{\odot} = 6.96 \cdot 10^{10}$ cm
- Age: $t_{\odot} = 4.57 \cdot 10^9$ y

Three parameter are the left free in the construction of the SSM: the initial helium and metals abundance and a parameter used in the modelization of the convective energy transport. After the interaction, the successful model has to match the present physical properties of the Sun like radius, abundance and luminosity. Is also possible to made predictions about neutrino fluxes from nuclear reactions, the speed of sound and so on, that can be tested with direct measurements or compared with helioseismological observation.

1.2.2 Nuclear reactions in the Sun

As already mentioned, the thermal equilibrium of the Sun is granted by the energy produced in nuclear reactions. The main reactions (98% of the total energy) belong to the proton-proton (p-p) chain in Fig. 1.5; its energy balance gives:



The 3% of the released energy is transformed into neutrinos kinetic energy. The second chain,

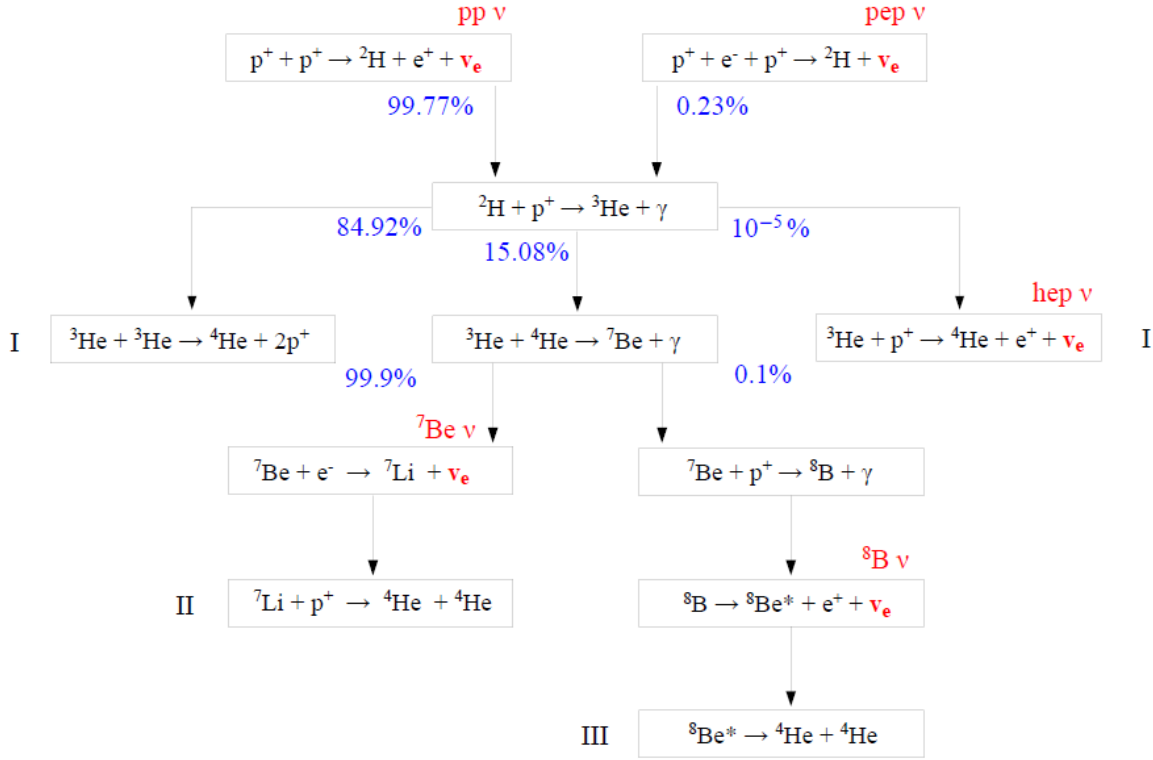


Figure 1.5: The proton-proton chain.

hypothesized by Bethe in 1939, is the Carbon-Nitrogen- Oxygen cycle (CNO), in shown in Fig 1.6, the energy balance is similar to the previous one, but is mediated by the ${}^{12}\text{C}$:

$$4p \rightarrow {}^4\text{He} + 2e^+ + 2\nu_e + 25.3\text{MeV} \quad (1.30)$$

The slightly lower energy gain in this second cycle is due to the major contribution to neutrinos kinetic energy. Most of the solar models assume the CNO cycle to contribute only marginally to the luminosity of our star: this assumption is confirmed by the study of isotopic abundances inside the Sun (isotopic abundances are extrapolated from stellar atmosphere composition, which can be observed directly) and, more recently, from precise measurements of solar neutrino fluxes [45].

The pp chain

The hydrogen burning in the Sun occurs mainly within the pp chain, where there is a fusion of two protons. The pp chain is typically divided into three branches, as shown in Fig. 1.5. The first step of the chain is one of the two following reactions with the relative branching ratios:

$$p + p \rightarrow {}^2\text{H} + e^+ + \nu_e \quad 99.8\% \quad (1.31)$$

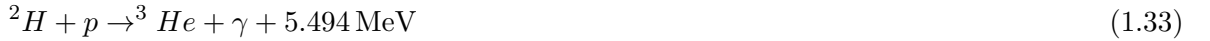
$$p + e^+ + p \rightarrow {}^2\text{H} + \nu_e \quad 0.2\% \quad (1.32)$$

Both reactions produce neutrinos that are named according to the particles involved in the fusion process. The pp neutrinos represent the largest solar neutrino flux.

The endpoint energy is at 0.42 MeV. The pep neutrinos are mono-energetic with an energy of 1.44

MeV. The flux of pep neutrinos is ~ 400 times weaker than that of the pp neutrinos due to the fact that not two but three particles have to interact at the same time. The energy spectrum for the pp neutrinos is a continuum with an endpoint at about 420 keV, however the direct measurement of such a low energy neutrino is very complicated due to the presence of naturally occurring background in the energy region of interest. The pep neutrinos on the contrary are mono-energetic at 1.44 MeV, and therefore lie above the vast majority of naturally occurring background, and a direct measurement is a slightly easier task. For the moment only Borexino succeeded in measuring it [24]. Nevertheless, taking into account that both reactions have an almost identical matrix element, both neutrino fluxes are strictly correlated. Thus a measurement of the pep neutrinos can constrain the pp flux and moreover, pep neutrinos can test the MSW effect in the transition region between matter and vacuum dominated regime expected in the interval around 1-3 MeV (see Fig. 1.3).

The generated deuterium nuclei is quickly captured by a free proton via:



As it is shown in Fig. 1.5 the created ${}^3\text{He}$ nuclei can undergo three different fusion processes:

1. In $\sim 85\%$ of cases there is a fusion of two ${}^3\text{He}$ nuclei:



The chain is completed at this point is reached.

2. For the $\sim 15\%$ of the cases a ${}^3\text{He}$ find a ${}^4\text{He}$ nucleus and undergo:



3. The very rare reaction is the one that releases the so-called hep neutrinos:



The chain would also conclude at this point since a helium nucleus is produced.

The hep neutrino flux is the weakest compared to all other solar neutrino fluxes but at the same time the highest energetic neutrino type. Reactions (1.34) and (1.36) terminate by releasing ${}^4\text{He}$ atoms which do not fuse further, while the reaction (1.35) ends in two different branches pp-II and pp-III.

After the conclusion of the pp-I branch, there is only the reaction (1.35) that has not led to a termination. If a pp-I branch results in ${}^7\text{Be}$, then the chain continues with the pp-II and pp-III branches with two possible interactions to burn the ${}^7\text{Be}$:

1. The majority of the time the ${}^7\text{Be}$ undergo first an electron capture:



under the emission of the mono-energetic ${}^7\text{Be}$ neutrinos at the energies of 0.38 MeV and 0.862 MeV, since the electron capture can occur both to the ground state and the first excited state of ${}^7\text{Li}$.

Once the ${}^7\text{Li}$ has been produced it quickly captures a free proton:



2. For the 0.016% of the time, the ${}^7\text{Be}$ captures a proton in the reaction:



The ${}^8\text{B}$ produced is unstable and β^+ -decay under release the ${}^8\text{B}$ neutrinos:



The CNO chain

The CNO cycle represents a second fusion mechanism that burns hydrogen into helium, depicted in Fig. 1.6. The elements C, N, O act as catalysts. Due to the high Coulomb barriers of the mentioned elements the CNO cycle plays a secondary role in the actual energy production of the Sun. Only at high central temperatures ($T_C > 2 \times 10^7$ K for $M \geq M_\odot$) and high C,N,O abundances the CNO cycle becomes dominant. In stars significantly larger than the Sun, the core temperature is high enough for the participating particles to overcome the Coulomb barrier and thus for the CNO cycle to become the dominant energy production scheme. This high degree of correlation to the core temperature introduces significant uncertainty in the CNO fluxes.

It consists of a main and a secondary loop. They include three reactions emitting neutrinos which are commonly referred to as CNO neutrinos.

The cycle begins with a ${}^{12}\text{C}$ nucleus capturing a free proton to form radioactive ${}^{13}\text{N}$ that then decaying produces a neutrino:



The neutrino produced has a continuous spectrum up to $2.221 - 2 \cdot 0.511 = 1.199$ MeV. The reaction continues with the decay of ${}^{13}\text{C}$ until it reaches a branching point after the production of ${}^{15}\text{N}$:



The neutrino produced has a continuous energy spectrum with an endpoint given by the Q value minus the energy of the annihilation gammas: 1.732 MeV. At this point, the ${}^{15}\text{N}$ can decay by one of two channels.

The channel with higher branching ratio, 99.9%, proceeds via:



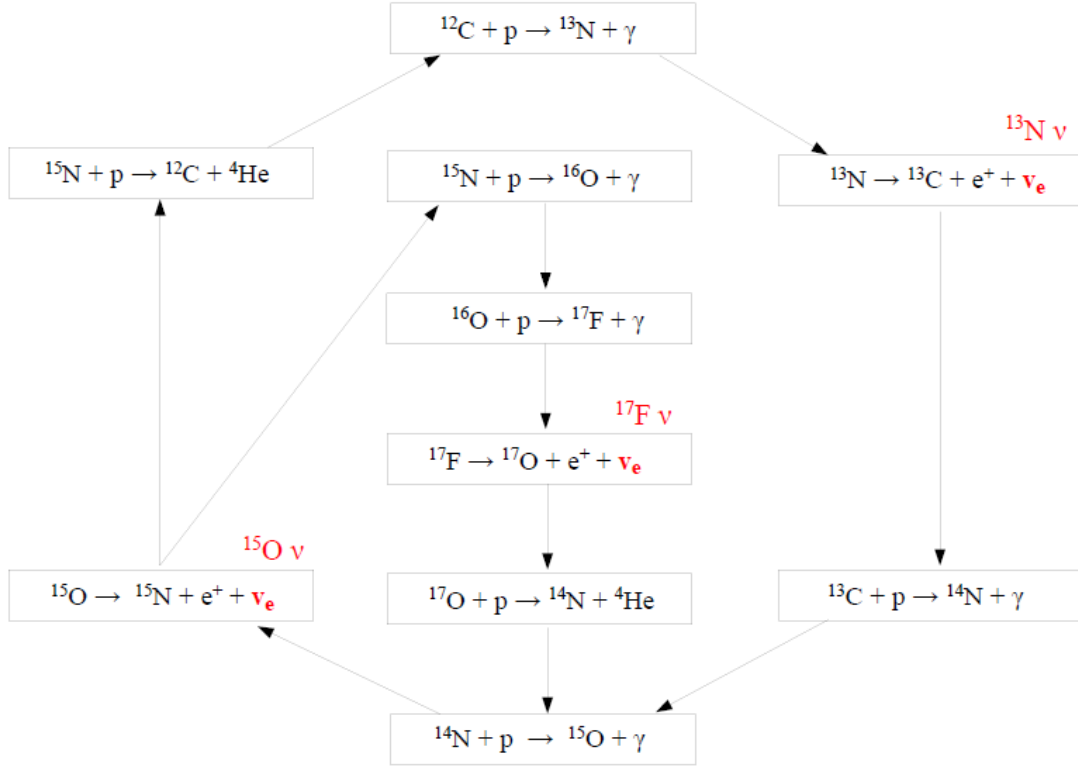


Figure 1.6: Representation of the solar fusion reactions in the CNO cycle.

This ^{12}C produced is now available to begin the chain again at reaction (1.42).

The other possible method of burning the ^{15}N proceeds at much lower rate because the temperature in the core is not sufficient to appreciably burn it.



Only in 0.01% of the cases the CNO chain produces a neutrino from the decay of ^{17}F , thus the flux is much lower. In Fig. 1.7 are shown also the fluxes of neutrinos from CNO cycle.

In Table 1.4 are shown the reaction in the Sun, the energy of the neutrinos emitted in the reactions and the percentage of the solar neutrino flux.

1.2.3 Solar neutrino fluxes

The interpretation of solar neutrino experiments relies on a theoretical model of the Sun which predicts the neutrino fluxes, along with their spectral composition (since the energy of emitted neutrinos depends on the particular reaction that produces them, the spectral distribution is a crucial point of solar models). The solar neutrino energy spectra predicted by the SSM is depicted in Fig. 1.7. It is based on the calculation by J.Bachall and collaborators using the best available

Reaction		Energy	Fraction (%)
$p + p \rightarrow {}^2\text{H} + e^+ \nu_e$	pp	0 → 0.42	91.3
$p + p + e^- \rightarrow {}^2\text{H} + \nu_e$	pep	1.44	0.216
${}^3\text{H} + p \rightarrow {}^3\text{He} + e^+ + \nu_e$	hep	0 → 18	10^{-5}
${}^7\text{Be} + e^- \rightarrow {}^7\text{Li} + \gamma$	${}^7\text{Be}$	0.862 (90%) 0.38 (10%)	7.76
${}^8\text{B} \rightarrow {}^2\text{H} + {}^4\text{He} + e^+ + \nu_e$	${}^8\text{B}$	0 → 14.06	0.009
${}^{13}\text{N} \rightarrow {}^{13}\text{C} + e^+ + \nu_e$	${}^{13}\text{N}$	0 → 1.2	0.431
${}^{15}\text{O} \rightarrow {}^{15}\text{N} + e^+ + \nu_e$	${}^{15}\text{O}$	0 → 1.7	0.319
${}^{17}\text{Fe} \rightarrow {}^{17}\text{O} + e^+ + \nu_e$	${}^{17}\text{Fe}$	0 → 1.7	0.009

Table 1.4: The reactions in the Sun that produces neutrinos, the energy range of the neutrinos produced and the percentage of the solar neutrino flux they represent.

ν flux	GS98	AGSS09	Change from GS98 (%)	Solar
pp	$5.98 (1 \pm 0.006) \times 10^{10}$	$6.03 (1 \pm 0.006) \times 10^{10}$	0.8	$6.05 ({}_{-0.011}^{0.003}) \times 10^{10}$
pep	$1.44 (1 \pm 0.012) \times 10^8$	$1.47 (1 \pm 0.012) \times 10^8$	2.0	$1.46 ({}_{-0.014}^{0.010}) \times 10^8$
hep	$8.04 (1 \pm 0.30) \times 10^3$	$8.31 (1 \pm 0.30) \times 10^3$	3.4	$18 ({}_{-0.5}^{0.4}) \times 10^3$
${}^7\text{Be}$	$5.00 (1 \pm 0.07) \times 10^9$	$4.56 (1 \pm 0.07) \times 10^9$	-8.8	$4.82 ({}_{-0.04}^{0.05}) \times 10^9$
${}^8\text{B}$	$5.58 (1 \pm 0.14) \times 10^6$	$4.59 (1 \pm 0.14) \times 10^6$	-17.7	$5.00 (1 \pm 0.03) \times 10^6$
${}^{13}\text{N}$	$2.96 (1 \pm 0.14) \times 10^8$	$2.17 (1 \pm 0.14) \times 10^8$	-26.7	$\leq 6.7 \times 10^8$
${}^{15}\text{O}$	$2.23 (1 \pm 0.15) \times 10^8$	$1.56 (1 \pm 0.15) \times 10^8$	-30.0	$\leq 3.2 \times 10^8$
${}^{17}\text{Fe}$	$5.52 (1 \pm 0.17) \times 10^6$	$3.40 (1 \pm 0.16) \times 10^6$	-38.4	$\leq 59 \times 10^6$

Table 1.5: Predicted solar neutrino fluxes from the standard solar model GS98 and AGSS09 [47–49]. Neutrino fluxes are given in units of $\text{cm}^{-2}\text{s}^{-1}$. The column entitled *Solar* are the neutrino fluxes inferred from all available neutrino data (Borexino collaboration 2011) [47].

physics and input data up to 2008. The expected fluxes of neutrino from all solar fusion reactions are given at the average distance of the Earth from the Sun corresponding to one Astronomical Unit (AU). The total flux is $6.6 \times 10^{10} \text{ cm}^{-2}\text{s}^{-1}$ making the Sun an intense source of low energetic neutrinos.

1.2.4 Solar abundance problem

Nowadays one of the bigger controversy about in the solar models scenario is about the solar chemical composition. The solar metallicity is the abundance of the elements heavier than helium, and can be inferred both from meteorites and from the solar photospheric spectrum. In solar astrophysics, the mass fraction of hydrogen is labeled as X, the mass fraction of helium is labeled as Y, and the summed mass fraction of all other elements is known as the metallicity, Z.

The typical process for constructing a solar model is to evolve a main sequence star to the age of the Sun under the constraints that after the lifetime of the Sun, it has reached the present size,

luminosity, and current ratio of metallicities Z/X in the photosphere (the present day photospheric abundances are assumed to reflect the initial solar abundances). The study performed by Asplund, Grevesse, and Sauval published in 2005 (AGS05 [50]) initiated what is now referred to as the "solar abundance problem".

In Table 1.5 are shown the solar neutrino fluxes for the reactions of the pp and CNO cycles for the various neutrino source, the different columns for the fluxes assumes different values for the metallicity as evaluated in different studies in 1998 and 2009.

The solar model based on the solar abundances obtained from the study performed by Grevesse and Sauval in 1998 (GS98 [51]) is commonly referred to as the *High-Z* model and is the only one which is in agreement with the helioseismology measurements performed by Basu and collaborators [52]. The AGSS09 model is an update of the AGS05 model, known as the *Low-Z* model due to a change in the photospheric ratio Z/X of almost 30%, the net result of which is a lower core temperature for the AGS05 solar models. The Beryllium and especially the Boron solar neutrino fluxes are highly dependent on the core temperature ($\Phi_{(8B)} \propto T^{18}$), thus the neutrino fluxes dropped considerably for these two neutrino sources for the solar models based on these results. Since less energy is released by the ${}^7\text{Be}$ solar neutrinos for the lower metallicity case, this change must be compensated by an increase in the other prominent reaction, the pp neutrinos.

This update to the solar abundances published by Asplund, Grevesse, Sauval, and Scott in 2009 (AGSS09 [53]) determines a value for Z/X which is slightly higher than the AGS05 numbers, but

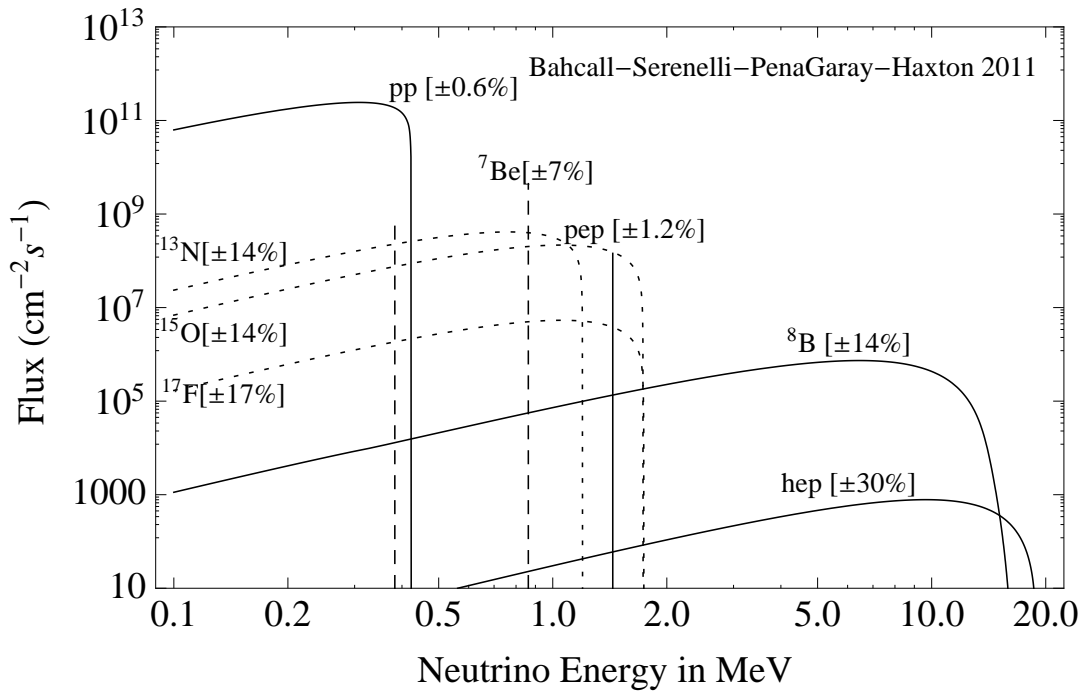


Figure 1.7: The predicted solar neutrino energy spectrum according to the standard solar model taken from SSM BPS(GS98) 2008 [47]. The neutrino fluxes are given for a distance of 1 AU from the Sun. The units are $\text{cm}^{-2}\text{s}^{-1}\text{MeV}^{-1}$ for continuum neutrino sources and $\text{cm}^{-2}\text{s}^{-1}$ for mono-energetic neutrino sources.

is still $\sim 22\%$ lower than the GS98 abundances. The solar abundances may be determined by two complementary methods: one is via the mass spectroscopy of meteorites (assumed to have the same composition as the Sun), the other is through identification of the Fraunhofer lines in the visible spectrum from the photosphere. Until recently, the meteoritic method was preferred over the photospheric one due to problems with the accuracy of the photospheric method. However, in the AGS09 paper, the authors published Z/X for both meteoritic and photospheric abundances and they were in excellent overall agreement. However, the individual elemental abundances for some of the heavier elements do show a difference from the meteoritic abundances. See reference [54] for a more complete discussion on the flux differences between the two sets of abundances.

The crux of the solar abundance problem is the incompatibility between the best solar atmosphere model and the best solar interior model, since the AGS09 solar abundance model would presumably reflect the current best-estimate of the metallicity of the Sun, however, these data are at odds with the independent measurements of the density structure of the solar interior by way of helioseismology [52].

The solar model constructed with AGS05 metallicities has a 5.5σ discrepancy for the surface helium abundance (Y_S) relative to helioseismological results, and a 15σ discrepancy for the depth of the convective envelop (R_{CZ}/R_\odot), the differences have decreased to 5σ and 11σ [53] for the solar model based on the AGS09 abundances.

Solar neutrinos now play a very important role in that they provide the only method currently available to distinguish between the different abundances. As shown in the 4th column of table 1.5, the drop in metallicity cause a 9% reduction in the ${}^7\text{Be}$ flux, the decrease is larger for ${}^8\text{B}$ neutrinos and for neutrinos produced in the CNO cycle. The differences in the neutrino fluxes are as large as $\sim 40\%$ for components of the CNO cycle, and $\sim 20\%$ for the ${}^8\text{B}$ neutrinos in the pp chain. However, due to the uncertainty of the models, even a precise measurement of ${}^7\text{Be}$ or ${}^8\text{B}$ neutrino flux is not enough to discriminate between models. Instead with a CNO measurement, could be possible to determine the solar core composition since CNO neutrinos are the most sensitive to the difference in metallicity. Borexino has published in [24] an upper limit on the CNO flux.

1.2.5 Electron neutrino survival probability

As described in Section 1.1.2.1, matter interaction effects influence the pattern of neutrino oscillations in the Sun, since the neutrino matter interaction cross sections are flavor dependent and the matter distribution in the Sun contains only first generation particles (electrons). The oscillation theory in the LMA-MSW scenario predicts a behaviour of the electron neutrino survival probability (P_{ee}) that is a function of the neutrino energy:

- at low energies ($E < 1\text{MeV}$) the oscillation mechanism is the same as in the vacuum and $P_{ee} \sim 60\%$,

- at high energies ($E > 5 \text{ MeV}$) the oscillations are dominated by matter effects during the travel through the Sun, and P_{ee} decreases down to 30%.

Real time Čerenkov experiments like SNO and SuperKamiokande can measure the solar neutrino fluxes with an higher threshold ($\sim 5 \text{ MeV}$) because of the low light yield and the high intrinsic background. In this way they are only sensitive to ${}^8\text{B}$ solar neutrinos and can investigate only the matter-enhanced region of neutrino oscillations. In 2008 the Borexino collaboration published the measurement of ${}^7\text{Be}$ solar neutrino flux investigating in real-time the vacuum region and giving a strong constraint on the pp value [55]. In 2008 the situation of the P_{ee} mapping is shown in Fig. 1.8 where is possible to note that the transition region between 1 and 4 MeV was not yet explored. As will be explained in Section 2.7 new experimental points have been added thanks

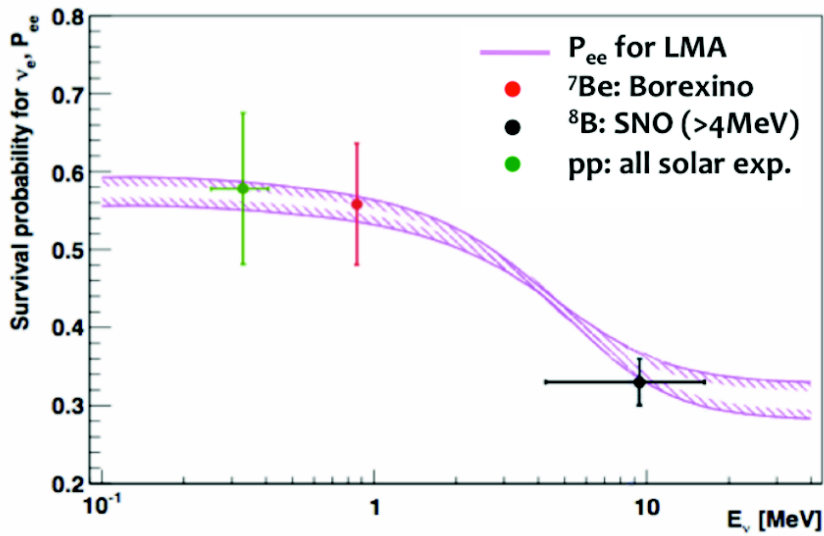


Figure 1.8: Electron neutrino survival probability as function of the neutrino energy, assuming the BPS09(GS98) Standard Solar Model [54,56] and the oscillation parameters from the MSW-LMA solution $\Delta m^2 = 7.69 \cdot 10^{-5} \text{ eV}^2$ and $\sin^2 2\theta_{12} = 0.87$ [25]. Dots represent the experimental results: ${}^7\text{Be}$ by Borexino (red), ${}^8\text{B}$ from SNO (black) and pp from all the solar neutrino experiments (green).

to the ${}^8\text{B}$ solar neutrino measurements performed by Borexino [57] and SNO [58] experiments. Borexino has also reduced the error on the ${}^7\text{Be}$ flux [59] and published the first pep solar neutrino measurement [24]. The situation on the mapping of the P_{ee} in 2011 is shown in Fig. 1.3. To validate completely the MSW-LMA solution the transition region has to be investigated with more accurate measurement of low energy solar neutrinos.

Chapter 2

The Borexino Experiment

2.1 Overview

Borexino is a real-time large-volume liquid scintillator detector installed in the underground halls of Laboratori Nazionali del Gran Sasso (LNGS) in central Italy . The Borexino proposal dates back to 1991 [60,61], in connection with the so called solar neutrino problems, whose predicted solutions were then either an experimental problem, or difficulties in the solar modeling or in the neutrino propagation description.

After several years of construction, data taking started in May 2007, providing immediately the evidence of the unprecedented radiopurity of the target mass. Borexino is the first experiment to measure in real time low-energy solar neutrinos below 1 MeV. The high light yield of the liquid scintillator and the extreme radiopurity achieved during the purification processes allow the real-time detection of solar neutrinos down to about 200 keV of electron recoil energy, being limited below this value by the presence of the unavoidable ^{14}C background.

In three years of data taking, the main results include the measurements of the ^7Be solar neutrino flux [55] and that of the ^8B neutrino with electron recoil energy threshold of 3.0 MeV [57]. Borexino also provided the first clear observation of geo-neutrinos [62](antineutrinos from the Earth) and sets the world best limits on hypothetical antineutrino fluxes from the Sun (assuming undistorted ^8B spectrum) and from unknown sources in the energy range of 1.8 to 17.8 MeV [63]. Borexino has completed in 2009 a large calibration campaign, that has lead to better results on ^7Be solar neutrino measurement [59] and the absence of the day-night asymmetry [64]; a better understanding of the detector has also allowed the achievement of the detection of solar CNO and pep neutrinos [24].

At the moment Borexino is almost entering in his fifth year of continuous data taking. Originally proposed by R.S. Raghavan in 1989, the BOREX experiment was going to be a detector filled with several kilotons of a trimethylborate scintillator capable of measuring the ^8B solar neutrinos [65]. Neutral current interactions would lead to nuclear de-excitations of the ^{11}B in the scintillator, while the charged current neutrino capture reactions would lead to production of the positron emitting ^{11}C . The Borexino experiment was to be the 100 ton fiducial mass prototype for

the BOREX experiment.

However, it was quickly realized that, if a scintillator could be purified sufficiently, an experiment such as Borexino with a 100 ton fiducial mass could be an effective detector for the much higher rate ${}^7\text{Be}$ neutrinos.

A one ton fiducial mass prototype (see picture in Appendix A), the Counting Test Facility (CTF), was constructed in the middle of the 90s with the task of demonstrating the feasibility of large scale purification of organic liquid scintillators to the levels required for ${}^7\text{Be}$ neutrinos detection. After successful demonstration of the purification techniques used, construction of the Borexino detector began in 1998. Finally, in late 2006, the filling process of Borexino began, first with water, and then with scintillator. After nine months of filling, data taking began with a full detector on May 15, 2007. In Fig. C.4 of Appendix C are shown the phases of the detector filling.

As already pointed out in the Chapter 1, the motivations that drive a solar neutrino experiment are twofold:

- a better understanding of physics of neutrino oscillation since a precision measurements of solar neutrino fluxes can help map out the transition region sensitive to new physics,
- a better understanding of solar physics since a spectroscopic measurement of the different solar neutrino rates can verify the Standard Solar Model predictions, rule out accretion scenarios and help determine the core C+N abundance.

2.2 Location: Laboratori Nazionali del Gran Sasso

The study of neutrino properties from natural and artificial sources requires capability of detecting extremely weak effects. Underground laboratories provide the necessary low radioactive background environment to investigate these processes. These laboratories appear complementary to those with accelerators in the basic research of the elementary constituents of matter, of their interactions and symmetries.

As explained in Chapter 1, there are two classes of motivations to push beyond the Standard Model: There are *particle physics* reasons: the SM does not truly unify the elementary interactions, it leaves the problem of fermion masses and mixing unsolved and it exhibits the gauge hierarchy problem in the scalar sector, and there are “astroparticle physics” issues as the problems of the solar and atmospheric neutrinos deficits and the Majorana or Dirac nature of neutrinos. These astroparticle physics issues can be faced by contemporary experimental physics and constitute a formidable motivation for the underground laboratories activity.

In underground physics the struggle to go beyond the standard model is the struggle for background control and reduction. Environment is the principal source of background: the environmental backgrounds of the laboratory depend on the depth and on the nature of the surrounding rocks and, as a consequence, may differ in the different facilities:

- the high-energy cosmic rays muons flux decreases almost exponentially with increasing depth, this being the main reason to go underground;
- the neutron flux at low energies is mainly due to fission and (α, n) from Uranium and Thorium in the rocks. As such, it depends on local geology, but becomes depth-independent, already at shallow depth;
- muon spallation processes are negligible at low (MeV) energies but produce a depth-dependent flux of high-energy (GeV) neutrons;
- the gamma flux, including radon and its progeny, depends again on local geology and is practically depth independent;
- other sources of backgrounds, the ultimate contribution in some cases, include the detector materials, supports, shielding, electrical connections, etc;
- cosmic rays may produce traces of radioactive nuclides both during the construction phase of the detectors and of its materials on the surface and during the operational phase underground.

The INFN Laboratori Nazionali del Gran Sasso (LNGS) [66] are located besides a freeway tunnel under the Apennines, in central Italy near the town of L'Aquila, 120 km from Rome; they consist of the external laboratories, Fig. 2.1, and of three underground halls, Fig 2.2. The proposal to build a large, high technology, underground laboratory was advanced in 1979 by Antonino Zichichi, then President of INFN, and approved by the Italian Parliament in 1982. Since the original project the orientation of the three laboratory halls was towards CERN, in order to host detectors to study neutrino oscillations on a future beam produced at that laboratory. Civil engineering works, under the responsibility of ANAS, the Italian Road Department, started in autumn 1982 and were completed by 1987. In Fig 2.3 is pictured one of the three underground halls in LNGS during the



Figure 2.1: Picture of the external LNGS laboratories.

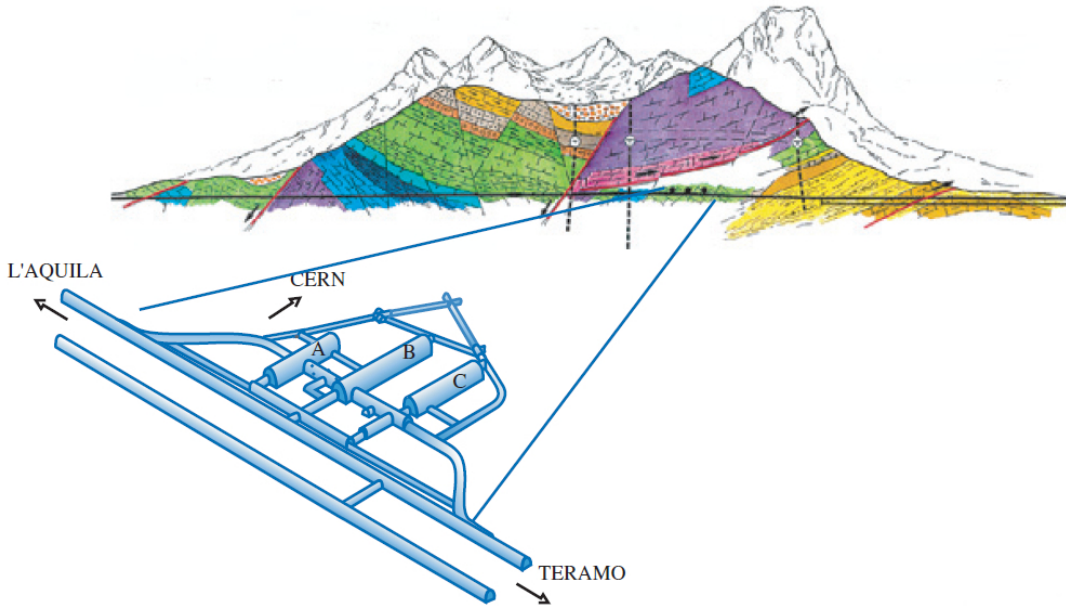


Figure 2.2: The underground facilities and the Gran Sasso massif geology. The direction of CERN is indicated due to the CERN to LNGS (CNGS) neutrino beam used for the OPERA experiment which sits directly in front of Borexino in Hall C.

excavation and after.

The massive natural rock shielding of the Gran Sasso laboratory provides a μ flux attenuation of 10^6 in hall C down to $1.2 \mu/\text{m}^2/\text{hr}$ with a mean energy of $\langle E_\mu \rangle = 320 \text{ GeV}$ [27,67]. The Radon activity in the experimental halls is $\sim 100 \text{ Bq}/\text{m}^3$ in the air, this value is constantly maintained by the continuous ventilation with the fresh outside air. The neutron flux is $= 3.7 \pm 0.3 \cdot 10^{-2} \text{ m}^{-2} \text{ s}^{-1}$.

2.3 Conceptual design of the detector

Borexino is an organic liquid scintillator detector located in hall C, the major components of the Borexino experiment are depicted in Fig. 2.4. Its technology is based on ultra high purity liquid scintillator as a target and a multiple layer structure for the detector, see Fig. 2.9 and 2.10. This permits a high neutrino interaction rate and thus to perform a precise, real-time measurement. All this lead Borexino to become an extraordinary neutrino observatory.

Radiopurity requirements

Any radioactive decay inside the detector has some probability of being mistaken for a neutrino interaction. Many naturally occurring radioactive isotopes, in their decays, release energies in the sub-MeV range which is most important for the detector. Borexino is therefore designed around the principle of graded shielding, in which the central portion of the detector is the least contaminated. The detector design arises from signal and background requirements and was driven by the following considerations:



Figure 2.3: One of the tree underground halls in LNGS during the excavation and after.

- **Neutrino count rate:** given the low cross section for neutrino interactions, the only way to maximize the ν count rate is to increase the target mass as much as possible. To have a SSM neutrino count rate of about 50 ev/day in a pseudocumene scintillator, the detector target mass should be at least 100 tons.
- **Signal/Noise ratio:** in order to discriminate the signal, the experiment require a signal-to-noise ratio equal or less then 1. So the strict constraints on the background level in Borexino requires both the reduction of the naturally occurring radioactive contaminants in the scintillator and the shielding of the active volume. The first demand is achieved through the implementation of purification procedures, both for the active scintillator and for the surrounding shields. Instead, the fiducial volume shielding is realized by means of a detector structure based on a succession of increasing pure shells. Very stringent requirements are also placed on the construction of materials used for Borexino: from the scintillator containment vessels, to the phototube glasses or the metallic supports. In order to have a low background many things have to taken in account (see Tab. B.1 of Appendix B):
 - choice of construction materials,
 - assay of materials during the assembly,
 - special precautions for installation procedures (clean room, cleanliness of the surfaces),
 - accurate strategy for liquid manipulation and purification,
 - special issue: particular care for nitrogen purity,
 - strategy against the cosmic muon: underground, muon veto, tagging of the residual cosmogenic products.

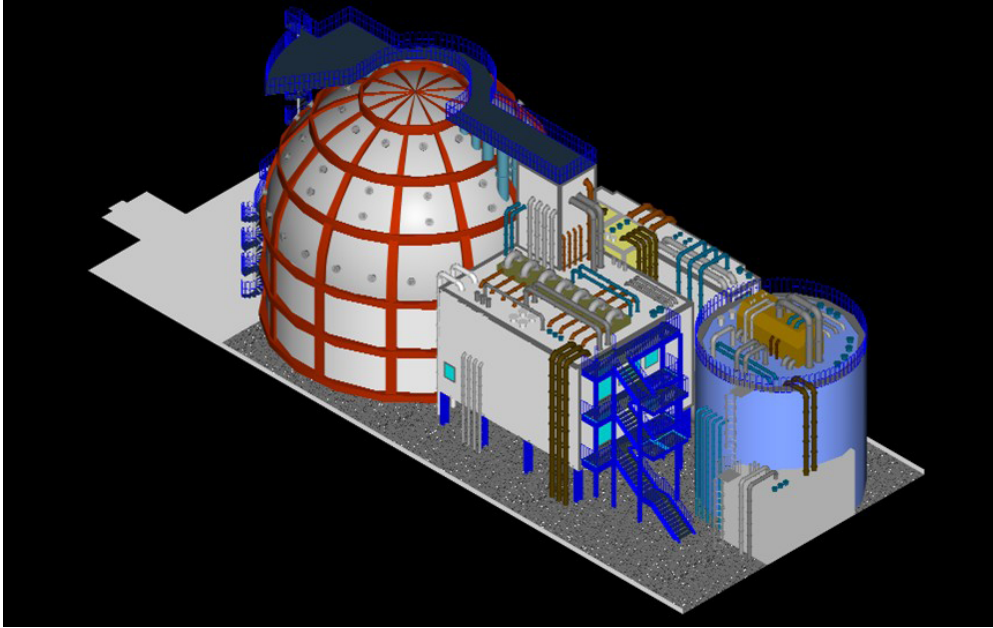


Figure 2.4: The major components of the Borexino experiment in Hall C. From left to right: The Borexino water tank; The “Big Buildings” (East and West) which house the control room, DAQ, and portions of the purification system; the purification skids; the CTF detector.

- **Detector resolution:** on optimum scintillation-light collection efficiency leads not only to an improved energy resolution, necessary for the identification of the ${}^7\text{Be}$ neutrino edge, but also to a better spatial position reconstruction and α/β discrimination, important for the background rejection.

2.4 Neutrino detection in Borexino

Scintillation detectors as Borexino allow the real-time spectroscopy of neutrinos: neutrinos transfer energy to charged particles in the detector which leads to light emission through the processes that will be described in Section 2.5. The information on energy and interaction time of the incident particles is then available by measuring the amount of light and the photon arrival times at photomultiplier tubes covering the walls of the detector.

Due to the low cross sections of neutrinos, the target mass must be at least of the order of tons: this need can be partially compensated by exposure times of several years, this requires on the other hand sufficient time-stability of both the detector target and the electronic read-out of the signals.

The need for extensive passive shielding from cosmic rays is an aspect common to all neutrino detectors as already pointed out. Usually, overburdens of several 1000 meters of water equivalent (m.w.e.) are necessary to achieve a sufficiently low level of atmospheric muons, neutrons and cosmogenic radioisotopes. The background issues for low energy neutrino detection will be described in Section 2.6.

In any neutrino detector as Borexino, the expected low event rate must be faced by a low rate of background events. In underground laboratories, the internal radioactivity of the detector components, radioactive noble gases emanating from the walls, and the cosmogenic background induced by muons are the main background sources. In Borexino the use of standard techniques (described in Section 2.5.3) like distillation, water extraction, nitrogen purging, and column chromatography for an efficient purification of the scintillator has allowed to achieve extremely low concentrations in radioimpurities. The self-shielding by the outer layers of liquid, the buffer, allows the definition of a fiducial volume: events within this volume are selected by spatial reconstruction.

Moreover, a liquid scintillator provides several means to discriminate signal from background events, for example:

- the coincidence signals of inverse beta decay,
- the fast sequence of ^{214}Bi β and ^{214}Po α decay,
- for long time span, the combination with a spatial information allows to extend the time gate, as is done with the threefold coincidence of muons, neutrons and ^{11}C decay,
- pulse shape discrimination to distinguish signals generated by protons and alpha-particles from beta-decays.

2.4.1 Detection reactions

The solvents of liquid scintillators are based on hydrocarbons: the target therefore offers electrons, the free protons of Hydrogen, and the bound protons and neutrons of Carbon nuclei as interaction partners for neutrinos. Both neutral and charged current reactions can be observed.

- **Elastic scattering**

The principal detection method employed in the Borexino detector is the neutrino-electron scattering which proceeds via the charged and neutral current processes depicted by the

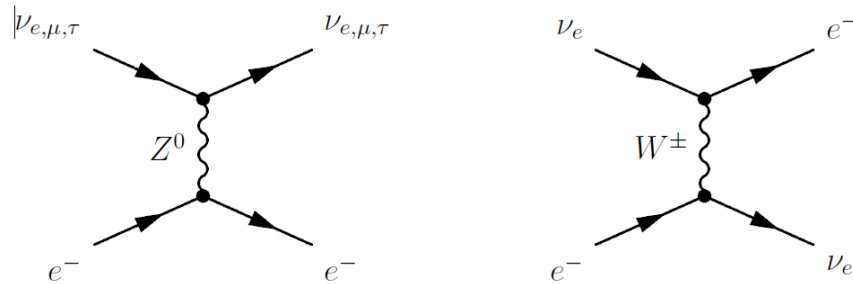


Figure 2.5: First-order Feynman diagrams for the neutral (left) and charged (right) current neutrino-electron scattering interaction. Note that the charged current interaction is only possible for electron neutrinos, therefore the electron neutrinos have higher probabilities for scattering than the μ or τ flavors.

Feynman diagrams in Fig. 2.4.1:

$$\nu_e + e^- \rightarrow \nu_e + e^- \quad (2.1)$$

$$\nu_x + e^- \rightarrow \nu_x + e^- \quad (2.2)$$

The charged current interaction, mediated by the charged W^\pm vector bosons, is possible only for electron flavor neutrinos. The neutral current interaction, mediated by the Z_0 boson is sensitive to all three flavors of neutrinos, albeit with a smaller cross section.

In a neutrino-electron scattering experiment such as Borexino, the neutrino interacts with an electron in a scintillator molecule (typical binding energy of a few eV, so, without loss of generality, we can take it to be free) which then produces scintillation light from excitation and ionization of other scintillator molecules which it encounters. This situation is analogous to Compton scattering, and the recoil-electron spectrum is a continuum with a sharp edge occurring at:

$$E_{max} = \frac{2E_\nu^2}{2E_\nu + m_e c^2} \implies E_{max}(E_\nu = 862 \text{KeV}) \approx 667 \text{KeV} \quad (2.3)$$

The zero.th order (tree level) neutrino/electron scattering formula was first calculated in [68]: it gives the differential cross section for producing a recoil electron with kinetic energy T as a consequence of scattering with a neutrino with initial energy E_ν [69]:

$$m_e c^2 \frac{d\sigma}{dT} = \frac{2G_F^2 m_e^2}{\pi \hbar^4} \left(g_L^2 + g_R^2 \left(1 - \frac{T}{E_\nu} - g_L g_R \frac{m_e c^2 T}{E_\nu^2} \right) \right) \quad (2.4)$$

where:

$$g_L = \sin^2(\theta_\omega) + \frac{1}{2} \quad (\nu_e - e \text{ scattering}) \quad (2.5)$$

$$g_L = \sin^2(\theta_\omega) - \frac{1}{2} \quad (\nu_\mu - e \text{ scattering}) \quad (2.6)$$

$$g_R = \sin^2(\theta_\omega) \quad (2.7)$$

θ_W is the Weinberg mixing angle, is related to the ratio of the masses of the W and Z bosons: $\theta_W = \arccos(M_W/M_Z) \sim 28^\circ$. Note that the value of g_l for electron flavor neutrinos leads to an overall larger cross section relative to the heavier flavors; this is due to the fact that electron neutrinos may interact via the charged and neutral current interactions, whereas the heavier flavors can only interact through the neutral current interaction.

Cross sections for various electron scattering interactions are presented in Tab. 2.1. As the particles in initial and final state are the same, the reaction has no intrinsic energy threshold; the detection at low energies is therefore impeded only by instrumental limitations and the radioactive background (e.g. ^{14}C) because there is no intrinsic mean to discriminate neutrino signals from beta decay events.

Once the differential cross section is given, it is possible to calculate, for a given neutrino energy E_ν , the total cross section by integrating the differential cross section formula between

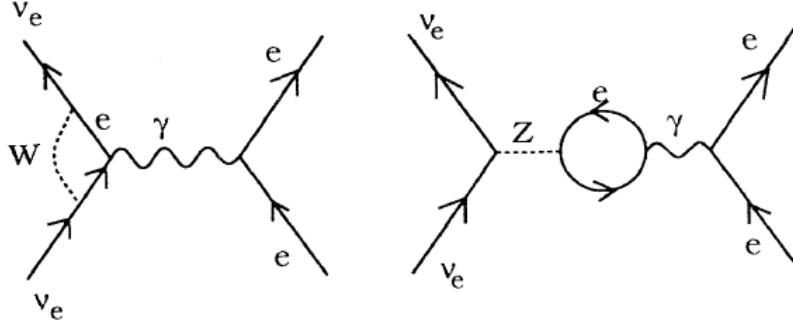


Figure 2.6: Feynman diagrams of second order electroweak ν_e -e scattering.

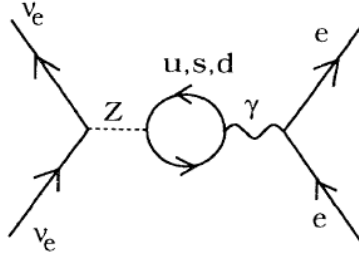


Figure 2.7: Feynman diagrams of second order electroweak neutrino-electron scattering : QCD contribution.

the appropriate limits:

$$\sigma(E_\nu) = \int_0^{T_{max}} \frac{d\sigma}{dT} dT \quad (2.8)$$

Finally, when considering a continuous neutrino source, one has to integrate over the spectrum of incoming neutrino energies. If $\lambda(E_\nu)$ is the normalized neutrino spectrum then:

$$\sigma = \int \lambda(E_\nu) \sigma(E_\nu) dE_\nu \quad (2.9)$$

which is the integrated cross section seen by a given neutrino source.

The effect of radiative corrections to the lowest order $\nu e \rightarrow \nu e$ scattering has been calculated in [70]. In Fig. 2.4.1 and 2.4.1 are shown the Feynmann diagrams for the electroweak and QCD second order corrections. Here only the νe^- final state is considered and electroweak+photonic corrections are applied in order to get the correct electron recoil spectrum. The final formula is:

$$m_e c^2 \frac{d\sigma}{dT} = \frac{2G_F^2 m_e^2}{\pi \hbar^4} \{ g_L^2(T) [1 + \frac{\alpha}{\pi} f_-(z)] + g_R^2(T) (1-z)^2 [1 + \frac{\alpha}{\pi} f_+(z)] \} \quad (2.10)$$

$$- g_L^2(T) g_R^2(T) \left(\frac{z m_e c^2}{E_\nu} \right) [1 + \frac{\alpha}{\pi} f_{+-}(z)] \} \quad (2.11)$$

where $z=T/E_\nu$ and where g_L and g_R are now functions of T because of the effect of the electroweak corrections. The photonic corrections are incorporated in the $f(z)$ functions and are proportional to α (for the explicit formulas see [70]). The effect of including these corrections

Reaction	Current	Threshold [MeV]	Cross Section [10^{-44}cm^2]
$\nu_e + e^- \rightarrow \nu_e + e^-$	NC/CC	-	$0.92 E_\nu$
$\bar{\nu}_e + e^- \rightarrow \bar{\nu}_e + e^-$	NC	-	$0.38 E_\nu$
$\nu_x + e^- \rightarrow \nu_x e^-$	NC	-	$0.16 E_\nu$
$\bar{\nu}_x + e^- \rightarrow \bar{\nu}_x + e^-$	NC	-	$0.13 E_\nu$
$\nu_\mu + e^- \rightarrow \nu_\mu + e^-$	NC	-	$0.22 E_\nu^2$
$\bar{\nu}_e + p \rightarrow n + e^+$ $n \rightarrow p + d + \gamma(2.2\text{MeV})$ (250 μsec)	CC	1.8	$9.5 (E_\nu - 1.29)^2$
$\nu_e + {}^{12}\text{C} \rightarrow {}^{12}\text{N} + e^-$ ${}^{12}\text{N} \rightarrow {}^{12}\text{C} + e^+ + \nu_e$ β^+ : $\tau = 11.0$ ms	CC	17.34	28.7 @ 20 MeV
$\bar{\nu}_e + {}^{12}\text{C} \rightarrow {}^{12}\text{B} + e^+$ ${}^{12}\text{B} \rightarrow {}^{12}\text{C} + e^- + \bar{\nu}_e$ β^+ : $\tau = 20.2$ ms	CC	13.37	71.1 @ 20 MeV
$\nu_x + {}^{12}\text{C} \rightarrow \nu_x + {}^{12}\text{C}^* + \gamma(15.1\text{MeV})$	NC	15.11	30.2 @ 20 MeV
$\bar{\nu}_x + {}^{12}\text{C} \rightarrow \bar{\nu}_x + {}^{12}\text{C}^* + \gamma(15.1\text{MeV})$	NC		27.9 @ 20 MeV
$\nu_e + {}^{13}\text{C} \rightarrow {}^{13}\text{N} + e^-$ ${}^{13}\text{N} \rightarrow {}^{13}\text{C} + e^+ + \bar{\nu}_e$ β^+ : $\tau = 862$ s	CC	2.22	8.57 @ $\langle E_{sB} \rangle$
$\nu + {}^{13}\text{C} \rightarrow \nu + {}^{13}\text{C}^* + e^+ \gamma$	NC	3.68	1.16 @ $\langle E_{sB} \rangle$

Table 2.1: Detection reactions along with the applying weak current, threshold, the energy dependent cross Section(energy in MeV), and the subsequent reaction. Values are cited from [71–73].

is a modification of the electron recoil spectrum and the effect on the total cross section is on the order of 2%.

- **Inverse Beta Decay**

The capture of a $\bar{\nu}_e$ on a proton is the primary channel for ν_e detection in a liquid scintillator detector. It has the largest cross section at low energies (Tab. 2.1), and it provides a clear event signature: a first signal is due to the positron that carries away most of the kinetic energy transferred from the neutrino:

$$\bar{\nu}_e + p \rightarrow n + e^+ \quad (2.12)$$

This prompt signal caused by the ionization and annihilation of the positron provides energy and time information. A second signal is generated about 250 μs later when the generated free neutron is captured on a free proton of the scintillator:

$$n \rightarrow p + d + \gamma(2.2\text{MeV}) \quad (2.13)$$

thereby releasing the deuteron binding energy of 2.2 MeV in a gamma quantum. The delayed coincidence can be used for an efficient background discrimination (in Fig 2.4.1 is shown a pictorial view of the $\bar{\nu}_e$ in a scintillator detector.)

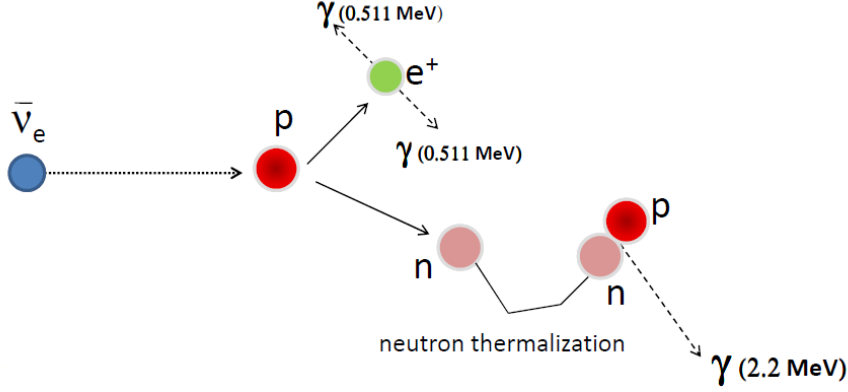


Figure 2.8: Pictorial view of the $\bar{\nu}_e$ in a scintillator detector: it is observed through a prompt signal from the positron followed by the neutron gamma capture on proton releasing a 2.2 MeV gamma.

- **Reactions on Carbon**

^{12}C offers three possible reaction channels to neutrinos, two charged current and one neutral current reaction with thresholds around 15 MeV (Tab. 2.1). While the thresholds are too high and the cross sections too low for most applications, SuperNova neutrino observation significantly benefits from these channels.

The charged current reactions both provide a very similar delayed coincidence. The incoming $\nu_e/\bar{\nu}_e$ interacts with the nucleus, thereby creating an e^+/e^- and an instable isotope. The signal due to the e^\pm is then followed 10 ms/20 ms later by the re-decay of the $^{12}\text{N}/^{12}\text{B}$ under emission of an e^+/e^- . Once again, this delayed coincidence can be used as event signature. It must however be stated that, as the subsequent β^\pm -decays feature similar endpoints and the half-life is very similar, it is experimentally challenging to discriminate on an event-by-event basis ν_e from $\bar{\nu}_e$ events.

The third channel, inelastic scattering exciting the Carbon nucleus, is possible for all neutrino flavors. As there is no prompt signal, the only event signature is the de-excitation gamma of 15.11 MeV.

As the natural isotopic abundance of ^{13}C is 1.1 %, a liquid scintillator detector can also exploit neutrino reactions on this isotope. Albeit event rates are low due to the reduced number of target nuclei, both the CC reaction of ν_e and the NC inelastic scattering are interesting as their thresholds are low, 2.2 and 3.7 MeV, respectively. Especially the delayed coincidence signal of the CC reaction could be utilized in the detection of solar ^8B and SuperNova ν_e . This argument is the subject of this thesis and it will be treated in Chapters 4 and 5 and 6.

2.5 Main components of the detector

The Borexino detector was designed to reach the extremely low background levels required for the sub-MeV solar neutrinos measurement, therefore a series of large volumes of liquid buffer provides a graded shielding against the external background to the scintillator in the center of the detector as depicted in Figure 2.9. Requirements of radiopurity for construction material obviously become more stringent the closer the materials are to the detector's active volume. Additionally, cosmic radiation can be vetoed.

The Borexino detector is divided into two subcomponents: the Inner Detector (ID) and the Outer Detector (OD). The following pages give a brief description of the fundamental detector components going outward from the center. The structure of the detector is shown in Figure 2.10.

2.5.1 Structural components

The target: the scintillator

The heart of Borexino are the 278 tons (315m^3) of active scintillator contained inside of the inner vessel. After careful research on different organic scintillators both as small scale lab tests and as larger tests in the CTF detector, it was chosen as final solution a mixture of pseudocumene (PC, 1,2,4-trimethylbenzene, $\text{C}_6\text{H}_3(\text{CH}_3)_3$) as solvent and PPO (2,5-diphenyloxazole, $\text{C}_{15}\text{H}_{11}\text{NO}$)

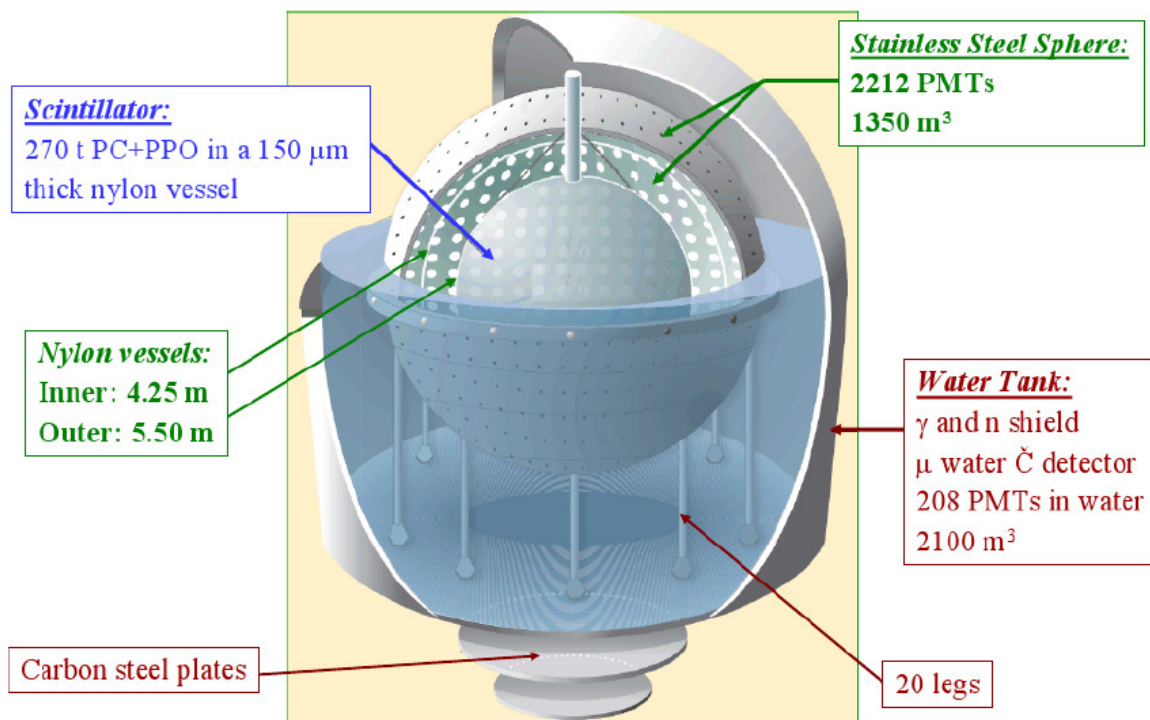


Figure 2.9: A partial section view of the Borexino experiment.

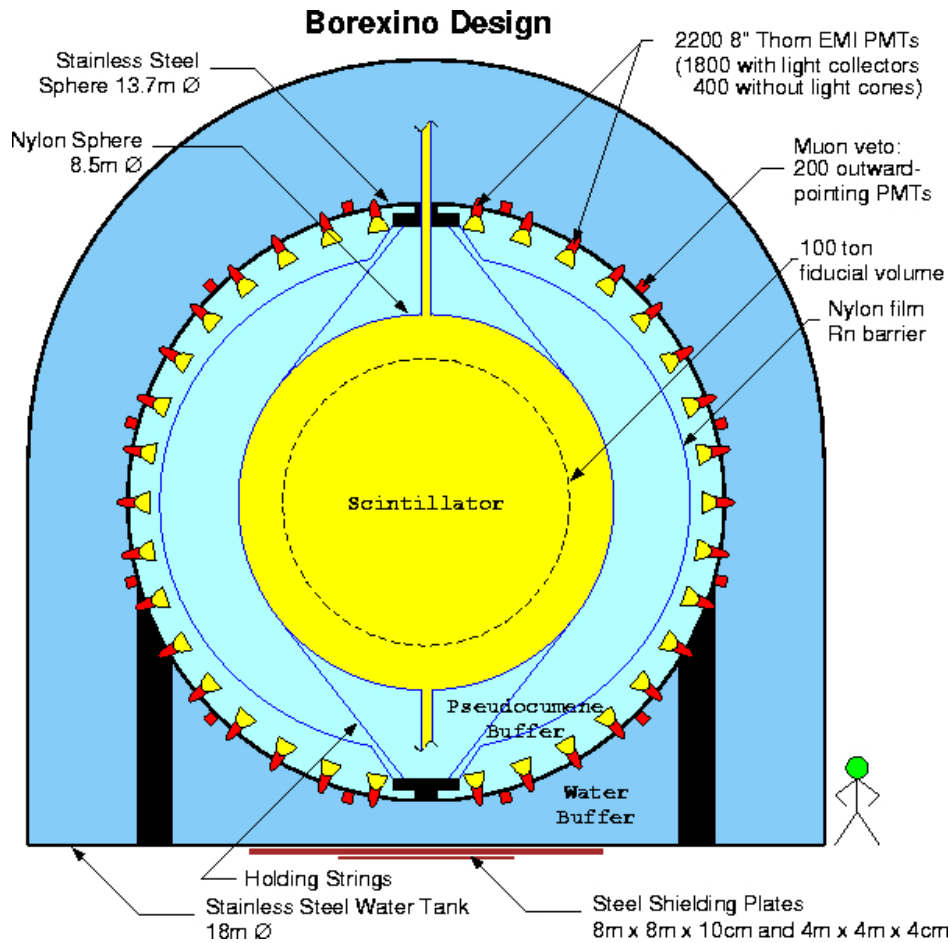


Figure 2.10: Borexino detector scheme.

as fluor, with a 1.5g/l concentration. Many aspects of the scintillation process and light propagation in Borexino are covered in Section 2.5.2 and Appendix D.

The Inner Vessel (IV)

The scintillator is held in a transparent spherical nylon membrane, 8.5 m diameter and 125 μm thick, which must be absolutely tight as it separates fluids which should never mix. Pipes made out of steel and nylon connected to the upper and lower poles allow liquid loading and circulation from the numerous liquid handling facilities. Anchoring of inner vessel is guaranteed by a set of longitudinal nylon strings.

Since the scintillator used in the three volumes separated by these two vessels have almost the same density, the vessels need only to be able to support their own weight (under the assumption of isotropic temperature), and thus could be made very thin. To prevent radon daughters and dust from collecting on the surfaces of the nylon vessels, they were constructed inside a radon-filtered Class 100 clean room located in Jadwin Hall, Princeton University.

In Fig. 2.11 is shown, on the left, the test of the Nylon Vessels at Princeton University and on the right the Vessel in Borexino before inflation.

The main purpose of the IV is the reduction of all internal and external backgrounds to the lowest

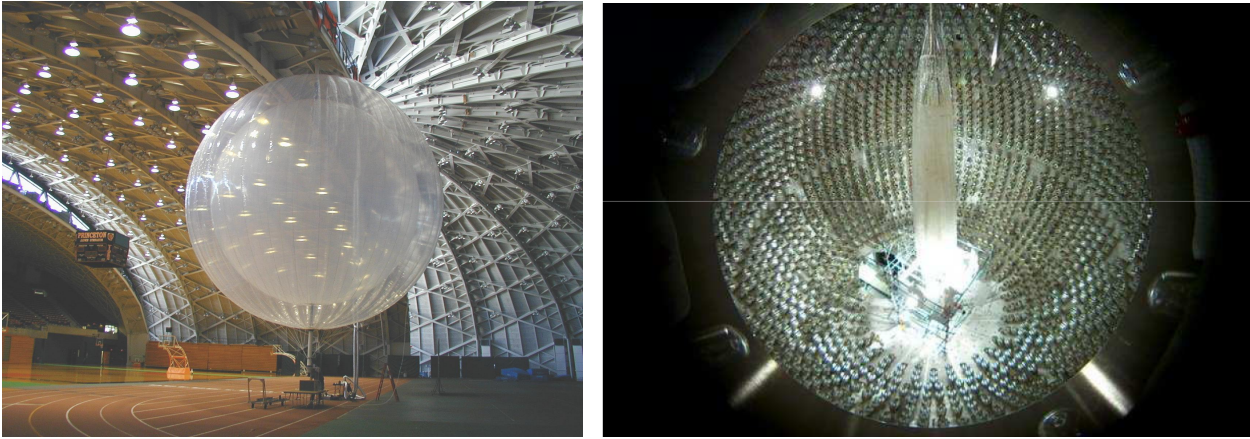


Figure 2.11: Test of the Nylon Vessels at Princeton University (left) and Vessel in Borexino before inflation (right)

levels possible, however, the detector components themselves (Stainless Steel Sphere (SSS), photomultipliers (PMTs), etc.) contribute to the backgrounds, some in non-negligible ways. For instance, the glass bulbs of the PMTs contain a considerable amount of ^{40}K ; the stainless steel of the SSS contains some ^{238}U and ^{232}Th : these are examples of intrinsic radioactivity that cannot be removed by cleaning or other surface treatments. This background radiation is at a level high enough that, if allowed to produce scintillation light, would overwhelm the data acquisition system. Therefore, the liquid in the region closest to the detector materials must be non-scintillating. Obviously then, we must have a physical barrier to separate the scintillating and non-scintillating volumes: this barrier is provided by the Inner Vessel (IV).

Since Borexino performs its position reconstruction based on the arrival time of photons at the PMTs, the vessel material also needs to have a nearly identical index of refraction as that of the scintillator itself.

Since in 2008 a leak appeared in the IV¹ and became necessary to monitor the vessel position because this fact can become problematic for the analysis with a fiducial volume larger than 3 m. The vessel position can be monitored visually with the aid of the calibration cameras (for a detailed description of IV see [74] and [75]), however, this requires illuminating the entire detector with very high levels of light which requires turning off the high voltage to the PMTs first. This operation turned to be a catalyst for various problems with PMTs, so, is avoided when possible.

A less intense method is possible with the aid of 78 point light sources attached on the surface of the inner and outer vessels.

Another method, that has been developed recently, obtains the vessel shape by fitting the distribution of events in the energy range in the spectrum valley² between the ^7Be shoulder and the beginning of β -decay spectrum of ^{11}C , that is mostly populated by ^{210}Bi that is present only near

¹The leak was possibly a result of an increasing buoyant force due to the density difference between the inner, and the buffer volumes, possibly related to an early refilling with a warmer batch of PC that caused a progressing deformation of the vessel.

²In Fig. 2.18 and 2.19 is shown the Borexino spectrum where is possible to see the valley.



Figure 2.12: View of the Borexino "Stainless Steel Sphere" (SSS) from from the "Water Tank", before cables and PMTs installation (left) and with PMTs for the outer muon veto mounted outside the SSS (right).

the surface of the vessel itself [76,77]. Information obtained from the reconstruction of the position of the inner vessel can be applied in many fields of the analysis, as well as, it can be used for monitoring of the vessel shape and volume conditions.

The Buffer liquid

A mass of 1040 t shielding liquid is located outside the inner vessel. The density of the buffer liquid cannot be too different from the scintillator one, as the inner vessel nylon film would not sustain a big hydrostatic pressure without losing its spherical shape or even risking mechanical ruptures. Pseudocumene density is 0.88 g/cm^3 , too far from the water density. It is therefore necessary to use pure pseudocumene as buffer liquid with the addition of a quencher, dimethylphtalate (DMP) in 5 g/l concentration, to further reduce residual fluorescence of pseudocumene in absence of fluor. DMP does not influence photon mean path, nor Cerenkov light emission.

The Outer Vessel (OV)

After CTF experience revealed radon sources outside the inner vessel, a second nylon membrane in the buffer liquid was added in the design to stop radon gas diffusion toward the inner vessel. It has a diameter of 12.6 m and a thickness of $125 \mu\text{m}$.

The Stainless Steel Sphere (SSS)

All the components described so far are housed in a stainless steel sphere 8-10 mm thick with a 13.7 m diameter, which also supports the photomultipliers. 20 legs hold the sphere and are welded to the external water tank floor, see Fig. 2.12.

The photomultiplier tubes (PMTs)

The determination of the event energy and position strongly depends on the PMT resolution in the single photoelectron charge and in the photon arrival time. For this reason, the PMT model

has been chosen in order to have a good single photoelectron performance.

Photomultipliers used in Borexino are 8" ETL-9351, developed out of a special low radioactivity glass and with a complex sealing studied to resist pseudocumene corrosive action. They are sensitive to light with wavelength between 350 nm and 500 nm with a quantum efficiency peak of 26% at 420 nm.

They are installed in the sphere in dedicated feed-throughs and are connected from outside the SSS with a single submarine cable for signal and high voltage. Cables exit the water tank from dedicated openings in the upper dome named organ pipes and reach in 55 m length the electronic room situated in the nearby Big Building West(BBW) (fig. 2.4). 2212 photomultipliers are installed in the sphere, 1838 of which are equipped with aluminum light concentrators to increase light collection capability, see Fig. C.1 and C.3 in Appendix C. The overall geometrical coverage achieved in this way is $\sim 30\%$.

Muon Veto

The about 400 PMTs without light concentrators are the so-called Inner Muon Veto (Fig.2.13). Their higher acceptance angle allows them to collect a stronger signal in response to Cerenkov tracks produced by muons crossing the buffer liquid.

The Outer Muon Veto is instead composed of additional 208 PMTs installed in the water tank to detect Cerenkov light produced by muons in the shielding water, they are shown in Fig. 2.12 (right).



Figure 2.13: PMTs installed on the Borexino SSS. You can see PMTs with and without light concentrator. The latter are used for the "internal muon-veto" system.

External Tank (WT) and buffer water

The full experimental setup is housed in a dome shaped steel tank (Fig. C.2 in Appendix C). The base cylinder diameter is 18 m while the highest point of the dome is 17 m above the floor. The tank is filled with 2400 t of ultra pure water as the outermost shielding of the detector. Cosmic muons traversing the water tank will produce Cerenkov radiation which is subsequently detected by 208 photomultiplier tubes (PMTs) placed on the outer surface of the stainless steel sphere (SSS)

and the floor of the water tank. In order to enhance light collection, the area between the water tank inner wall and the outside of the stainless steel sphere is covered with highly reflective Tyvek sheets. For a detailed description of the outer muon detector see the PhD theses by D. D'Angelo and M. Wurm in references [78] and [79] respectively and reference [80].

The overall height of the Water Tank is limited by the height of Hall C, and as such, it was not possible to have the same quantity of shielding water below the SSS as there is above it. To compensate for the reduced shielding at the south pole of the SSS, there are two large steel plates underneath the Water Tank to balance the shielding capability.

Not depicted in Fig. 2.4 is a small tunnel underneath the Water Tank where is possible to place an intense ^{51}Cr neutrino source for neutrino sterile search and calibration studies.

In Fig. C.4 of Appendix C are shown four nice pictures of the various phases of the detector filling: firstly the Inner Vessel was gas inflated, then was filled by water, and then the water was replaced by Pseudocumene.

2.5.2 The scintillator and buffer properties

The active target of Borexino are ~ 300 tons of organic scintillator. A lot of measurement were done to find the best solution for the choice of the scintillator. Finally with the CTF data analysis the collaboration decided for a binary mixture of pseudocumene (1,2,4-trimethylbenzene, $\text{C}_6\text{H}_3(\text{CH}_3)_3$), used as a solvent, with PPO (2,5-diphenyloxazole, $\text{C}_{15}\text{H}_{11}\text{NO}$), used as primary fluor on the concentration of 1.5 g/l.

The addition of PPO to the scintillator has a double function:

1. PPO enhances the light emission: at the concentration of 1.5 g/l, it increases the light response of about a factor 20. In this way, the overall light yield is 10000 photons per MeV, that, considering the PMT quantum efficiency, corresponds to $\simeq 500$ collected photo electron per MeV. Thus, the energy resolution is 5% at 1 MeV.
2. PPO works as wavelength shifter, namely it shifts the emission spectrum towards the region of sensitivity of the PMTs (see Fig. 2.14).

Incident charged particles (e.g. recoiled electrons in scattering processes with neutrinos, α and β particles) losing energy in the PC+PPO medium lead to the ionization and excitation mostly of the PC molecules which are present in larger quantities with respect to PPO ones. The PC excited molecules transfer their energy to the PPO ones and the radiative decay of the PPO excited molecules from the first excited state to the ground state is responsible for the observed fluorescence. The PPO concentration in the PC has been optimized in order to reach:

- An high primary photon yield: about 10^4 photons/MeV.
- An emission wavelength peak at 430 nm i.e. well above the PMT's sensitivity threshold (~ 350 nm). The emission spectrum of PPO matches the PMT sensitivity, which lies around

[350,500] nm, more closely than PC. Fig. 2.14 depicts the final emission spectrum of PC+PPO in the concentration used for the Borexino scintillator.

- A fast light response for a precise position reconstruction.
- A good alpha-beta discrimination, in order to distinguish particles.
- High radiopurity level (10^{-16} g/g of ^{238}U and ^{232}Th), attainable also on a large mass scale, as shown with the CTF detector.

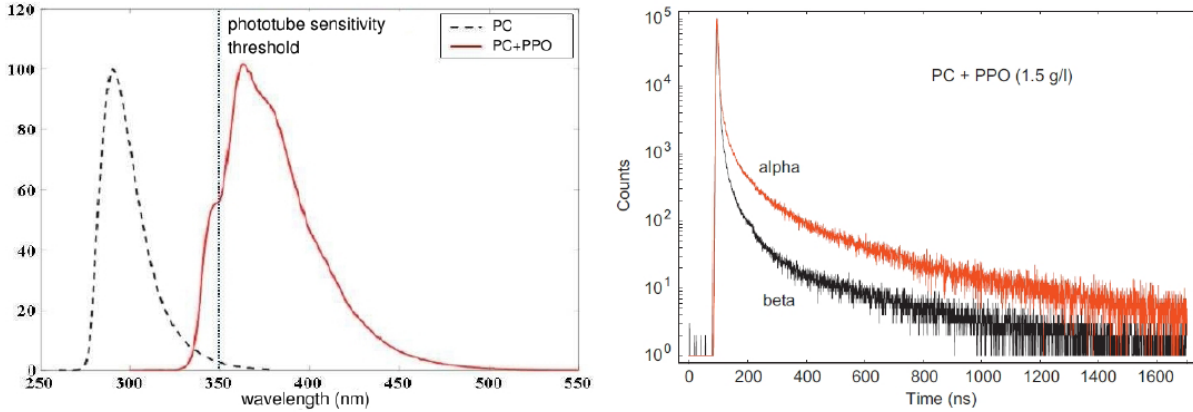


Figure 2.14: *Left:* Emission spectrum of PC (black dotted line) and of PC+PPO (1.5 g/l) mixture (red line) [81]. *Right:* Normalized scintillation emission spectra from α and β excitation of the Borexino scintillator. The higher density of ionized molecules produced by the α 's causes a higher percentage of light emission via the delayed fluorescence process [82].

Light emission mechanism

Organic scintillator have a molecular structure made essentially of benzene rings. In these planar molecules, 2 or 3 the valence electrons are tied to the Carbon atoms in σ and π bonds. When a particle dissipates its energy in the scintillator, both σ and π can switch to an excited state. Transitions among the π energy levels are responsible for the scintillation mechanism, while interactions involving excitation or ionization of σ electrons determine de-excitation or recombination processes where the energy is dissipated thermally, rather than through photon emission.

Electron excitations can lead to singlet or to triplet states. Singlet states (S_0, S_1, S_2) are further divided into vibrational sub-states. While the separation between the singlet states is of the order of 1 eV, the separation of the vibrational sub-states is of the order of 0.15 eV. At thermal energies (0.025 eV) most of the molecules are therefore in the S_{00} ground state, and when excited to, for instance, S_{12} , will quickly fall back to the S_{10} state in less than a nanosecond.

From S_{10} it de-excites to one of the S_0 states through the so called radiative transition that accounts for the quick component of the scintillator light response on the time scale of 1-10 ns, a process known as **fluorescence** which is the main part of scintillation.

Excitations to triplet states are responsible for the so called **phosphorescence**, namely photon

emission with a decay time of 1-10 ms, due to the longer mean life of triplet states. Moreover, light is emitted at longer wavelengths as $E(T_1) < E(T_2)$: for these reasons, phosphorescence is not relevant in the scintillation process.

However, a pair of triplet states can recombine into two singlet states, leading to a de-excitation with the fluorescence spectrum but at longer times: this is the so called **delayed fluorescence**.

Binary organic mixtures like the one used in Borexino involve a solvent and a solute (fluor), whose molecular levels structure is similar to the solvent but where any level lies at a slightly lower energy. Particles dissipating their energy in the scintillator mainly cause the excitation of PC molecules, which get excited to the levels S_1 or T_1 . Then, energy is directly transferred to the PPO molecules, which radiatively de-excite with a higher scintillation efficiency. Light emission by the PC+PPO mixture has a time distribution that is suitable both for event's position reconstruction and for particle identification.

The scintillating mixture PC+PPO (1.5g/l) has a time profile of the light pulse which can be modeled as a superposition of exponential functions: the one describing the fastest component accounts for 90% of the emitted light and has a proper decay time of 3.5 ns, fast enough for a good position reconstruction. The other exponentials describe the delayed fluorescence and are the basis for particle identification: in fact, α particles are characterized by a high energy loss and produce more frequently excitations to triplet states. Therefore, α particles cause light pulses with a higher light emission at longer times, as it is shown in Fig. 2.14. This feature makes it possible to recognize α -like events via the pulse-shape discrimination technique.

Quenching

There are a multitude of processes by which scintillator molecules may relax to their ground state, only some of which involve the emission of light. Like triplet excitation, non radiative molecular recombination to the ground state is itself a function of the density of ionized molecules, and therefore occurs much more often for those particles with a large value for $\frac{dE}{dx}$. This processes, called *quenching effects*, are responsible for the reduction of the deposited energy down to the energy one actually observes. For α particles in Borexino, the observed number of photons is approximately 10% of that expected from an equal energy β .

The non-linear process of conversion in light of the deposited energy is described by different models. The one used in Borexino is the Birks parametrization, in which the light emission per unit length depends on the energy loss by means of two parameters, according to the semi-empirical relation [83, 84]:

$$\frac{dL}{dx} = \frac{LY \frac{dE}{dx}}{1 + kB \frac{dE}{dx}} \quad (2.14)$$

where LY is the absolute scintillation efficiency and is defined as the fraction of the incident energy actually converted to photons, $B \cdot dE/dx$ is the density of ionized molecules along the track and k is the fraction of these that undergo quenching effects. kB is called the *Birk's parameter* and is treated as a single parameter characteristic of the specific scintillator in use and it must be

empirically determined. However, in a fixed experimental environment, it is expected to be the same for all the particle types [85]. In Borexino, the scintillator light yield is of the order of 10000 photons/MeV. The experimental determination of kB is not a trivial task: unpublished laboratory measurements indicated $kB = 0.015$ cm/MeV, but a modeling of the CTF data seems to indicate $kB \simeq 0.010$ cm/MeV.

- For particles with a small $\frac{dE}{dx}$ such as high energy β 's, equation 2.14 reduces to:

$$\frac{dL}{dx} = LY \frac{dE}{dx} \approx LY \quad (2.15)$$

Thus, in this regime, the light produced is linearly proportional to the energy of the incident particle as expected.

- On the contrary for α particles with a rather large $\frac{dE}{dx}$, the denominator in equation 2.14 can be taken to be just $kB \frac{dE}{dx}$ and it reduces to:

$$\frac{dL}{dx} = \frac{LY}{kB} \quad (2.16)$$

In this regime, we have saturation, and the light output varies linearly with the range of the particle.

A parameter often quoted in describing a scintillator is the quenching factor $Q = L(\beta)/L(\alpha)$, the ratio of luminosity emitted by β and α particles of the same energy:

$$Q(E) = \frac{L_\beta}{L_\alpha} \quad (2.17)$$

A small scale laboratory test indicates:

$$Q(E_\alpha) = 20.3 - 1.3 E_\alpha \quad (2.18)$$

where the energy is in MeV and is referred only to the energy of the α particle. The quenching pushes the 5-10 MeV α s of the ^{238}U and ^{232}Th chains down into the Neutrino Window making α/β separation a fundamental background rejection tool.

2.5.3 Purification plants

The most technically difficult aspect of the Borexino experiment is the production of a large, ultra high purity target mass for neutrinos. In fact, the reduction in the level of intrinsic background radiation down to that required to perform an efficient measurement of solar neutrinos necessitates a very intense purification effort.

According to SSM predictions, the expected rate of ^7Be solar neutrinos in Borexino is about 50 counts per day in 100 tons of the fiducial volume. In order to detect a signal in the energy window of (250-850) keV in the multi-ton scale, the background rate must be $\simeq 0.05$ events/day/ton, or 5×10^{-10} Bq/kg. To achieve this level of purity, severe purification procedures must be developed. Purification of the shielding and detecting fluids, and also the choice of the construction materials

(nylon of the scintillator containment bag, stainless steel of the metal sphere and piping of the filling station, phototube glass), is of crucial importance.

The Borexino purification plants were specially designed to produce a high purity pseudocumene based scintillator. This required the typical chemical resistance to solvents and since pseudocumene is flammable with a flash point at 48°C the electronics and sensors in the purification plants must be explosion proof to prevent electrical arcing which could ignite the vapors. The toxicity of pseudocumene also required all the plants containing scintillator to be double-contained to prevent leaks to the environment. The main requirements used in the Borexino construction are listed in Appendix B.

Pseudocumene purification during the filling of the detector

After being delivered in specially designed tanker trucks, the pseudocumene is pumped into one of four storage tanks (each holding approximately 100 tons) From here, the pseudocumene first undergoes vacuum distillation to remove compounds which adversely affect the light yield and attenuation length. Following distillation, it is possible that the pseudocumene still contains some dissolved gases such as radon and krypton, both troublesome for Borexino, therefore, the scintillator is sent through a nitrogen stripping stage to remove these contaminants. The pseudocumene is introduced at the top of a very tall packed column and allowed to flow downwards against a stream of special Low Argon and Krypton Nitrogen (LAKN) which is introduced at the bottom of the column. After leaving the nitrogen stripping column, the now purified PC is sent to a storage tank to await its mixing with either PPO or DMP. Due to its very high melting point (70° C), PPO cannot be purified directly without extensive measures being taken to avoid solidification. The method adopted is to prepare a highly concentrated “master solution” of PC with 140 g/l of PPO which can be purified by flash distillation. This solution is then metered into the pure PC when filling the inner vessel.

To guard against possible re-contamination of the scintillator during and after the purification process, all critical valves, fittings, and pumps are outfitted with sealed, nitrogen-blanketed, secondary enclosures. During the commissioning phases, all components were individually leak checked to provide further assurance against air leaks. A schematic of the overall fluid handling and filling system can be seen in Fig. 2.15.

Pseudocumene purification methods

The purification methods in Borexino were chosen to effectively remove a wide range of radioactive isotopes. Multiple methods are used to account for the chemistry of the different elements which vary in reactivity, solubility, polarity, and vapor pressure. Each technique is optimized to remove impurities with certain properties. The purification operations include distillation, water extraction, nitrogen stripping, and silica gel adsorption.

- **Distillation**

Distillation is the process of heating a solution and extracting the purified vapor phase. It uses differences in the boiling points or vapor pressures of the different species. At a given

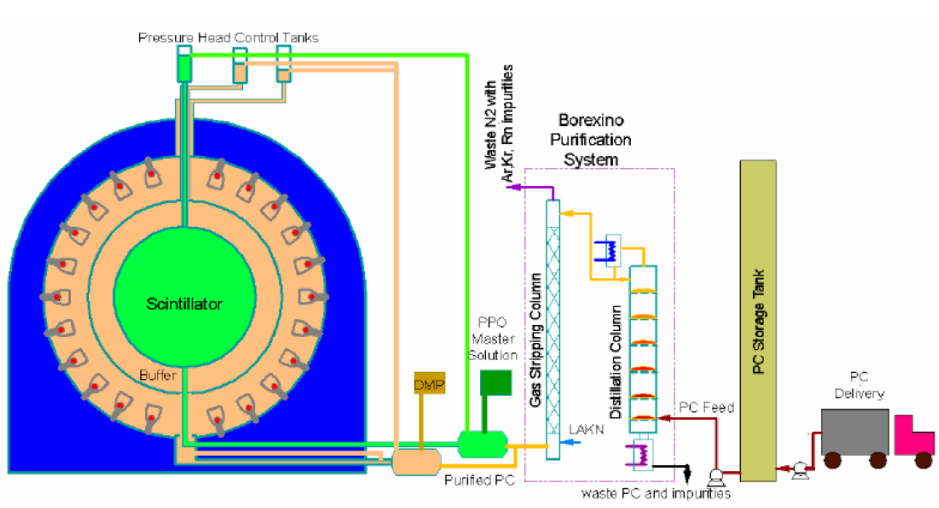


Figure 2.15: Overall view of the purification and filling procedure for Borexino. After being delivered in special tanker trucks, the PC is unloaded into storage tanks and then undergoes distillation, nitrogen stripping, and then mixing with either a flash-distilled concentrated master solution with PPO, or a master solution of the quencher DMP.

temperature, components of a solution will typically have different mole fractions in the liquid and vapor phase. The Borexino reflux distillation column is 75 cm diameter \times 7 m tall and has six sieve trays.

- **Water Extraction**

The purification skids contain a countercurrent water extraction column where the water is added to the top and the feed of pseudocumene is inserted at the bottom. After mixing with the water, the pseudocumene separates and floats to the top of the column where it is removed. Water is drained from the bottom. Liquid-liquid extractions place two immiscible liquids in contact in order to transfer a solute to the liquid with the higher affinity. The different affinities are due to the relative strengths of the intermolecular forces between an impurity and surrounding liquid. Water extraction takes advantage of the relative polarity of the molecules.

- **Nitrogen Stripping**

Stripping or sparging refers to the removal of impurities from a liquid with a gas. Absorption is the reverse process where components of a gas are transferred to a liquid phase. Both rely on the difference in solubility of a compound between a gas and liquid. Stripping is typically done in a column with counter currents of liquid and gas. Liquid is inserted at the top and drips down through a series of packing trays while gas is inserted at the bottom and removed at the top. The packing maximizes the contact area between the two phases and ensures good mixing.

- **Silica Gel Adsorption**

Silica gel adsorption works by preferentially adsorbing impurities on silica that is packed in a

column while allowing the scintillator to flow through. This technique utilizes the difference in surface binding energies. The materials most commonly used for adsorption are activated charcoal or silica gel. Both can be produced in a form where they have a very high surface area per unit mass.

Even though Borexino has reached highest radiopurity levels and the internal calibrations of the detector did only introduce a very small contamination, the collaboration decided to try to even further reduce the concentrations of ^{85}Kr , ^{210}Po and ^{210}Bi which impede the first direct measurement of the pp and CNO neutrinos. Thus, new purification campaigns of the scintillator have been carried out. The possibilities listed above were taken in account and after several tests in the CTF was selected the Water Extraction [86]. The first purification campaign started in July 2010. At the moment of the writing 6 purification campaign have been carried out, permitting to remove ^{85}Kr , to low down the background levels and permitted in this way the first measurement of the pep and CNO flux, see section 2.7 for details.

2.6 Background issues in low energy ν detection

The scientific campaign of Borexino is centered around measuring very rare event rates, often with signals in areas normally dominated by natural background radiation. The uncertainty of a neutrino rate measurement depends on:

- the collected statistics,
- the knowledge of the detector response,
- the neutrino-to-background ratio.

Obviously, the presence of systematic errors (for example it was at the level of 8% in the first ^7Be measurement performed by Borexino [87]) added in quadrature with the statistical error makes the reduction of backgrounds of paramount importance for achieving a low percentage error measurement.

Background events to neutrino detection in a liquid scintillator detector originate from two main sources:

1. Radioactive contamination:

The residual radioactivity in the detection volume, in the tank containing the scintillator, in the phototubes mounted to it, and in the surroundings of the detector. This background is central at very low energies but plays almost no role above a few MeV.

2. Muons and cosmogenic isotopes:

The second component is caused by cosmic radiation. As most neutrino detectors are deep underground, only muons generated by air showers in the atmosphere can reach the detector cavern. Apart from the signals that are caused by the muons themselves, they create radionuclides by spallation. Some of them are long-lived enough to make the correlation with

the parent muon challenging. Moreover, muons passing nearby the detector give rise to a background of fast neutrons that can enter the detector unnoticed and mimic the signature, for an example, of an inverse beta decay.

Table 2.2 shows the major sources of background present in Borexino, the approximate natural activity level encountered in Hall C of the underground labs, the contaminant level which is tolerable by Borexino, the method by which the contaminant is removed and the level actually obtained by Borexino.

Most of the background components have met or even surpassed the specifications. In terms of radiopurity, the lowest ever measured levels of natural contaminants from Uranium and Thorium have been established:

$$^{238}\text{U} : (1.6 \pm 0.1) \times 10^{-17} \text{g/g} \quad (2.19)$$

$$^{232}\text{Th} : (6.8 \pm 1.5) \times 10^{-18} \text{g/g} \quad (2.20)$$

The upper limit on the level of ^{85}Kr is higher, by a factor of about three, than what was originally planned; this could be due to an air leak that occurred during the filling. The reduction of the ^{85}Kr is one of the results of the purification campaigns since the initial filling, which began in the Spring of 2010: being a noble gas, krypton, can be removed by nitrogen stripping with special Low Argon and Krypton Nitrogen. Actually the contamination of Krypton by spectral fits indicates $\sim 2.58 \times 10^{-9}$ cpd/100t, so, it seems that, thanks to the several purification campaigns, the Krypton could have probably been railed.

2.6.1 Intrinsic radioactive contaminants

The most relevant backgrounds in the solar neutrino energy window are ^{14}C , ^{210}Po , ^{214}Pb , ^{210}Bi and ^{85}Kr , coming from the intrinsic contamination of the scintillator and of the materials surrounding it³:

- ^{14}C (β^- decay, $Q=156$ KeV, $t_{1/2}=5730$ y)

At earth surface ^{14}C is cosmogenically produced via $^{14}\text{N}(n, p)^{14}\text{C}$, leading to a relative abundance on ^{12}C of $\sim 1.2 \cdot 10^{-12}$ g/g in living organic matter. In oil reservoirs, due to the old age, this contribution has decayed away. The concentration is therefore determined by a few site-dependent underground production mechanisms, initiated by the natural radioactivity of the rocks. In scintillator procurement for the experiment, the choice of oil batches with lowest ^{14}C level was a major requirement, as ^{14}C , chemically identical to ^{12}C , cannot be removed by any purification process.

The PC scintillator for Borexino was obtained from a crude mineral oil with a $^{14}\text{C}/^{12}\text{C}$ ratio of $\sim 10^{-18}$. This corresponds to a rate of ~ 30 decays/s/100ton. The probability for two

³Here are described only the contaminants from the ^{238}U decay chain that falls in the solar ^7Be neutrino window, the backgrounds at higher energies from ^{238}U and ^{232}Th decay chains that matter for the argument of this thesis are deeply treated in Chapter 5.

Contaminant	Source	Normal/Expected conc./flux/rate	Required	Reduction method	Achieved in Borexino
μ	cosmic	200 s/s/m ² (at sea-level)	$\sim 10^{-10}$	underground, OD, veto Pulse-shape	$< 10^{-10}$
¹¹ C	in-situ μ -ind.	~ 15 c/d/100t		TFC-method	~ 27 c/d/100t
Ext. γ/n Ext. γ	rock PMTs, SSS, vessels			WT shielding, FV cut material selection buffer, FV cut	
¹⁴ C	Intrinsic in PC/PPO	$\frac{^{14}\text{C}}{^{12}\text{C}} \leq 10^{-12}$	$\frac{^{14}\text{C}}{^{12}\text{C}} \leq 10^{-18}$	old oil tests in CTF	$\leq 2 \times 10^{-18}$ g/g
²³⁸ U	suspended dust	$\sim 2 \times 10^{-5}$ g/g	$< 10^{-16}$ g/g	Si-gel, water extraction	$(1.6 \pm 0.1) \times 10^{-17}$ g/g
²³² Th	dust	$\sim 2 \times 10^{-5}$ g/g	$< 10^{-16}$ g/g	distillation	$(6.8 \pm 1.5) \times 10^{-18}$ g/g
⁴⁰ K _{nat}	dust or flour contamination	$\sim 2 \times 10^{-6}$ g/g	$\sim 10^{-18}$ g/g	water extraction	spectral fit: $< 3 \times 10^{-18}$ g/g
⁷ Be	cosmogenic at sea level	3×10^{-2} Bq/ton	$< 10^{-6}$ Bq/ton	distillation or underground storage of scintillator	not measurable
²²² Rn	air and emanation from materials	100 ²²² Rn atoms per cm ³ of air	$< 10^{-16}$ g/g	nitrogen stripping	$\sim 10^{-17}$ g/g $\sim 1/\text{count}/\text{day}/100\text{t}$
²¹⁰ Po ²¹⁰ Bi	surface contamination from ²²² Rn		1 c/d/t	cleanliness, dist. α/β subtraction	~ 70 c/d/t (May 2007) ~ 7 c/d/t (Sep 2008)
²¹⁰ Pb	surface contamination from ²²² Rn			cleanliness, dist.	not measurable not in equil. with ²¹⁰ Po
³⁹ Ar	air/nitrogen	17 mBq/m ³ (air)	< 1 c/d/100t	select vendor leak tightness	not measurable $\ll \ll ^{85}\text{Kr}$
⁸⁵ Kr	air/nitrogen	1 Bq/m ³ (air)	< 1 c/d/100t	select vendor leak tightness water extraction	Spectral fit: (25 ± 5) c/d/100t Fast coincidences: (30 ± 5) c/d/100 Oct 2011 $\sim 2.58 \times 10^{-9}$

Table 2.2: Borexino main background sources, the normal/required/achieved background levels including the rejection methods. For the concentrations of ²³⁸U and ²³²Th secular equilibrium is assumed.

^{14}C decays to occur simultaneously is relatively high, which leads to a pile-up. Due to the finite detector resolution and the pile-up, the ^{14}C spectrum ends at ~ 200 KeV. This energy marks the lower threshold for all Borexino physics analyses. Since the spectral shape factors of ^{14}C , and its pile-up are not well known, this energy region is sometimes excluded in global spectral fit analyses.

- ^{210}Bi (β^- , $Q=1.16$ MeV, $t_{1/2}=5$ days)
- ^{210}Po (α , $Q=5.31$ MeV, $t_{1/2}=138$ days)
- ^{214}Pb ($\beta^- + \gamma$, $Q=1.02$ MeV, $t_{1/2}=27$ min)

This contaminants are radioactive isotopes produced in the ^{238}U decay chain and belong to the ^{222}Rn sub-chain (see Fig. 5.10). The source of these isotopes is the stainless steel of the sphere, the glass and inner components of the PMTs, the nylon of the inner vessels, etc. Assuming secular equilibrium, Borexino can tolerate concentrations of Uranium not much greater than 10^{-16} g/g . This heavy-element decay chain produce ten or more isotopes with different energies and particle types.

- ^{214}Pb undergoes a $\beta + \gamma$ decay, with a $Q=1.024$ MeV.
- ^{210}Po belongs to the ^{222}Rn sub-chain as well. Since ^{222}Rn is a gas diffused in air, it is strictly necessary to avoid any contact of scintillator with air: the presence of ^{222}Rn in the scintillator is mainly due to minor air contaminations occurred during the detector filling. In addition, each operation involving the scintillator (as calibration campaign, water loop, water extraction, refilling...) can easily cause Radon introduction. α particles from ^{210}Po decays (α , $Q=5.41$ MeV, $\tau=138$ d) are quenched by a factor of ~ 13 , therefore the ^{210}Po peak is located at ~ 0.3 MeV in the Neutrino Window. The non-presence of ^{210}Pb proves that the secular equilibrium within the ^{222}Rn subchain is largely broken. The ^{210}Po rejection strategies are waiting for its decay and the efficient α/β discrimination. Thus, the ^{210}Po peak has not be problematic for the ^7Be neutrino analysis. However, it is worth to note that the ^{222}Rn rate increased several times due to detector operations like water extraction. Also ^{210}Po , present on the internal surface of tubes can be introduced; for this reason, a great accuracy and an on-line check on data is necessary during this kind of operations. Done these considerations, the isotopes of the sub-chain are not in equilibrium with the ^{238}U chain.
- Another troublesome contaminant which is visible in the Borexino energy spectrum might be attributed to the ^{238}U daughter nuclide ^{210}Bi : ^{210}Bi decays (β^- , $Q=1.162$ MeV) to ^{210}Po .

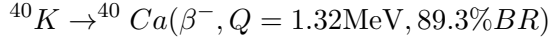
The energy spectrum of the observed ^{210}Bi -like contaminant is very similar to the CNO neutrino spectrum. This makes a disentanglement of the CNO neutrino signal from the ^{210}Bi -like contaminant very difficult.

- **Background:** ^{40}K

Radioactive ^{40}K is abundant in the earth's crust and is often found in large amounts in glass (the PMT bulbs and camera lenses in particular), fortunately the ^{40}K present in the outer

buffer does not have the ability to penetrate into the inner vessel. It decays with a half life of 1.3×10^9 y in two different channels:

- β decay to ^{40}Ca with a 89.28% branching ratio. The reaction proceeds with a Q value of 1.311 MeV which means that any potassium present in the inner vessel will create β 's with energies in the ^7Be , pep, and CNO neutrino windows.



- Electron capture decay to ^{40}Ar with a 10.72% branching ratio (see Fig. 2.16 for the decay scheme). This decay is identifiable because the decay is to an excited state of ^{40}Ar , which subsequently de-excites with the emission of a 1.46 MeV γ . Unfortunately, the mono-energetic line that this γ provides is initially hidden under the β spectrum of the cosmogenically-produced ^{11}C . After ^{11}C subtraction has been performed, it will in principle be possible to obtain a value for this contaminant.

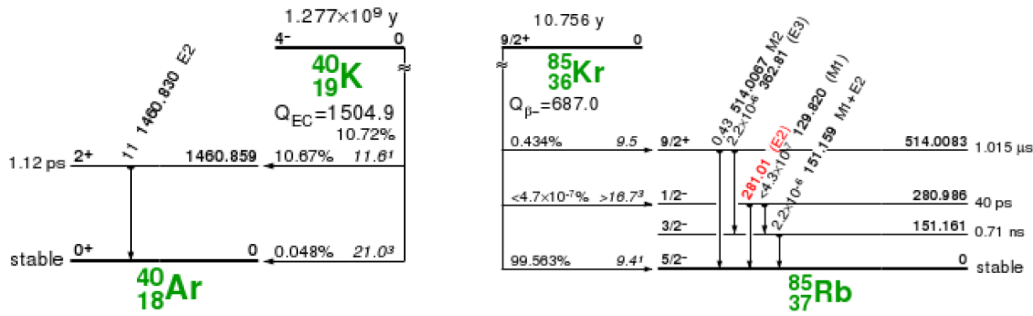
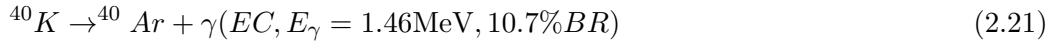


Figure 2.16: *Left:* Level scheme of ^{40}K electron capture decay to ^{40}Ar [88]. The 10.72% branch to the excited state of argon produces a 1.46 MeV gamma ray which should be visible in Borexino after subtraction of the ^{11}C background which covers this area. *Right:* Level scheme of ^{85}Kr β decay to ^{85}Rb . The 0.434% decay to the metastable ^{85m}Rb allows a means, albeit a rare one, for a delayed coincidence tagging of the ^{85}Kr content of Borexino [88].

• Background: ^{85}Kr

The air of the experimental hall also contains traces of ^{85}Kr (a man-made fission product) with activity of $\sim 1.1\text{Bq}/\text{m}^3$. Avoiding air exposure of fluids is also important in order to limit this contamination. Nitrogen stripping proved to be successful in purifying the scintillator from these gases, however since krypton and argon are present also in the incoming liquid nitrogen (used throughout the fluid handling system of the experiment), the collaboration has investigated the product offered by different companies in terms of these trace contaminants and a Low Krypton and Argon Nitrogen used in the final filling and purification phases.

The ^{85}Kr man-made radioisotope is the most problematic contaminant for the solar ^7Be neutrino analysis, since the rate and the spectral shape of ^{85}Kr are similar to those of the ^7Be neutrinos. ^{85}Kr is released into the atmosphere as a fission product from nuclear reactions

in nuclear reactions and from nuclear fuel reprocessing plants. In the atmosphere in Central Europe an activity of $\sim 1.1\text{Bq/m}^3$ was measured.

^{85}Kr (β^- , $Q=0.687\text{ MeV}$, $\tau=15.52\text{ y}$) decays via two channels (Fig. 2.16):

- β -decay into the ground-state of ^{85}Rb (BR: 99.566%)
- decay into the meta-stable state of ^{85m}Rb which decays ($\tau=1.464\ \mu\text{s}$) to ^{85}Rb under emission of a characteristic 0.514 MeV γ ray (BR: 0.434%)

The ^{85}Kr content was measured via the second decay mode. The best estimation of the ^{85}Kr activity is (30 ± 5) event/d/100ton. This result is in agreement with the value obtained from the spectral fit analysis of $(25 \pm 3_{stat} \pm 2_{syst})$ events/d/100ton. This value is 3-4 times higher than the specification, even though the value is two orders of magnitude lower than in air. The ^{85}Kr contamination of the scintillator was probably introduced by a small air leak during the initial filling operations.

After six water extraction campaigns seem that the Krypton could have been removed, since from the spectral fit is obtained a value of $\sim 2.58 \times 10^{-9}$ cpd/100t.

2.6.2 Muons and cosmogenics isotopes

Even with all the care taken to avoid natural radioactivity, radon diffusion and other intrinsic contaminants, by means of the techniques described in Section 2.5.3, Borexino is still subject to a non negligible cosmic-ray background. The origin and the properties of cosmic-rays in the atmosphere and underground are widely described in literature (see [89–91]). Muons and atmospheric neutrinos are the most frequent particles (compared to e.g. neutrons, protons, e^+ , e^- , π^+ , π^-) that reach the sea level. Both particle types can penetrate deep into the subsurface. Within the rock, secondary muon-induced electromagnetic and hadronic showers can occur.

The mean muon energy at sea-level is $\approx 4\text{ GeV}$. At the LNGS experimental site, which is covered by a $\simeq 1.4\text{ km}$ thick barrier of dolomite stone corresponding to 3800 meters of water equivalent (m w.e.), the mean muon energy is $320 \pm 4 \pm 11\text{ GeV}$ [92]. Furthermore, the muon rate is reduced by six orders of magnitude from $1\ \mu/\text{min}/\text{cm}^2$ to $1.16 \pm 0.03\ \mu\text{ m}^{-2}\text{hr}^{-1}$ [93, 94]. In the case of the Borexino detector, this residual muon flux translates to about 10000 events/d in total.

However, not only the muons and muon showers have to be rejected. Apart from the very large prompt signal that momentarily blinds the detector, a muon is able to create additional background by spallation processes: a muon may create unstable nuclei in the detector by spallation processes that knock-out one or several of the nucleons of a target nucleus, in a liquid scintillator, Carbon and especially ^{12}C is the most abundant nucleus. So, Borexino must also handle two other types of muon-related background events.

Muon and cosmogenic isotopes will be treated in detail in Chapter 5 since are the main background source for the measurement of the neutrinos CC interaction in ^{13}C in Borexino.

2.7 Borexino physics program, results and outlook

Thanks to its unprecedented low level of radioactive contamination, Borexino is the only running experiment able to detect solar- ν of energy below 1 MeV. The motivating goal of low energy solar- ν detection experiments is to directly probe the mechanisms of nuclear energy generation in the Sun and to study the properties of neutrinos, such as neutrino mixing and oscillations.

The main goal of Borexino is the measurement of the 862 keV ${}^7\text{Be}$ solar- ν rate. This measure can be used to probe the transition from vacuum- dominated to matter-enhanced oscillation regimes. In four years of data taking, the main Borexino results include:

- the precise measurements of the ${}^7\text{Be}$ solar neutrino flux. This ${}^7\text{Be}$ measurement benefits from an intense calibration campaign for the control of the systematics, and uses a larger data set than previously released results, yielding a total uncertainty of about 5% [55, 59],
- measurement of the ${}^8\text{B}$ neutrino flux with electron recoil energy threshold of 3.0 MeV [57],
- the first measurement of the flux of neutrinos from pep (mono-chromatic at 1.44 MeV) and a limit on the CNO neutrino flux [24],
- validation of the neutrino oscillation model through the solar neutrino measurement, impact of these results for the validation of the MSW-LMA oscillation model in vacuum, constraints of uncertainties in the pp flux evaluation, and consequences for the global analysis of solar neutrino experiments [95],
- absence of night-day effect measured by Borexino in the ${}^7\text{Be}$ energy region [64],
- the first clear observation of geo-neutrinos (antineutrinos from the Earth) [62].

2.7.1 Solar neutrinos

In Borexino has been possible to measure neutrinos fluxes from the Sun from various different sources thanks to the excellent levels of radiopurity achieved.

The real time measurement of solar ${}^7\text{Be}$ neutrinos is the first direct measurement of the survival probability for solar ν_e in the vacuum region. Regarding the ${}^8\text{B}$ neutrinos has been reached a threshold energy of 3 MeV that is lower than any previous experiment. For the first time the same apparatus can measure two different oscillation regions, both the vacuum region and the matter-enhanced region, predicted by the MSW-LMA model.

As explained in Section 1.2, solar electron neutrinos are produced in nuclear reactions happening in the sun through the pp chain and the CNO cycle. The theoretical model describing the evolution of the sun, the Standard Solar Model, allows to predict the spectra and the fluxes of all the neutrinos sources. Solar neutrino oscillations, i.e. the possibility for a solar ν_e of changing its flavour propagation from the Sun's core to the Earth, enhanced by MSW effect [20] have been well

established by radiochemical experiments and by water Čerenkov detectors. Data from solar and reactor neutrinos experiments allowed to constrain the range of the two parameters that describe the oscillation phenomenon: according to the MSW-LMA solution, the widely accepted at the moment: $\sin^2 2\theta_{12} = 0.87 \pm 0.03$ and $\Delta m_{12}^2 = 7.59 \pm 0.20 \cdot 10^{-5} \text{eV}^2$) [25]. The LMA-MSW solution predicts two main features:

1. The shape of the energy dependence of the neutrino survival probability P_{ee} . It predicts that neutrino oscillations are dominated by vacuum oscillations at low energies ($E < 1 \text{ MeV}$) and by resonant matter-enhanced oscillations, taking place in the Sun's core, at higher energies ($E > 5 \text{ MeV}$). The region in between is called the transition region. While the LMA-MSW predicts a well defined shape for the P_{ee} function in the transition region, current experimental data do not constraint it at all, and some theoretical models, including non standard interactions, predict survival probability curves with different shapes. That is why is important a measurement of the P_{ee} as a function of energy especially in the transition region.
2. The lack of day-night asymmetry. This is an asymmetry in the flux of neutrinos from ${}^7\text{Be}$ during the day and during the night due to the fact that during the night solar neutrinos arriving to terrestrial detectors travel a certain distance through the Earth's matter, which affects the oscillations pattern. This leads to a partial regeneration of the electron neutrino flux, a phenomenon known as the day-night effect.

Real time Čerenkov experiments like SNO and SuperKamiokande can measure the solar neutrino fluxes with an higher threshold ($\sim 5 \text{ MeV}$) because of the low light yield and the high intrinsic background. In 2010 the lowest energy threshold in Čerenkov experiments, corresponding to 3.5 MeV , has been reached by the SNO experiment [58]. But also in this way, they are only sensitive to ${}^8\text{B}$ solar neutrinos and can investigate only the matter-enhanced region of neutrino oscillations. Borexino is the only experiment that has measured the signal rate due to the 0.862 MeV ${}^7\text{Be}$ solar ν and besides the ${}^8\text{B}$ solar ν flux with an energy threshold lower than any previous experiment. In Fig. 2.17 are shown the predictions of the P_{ee} shape according three different models: as is possible to note the measurements done before Borexino were not permitting to choose in between the different three curves, while after Borexino the values for the experiments has been recalculated and are consistent with the MSW-LMA prediction.

The neutrino count rate depends on both solar neutrino flux and oscillation parameters. The relevance of the measurements of the various components of the solar neutrino measurements in Borexino is then twofold: from one side they can increase the confidence in the oscillation scenario and from the other side, assuming the knowledge of the oscillation parameters, they provide a measurement of the absolute solar neutrino flux and may yield very valuable information about solar physics, particularly on the metallicity controversy and about the role of the CNO cycle in the Sun. The precision of the actual data about solar neutrinos does not allow to distinguish between high and low metallicity models but future high precision measurements of the ${}^7\text{Be}$ might give useful

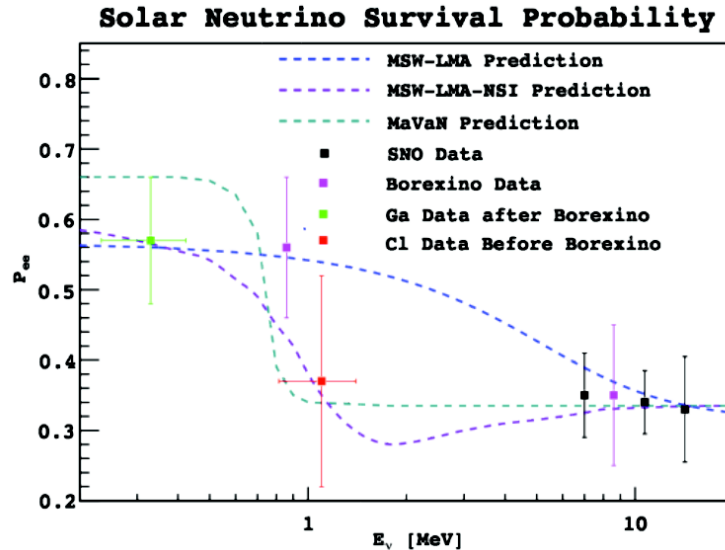


Figure 2.17: Electron neutrino survival probability as a function of the energy. Here are shown the value of the measurements performed including the Borexino ones and the value of the Gallium experiments recalculated.

constraints. In the future, if the purification program will be fully successful, Borexino may detect more precisely CNO neutrinos, providing a direct determination of the Sun metallicity.

Measurement of ${}^7\text{Be}$ solar neutrinos

In liquid scintillator, low-energetic neutrinos are detected via the Compton-like electron recoils of ν_e -scattering. As ${}^7\text{Be}$ neutrinos are mono-energetic, the spectrum features a distinctive “shoulder” at the maximum recoil energy of 667 keV.

From the very beginning of data-taking in Borexino, background levels in the “neutrino window” (NW) from 200 to 800 keV were low enough that this shoulder was clearly visible in the spectrum. The first Borexino analysis of the ${}^7\text{Be}$ -neutrino event rate was published in May 2008, based on 192 days of solar data, then new results with 4 times increased statistics, lower systematic errors thanks to calibration campaigns, and $<5\%$ total error, have been published in 2011:

- First measurement: 192 days [PRL 101 (2008) 091302]
Rate ${}^7\text{Be} = 49 \pm 3(\text{stat}) \pm 4(\text{sys})$ events/day/100 ton
- New results [arXiv:1104.1816]
Rate ${}^7\text{Be} = 46 \pm 1.5(\text{stat}) \pm_{-1.6}^{+1.5}(\text{sys})$ events/day/100 ton [59]

In Table 2.3 are shown the expected ${}^7\text{Be}$ neutrinos flux in the various different scenarios: while the no-oscillation hypothesis is rejected at 5σ , this measurement doesn’t allow to distinguish between the High and Low metallicity solutions.

Because of the 200 keV threshold due to the ${}^{14}\text{C}$ contamination, the energy region considered for the ${}^7\text{Be}$ analysis is between 200 keV and 2 MeV. After removing the taggable background sources⁴, a spectral fit of the remaining components is applied as analysis strategy.

⁴cosmic muons, muons products, contamination from internal ${}^{238}\text{U}$ and ${}^{232}\text{Th}$ chains, external background.

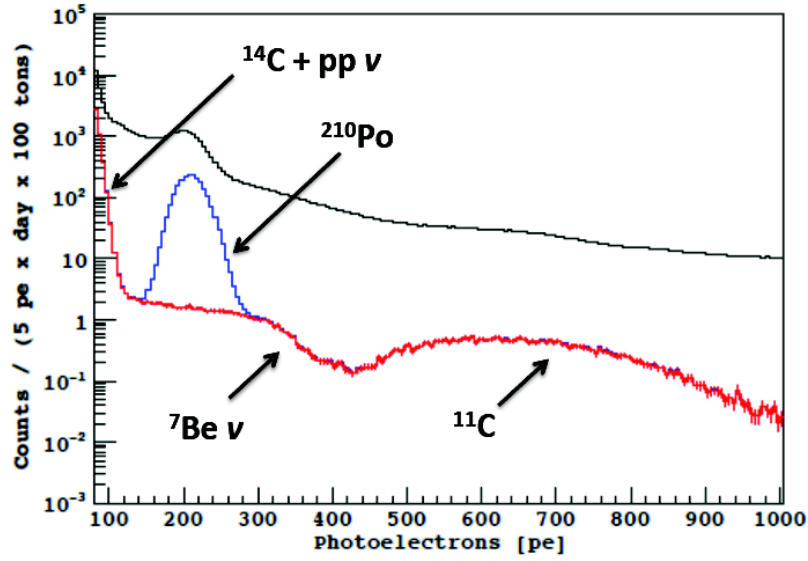


Figure 2.18: The raw charge spectrum and the affects of the different analysis cuts: in black are all the data, in blue the data after the basic selection cuts, and in red after the statistical subtraction of the α s.

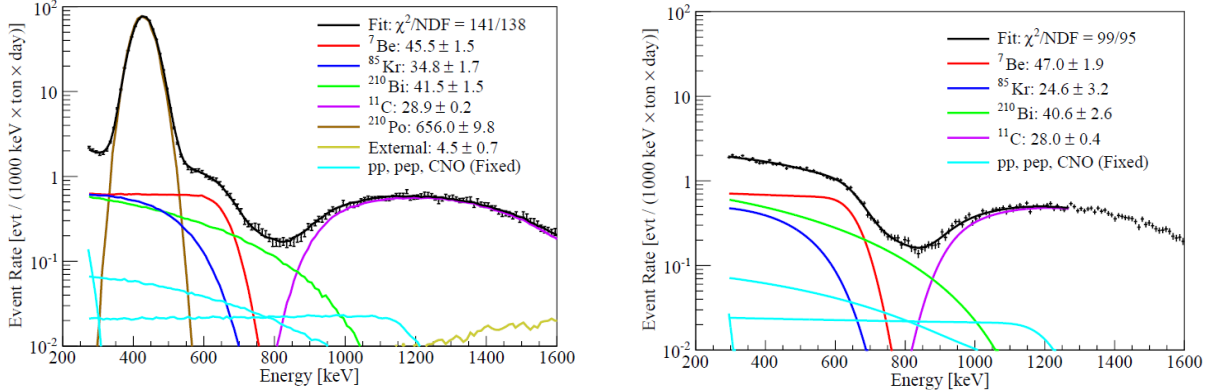
The basic signature for the mono-energetic 0.862 MeV ${}^7\text{Be } \nu$ is the Compton-like edge of the recoil electrons at 667 keV. In Fig. 2.18) is shown the raw charge spectrum and the affects of the different analysis cuts: in black are all the data, in blue the data after the basic selection cuts, and in red after the statistical subtraction of the α s. The peak around 400 keV is due to the ${}^{210}\text{Po}$ α -decay, while at energies above 800 keV the beta spectrum of the cosmogenic isotope ${}^{11}\text{C}$ is clearly visible. The ${}^7\text{Be}$ signal rate in Borexino is obtained fitting the energy spectrum by a superposition of the spectra due to solar neutrinos and to the not taggable backgrounds.

Two independent fit methods were used, as shown in Fig. 2.19, one which is Monte Carlo based and one which uses an analytic description of the detector response. In both methods, the weights for the ${}^7\text{Be}$ neutrino signal and the main radioactive background components (${}^{85}\text{Kr}$, ${}^{210}\text{Po}$, ${}^{210}\text{Bi}$, and ${}^{11}\text{C}$) were left as free parameters in the fit, while the contributions of the pp, pep, CNO, and ${}^8\text{B}$ solar neutrinos were fixed to the SSM-predicted rates assuming MSW neutrino oscillations parameters [25].

Scenario	Expected rate (events/day/100 tons)
No oscillations	74 ± 5 rejected at 5σ
BPS07(GS98) - High metallicity	48 ± 4
BPS07(AGS05) - Low metallicity	44 ± 4

Table 2.3: Expected ${}^7\text{Be}$ neutrinos flux in the various differente scenarios: while the no-oscillation hypothesis is rejected at 5σ , this measurement doesn't allow to distinguish between the High and Low metallicity solutions.

Figure 2.19: Two example fitted spectra; the fit results in the legends have units [counts/(day 100 ton)].



(a) A Monte Carlo based fit over the energy region 270-1600 keV to a spectrum from which some, but not all, of the α events have been removed using a PSA cut, and in which the event energies were estimated using the number of photons detected by the PMT array [59]

(b) An analytic fit over the 290-1270 keV energy region to a spectrum obtained with statistical α subtraction and in which the event energies were estimated using the total charge collected by the PMT array. In all cases the fitted event rates refer to the total rate of each species, independent of the fit energy window. [59]

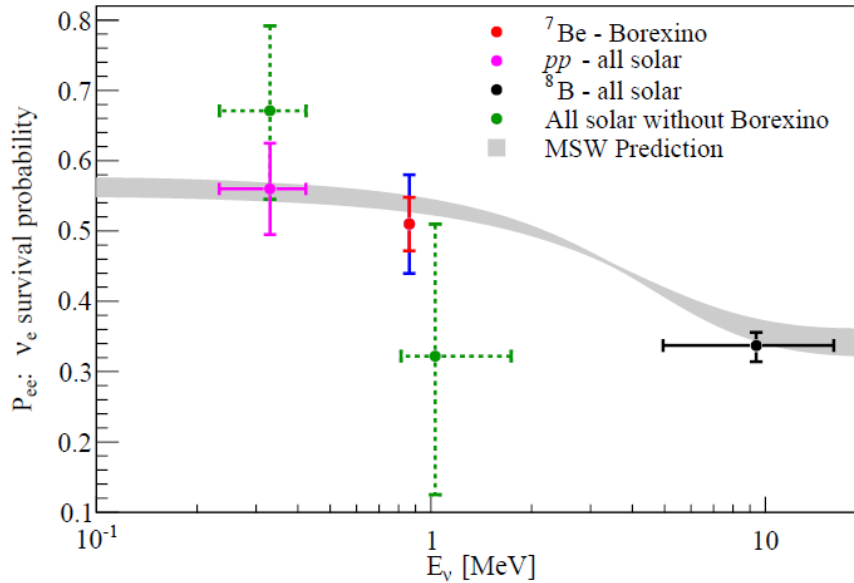


Figure 2.20: The global experimental constraints on the low energy solar P_{ee} . In red and blue are included the measurement on ⁷Be flux: the inner (red) error bars show the experimental uncertainty, while the outer (blue) error bars show the total (experimental + SSM) uncertainty. The remaining points were obtained following the procedure in [97], wherein the survival probabilities of the low energy (pp), medium energy, and high energy (⁸B) solar neutrinos are obtained, with minimal model dependence, from a combined analysis of the results of all solar neutrino experiments. To illustrate Borexino's effect on the low energy P_{ee} measurements, the green (dashed) points are calculated without using the Borexino data. The MSW-LMA prediction is also shown for comparison; the band defines the 1- σ range of the mixing parameter estimate in [25], which does not include the current result.

Assuming the flux of the Standard Solar Model (SSM) with high metallicity the expected rate without oscillations is 74 ± 5 cpd/100 tons which should reduce to 48 ± 4 cpd/100 tons using the LMA-MSW oscillation parameters. The ${}^7\text{Be}$ measurement of Borexino confirms the prediction at low energy of the LMA oscillation model and the non-oscillation hypothesis is rejected at 4.9σ CL. This result permits a precise determination of P_{ee} for solar ν_e in vacuum and probe the transition between the matter-enhanced and vacuum-dominated oscillation regimes as shown in Fig. 2.20.

Furthermore, the analysis of the day and night spectra [64] provides a further confirmation of the prediction of the LMA model through the absence of a significant day-night asymmetry in the ${}^7\text{Be}$ flux. For each event, from the absolute time was computed the value of the Sun zenith angle at the LNGS latitude. The measured value for the day-night asymmetry of the ${}^7\text{Be}$ solar- ν rate is $A_{dn} = 0.001 \pm 0.012_{stat} \pm 0.007_{syst}$.

This result alone rejects the LOW region of neutrino oscillations parameters at more than 8.5σ CL.

Combined with the other solar- ν data, Borexino results isolate the LMA-MSW solution without including data from the KamLAND $\bar{\nu}_e$ reactor experiment in a combined fit, i.e. without relying on the assumption of CPT invariance in the neutrino sector.

The low-energy threshold ${}^8\text{B}$ -neutrino signal

The excellent radiopurity levels obtained by Borexino combined with the efficient software rejection of the cosmogenic background, made possible a measurement of the ${}^8\text{B}$ solar neutrino flux with the unprecedented energy threshold of 3.0 MeV [57].

This threshold is mainly determined by the need to cut the residual 2.6 MeV γ background due to the Thallium decay in the PMT materials. The major background sources above 3 MeV are: cosmic muons, gammas from the cosmogenic neutron capture on ${}^{12}\text{C}$ (4.9 MeV), radon emanation from the nylon vessel and the sphere, short-lived and long-lived cosmogenic isotopes, and internal ${}^{208}\text{Tl}$ contamination. Data selection procedure includes removal of muons, short lived cosmogenic isotopes, ${}^{10}\text{C}$ by the triple coincidence, statistical subtraction of ${}^{11}\text{Be}$ and statistical subtraction of the Thallium spectrum due to the internal radioactivity.

The expected signal rate, including neutrino oscillations, is (0.26 ± 0.03) cpd/100 tons. The resulting ${}^8\text{B}$ neutrino signal rate is:

$$R_{({}^8\text{B})} = (0.217 \pm 0.038_{stat} \pm 0.008_{sys}) \text{cpd}/100\text{tons} \quad (2.22)$$

after 345.3 days of exposure.

The final spectrum is shown in Fig. 2.21 together with a comparison with the expected signal from Monte Carlo (MC) simulation. This result corresponds to a neutrino flux of $(2.7 \pm 0.4 \pm 0.1) \times 10^6 \text{cm}^{-2}\text{s}^{-1}$, in a very good agreement with previous more precise measurements performed by Čerenkov detectors.

The survival probabilities of both ${}^7\text{Be}$ and ${}^8\text{B}$ neutrinos are measured by the same experiment

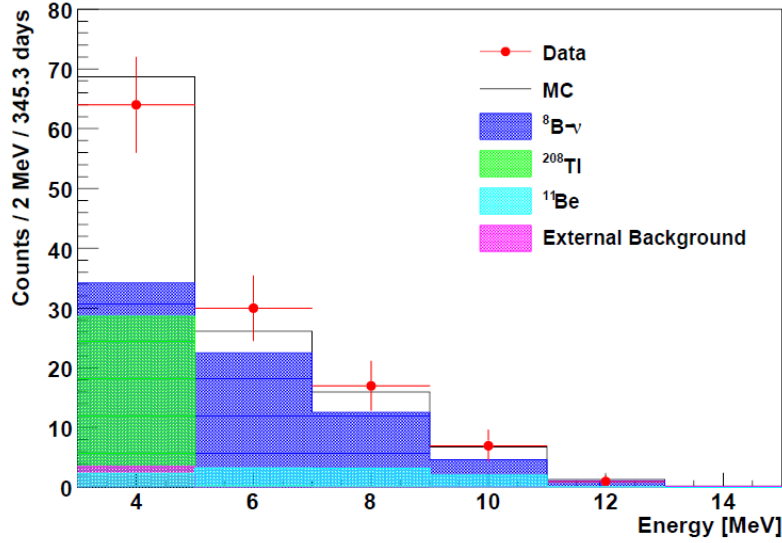


Figure 2.21: Comparison of the final spectrum after data selection (red dots) to Monte Carlo simulations (black line). Is shown the expected electron recoil spectrum from to oscillated ${}^8\text{B}$ ν interactions (filled blue histogram), ${}^{208}\text{Tl}$ (green), ${}^{11}\text{Be}$ (cyan) and external background (violet).

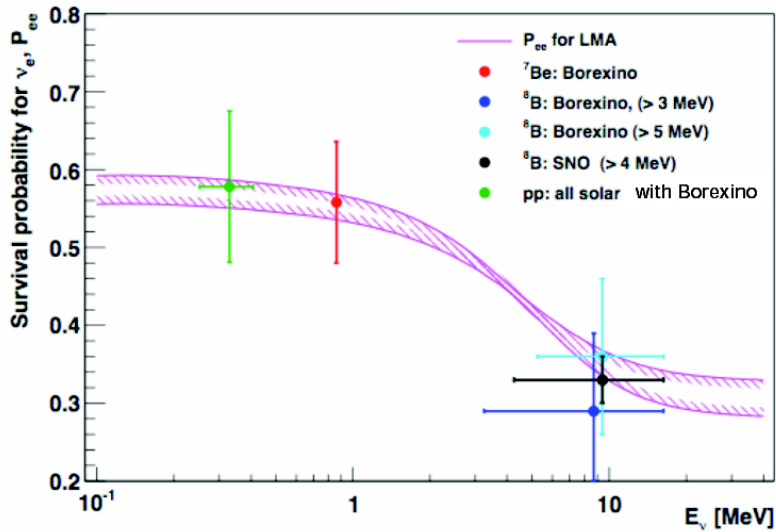


Figure 2.22: Electron neutrino survival probability as function of the neutrino energy, evaluated for the ${}^8\text{B}$ neutrino source assuming the BPS09(GS98) Standard Solar Model [54, 56, 98] and the oscillation parameters from the MSW-LMA solution. Dots represent the Borexino results from ${}^7\text{Be}$ and ${}^8\text{B}$ measurements. The error bars include also the theoretical uncertainty of the expected flux from the Standard Solar Model.

for the first time, yielding a further confirmation of the transition between the matter dominated regime above 3 MeV and the vacuum regime at lower energies. Eliminating the common sources of systematic errors the ratio between the two probabilities is 1.6 ± 0.33 confirming the expectation of the LMA-MSW oscillation scenario at 93% C.L. In Fig. 2.22 is show the shape of the electron neutrino survival probability as function of the neutrino energy with two other points that are the Borexino solar neutrino ${}^8\text{B}$ measurements.

CNO, pep and pp neutrinos

The newest Borexino publication is the solar pep and CNO neutrino detection. Adopting novel data analysis techniques for the rejection of the dominating background in the 1-2 MeV region, cosmogenic ^{11}C , was measured the rate of pep solar neutrino interactions in Borexino (Fig. 2.23):

$$R_{\text{pep}} = 3.13 \pm 0.55(\text{stat}) \pm 0.23(\text{syst}) \text{ counts/day/100ton} \quad (2.23)$$

and constrained the CNO neutrino interaction rate to:

$$R_{\text{CNO}} < 7.6 / (\text{counts/day/100ton})(95\% \text{C.L.}) \quad (2.24)$$

Assuming the MSW-LMA solution to solar neutrino oscillations, these values correspond to solar neutrino fluxes for pep and CNO of $(1.6 \pm 0.3) \times 10^8 \text{ cm}^{-2} \text{ s}^{-1}$ and $< 7.4 \times 10^8 \text{ cm}^{-2} \text{ s}^{-1} K$ (95% C.L.), respectively, in agreement with the Standard Solar Model. These results represent the first direct measurement of the pep neutrino flux and the strongest constraint of the CNO solar neutrino flux to date.

The pep and CNO neutrinos are of major importance for several reasons. In terms of neutrino oscillations one has to note the energy-dependent survival probability P_{ee} of these neutrino components. The P_{ee} of pep and CNO neutrinos lies directly in the transition region between the matter and vacuum-dominated regime according to the MSW-LMA oscillation scenario expected to be between 1 MeV and 3 MeV as already explained. The pep neutrinos are monochromatic with 1.44 MeV energy resulting in a characteristic Compton-like edge at 1.22 MeV in the ν_e -e scattered

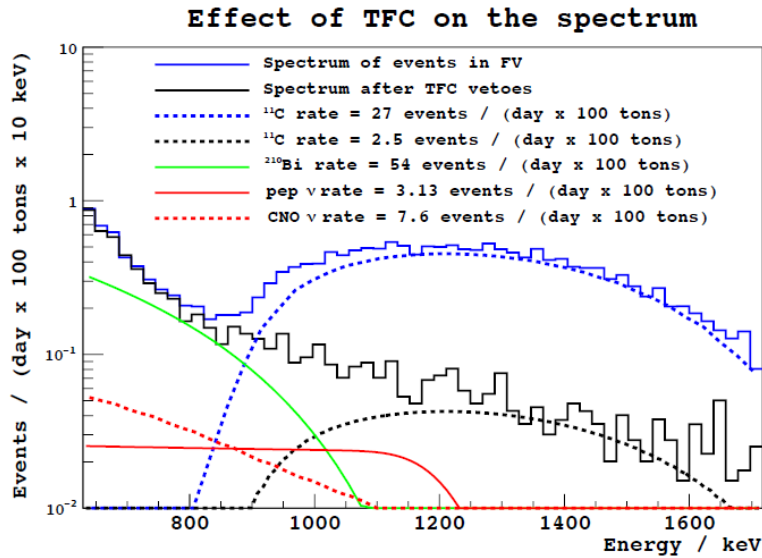


Figure 2.23: Energy spectra of the events in the fiducial volume (FV) before and after the three-fold coincidence method is performed. The blue lines show the data (solid) and estimated ^{11}C rate (dashed) before any veto is applied. The solid black line shows the data after the procedure, in which the ^{11}C contribution (dashed) has been greatly suppressed. The next largest background, ^{210}Bi , and the electron recoil spectra from the best estimate of the pep neutrino rate and from the 95% U.L. of the CNO neutrino rate are shown for reference [24].

energy spectrum. The CNO neutrinos have energies up to 1.73 MeV. Hence Borexino is the first experiment to provide measurements in all three oscillation regions. In Fig. 1.3 has already been shown the electron-neutrino survival probability as a function of energy with all the measurements performed by Borexino.

Moreover, the pep neutrinos are directly correlated with the dominant pp fusion reactions which release the pp neutrinos. Thus, a measurement of the pep neutrinos would also constrain the flux of the pp neutrinos. CNO neutrinos play instead a key role in astrophysics, since the CNO cycle becomes dominant in some type of stars stars with core temperatures above $T_C > 2 \times 10^7$ K for $M \geq M_\odot$. The result for the pep interaction rate does not yet have the sufficient precision to disentangle between the P_{ee} predictions of various oscillation models, while the constraint on the CNO neutrino flux cannot yet discern between the High Metallicity and Low Metallicity SSM. However, the success of this analysis in the reduction of ^{11}C background demonstrates that higher precision measurements of pep and CNO neutrino interaction rates are within the reach of Borexino if the next dominant background, ^{210}Bi , is reduced through purification of the scintillator.

2.7.2 Antineutrinos

Geophysical $\bar{\nu}$ from the Earth and reactor neutrinos

Another goal of the Borexino experiment is the detection and identification of antineutrinos ($\bar{\nu}_e$). The detection mechanism in Borexino is induced inverse β decay $\bar{\nu}_e + p \rightarrow e^+ + n$. The neutron will capture onto a proton, emitting a 2.2 MeV capture gamma in the process, and the positron will eventually annihilate with an electron, releasing 1.1 MeV via two annihilation gammas. These two signals allow a very efficient method of tagging geo-neutrino signals, efficient enough to allow almost the entire Borexino inner-vessel volume to be used as the target mass since external gammas cannot mimic the coincidence signal.

Due to the neutron-proton mass difference, there is a threshold on the incoming anti-neutrino energy of 1.8 MeV. This threshold makes the detection of anti-neutrinos from ^{40}K impossible due to the fact that the Q value for the β^- decay of ^{40}K is only 1.3 MeV.

Two sources for antineutrinos are geo-antineutrinos and reactor-antineutrinos. Geo-antineutrinos (geo- $\bar{\nu}_e$) are electron anti-neutrinos ($\bar{\nu}_e$) produced in β -decays of ^{40}K and of several nuclides in the chains of long-lived radioactive isotopes ^{238}U and ^{232}Th , which are naturally present in the Earth and represent a unique probe of the radionuclide heat generation in the interior of our planet. According to the Bulk Silicate Earth (BSE) geochemical model in [100] a detection rate of $R_{geo} = (2.5_{-0.5}^{+0.3})$ events/y/100ton is expected in Borexino. On the other hand, reactor-antineutrinos at a rate of (5.7 ± 0.3) events/y/100ton are expected from the nuclear plants distributed across Europe, however, at higher energies. The measured rate $R_{reactor} = (4.2_{-1.4}^{+1.7})$ events/y/100ton is consistent with the expectation assuming an antineutrino oscillation scenario.

Concerning the geo-antineutrinos a first observation was reported by KamLAND [101]. How-

ever, Borexino is the first experiment that has been able to observe geo-antineutrinos with a high statistical significance (see Fig. 2.24). The measured rate is $R_{geo} = (3.9_{-1.3}^{+1.6})$ events/y/100ton (1σ) and the null hypothesis, i.e. $R_{geo}=0$ events/y/100ton, was rejected at 99.997%. The hypothesis of a geo-reactor at the Earth's core with a typical power of 3-10 TW was also investigated and an upper bound for a 3 TW geo-reactor could be set at 95% C.L. [63].

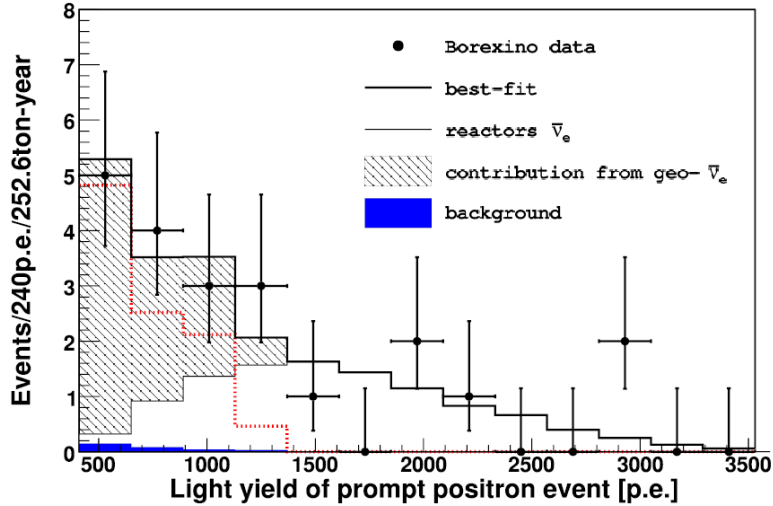


Figure 2.24: Charge spectrum for the positron prompt events of the 21 $\bar{\nu}_e$ candidates and the best-fit (solid thick line). The horizontal axis shows the number of p.e. detected by the PMTs. The small filled area on the lower left part of the spectrum is the background. Thin solid/dotted red lines: reactor and geo- $\bar{\nu}_e$ signal from the fit, respectively. The darker area isolates the contribution of the geo- $\bar{\nu}_e$ in the total signal. The conversion from p.e. to energy is approximately 500 p.e./MeV.

$\bar{\nu}$ from type II Supernovae

Borexino also has the potential of detecting stellar core collapses, which are expected to occur ~ 3 times per century in our galaxy. A supernova at 10 kpc distance releasing a binding energy of 3×10^{53} ergs is expected to induce more than 150 events above Borexino's quoted energy threshold (~ 0.2 MeV) within tens of seconds.

According to standard supernova theory, the prompt neutrino signal, which precedes the electromagnetic signal by hours or even by days, can provide an early alert to the astronomical community leading to unprecedented observations with optical telescopes of the very early turn-on of supernova light curves. Moreover, the duration of the neutrino bursts (width of the neutrino pulse at the neutron star) allows to find an upper limit for the electron neutrino mass.

In July 2009, Borexino joined the SuperNova Early Warning System (SNEWS) collaboration, whose other members are SuperKamiokande, SNO, LVD and IceCube.

2.7.3 The future

In addition to these important results already achieved, the Borexino scientific program is not finished yet, and the main activities in progress are:

- Continuation of the solar physics program:
 - Borexino has taken the first steps toward the measurement of pep and CNO solar neutrinos but the results do not yet have sufficient precision to resolve the solar composition problem. In order to improve the result, and enter in a second phase, Borexino is performing since July 2010 purification campaigns to decrease the radioactive backgrounds, in particular the ^{210}Pb present in the scintillator, which is the source of ^{210}Bi . The campaigns had been successful in reducing the levels of ^{232}Th and ^{238}U and ^{85}Kr .
 - The feasibility of the pp-neutrino flux measurement is under study (better understanding of the detector at low energies and the precise spectral shape of ^{14}C is needed).
 - the Borexino collaboration is also studying annual and seasonal solar neutrino flux variations at low energies.
- Measurement of the CNGS ν velocity to check the OPERA result about the CNGS neutrino velocity [102]. The goal is to check in a manner independent from OPERA all the steps of the measurement (clock synchronization, determination of the neutrino start time, baseline measurement, detector time response).
- Check the short baseline anomaly in ν oscillation and the sterile ν hypothesis by using ν or anti- ν source in Borexino at 10 PBq level.
- Antineutrino studies with more statistics: geo, reactor.

Chapter 3

Data acquisition and event reconstruction

The Borexino Data Acquisition (DAQ) System has been designed to provide for each event two fundamental informations in order to reconstruct the data: **charge and time** of each photoelectron. Indeed each scintillation event has to be reconstructed in energy and position: the energy reconstruction is needed for the spectral neutrino analysis, while the position reconstruction permits the Fiducial Volume definition and background discrimination.

The electronics and data acquisition system for Borexino are designed to perform the following functions:

- Trigger the detector when a specified threshold is reached.
- Measure the energy of an event by summing PMT signals, so the photon emitted have to be efficiently collected and summed.
- Capture relative timing information from individual PMTs for position reconstruction: the arrival time of each photon at the PMT has to be determined with a ns precision both for reconstructing the event position, and for exploit the $\alpha - \beta$ discrimination techniques from the impulse shape.
- Record delayed coincidence events for event discrimination and analysis: it is important to know the time difference between two events, fundamental to use the delayed coincidence method for background discrimination.

3.1 The electronic chain

The electronics of the Borexino detector is housed in a dedicated room at the second floor of the building named Big Building West near the detector, as depicted in Fig 2.4. Here in fact arrive the submarine cables connected to inner and outer detector PMTs along which high voltage and signal travel.

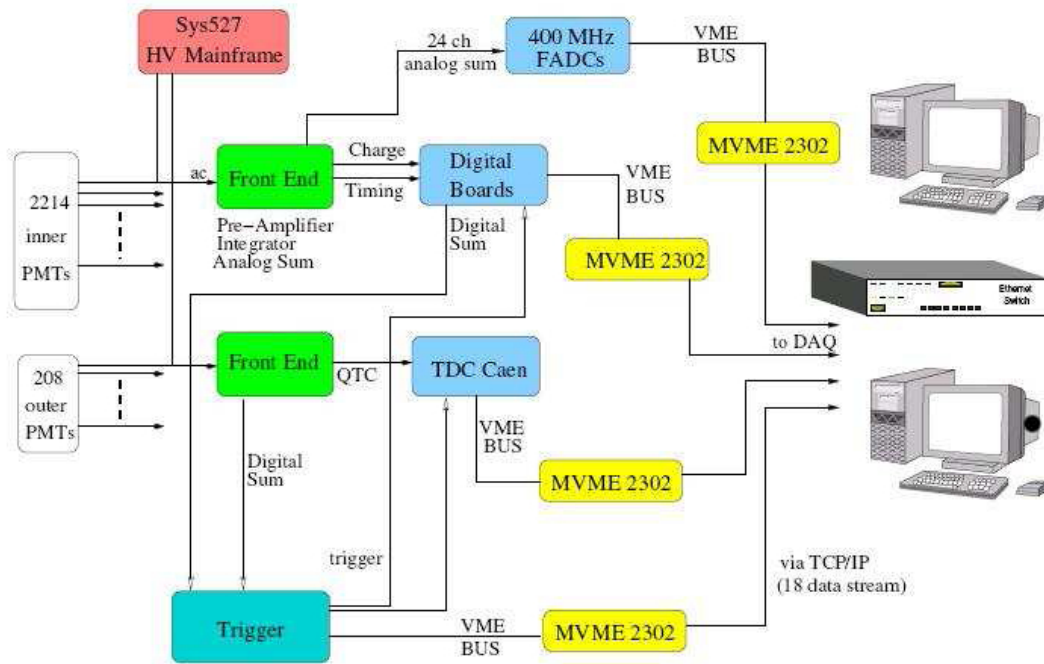


Figure 3.1: Block diagram of the electronics system and DAQ structure for the Borexino detector. Are shown the two independent system: the 2214 Inner Detector PMTs and the 208 Outer Detector PMTs.

Borexino electronics can be divided in two independent sub-system, as described in [103]: the Inner Detector (ID) and the Outer Detector (OD) read-outs, as shown in Fig. 3.1. The reconstructed information of an event detected with the Borexino detector relies on the precise time of arrival and the number of photons reaching the PMTs both for scintillation light events (in the Inner Detector) and Čerenkov light events (in the Inner and Outer Detector). They have two different designs, that reflect the signal processing needs of the two detectors:

1. the electronic read-out system of the Inner Detector, composed of 2212 PMTs mounted on the internal surface of the Stainless Steel Sphere: ~ 1800 dedicated to the neutrino detection and ~ 400 to the muon veto system.
2. the electronic read-out system of the Outer Detector, composed of 208 PMTs mounted to the external surface of the Stainless Steel Sphere.

A complex trigger system takes care of the integration. The ID PMTs also provide signal to the additional waveform digitizers (Flash ADC) [104], which constitutes an independent subsystem.

High Voltage

All Borexino PMTs are operated at the nominal gain of 10^7 . Operative voltages for this gain have been measured in dark room tests before the installation of the PMTs in the detector. They

span from ~ 1150 V up to ~ 1750 V and the current drawn is in average ~ 100 μA /channel. Two multi-wire cables per board bring High Voltage (HV) to the decoupling stage of the front-end electronics.

3.1.1 Inner detector DAQ

The Inner Detector electronics (called *Laben* system) includes 13 identical racks that perform HV distribution (a schematic view is shown in Fig. 3.1), complete analog signal handling, digitalization, data processing and data transfer to the main Data Acquisition (DAQ) cpu. The PMT cable is connected to a front-end channel that decouples it from HV and extracts a fast linear signal for timing purposes and an integrated signal for charge evaluation.

The two signals reach then the digital part of the chain where they are acquired. Here the coincidence condition is also evaluated and sent to trigger for eventual trigger formation. Whenever a trigger is received back the digital memory is read and sent to DAQ system.

Every rack has 168 channels (160 channels for the PMT signals plus 8 spare channels) and each one houses (see Fig. 3.2 from the top to the bottom):

- a patch panel with the connections between the water-proof cable arriving from the PMTs and the analog electronics
- the calibration system fan-out: a resistive fan-out (the test and calibration signal distributor) which allows the possibility to inject a charge into the calibration input of each front-end board,
- a low voltage power supply for the front end crate,
- the adder board with the scaler module,
- the front-end (FE) crate,
- the VME crate (Laben boards) with the digital electronics and Power-PC,
- the High Voltage (HV) mainframe.

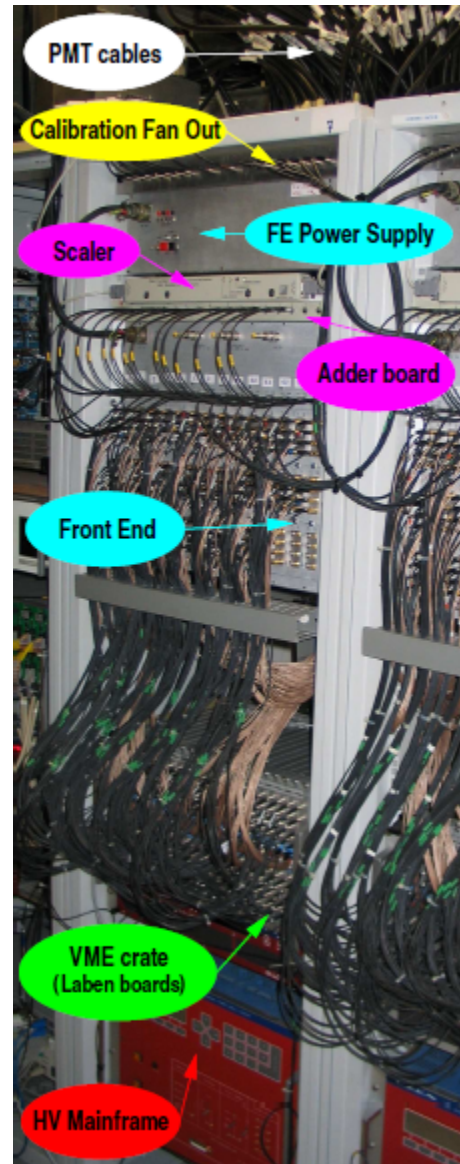


Figure 3.2: One of the 13 ID racks. Picture from [78].

The Borexino PMTs are coupled, i.e. the signal and the HV travel along the same cable. After the necessary decoupling stage, the negative signal has therefore a bipolar shape with a positive overshoot and a null area. The overshoot is however very small and long (\sim ms) and its interference in the signal processing can be easily kept to a minimum. The PMT operating voltage is regulated in order to obtain a gain of $\sim 10^7$. In this condition the Single Photo-Electron signal has the characteristics shown in Table and Fig. 3.3. The electronic chain to which each PMT is connected is composed of two system:

1. the front-end board where are handled the analogic signals; for determining energy and position of a scintillation event, the charge and the timing distribution of each photoelectron has to be measured.
2. the laben digital board that provide the digitization of the timing and charge information of the photoelectron coming from the front-end.

Front-end electronic

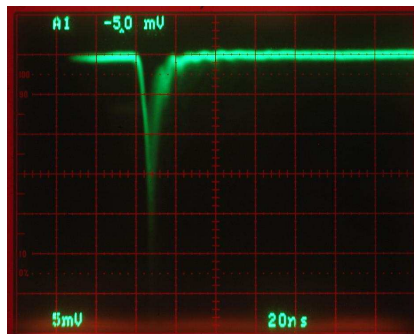
When a scintillation event occurs in the detector, energy released by a particle converts into photons, through the mechanism described in Section 2.5.2, which then reach the PMTs.

Normally, each PMT works in the single photon regime. In case of a 1 MeV event at the center of the detector, the probability of multiple photo-electrons originating within the same PMT is below 10%. This number scales with the energy of the event and increases with the radial distance as the solid angle seen by PMTs closer to the event will increase in that case. In other words, within the ${}^7\text{Be}$ energy window (250 keV - 800 keV) and applying a radial cut, the number of hit channels can give, within a first approximation, the energy of the event. A precise energy evaluation should instead take into account the charge seen by the single channel and the electronic is designed to ensures this possibility. The ratio between the number of registered photo electrons (p.e.) and the deposited energy in Borexino (the effective light yield) is approximately 500 p.e. at 1 MeV.

In order to reconstruct the energy and the position of the scintillation events, their charge (pulses registered by the PMTs) and hit arrival time should be measured. In general, for a single gamma or

Single Photo-Electron Signal	
Amplitude	-12mV
FWHM	5ns
Rise time	4ns
Fall time	10ns
Charge	1.6pC

(a) Single Photo-Electron characteristics for PMT ETL-9351 [78].



(b) PMT signal shape as seen on the analog oscilloscope.

Figure 3.3: Characteristic of the Single Photo-Electron signal.

beta particle the proper time interval of the deposited energy collection depends on the scintillation light decay time and on the time of flight.

A registered PMT pulse arrives with a PMT cable to the Patch Panel (on top of the rack) and then to the front-end (FE) circuit. The Borexino PMT cable contains both the HV and PMT signals, their separation occurs in the FE circuit. After the separation, the FE circuit builds two signals from the obtained PMT pulse: one for the Charge and one for the Timing.

The FE board performs the following functions:

- send HV, provided by the mainframe, to the PMT cable,
- extract from the PMT cable the arriving PMT signal,
- build a fast inverted and amplified (with factor ~ 20) timing signal from the initial PMT signal,
- build an inverted and integrated Charge signal from the same initial PMT signal,
- distribute the calibration signal in parallel to every channel,
- build a sum of the fast signals all channels.

These timing and charge information are then given as input to the Laben digital electronic.

Laben digital electronic

The goal of the digital electronics is to digitize time and charge information for every PMTs signal and to provide information to the trigger system (see section 3.1.3) on the number of channels firing in coincidence.

The Charge signal (integrated PMT pulse) and Timing signal (amplified copy of the PMT pulse) arrive on the inputs of the digital Laben electronics. In every VME crate are housed 20 boards, each one processing 8 channels. These boards were developed in collaboration with the *Laben S.p.A.* company. The main purpose of the digital electronics is:

- to digitize charge and time information for each valid PMT signal and to store them in the local FIFO buffer memory (one for each channel),
- to collect the total number of PMTs fired within a certain time window (trigger time window (TTW)), see section 3.1.3,
- to communicate this number to the Borexino Trigger System for the eventual formation of the trigger by the Borexino Trigger Board (BTB).

These boards accept the timing and integrated charge outputs produced by the front-end boards and subsequently perform the time pick-off to an accuracy of 200 ps. For trigger evaluation, each board contains a coincidence unit with a coincidence time of 50 ns and sends its output to the trigger processing logic. Each channel also contains its own memory registers where the data are stored for a duration of 6 μ s. If a trigger is received, these data are copied to on board RAM in

preparation for event-building. Each VME crate possesses one Power-PC module, having three consequent tasks:

1. retrieving the data from all the channels in all the boards in its crate;
2. building this data into part of one event;
3. sending the event over an internal network to the main event-building computer, called BxBuild.

3.1.2 Outer detector DAQ

As explained in Section 2.6, even if the cosmic muon flux underground is reduced by a factor 10^6 , there are still 10000 muons per hour crossing the detector that are a dangerous source of background. The Outer Detector has been designed for tagging the muons: it is a Water Čerenkov detector composed of 208 PMTs mounted on the outer surface of the SSS and on the floor.

The Inner Detector electronics are designed primarily for the detection of rather small amounts of light ($\sim 0.2 - 2$ photoelectrons for events with energies in the neutrino window) and as such, are not well suited for the detection of the large amount of light produced by muons.

In contrast to the ID, the OD electronics deal with a different hit multiplicity. If an OD photomultiplier sees a direct Čerenkov light cone, it can easily receive 100 p.e., while the ID photomultipliers saturate at ~ 6 p.e. In order to be able to work with such a wide dynamic range, a different electronic system was designed and constructed [80]. The basic process is the same since the end results are identical.

The PMTs are decoupled in special decoupling units, and then sent directly to Charge-to-Time converters (QTC) and then forwarded to Time-to-Digital converter boards (TDCs). Here they are integrated to determine the total charge registered by that channel (the width of the output from the QTC), and the time of the hit (start of the pulse). There is also a dedicated trigger system for the outer-detector which provides a muon veto signal to the main Borexino trigger. When the OD trigger condition is satisfied (6 fired PMTs within 150 ns), the Muon Trigger Board (MTB) generates a trigger signal and sends it to the Borexino Trigger Board.

3.1.3 Trigger system

Most of the trigger electronics is housed in a dedicated rack at the center of the electronic room. The heart of the system is the Borexino Trigger Board (BTB) located in the VME crate. The trigger rack houses also the GPS receiver unit and the slow control server computer.

The main purpose of the Borexino Trigger System (BTS) is to efficiently and quickly identify scintillation events detected by the PMTs, characterized from the almost simultaneous response of a certain number of PMTs, and to produce a master trigger signal which allows the readout of the charge and timing information of the event.

The trigger starts when a certain number of PMTs have fired within a certain time window (TTW, Trigger Time Window). The choice of the TTW value is based on the distribution of the photon arrival time. A typical time for a photon to cross the Stainless Steel Sphere is about 50 ns, therefore, the allowed range for the TTW is (48-99) ns. Normally during data taking TTW is fixed at 60 ns. The number of photons, necessary for the trigger formation, is determined by the end-point energy of the ^{14}C β decay ($E_\beta = 156$ keV). Considering the effective light yield of the Borexino scintillator of $\simeq 500$ p.e. at 1 MeV, this energy corresponds to about 80 photons, but the necessity of auto-calibration require that at least the final part of the ^{14}C spectrum is acquired, therefore the trigger threshold lower down to around to around 40 photons or less, now it is fixed at 25.

The events acquired with this trigger logic are called *neutrino trigger* events and they have associated a specific trigger number (trigger type 1). The Borexino Trigger Board also receives the trigger request from the OD Muon Trigger Board (MTB) and handle other trigger types, in particular two of them permits the acquisition, in the data taking, and then the identification, in the analysis phase, of muons and neutrons.

1. **Muon trigger:** the muons are identified from the OD that is provided of a trigger system, Muon Trigger Board, that sends a signal to the Borexino Trigger Board in the case of a muon passing the OD (6 PMTs fired). If the muon cross also the ID the event is acquired with the same normal trigger procedure (trigger type 1) but it also has associated the OD information: from the combined study of the OD and ID information si possible to recognize the event as a muon.

If the muon crosses only the Water Tank the information is registered from the OD and tagged as trigger type 2.

2. **Neutron trigger:** it is known that cosmic muons can produce through spallation one or more neutrons that propagates through the scintillator and are susequently captured by a proton emitting a 2.2 MeV gamma. In Borexino is important to detect this neutrons, for main purposes, so that whenever a muon crosses the SSS is opened a 1.6 ms gate in which can be acquired all the neutron events, trigger type 128.

The trigger board also provides three types of service triggers to monitor the system: calibration triggers, random triggers and laser triggers. At the beginning of each run a programmable number of calibration events (typically 1000 events) are sent to all channels in order to check the synchronisation of the internal clock (called Gray Counter) to all Laben channels. The random triggers are the triggers generated for the study of PMT dark noise. The last type of service signal is the timing laser triggers. In these events, all Inner Detector PMTs are fired by the timing laser system.

Regardless of the source of the trigger, when it occurs, all of the data in both the inner and outer detector is recorded and sent to disk. The window during which data is recorded lasts a total of 16 μs , appropriately delayed such that the recording of the data starts before the hits causing the trigger.

As already mentioned, there are several sets of radioactive isotopes which decay in rapid succession, quickly enough that the two events will often occur inside of the same $16 \mu\text{s}$ trigger window¹. The tagging of these isotopes requires their identification as two separate event: a software reconstruction stage is actually focused on deconvolving the entire trigger window into as many physical events as appropriate.

The huge amount of visible energy deposited by a muon crossing the ID can saturate the Borexino electronics². The result is that these channels report a value of zero for their measured charge, biasing the event energy towards lower values. To fix this problem, when both the ID and OD triggers occur at the same time, the normal trigger is issued and immediately after it expires, a new 1.6 ms trigger gate is opened. In this way the ADCs are cleared and cosmogenic neutrons and isotopes can be detected.

At the end of the data taking run, the DAQ produces a so-called “raw-data” file, which contains the outputs of the digital electronics for all events collected during the run.

3.2 Data Acquisition

The Borexino Online Software is a complex system that runs on 27 CPUs (17 Power PCs and 5 PCs: bxmon, bxbuild, bxslow, bxweb, bxdb) of different architectures, involves over 100 processes, scripts and other software instances programmed in different languages and entirely custom made. The tasks fulfilled at run time are the following:

- Data read-out: read-out of the event information from digital electronics.
- Event Building: assembling the event from the sub-systems data chunks.
- Run Control: control over the data taking run.
- Slow Control: control over the hardware.
- Online Monitor: run-time detector performance check-up.
- Dark noise monitor: acquisition of the scalars.

Every VME crate (see Section 3.1.1), where digital electronics is to be read, houses a Power-PC that accesses the boards through the VME bus. A local software reads the data, formats and sends them through network to a remote process. Here the event is being built and written to disk by other processes. All the components implement a state machine and a run controller process issues commands to all other processes ensuring the synchronization and the overall behavior as a single state machine. Web technology is used to provide the user with comfortable interfaces to all relevant processes.

¹The mean life for the ^{212}Bi - ^{212}Po coincidence, from of the ^{232}Th decay chain is 431 ns.

²Immediately following a muon, a large number of channels see so much light that their ADCs are saturated.

All the data acquisition system is automatic, from the complete handling of the analogic signal from the PMT, to the HV distribution, to the data digitization and storage, and to the transfer of these data to the DAQ system for the event reconstruction. Typically, Borexino data are acquired without interruptions for a certain time span, that corresponds to one *Run*. In Borexino data are taken 24 hours a day and runs are usually 6 hours long. This run duration is long enough to have a good efficiency in the long coincidence search and short enough to allow the fast data reconstruction and the continue detector monitoring. Once per week a calibration run is taken, in order to check the channel alignment.

The data taking is controlled by a program called *RunSupervisor*, that has the tasks of starting the data taking, stop it when the time limit is reached, and therefore can handle and control some system errors stopping and restarting the data acquisition. In any case is always necessary the presence of two shifters that supervise everything, also in case of particular problems, and that produce, from the raw data provided by the DAQ, the data that will be used in the physics analysis. Shifters change each week; they are usually two and can be three when the third is in training. Their main duty is the presence underground and the run monitoring. When a run ends, shifters must start the data processing sequence as soon as possible in order to monitor the effects of scintillator operations in real time. When the data reconstruction is done, shifters must check the runs through a specific tool and if everything is fine validate the data.

In addition, in case of flasher or tripping PMTs, shifters must individuate the bad PMT and in case disconnect it. Shifters are always helped during their work by the *Run Coordinator* (RC). This person is in charge for a full month at LNGS. The RC must be the contact between the Operational Group, the experts and the shifters and ensure the weekly exchange of informations between shifters. He must be an expert shifter, able to help shifters in case of any problems or doubts and ensures the continuity and the transfer of informations between different shifter crews in order to keep the ducty cycle as high as possible and improve the quality of the data and the detector stability. During my two Run Coordination months, duty cycle has been 97%.

3.3 Software reconstruction

The task of transforming the time and charge information obtained from each channel into the variables used for analysis is performed by the software reconstruction programs.

The data acquisition system produces the so-called *rawdata files*, containing, for every event, the information in the “raw” form as recorded by the digital electronics of the various detector’s subsystems. However before the physics analyses can take place, rawdata files must be processed offline, computing the relevant physics parameters of the event. These include for example the position of the interaction vertex, the energy of the particle, the timing between successive events, Particle IDentification (PID) tags and many more parameters.

The main physics tasks performed by the reconstruction program are:

1. Pre-decoding (Pre-calibration): computation of electronics parameters;
2. Decoding of the raw information:
 - decoding GPS time for absolute time reference;
 - decoding of Laben hit time and charge from adc raw information using precalibration and calibration parameters;
 - analogous decoding of OD hit time and charge;
 - FADCs pedestal subtraction and construction of a digital sum of channels.
3. Clustering of hits into physical events and precise evaluation of event start time. Selection and synchronization of the correspondent FADCs windows;
4. Vertex position reconstruction of the event;
5. Splitting of overlapped events within a cluster;
6. Reconstruction of the event energy;
7. Computation of Particle IDentification tags:
 - (a) α/β discrimination;
 - (b) Muon tagging;
 - (c) Sphericity of the event and other geometrical parameters.
8. Muon track reconstruction;
9. Calibration tasks:
 - (a) Single channel calibration: time and charge for ID and OD;
 - (b) Dark rate of PMTs;
 - (c) Electronics status evaluation;
 - (d) Calibration system auto-monitor.

The raw data is contained in binary files, encoding the information on the trigger, and the data of ID and OD PMTs. In 2004, the Borexino collaboration started to develop a common software tool named **Echidna**. This code is written in the object-oriented programming language C++ and uses the analysis platform `ROOT` provided by CERN [105]. The Echidna code contains an infrastructure and a number of modules for event processing. The infrastructure manages e.g. the communication with the database (reading, writing) and of the initialization and running of the modules.

Since the beginning of data collection in May 2007, the Echidna code has been continuously improved and new modules have been added. After a given test phase of typically several months, the modules are merged and the resulting code is “frozen”. This terminates a development cycle. The officially released version is denoted by `Echidna cycle N`, with N being the number of the cycle. The analyses presented in this thesis are based on `Echidna cycle_14` version.

In 2007, the US-American Borexino collaborators from Princeton University and Virginia Polytechnic Institute and State University set up a second analysis tool called **Mach4**. So that the Borexino collaboration had the opportunity to perform the physics analyses with two independent codes with the advantage of a permanent cross-check of the results.

In 2009/2010, the two codes Echidna and Mach4 were merged in a new code named **Mach4-Over-Echidna (MOE)**. In that way was possible to compare for example small discrepancies of calculated physical parameters that can arise at different levels of the data reconstruction codes due to the application of different methods and cut selections.

In the Echidna code, following the object-orientated approach, both raw data and higher analysis information are stored in classes: these contain variables in which the data is stored and at the same time basic getter functions necessary to evaluate these variables. The defined output of these getters allows a high modularity of the code and provides the possibility that several persons work in parallel on improvements of individual classes without interference.

ROOT has been developed for the analysis of CERN experimental data and provides a basic framework of data-processing objects for this task. Most of the high-level analysis is performed using the **ROOT** interpreter that allows to run short macros or enter single command line inputs without the need of code compilation.

To ease the access to the data, the Echidna output files are organized by a customized **ROOT** tree (**BxTree**), basically a list of all the trigger events of a given DAQ run. The physics information belonging to each individual trigger is stored alongside in a defined set of classes (**BxEvent**). Each subsystem of the DAQ is represented by a class: while general information on trigger time and type are contained in the class **trigger**, the data retrieved from the ID is stored in the three classes **laben** (the main DAQ), **fadc**, and **neutron**, representing the three electronic subsystems. The data collected by OD PMs is stored in the class **muon**.

The Echidna framework contains about fifty modules: low-level modules write the data to the output root-file, check the stability of the detector systems using the service triggers and identify problematic channels. They also provide the connection to a common Borexino SQL database that contains information on detector geometry and preceding calibration runs. Higher-level modules identify PMTs hits associated to physical events inside the detector and determine energy, position, start time and pulse shape. At the end of this chain, data files combining DAQ runs of an entire week are created. The events contained in these DST (Data Summary Tape) root files are flagged according to low-level analysis filters that identify for instance muons, alpha-particles, or coincidence signals.

3.3.1 Precalibration, clustering and decoding

Precalibration

The first task performed the reconstruction code is that of precalibration, a special set of routines runs over the raw data file and calculates:

- Timing offset values are calculated on a channel-by-channel basis to equalize the timing of all channels. This information is obtained from the pulser triggers at the beginning of each run (these are the “fake” PMT signals fed to the calibration inputs of the Front End boards), and the calibration laser triggers at the start of each run. The pulser events are used to align the timing of the FE and Laben boards, and the laser events are used to account for any cable length differences between the FE boards and the PMTs themselves.
- Charge calibration is performed with the pulses from the calibration laser fibers pointed at each PMT. In particular, the charge histogram for each channel is fit to a function and the position of the single photoelectron peak is recorded and used later in calculating the number of photoelectrons seen by that channel in an event.
- Calculation of the dark rate for each channel is performed with the dedicated random triggers. These triggers occur both at the beginning of each run and also throughout the entire run. This dark rate is used during calculation of the number of photoelectrons or hits occurring during a cluster: the number of expected dark hits for each channel is computed and subtracted to yield the “true” number of hits.

During this process of precalibration, individual channels may be marked as dead for not possessing any events in laser and/or random triggers, having too high of a dark rate, having an abnormally wide or offset single photoelectron response, or requiring a timing correction too far out of specifications. There are some channels whose calibration fiber is broken or damaged. If the fiber is damaged is not possible to extract energy calibration data for this channel and it is simply not used for calculating the energy of an event. These damaged fibers do channel some light, but the laser statistics in a normal run are insufficient to allow the determination of its energy calibration variables. Therefore, at least once per week, a special laser calibration run is performed where the laser is fired at 100 Hz for a total of 250.000 triggers, this is usually sufficient to extract the energy calibration data with high accuracy from all channels, including those with damaged fibers.

Decoding

After pre-calibration is complete, the main event loop starts and the raw events undergo the first reconstruction step, i.e. decoding: depending on the parameters computed by pre-calibration and (channel) calibration modules, the raw data coming from the ID and OD have to be decoded, and calculated the charge of every fired PMTs and the precise time, respect to the absolute time given

from the GPS.

For all detector segments there are decoding modules which lead to a first reconstruction level of the events. In case of the Inner Detector (referred to as laben), two main tasks are carried out:

1. decoded hit time: it takes into account time corrections relative to the internal clock (Gray counter) installed on the laben boards.
2. decoded hit charge: it is calculated according to $Q_{dec} = (P - B)/s$, where P and B are the peak and base sampling of the PMT pulse and s is the peak position of the Single Photo Electron.

Clustering

In the acquisition time window is necessary to reconstruct the beginning and the end of a physical signal. The Borexino trigger gate for Laben electronics was $\sim 6.5\mu s$ wide but after the merging of the two codes in MOE is has been chosen a larger trigger gate equal to $16\mu s$.

A Borexino *event* is defined as a collection of PMT hits which occurs within a standard gate provided by the Borexino Trigger System (see Section 3.1.3). The collection of the hits that are identified as belonging to the scintillation event is called *cluster*. Usually in every gate is present only one cluster, but in 0.1% of cases (the case of fast coincidences, like the one due to the fast decay of ^{212}Bi - ^{212}Po , or of a neutron trigger, or pile-up) more clusters can be present in the $16\mu s$ time window; moreover, every cluster is analyzed to determine if it is due to a single scintillation event or to multiple events. The pile-up events are identified and rejected, the more than one

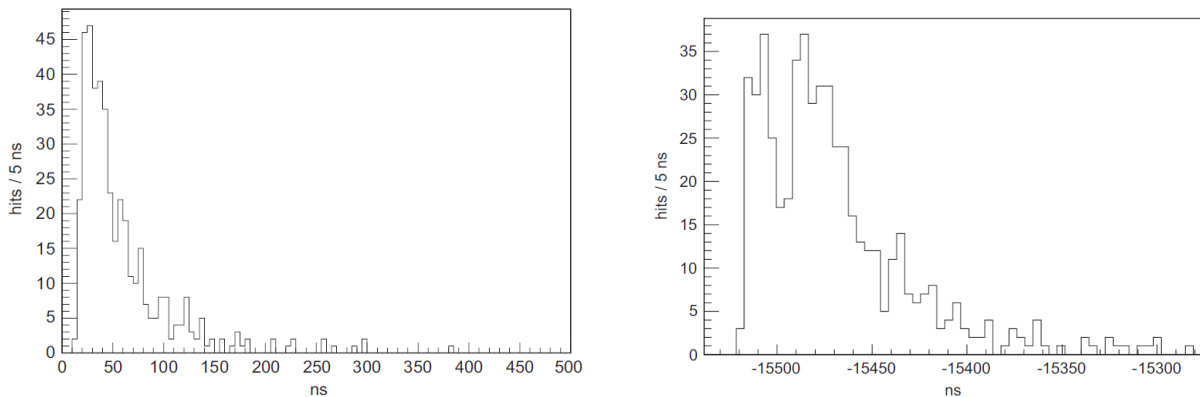


Figure 3.4: (a) Time distribution of the PMT hits in a single cluster event, (b) Two clusters partially overlapped and identified by the splitting software. The time distance of the two clusters is in this case about 25 ns. Clusters as close as 15 ns can be efficiently identified [106].

cluster events due to fast coincidences are studied for estimating the radioactive contamination in Borexino, while the more than one cluster events due to a neutron trigger are used for studying the cosmogenic contamination and the antineutrino signal.

Looking at the hit time distribution in a trigger gate of $16 \mu\text{s}$, the physical pulse is superimposed to the PMT random hits. In some cases, more than one physical peak from fast coincidences (for example ^{212}Bi - ^{212}Po coincidences) can appear in the trigger window of the same event, see Fig. 3.4. The clustering module groups the hits belonging to the same physical event into so-called **cluster**.

The clustering is done by scanning the time distribution of the decoded hits in 16 ns bins. The conditions for the start of a cluster are:

- the bin content exceeds the dark noise level by at least 3σ ,
- at least 20 hits are found in the first 48 ns,
- the integral of all hits exceeds the trigger threshold (typical BTB: 20 hit PMTs) by 80%.

The end of a cluster is set when the hits of a bin reach the dark noise fluctuation level again. Two subsequent physical events that are too close in time and do not fulfill the last condition are referred to as *pile-up*'s. Splitting algorithms can be used to disentangle such events .

3.3.2 Energy and position reconstruction

The position of a scintillation event is reconstructed using the timing information of the scintillation photons detected by the PMTs. The energy range of interest for BOREXINO goes from a few hundred keV to several MeV³. The track length of electrons with these energies in the scintillator is of the order of 1 cm, for alpha particles it is less than 1 mm. Compared to the spatial resolution of $\simeq 10$ cm at 1 MeV, the track length is negligible, and the scintillation events can be considered as point-like.

The electronic measures and provide for each triggered events :

- the photomultipliers pulse height, for energy measurement
- the photoelectron arrival times (better than 0.5 ns precisions), for position identification

To recall, Borexino is a self-triggering multiplicity detector, as explained in Section 3.1, the data acquisition trigger is produced when at least 25 PMT pulses occur within a tunable time window (60-99 ns), what corresponds to a threshold of $\simeq 40$ keV. When a trigger occurs, a $16 \mu\text{s}$ gate is opened and time and charge of each triggered PMT, so called hit, is detected. The readout sequence can also be activated by the outer muon detector by a trigger system that starts when at least 6 outer PMTs detect light in a time window of 150 ns. Regardless of the trigger type, data from both the inner and outer detectors are acquired.

The offline software identifies the shape of the scintillator pulse and reconstructs the position of the energy deposit by means of a time-of-flight based likelihood method that will be described in Section 3.3.2. while the energy of the incident particle is a function of the integral number of

³The ^7Be window is from 250 to 800 keV, while the ^8B neutrinos extend up to 16 MeV.

photoelectrons (p.e.) detected by all PMTs.

The calibration of the energy scale has been obtained by several methods: by studying the endpoint of the ^{14}C spectrum, fitting the ^{11}C energy spectrum, by keeping the light yield as a free parameter in the global fit and with calibration campaigns. All these methods provide a consistent light yield value of about 500 p.e./MeV of deposited energy. The energy resolution scales roughly as $5\%/\sqrt{E(\text{MeV})}$, while the position resolution is about 10 cm @ 1 MeV.

Energy reconstruction

The identified clusters from the clustering module are examined by further modules which deduce a large number of physical quantities. Some of the modules reconstruct the energy of the clusters.

Borexino's target material is an organic scintillator and, as such, energy spectroscopy can be performed by the measurement of the number of photons produced by a charged particle as it deposits its energy in the target. Borexino's electronics [103], as explained in Section 3.1, read out the number of photoelectrons produced by the PMTs. The β photon yield of the Borexino scintillator is $\simeq 10000$ photons per MeV of deposited energy [75]. The scintillation photons are emitted isotropically and a fraction of them will hit the cathodes of the PMTs and produce measurable photoelectrons. The number of detected photoelectrons should be proportional to both the number of produced photons and to the energy deposited and the photocathode coverage, to the extent that the scattering and absorption effects within the detector can be neglected.

In Borexino the total charge depends on several factors: the visible energy (E_{vis}), the Light Yield (the number of photoelectrons produced by a particle during the propagation in the scintillator per unit of deposited energy), the events reconstructed position (r), the non-linear quenching effects (f_q) and the saturation of the electronics:

$$Q(r, E_{vis}) = E_{vis}LY f(r, E_{vis}) f_q f_{el} \quad (3.1)$$

Several radioactive sources have been inserted in the detector during the calibration campaigns, (see Section 3.5) in order to convert this number into photoelectron in energy, to determine the Borexino Light Yield, to study the dependence of the released energy on the reconstructed position and the behaviour of the electronics in case of the events reconstructed near the edge of the vessel. Among them, the most important for this analysis are the $^{241}\text{Am}^9\text{Be}$ neutron source and the ^{228}Th source.

The calibration of the energy scale and the errors in its determination allows to establish with confidence the energy threshold and cuts for a neutrino flux measurement in Borexino. Distorsion of the energy scale are due to physical effects, like quenching, and geometrical effects, like light collection, and also to the electronics, which was designed for having the optimal performance in the low energy range for detecting solar ^7Be neutrinos, in a regime where a single photoelectron is expected for each PMTs. At higher energies the electronic response to multiple photoelectron hit on

a single channel is not linear.

The photocathode coverage is dependent on both time and position in the detector. Every run, Borexino's analysis software selects the working PMTs, which changes considerably due to, for example, PMTs dying when the high-voltage is reset or PMTs being disabled due to flashing. Furthermore, because of the asymmetric distribution of working (live) PMTs in Borexino, the photocathode coverage changes considerably at different positions within the IV.

To make a reliable measurement of the number of photons produced by an event and hence the energy deposit, it is necessary both to calibrate the energy scale and to take into account inefficiencies of the Borexino electronics in the measurement of the number of photoelectrons produced by individual PMTs.

Several variables are defined to evaluate the energy of the event. The most used in the analysis are:

1. **npmts**: it consists in the number of firing PMTs. Below 1MeV (~ 500 npmts) the number of firing PMTs is much less than the total number of working PMTs (~ 2200); in this energy region the npmts variable is in linear proportionality with event energy. Above 1 MeV, deviations from linearity are the more important the higher the energy and, eventually, saturation occurs.
2. **nhits**: it estimates the energy on the basis of the number of produced hits. Multiple hits on the same channel are taken into account, but also in this case deviations from linearity occurs at high energy. The unit is [hits]. An energy of 1 MeV deposited at the detector center corresponds to ~ 350 hits. The N_{hits} variable can be normalized introducing the reconstructed variable N_{rec} with the unit [nhits]. At higher energies the probability, that a single PMT is hit more than once, increases. By taking into account the binomial probability of such multiple hits and applying the normalization to 2000 alive PMTs one obtains:

$$N_{rec} = -2000 \cdot \ln \left(1 - \frac{nhits}{N_{pmt}} \right) \quad (3.2)$$

The N_{nhits}^{corr} variable is well-suited for analyses of events of which scintillation light deposited in the detector lies below ~ 1 MeV. Above this value another charge variable Q_{npe} is more adequate, because it has a wider dynamical range and follows an almost linear behavior at least above ~ 2 MeV up to ~ 9 MeV.

3. **charge** or Q_{pe} : it is the sum of the PMT integrated signals corresponding to the scintillation event, normalized to the mean value of the single photoelectron charge. Multiple hits within 80 ns are taken into account, hence it is the most linear variable. The unit is 1 photoelectron [pe]. 1 MeV deposited in the center of the detector corresponds roughly to ~ 500 pe. Q_{pe} is typically normalized and expressed by the reconstructed charge variable Q_{pe} with unit [npe] as follows:

$$Q_{rec} = 2000 \cdot \frac{Q_{pe}}{N_{pmt}} \quad (3.3)$$

with N_{pmt} being the number of PMTs that operate during a run. At the beginning of data acquisition in May 2007, most of the 2214 mounted PMTs were operational. However, after start of data collection several of the PMTs stopped working, especially in the lower hemisphere of the detector. During data collection, PMTs might be also switched off by subcomponents of the electronics. The normalization factor 2000 is a Borexino-internal arbitrarily chosen value. The energy unit after normalization is denoted by 1 normalized photoelectron [npe]. The normalization does not take into account the spatial distribution of the operating PMTs during a run, but only its total number, so this rescaling does not account for possible geometrical effects.

Additionally, at energies below ~ 1 MeV the light yield is not proportional to the deposited energy due to quenching effects. However, the calibration of the energy scale using a neutron source ^{241}Am ^9Be (see Fig. 3.11 and section 3.5) has also demonstrated that the charge variable grows almost linearly above ~ 2 MeV.

It is possible to convert the energy variables to MeV, taking into account that the Borexino Light Yield is about 500 photoelectrons (p.e.) per MeV. The charge variable already represents the number of p.e.. For the other two variables it is necessary to pass from the number of hits or PMTs to the number of p.e. [107]:

$$p.e. = -2000 \times \log \left(1 - \frac{N_{pmts \text{ or } Nhits}}{num. \text{ of live PMTs}} \right) \quad (3.4)$$

Within the Echidna framework the energy variable used for this thesis work is the **Normalized Charge**, because, as explained, this variable is more adequate in the analysis of events of which scintillation light deposited in the detector lies above 1 MeV, since it has a wider dynamical range and follows an almost linear behavior at least above ~ 2 MeV up to ~ 9.3 MeV (see Fig. 3.5). For determining the energy scale were used:

- calibration data to study the detector response to different type of particles depositing energy in the scintillator in different positions, see Section 3.5.
- MonteCarlo code: it simulates in detail all the detector components, the scintillation, the Čerenkov photon production, absorption and scattering of the light in the scintillator and in the buffer, and also the PMTs response, see Section 3.4. Each secondary electron in a γ -induced Compton electron cascade is affected by energy dependent ionization quenching, which amplifies the distortion in the γ energy scale. The quenching effect is modeled with the Birks formalism.

In Fig. 3.5 is shown the results of the calibration of the γ -equivalent energy scale in the detector center. Monte Carlo simulations reproduce γ peak positions and resolutions at $\sigma_1 = 1\%$ precision in the detector center, and at $\sigma_2 = 4\%$ precision at 3 m from the detector's center. Assuming the same accuracy for the γ -equivalent energy scale, was extrapolated it by simulating electrons uniformly distributed in the scintillator, and then selecting those with reconstructed position within

the fiducial volume. The error on the energy scale is obtained with a linear interpolation from σ_1 in the detector center to σ_2 at 3 m, along the radius. The γ -equivalent energy scale, in the energy region above 2 MeV, can be parametrized as:

$$N = a \cdot E + b \quad (3.5)$$

where N is the number of photoelectrons (p.e.) detected by the PMTs, $a = 459 \pm 11$ p.e./MeV and $b = 115 \pm 38$ p.e.. The non-zero intercept b is related to the fact that this description is valid only in this energy range and that the overall relation between N and E is non linear.

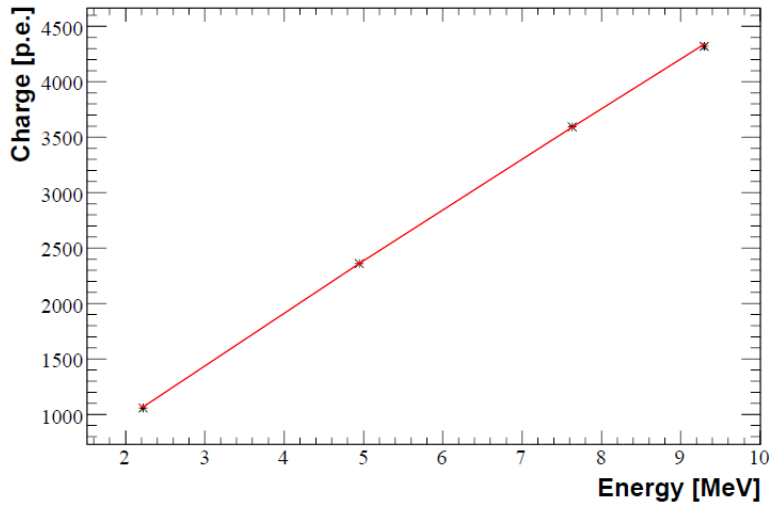


Figure 3.5: Energy scale of the charge variable: Black dots are the measured peak positions of γ radiation induced by neutron captures in 1H (2.223 MeV), ^{12}C (4.945 MeV), ^{56}Fe (7.631 MeV) and ^{54}Fe (9.298 MeV) in the detector center. Red line is the Monte Carlo prediction for γ rays generated in the detector center, plot from [57].

Position reconstruction

Every measurements done by Borexino consists of two parts: the numerator, that is the rate of neutrino events and the denominator, the target mass (or, the fiducial volume multiplied by the density of the scintillator). Therefore, the accuracy of the position reconstruction is linked with the accuracy with which Borexino can report a measurement.

For a spherical fiducial volume like that used in Borexino, applying standard propagation of errors yields the relationship between the fractional error on the fiducial mass due to the error on the reconstructed position:

$$\frac{\sigma_V}{V} = \frac{1}{V} \sqrt{\left(\frac{\partial V}{\partial r}\right)^2} \sigma_r = \frac{3}{r} \sigma_r \quad (3.6)$$

Thus, for a fiducial radius of three meters $\frac{\sigma_V}{V} = \sigma_r$, so, every 1 cm error on the fiducial radius adds another 1% error to the fiducial mass.

The Radon and ^{241}Am 9Be source data in the calibration campaign were used for estimating the

position reconstruction quality, comparing the reconstructed position with the nominal source position measured by a system of CCD cameras.

Due to the extremely low interaction rates of neutrinos and their antiparticles, it is necessary for a detector to contain a large mass of scintillator with very low levels of internal radioactive contamination [106]. In order to screen radioactivity from materials surrounding the detector [109] are used ultra-pure materials. Unfortunately, the photosensitive elements used to detect scintillation light can be the main sources of radioactivity in an ultra-low-background detector, therefore are inserted one or more layers of buffer material between the photosensitive elements and the scintillator to suppress radioactive background. This buffer has to be inactive, not scintillating in order to not overwhelm the neutrino signal.

Is required, since the compositions of the scintillator and inactive buffer are different, a scintillator containment system to and is the Borexino Inner Vessel. This physical separator, being in direct contact with the scintillator, must satisfy stringent intrinsic radiopurity requirements, as explained in Section 2.5.

For additional background prevention, the outer region of the scintillator volume can be used as an active buffer. This allows any residual radioactivity coming from the containment system, or passing through it, to be monitored and suppressed. A *fiducial volume* is commonly defined as a region at the center of the active volume of the detector in which radioactive background is expected to be at a minimum. The discrimination between events belonging to the fiducial and to the non-fiducial regions is performed by means of software implementation (reconstruction code) of an algorithm (reconstruction algorithm), which assigns to each single event a reconstructed position, either inside or outside the fiducial volume. The ability to reconstruct the position of the event within the inner vessel is crucial for the application of the radial cut that rejects the external background (see for example in Fig. 3.6 the spatial distribution of events in the energy range 900-1500 npe) and for an

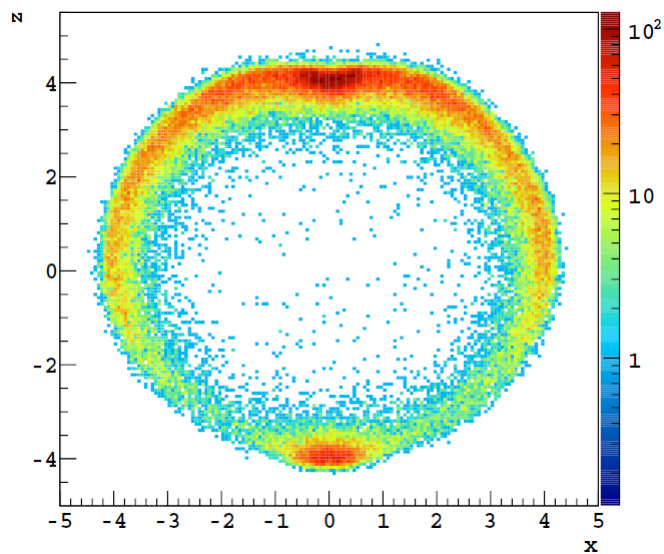


Figure 3.6: Spatial distribution of events in the 900-1500 npe energy region ($\sim[1.8,3]$ MeV), image from [108].

effective α/β discrimination.

The resolutions of detector reconstruction codes are generally studied with Monte Carlo methods. Event simulations allow close reproductions of the performance of these codes on real events. However, the reconstruction codes have to be fine tuned by calibrating the detector with the use of localized sources of radioactivity or light.

The Borexino detector utilizes a virtual fiducial volume centered on the origin in an effort to obtain the cleanest possible data sample; nevertheless, this volume does not have any physical structure associated with it, it is just a cut made in the software and as such, its precise definition relies on an accurate determination of the reconstructed position.

In order to perform fiducial volume cuts and external background reductions, is important to have a good position fitter code that, given the charge and time signal at the PMTs for each events, calculates the event position. The fitter is essentially a vertex reconstruction based on the principle that the shape of the time signal distribution depends on the distance between the event and the detector center.

After the identification of the scintillation events, this module reconstructs the vertex position (i.e. the light barycenter) of a point-like event from the hit time distribution. There are several algorithms in Echidna used for the calculation of the vertex position. The algorithms are referred to as *Milano*, *Dubna*, *Moscow* and *LNGS* according to the Borexino groups which developed them.

The time distribution of the clustered hits (see Fig. 3.4) is used by Echidna to determine the position of the scintillation event inside the ID.

The position reconstruction code used in this thesis is a modification of the *Milano* code: the *Lngs position reconstruction algorithm* in which are taken in account the effect of the timing shift by multi-photon. In fact was discovered, using the $Rn + ^{14}C$ source data from the calibration, that there was a shift in reconstructing the position that was energy dependent [110]: the arrival time of hits with large charge was found to be systematically earlier then the time with low charge. The explanation is that in the case of multi-photon hit is recorded the time of the fastest photon arriving at the PMT.

The code works on the information of the arrival time of the (first) photon on the photocathode in every channel. The time which passes from the excitation of the scintillator until the time when the PMT detect the photons has the following components:

$$t = t_{event} + t_D + t_{TOF} + t_{jitter} \quad (3.7)$$

where

1. t_{event} is the absolute time at which the energy deposit occurred.
2. The scintillator takes a finite amount of time for the de-excitation of the pseudocumene, energy transfer to PPO, and emission by the PPO. A given photon is emitted by the scintillator

after an interval t_D , which is distributed according to the probability distribution function for the scintillator. t_D is the scintillator decay time distributed as:

$$f(t, q, \lambda) = \sum_i q_i \lambda_i e^{-\lambda_i t} \quad (3.8)$$

where $\lambda_i = 1/\tau_i$ are the different decay constants of Table D.2 in Appendix D and q_i are the relative weights of the components ($\sum_i q_i = 1$).

3. t_{TOF} is the Time-of-Flight (tof) of the photon from the event real position r_e . Assuming linear propagation, it can be expressed as:

$$t_{TOF} = \sum_i \frac{n_i l_i}{c} \quad (3.9)$$

where n_i and l_i are respectively the refraction index and the distances covered in the different media crossed.

However the total reflection at the surface separating the two media and the phenomena described in appendix D (elastic scattering, absorption and re-emission) deviate the photon from a straight line propagation. These effects are difficult to model and are accounted for using an effective refraction index n_{eff} in place of the real scintillator one ($n_{PC} = 1.51$). Its value $n_{eff} = 1.68$ is determined from MC studies and especially from source tests, for which the nominal position of events can be compared with the reconstructed one. These tests involve radon sources inserted with a precise mechanical arm inside the inner vessel.

4. t_{jitter} is the PMT transit time jitter, represented by a Gaussian with $\sigma \simeq 1$ ns. It is the time required for the photoelectron emitted from the cathode to reach the first dynode. The path that the first photoelectron must take from photocathode to the first dynode depends upon where on the photocathode it was produced: this uncertainty is known as the PMT transit time jitter, and is on the order of 1 ns for the Borexino PMTs [111]. The jitter time simply acts to broaden the distribution of hit times slightly.

The Milano position reconstruction algorithm then use the PMT hit time signal corrected for the time-of-flight, to maximize, with the resources of the MINUIT code, the log-likelihood function ⁴:

$$f(t_0, x, y, z) = - \sum_{i=1}^{N_{hits}} \log \left(pdf \left(\frac{D_i \cdot n_{eff}}{c} - (t_i + t_0) \right) \right) \quad (3.10)$$

In order to consider the timing shift by the multi-photon, the variable pdf was introduced into the likelihood function in Eq. (3.10). At first were generated ten pdf s one for each number arriving at one PMT, from 1 to 10 (called here $pdf(1)$ to $pdf(10)$) as shown in Fig. 3.7 that shows the pdf s relative to different number of photons arriving. If the charge of the photon arriving is $1 < q < 10$, the variable pdf is defined as linear interpolation

$$pdf(int(q)) * ((int(q) + 1) - q) + pdf(int(q) + 1) * (q - int(q)) \quad (3.11)$$

⁴ D_i is the distance of the i^{th} PMT to the target position (x,y,z), c is the speed of light, n_{eff} is the effective refractive index, the pdf (Probability Density Function) is the simulated PPO emission curve.

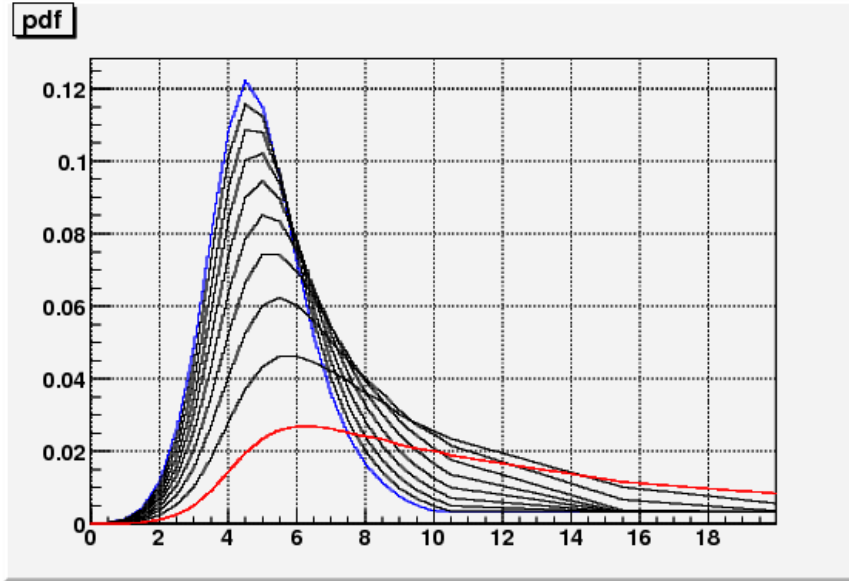


Figure 3.7: The pdf's in the case that the number of photons is from 1 (red, the original pdf) to 10 (blue), and the black lines show from 2 to 9. The horizontal axis shows the time from the first (ns) [110].

In the other case, $pdf(10)$, $c > 10$, to $pdf(1)$, $c < 1$, are used as the pdf value of each hit in Equation (3.10)⁵.

$$f(t_0, x, y, z, q) = - \sum_{i=1}^{N_{hits}} \log \left(pdf_q \left(\frac{D_i \cdot n_{eff}}{c} - (t_i + t_0) \right) \right) \quad (3.12)$$

The pdf so considers the effect of the timing shift by multi-photon, which is caused by recoding the fastest photon arrival time. Fig. 3.7 also shows the pdf functions, which are determined by the fastest hit timing for that the number of arrival photons are up to 10. Those functions are introduced as the pdf_q in Equation (3.12).

α/β discrimination

In Borexino signal comes largely from α , β or μ particles. While the last are detected and tagged by a dedicated Outer Muon system, this does not happen for α and β particles produced by the internal radioactivity. Furthermore the quenching effect of the scintillator moves the α emitted spectrum ($4 \div 8$ MeV) in the ${}^7\text{Be}$ energy range ($260 \div 990$ keV). To not overestimate the neutrino events because of the internal background, is needed an efficient α/β discrimination technique.

This is provided by the scintillator: in organic liquid scintillators α particles have a higher ionization density than electrons or γ -rays, resulting in a greater light emission in the longer time components of the scintillation pulse. The principle of the α quenching is explained in Section 2.5.2.

The efficiency for tagging various types of backgrounds that are present in Borexino is greatly improved when one can use particle identification techniques. Such methods are facilitated by

⁵This modified position reconstruction is named LNGS code and is present in Echidna with the getter `GetPositionLNGS()`.

exploiting the different time profiles of the scintillation light produced by variations in the ionization density of different types of radiation, see Fig. 3.8. There are two such methods employed by Borexino: the tail-to-total ratio (TTR), and the Gatti parameter [112]. In both cases, these statistical tests are based on the differences in the shapes of the light output, they are performed on the emission time spectrum, not the hit time spectrum. Once the position reconstruction module has determined the location and time of the event, it produces the emission time spectrum by subtracting the time of flight of each photon from the event position to each PMT that was hit.

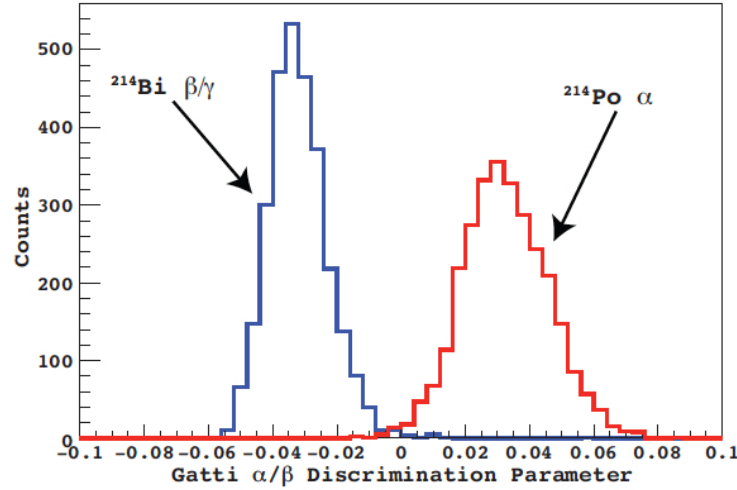


Figure 3.8: Gatti parameter for α events type (^{214}Po , red line) and for β events type (^{214}Bi , blue line).

- **tail-to-tail total ratio**

The tail-to-total ratio is given simply as the relative fraction of hits which occur in the tail of the pulse, where the tail start time is a user defined variable. Given Ω , the total number of bin used, a normalized sample $\mathbf{x}=x_i$ (x_i is the number of entries in the i -th bin), this ratio is:

$$t = \frac{\sum_{i=\text{tail}}^{\Omega} x_i}{\sum_{i=1}^{\Omega} x_i} \quad (3.13)$$

where the tail start time is a user-defined variable, it is a cut on time, generally placed around 20-30 ns for these data. Due to the fact that α events have a longer tail is expected the distribution for this ratio to be centered around higher values for α than for β events.

- **the Gatti linear discriminant**

This statistic aims to determine how similar the pulse under consideration is to one of two reference shapes. The $^{214}\text{Bi}^{214}\text{Po}$ delayed coincidences (see Fig. 3.8) provide a nice and clean sample of α and β events that can be used to develop and tune the α/β discrimination algorithms. These algorithms are based on the different time response of the scintillator to α and β particles. Let's define:

$\alpha_i = \frac{1}{N_\alpha} \sum_{j=1}^{N_\alpha} x_\alpha^{ij}$ the number of entries in the i -th bin for the average sample of the α training set

$\alpha = \alpha_i$ the average sample of the α training set

$\beta_i = \frac{1}{N_\beta} \sum_{j=1}^{N_\alpha} x_\alpha^{ij}$ be the number of entries in the i -th bin for the average sample of the β training set

$\beta = \beta_i$ the average sample of the β training set

The more general linear filter is given by a particle identification signal \mathbf{S} that can be written as a weighted sum of the α and β contributions:

$$S_\alpha = \sum_i P_i \alpha_i \quad S_\beta = \sum_i P_i \beta_i \quad (3.14)$$

The two signals differ by:

$$\Delta = S_\alpha - S_\beta = \sum_i P_i (\alpha_i - \beta_i) \quad (3.15)$$

The Gatti filter is the linear discriminant defined by the weights P_i that reduce the relative variance ($\epsilon_\Delta^2/\Delta^2$) of this difference to a minimum. It can be proved that in the hypothesis of statistical Poisson fluctuations for the α_i and β_i quantities and assuming the same size for the two training sets ($N_\alpha = N_\beta$), the weights P_i return to be:

$$P_i = \frac{\alpha_i - \beta_i}{\alpha_i + \beta_i} \quad (3.16)$$

The filter results to be an optimum linear discriminant and the quantity

$$G = \sum_{i=1}^{\Omega} \frac{\alpha_i - \beta_i}{\alpha_i + \beta_i} \cdot x_i \quad (3.17)$$

is the discriminant variable used. It is clear that α s are defined by $G > 0$ and β s as $G < 0$.

3.4 Simulation tools

The Monte Carlo code originally developed for Borexino was **GENEB** [113]. It was programmed by the Italian Borexino group in Milan and is based on the EGS4 code [114]. A second, more powerful simulation framework tool named **Bxmc** based on GEANT4 has been developed and continuously improved and is now widely used by the Borexino collaborators. A detailed description of the Monte Carlo code and the energy reconstruction algorithm is in preparation by the Borexino Monte Carlo working group.

Bxmc (BoreXino MonteCarlo) consists of the following part:

- Particle generation and propagation in the Inner Detector: the Monte Carlo code **G4BX** generates and propagates particles in the Borexino detector until they reach the photocathodes of the PMTs. Several particle generators can be selected. The decay of radionuclides is typically simulated by the Radioactive Decay Module (RDM) which is based on the ENSDF tables [115]. Each generated particle is propagated individually within the fully modelled

Inner Detector of Borexino. All materials used for the construction of the detector are included in the simulation. The simulation takes into account the production of the scintillation and Cherenkov light, the propagation and the energy loss mechanisms for light and for all other particle types. Each secondary electron in a γ -induced Compton-electron cascade is affected by energy-dependent ionization quenching, which amplifies the distortion in the γ energy scale. The quenching of the scintillation light is described by the Birks formalism (see Section 2.5.2). To some extent the code also uses a Borexino internal database containing values from laboratory measurements of the characteristic absorption and reemission time of the scintillation light in the scintillator mixture used. The output of this simulation can be directly converted into a ROOT file. At the same time it is used as input for the electronics-chain simulation.

- Electronics-chain simulation: The simulation tool `bx-elec` simulates the entire electronics chain starting from the photocathode of the PMTs. The trigger threshold, the Single Photo-Electron of each operating PMT, the time delays and the charge information loss within the electronics chain are included. In order to simulate a real data set, `bx-elec` can also adopt the exact pattern of operating PMTs and DAQ/electronics settings during the period of interest. The output of the simulation chain is a set of data that has precisely the same format as the real raw data file.
- Data reconstruction: at the end of the simulation, data are processed by the decoding and reconstruction code Echidna as described in Section 3.3. The final informations are then stored into a ROOT file, identical to the data ones and containing in addition all the informations about the original simulations (for ex.: original position and energy, the number of deposits and daughters,...).

This is the code that will be used to simulate also the neutrino charged-current interactions on ^{13}C in Chapter 6.

3.5 Calibration with sources

In order to measure accurately the solar neutrino fluxes, the Borexino detector must be carefully calibrated. As shown by several studies done with MonteCarlo simulations, and confirmed by the first measurement of ^7Be neutrinos [55] the main sources of uncertainty in the measurement of the solar neutrino fluxes are: the knowledge of the fiducial mass, i.e. the innermost part of the scintillator that is used as the neutrino target and whose volume is defined by means of a cut on the reconstructed position of the events, the knowledge of the energy scale for α , β and γ particles and the knowledge of the detector energy response as a function of the event position within the fiducial volume, of the particle type and of the energy itself. Thanks to the calibration campaigns a better understanding of the detector was reached opening leading to a new measurement of the ^7Be solar neutrino flux with a lower error [59].

For these reasons, was developed a system for the insertion of radioactive and light sources in Borexino. With the use of this system, a suitable set of α , β and γ sources can be put into various known positions within, and at the border of, the fiducial volume, so that the complete detector response can be determined. This system must fulfill stringent requirements in terms of radiopurity, cleanliness, mechanical strength and reliability, and must guarantee complete airtightness while inserting, operating, and removing the sources from the detector.

The Borexino detector design has foreseen from the beginning the possibility to perform a wide range of different calibration types: there is in fact an internal and an external calibration system. The internal calibration system allows to place radioactive sources within the Inner Vessel. The sources are inserted into the scintillator from a clean room (CR4) on the top of Borexino, where the detector can be opened. In case of the external calibration system, a source is transported through the Water Tank via a tube system and deployed right behind the Stainless Steel Sphere.

To summarize, a rigorous calibration with radioactive and optical sources can be used to reduce the errors associated with:

- The detector response function.
 - Energy response as a function of position, particle type, and energy.
 - Empirical measurement of the Birks quenching coefficient with gamma sources.
- Fiducial mass determination and position reconstruction bias as a function of energy, position and particle type.
- Alpha beta discrimination efficiency as a function of energy and position.
- Efficiency of a distance separation cut for events assumed to occur at approximately the same location.
- Efficiency of the Borexino trigger and its threshold.
- Temporal deviations in all of the aforementioned parameters due to PMTs being connected or disconnected, board changes, modifications to the software reconstruction, etc.

3.5.1 Internal calibrations

Two calibration campaigns were performed in 2008 and 2009 aimed to reduce systematic uncertainties, to tune the reconstruction algorithm and Monte Carlo simulation, to study possible systematics associated to the position reconstruction of the events, and to determine the energy scale and the detector response function with high precision.

Before calibrations, reconstruction of position and energy was tested and tuned on internal contaminants (like ^{14}C or ^{222}Rn) in a non optimal way and this was reflected in the high systematic error associated to the first ^7Be measurement.

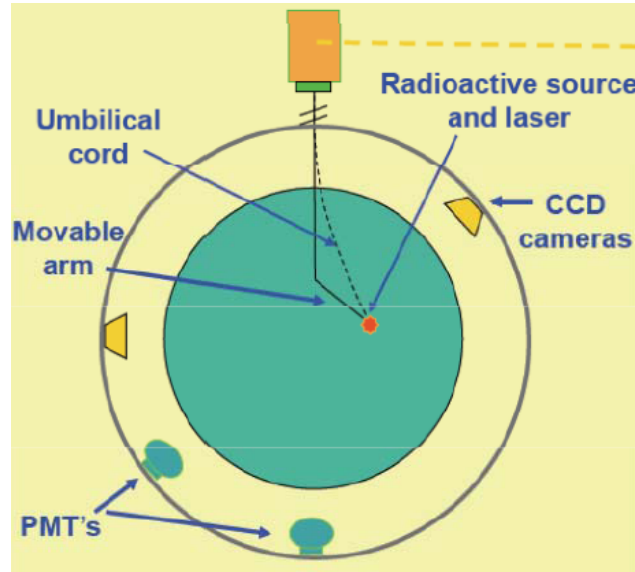


Figure 3.9: Pictorial view of the internal calibration source insertion system in Borexino.

In order to avoid additional background contaminations into the detector, the source vials were carefully developed. In October 2008, the first internal calibration campaign was performed, in which the sources were only placed along the z-axis (on-axis) perpendicular to the point of insertion. In 2009, was performed an off-axis calibration using a movable arm that allowed to scan the interior of the Inner Vessel. The calibration arm, see Fig 3.9, consists of several rods which are coupled but still free to move off-axis like an *arm* via a tether tube made of Teflon. A source can be fixed on a special coupler mounted on the end of the deployment system. To locate the source, a fiber optic cable transmits a red laser light to a diffuser bulb mounted close to the source. This is shown also in the picture in Fig. 3.10. A detailed description of the calibration system in the Inner Detector of Borexino can be found in [74]. The calibration strategy is based on several sources, alphas, betas, gammas, and neutrons, at different energies. In total, around 300 positions in the Inner Vessel were scanned using different calibration sources: γ emitters (^{139}Ce , ^{203}Hg , ^{85}Sr , ^{54}Mn , ^{65}Zn , ^{60}Co , ^{40}K), β -emitters (^{14}C , ^{214}Bi), the α emitter ^{214}Po and the neutron emitter $^{241}\text{Am}^9\text{Be}$ (Table 3.1).

	γ sources							
	^{57}Co	^{139}Ce	^{203}Hg	^{85}Sr	^{54}Mn	^{65}Zn	^{60}Co	^{40}K
E(MeV)	0.122	0.165	0.279	0.514	0.834	1.1	1.1, 1.3	1.4
	β sources		α		neutrons			
	^{14}C	^{214}Bi	^{214}Po		n-p	n+ ^{12}C	n+Fe	
E(MeV)	0.15	3.2	7.6		2.22	4.9	~ 7.5	

Table 3.1: Sources used in the internal calibration campaign

- As the gamma rays are the only particles that succeed in escaping the source and release their energy in the scintillator, a series of gamma sources have been chosen to study the energy scale. The energy scale was studied by inserting 8 different gamma-emitting sources spanning the energy range of interest for the ${}^7\text{Be}$ analysis (from ~ 100 keV to 1.4 MeV). The calibration campaigns allowed to reduce the uncertainty on the energy scale between 0 and 2 MeV to less than 1.5%.
- In order to have calibration points at higher energies, relevant for ${}^8\text{B}$ solar neutrinos and geo-neutrinos, was used an ${}^{241}\text{Am}{}^9\text{Be}$ neutron source. Due to the quenching phenomenon, the energy scale of a scintillator is not linear and depends also on particle type. In fact, the neutron captures can happen on protons, ${}^{12}\text{C}$ or ${}^{56}\text{Fe}$ with a consequent γ emission with energy of 2.2 MeV, 4.9 MeV and 7.5 MeV, respectively. In order to obtain the conversion factor between the measured value of Charge and the visible energy in MeV, four points were used. The peaks used are: 2.2 MeV gamma from the capture on hydrogen, 4.95 MeV gamma from the capture on ${}^{12}\text{C}$, 7.65 MeV gamma from the capture on ${}^{56}\text{Fe}$ and the 8.88 MeV peak which is the combination of two 4.4 MeV gamma (first one is produced together with fast

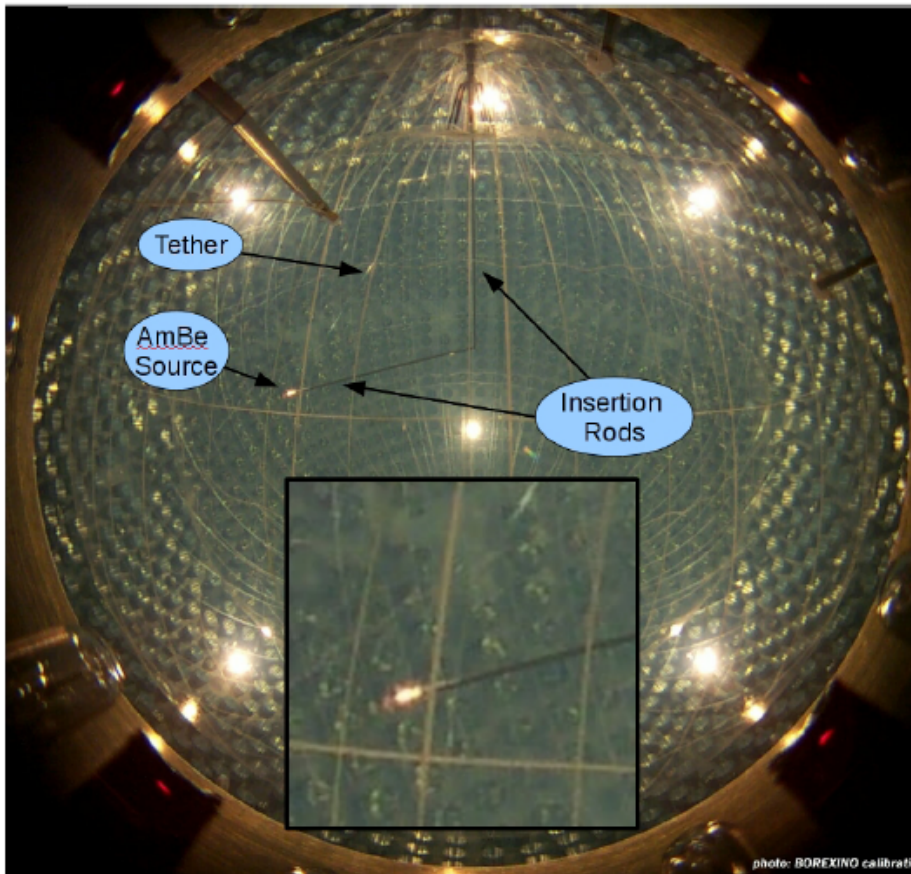


Figure 3.10: ${}^{241}\text{Am}{}^9\text{Be}$ neutron source deployed at the conclusion of the calibration in June 2009 as seen by camera 1. The insertion rods are clearly visible entering the detector through the inner vessel fill pipe, the tether tube is visible at several locations where the halogen lights reflect from it. The inset is zoomed-in to better show the source, the illuminated area is a combination of the red laser light and reflection of of the source coupler. Picture from [74].

neutron inside the source and the second one is produced by the escaped ^{12}C atom after interaction with the fast neutron exited from the source). The result of this calibration is shown in Fig. 3.11.

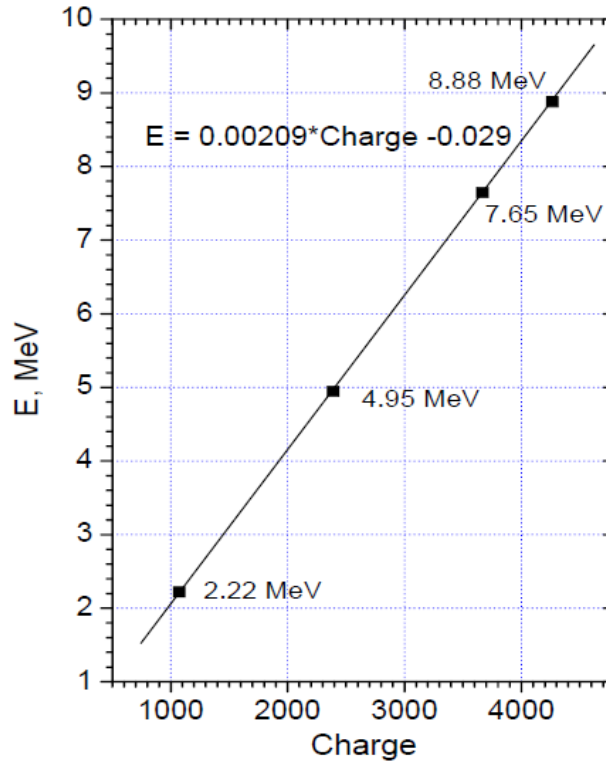


Figure 3.11: The dependence between the measured Charge and the event energy in MeV. The data is obtained from the calibration performed with an $^{241}\text{Am}^9\text{Be}$ neutron source. By the squares on the plot the following points are represented: capture on the hydrogen (2.2 MeV), capture on ^{12}C (4.95 MeV), capture on ^{56}Fe (7.65 MeV) and 2×4.44 MeV [116].

- The ^{222}Rn source comprises all the isotopes of the sub-chain, emitting both alpha and beta particles at different energies. Since alpha and beta particles would not succeed in escaping the vial, the source is dissolved in a sample of Inner Vessel scintillator, accurately treated in order to avoid contact with air.

The ^{222}Rn source, deployed in more than 200 positions, was mainly used to study the position reconstruction and the position dependence of the detector response. The nominal source position was determined independently by a system of 7 CCD cameras located on the Stainless Steel Sphere (where also the 2200 phototubes are mounted). The calibration campaign allowed to reduce the overall systematic uncertainty on the Fiducial Volume selection from 6% down to $\sim 1\%$.

- The ^{57}Co has been selected also to study the trigger efficiency, which is tested at low energy (122 keV), in order to check the trigger threshold effect and because the low energy range is the most delicate region, where the trigger could have the worst behaviour.

3.5.2 External calibration

Radioactive decays and nuclear interactions in the buffer, the photomultiplier tubes (PMT), the light concentrators, the Stainless Steel Sphere (SSS) and from the environment emit highly energetic γ rays and neutrons which can penetrate the buffer layers, producing a signal in the fiducial volume. A discrimination of these signals is not possible as opposed to an internal contamination by ^{232}Th (where is possible to look for e.g. fast coincidences from ^{212}Bi - ^{212}Po decays), because in the latter is assumed a secular equilibrium that can't be done for the external background.

Is the 2.615 MeV γ rays that mainly contribute to the external background: is the highest energetic photons released from naturally occurring radioactive decays and originates from decays of the ^{232}Th daughter nuclide ^{208}Tl .

The energy spectrum of the external background has this peak around 2.6 MeV and decreases to lower energies. The rate of the events also decreases for smaller fiducial volumes but was found to be still visible within a spherical fiducial volume with radius $R < 2.5$ m (see Fig. 3.12).

For all the neutrino analysis that are based on fiducial volumes with different radii above $R \approx (2.0-2.5)$ is necessary to know the total spectral shape from the external background.

Therefore, as also previous Monte Carlo simulations have shown [117], the spectral shape is expected to change dramatically with the size of the fiducial volume: the larger its radius the larger the probability to encounter Compton-scattered γ rays, which are still able to reach the outer region of the scintillator in the Inner Vessel. This leads to an increased Compton continuum below the

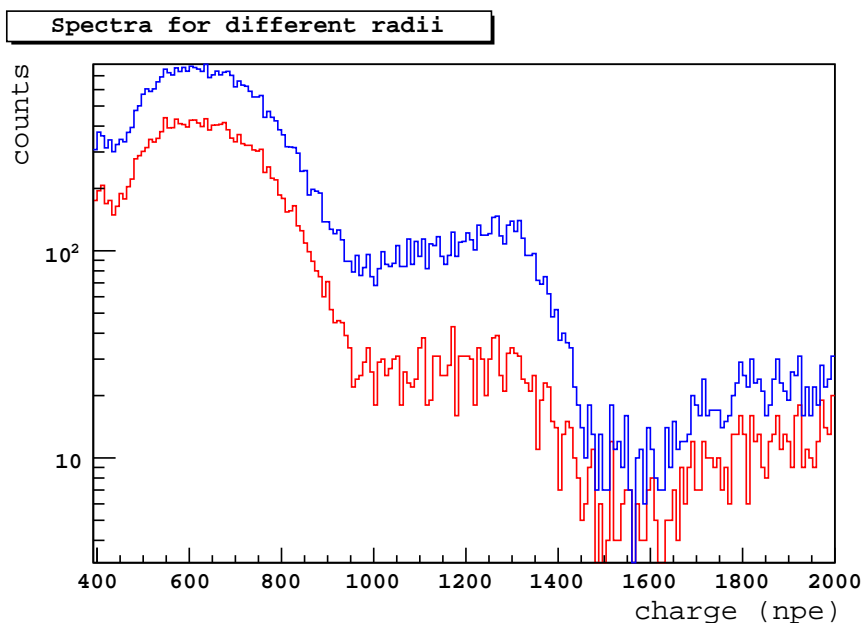


Figure 3.12: Spectra of events builded with different fiducial volumes, the red with $R < 2.5$ m and the blue with $R < 3$ m, is still visible in both spectra the external background peaked around 1250 p.e.

full-energy peak of the 2.615 MeV γ line as shown in Fig. 3.13⁶.

The gamma-rays from external background will be treated in Chapter 5 since are the main reason for the energy threshold that will be chosen for this CC interaction analysis. ^{208}Tl has a Q-value of 5.01 MeV and, therefore, is an important component of the Borexino spectrum above 3 MeV. The parent of ^{208}Tl is ^{212}Bi , which β -decays into ^{212}Po ($Q = 2.25$ MeV) with a lifetime of $\tau = 431$ ns and a branching ratio of 64%. The other 36% of ^{212}Bi α -decays into ^{208}Tl with lifetime of $\tau = 4.47$ min.

A first external calibration was performed in July 2010 and the second is ongoing at the moment of the writing. The external calibration system was designed for the purpose of positioning highly active γ sources. For this purpose a custom-made ~ 5 MBq ^{228}Th source emitting long-range 2.615 MeV γ rays has been produced and deployed at 6.85 m distance from the center of the detector. This distance corresponds to the radius of the stainless steel sphere. Two positions, one in the north and one in the south hemisphere of the detector, were measured. In Fig. 3.13 are shown the

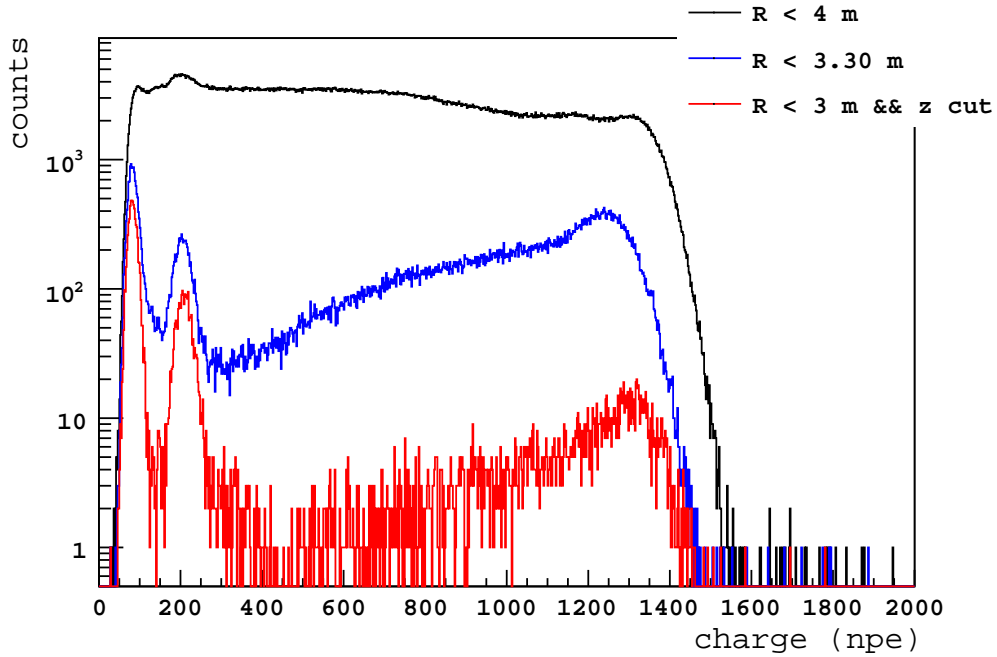


Figure 3.13: Energy spectra of the external ^{228}Th source depicted for different fiducial volumes. The black line is the energy spectra within a sphere of radius 4 m, the blue is with FV with radius 3.30 m, that will be used in the analyses relative to this thesis, and the red is with the FV used for the ^7Be neutrinos, a sphere of radius = 3 m with a z cut to reduce the contamination from the poles of the IV.

energy spectra of the external ^{228}Th source for different fiducial volumes⁷.

⁶For some analysis, like pep flux measurement, is necessary to estimate the spectral shape of the external background below the clear signature from the 2.615 MeV full-energy peak.

⁷These spectra are plotted in the variable **normalized charge**, corrected with the geometrical function studied in [118] in order to eliminate difference in the detector's response for the source positions in the north and south hemisphere

$$Q_{corr} = Q_{rec} \cdot \frac{1}{(1+A \cdot Z \cdot |Z|^n + B \cdot |Z|^k)} \cdot \frac{1}{1+C \left(\frac{d}{1+|Z|}\right)} \quad d = \sqrt{x^2 + y^2}, \quad A=8.65 \cdot 10^{-3}, \quad B=4.93 \cdot 10^{-5}, \quad C=2.1 \cdot 10^{-3}, \quad n=0.58,$$

Summarizing, the benefit of the external calibrations are:

- Energy reconstruction:
 - Using the spectral shape information of the external background for neutrino analyses (${}^7\text{Be}$, CNO, pep, ${}^8\text{B}$, anti-neutrinos).
 - Testing the energy uniformity by looking for North/South asymmetries in the detector.
 - Supplying an energy calibration point and defining the energy resolution at 2.615 MeV.
- Position reconstruction:
 - Definition of the spatial resolution of position reconstruction.
 - Periodical monitoring of the position reconstruction stability. This is important to check the validity of the solar neutrino signal time variation measurements such as the annual 7% variation due to the Earth orbit eccentricity.
 - Studying of the radial distribution: estimating the external background rejection efficiency.
- MC simulation:
 - Comparison of data versus MC calculated spectra for different source positions and tuning of the MC code.
 - Using the tuned MC code to perform a simulation of the full external background.

Chapter 4

CC neutrino interactions on ^{13}C in high purity liquid scintillators

There are a variety of neutrino-nucleus reactions that permits the terrestrial observation of astrophysical neutrinos. Generally, the following types of neutrino-nucleus reactions are possible:

$$\nu_l + {}^Z A \rightarrow l^- + {}^{Z+1} A \quad (4.1)$$

$$\bar{\nu}_l + {}^Z A \rightarrow l^+ + {}^{Z-1} A \quad (4.2)$$

$$\nu_l + {}^Z A \rightarrow \nu_l + {}^Z A \quad (4.3)$$

$$\bar{\nu}_l + {}^Z A \rightarrow \bar{\nu}_l + {}^Z A \quad (4.4)$$

In the first two charged-current (CC) reactions, the script l is limited to the electron family unless the incident energy is high enough to produce a muon or a tau-lepton, whereas the neutral-current (NC) reactions in the last two equations, can always occur for $l = e, \mu$ and τ . The final nuclear state A can in general be either bound or unbound (if the latter is allowed energetically), and all these will contribute to inclusive events in which only the final leptons are monitored. Neutrinos play fundamental roles in various astrophysical phenomena, and terrestrial experiments to detect these neutrinos can give astrophysical informations of high value, in particular, as already pointed out in Section 2.4, in Borexino is interesting to study the interaction channel of low energy neutrinos from the Sun with nucleus.

As shown in Fig. 1.4, it is useful to distinguish three different energy regimes of the astrophysical neutrinos:

- (i) The low energy region ($E_\nu \leq 20$ MeV), which includes the solar neutrinos and the lower energy part of the supernova neutrinos,
- (ii) The medium-energy region (20 MeV $\leq E_\nu \leq 50$ MeV) exemplified by the higher energy region of supernova neutrinos,
- (iii) The high-energy region (50 MeV $\leq E_\nu$) represented by the solar flare neutrinos and atmospheric neutrinos, whose energy can reach as high as 1- 2 GeV.

Solar neutrinos will be the main source of astrophysical neutrinos considered in this Chapter.

As explained in Section 1.2.2, the Sun generates its energy primarily by changing protons into α -particles. The actual reaction chain through which $4p \rightarrow {}^4\text{He} + 2e^+ + 2\nu_e$ takes place involves many intermediate nuclear reactions, some of which are weak-interaction processes emitting neutrinos. The standard solar model (SSM) [119–122] gives a definite prediction of the neutrino flux coming from each of these neutrino-emitting reactions. In this Chapter we investigate the possibility to use a particular neutrino interaction channel on nuclei contained in organic liquid scintillators to detect low energy neutrinos from the Sun.

4.1 The physics case

In organic liquid scintillators is possible to measure neutrino fluxes by means of the ν_e charged-current interactions with Carbon nuclei. The possibility to use ^{13}C as a target for ${}^8\text{B}$ neutrinos was pointed out in the past by J. Arafune, M. Fukugita, Y. Kohyama, and K. Kubodera in [123–125] and was investigated a possible advantage of using a ^{13}C -enriched scintillator counter as a solar neutrino detector. ^{13}C is a stable isotope of Carbon with a natural isotopic abundance $I=1.07\%$. A replacement of ^{12}C in a scintillator detector with its isotope ^{13}C not only makes the detector much more sensitive to charged-current reactions, but also turns into a highly efficient detector for neutral current reactions.

At the moment of these studies on neutrinos CC interactions on ^{13}C , in the 1990s, there was a serious disagreement between the Davis experiment [126] and the prediction by the standard solar model [122] and the Solar Neutrino Problem was one of the most important issues in astrophysics. Many ideas to solve this problem had been proposed, which were involving either modification of the solar model or introduction of non-standard properties of neutrinos [127].

Several experiments have been proposed in order to distinguish various possibilities, with different characteristics from the chlorine experiment by Davis. The list of distinctive characteristics that could have been useful in a different experiment were including for example different threshold energies, different energy response, real-time detection, natural-current detection, etc. The proposals for solar neutrino detectors were yet employing radiochemical or geochemical methods [128], but more stress was placed on direct counting, which allows a real-time measurement. The methods proposed or also operating at that time, mostly were using either Čerenkov counters (with H_2O [129] or D_2O [130]) or liquid scintillators (CH_2) [131]. These experiments (except for D_2O) mainly were aiming at measuring $\nu_e e^- \rightarrow \nu_e e^-$ scattering.

The merit of using liquid scintillators (or liquid track counters) is that one can, in principle, decrease the detection threshold for recoil electrons. Since the recoil electrons from ν -e scattering have quite a soft energy spectrum¹, the lowering of the detection threshold energy largely enhances the sensitivity. Lowering the detection threshold is of importance, also because it is highly desirable to measure the energy spectrum of neutrinos for as wide a range as possible. This would offer

¹e.g., if $E_{th} \sim 7.5$ MeV only 10% of the $\nu_e e^- \rightarrow \nu_e e^-$ events can be measured for ${}^8\text{B}$ solar neutrinos, see Fig 1.7

valuable information on the nature of the solar neutrino problem.

These studies on neutrinos interactions on ^{13}C are among the various ideas for solar neutrino experiments with different characteristics from the original ^{37}Cl experiment. The willing was to perform a measurement of the neutral current interaction to unambiguously settle the long standing issue of the deficit of neutrino capture rate in the Davis experiment. In fact the information on the neutral-current reaction would have been crucial in discriminating among solutions to the solar neutrino problem [130, 132].

It is also to consider that, if the target volume of liquid scintillator is large enough, it is possible to detect neutral-current reactions even with the natural isotopic abundance of ^{13}C and without any enrichment.

Nowadays, observations of solar neutrinos [133–139] have offered the first experimental evidence in favor of non-standard effects, in particular neutrino flavor transitions induced by non-zero neutrino masses and mixing. Solar neutrinos have been detected by radiochemical experiments (i. e., Homestake [133], Gallex/GNO [134, 135] and SAGE [136]) which give an energy-integrated information on the solar neutrino fluxes, and by real time water Čerenkov detectors (i. e., Kamiokande, Super-Kamiokande [137, 138] and SNO [139]) which allow to observe the spectral distribution of solar neutrino events. However, the detection threshold in Čerenkov detectors before 2010 was limited to about 5 MeV by the radiopurity level. In 2010 the lowest energy threshold in Čerenkov experiments, corresponding to 3.5 MeV, has been reached by the SNO experiment [58]. Liquid organic scintillator detectors, such as KamLAND [140] and Borexino, are operating with the main goal of measuring the low energy solar neutrino fluxes, in particular ^7Be , CNO and pep solar neutrinos.

The KamLAND experiment is a 1 kT detector located in the Kamioka mine (Japan), at a depth of 2700 m.w.e. of rock, operating continuously since January 2002, with the main goal of measuring the flux of the $\bar{\nu}_e$'s coming from all the Japanese nuclear power plants. This experiment has spectacularly confirmed the so-called Large Mixing Angle (LMA) solution to the solar neutrino problem.

There are also two proposed detectors, a ~ 1 kT liquid scintillator detector, denominated SNO+, at the SNO site (SNOLab, Canada) under 6000 m.w.e. of rock, at present in construction.

It is also under discussion the possibility to realize a gigantic (≥ 30 kT) liquid scintillator detector, the Low Energy Neutrino Astrophysics (LENA) detector [141], in the Pyhäsalmi mine (Finland) at a depth of 1450 m (~ 4000 m.w.e.), although other sites (e. g., underwater in the site of Pylos in Greece) have also been proposed. The observation of solar neutrinos in these detectors, through $\nu - e$ elastic scattering, is not a simple task, since neutrino events cannot be separated from the background on event-by-event basis, and it can be accomplished only if the detectors contamination will be kept very low. Moreover, only mono-energetic sources such as ^7Be or pep neutrinos can be detected, taking advantage of the Compton-like shoulder edge produced in the event spectrum.

From this starting point, the possibility to observe ^8B solar neutrinos in scintillators detector, thorough a different channel then the $\nu_e - e^-$ scattering, was investigated by A. Ianni, D. Montanino, F.L. Villante in [71], showing that in organic liquid scintillator detectors it is possible to measure the ^8B solar neutrino flux by means of the electron neutrino charged current interaction with the ^{13}C nuclei naturally contained in the scintillators. Here, was proposed a technique to tag the solar neutrino events that consist in identifying the signal by looking at the time and space coincidence with the decay of the produced ^{13}N nuclei and was performed a detailed calculation of the solar neutrino signal and of the background in some experiments like KamLAND, Borexino and SNO+, showing that these detectors would have been able to extract the signal with a reasonable uncertainty in a few years of data taking.

It should also be stressed that the proposed technique does not involve any modification of the experimental setup, since one expects a background-to-signal ratio of the order of 1 or less even assuming the natural isotopic abundance of ^{13}C ($\sim 1\%$) and the contamination levels already reached in the detectors².

4.1.1 Neutrinos on Carbon

As already pointed out in Section 2.4, since the solvents of organic liquid scintillators are based on hydrocarbons, in between the other targets are offered also the bound protons and neutrons of Carbon nuclei as interaction partners for neutrinos. In liquid scintillators can be observed both neutral and charged current reactions with Carbon.

Neutrinos on ^{12}C

In Borexino, in all the Inner Vessel the number of ^{12}C nuclei is $1.24 \cdot 10^{31}$.

As shown in Table 4.1, ^{12}C offers three possible reaction channels to neutrinos, two charged-current and one neutral current reaction with thresholds around 15 MeV. While the thresholds are too high and the cross sections too low for most applications, SuperNova neutrino observation significantly benefits from these channels.

The charged current reactions both provide a very similar delayed coincidence. The incoming $\nu_e/\bar{\nu}_e$ interacts with the nucleus, thereby creating an e^-/e^+ and an instable isotope. The signal due to the e^\pm is then followed 10 ms/20 ms later by the re-decay of the $^{12}\text{N}/^{12}\text{B}$ under emission of an e^-/e^+ . Once again, this delayed coincidence can be used as event signature. It must however be stated that, as the subsequent β^\pm - decays feature similar endpoints, and the half-life is very similar, it is experimentally challenging to discriminate on an event-by-event basis ν_e from $\bar{\nu}_e$ events.

The third channel, inelastic scattering exciting the Carbon nucleus, is possible for all neutrino flavors. As there is no prompt signal, the only event signature is the de-excitation gamma of 15.11 MeV. Apart from its threshold, the reaction bears no spectroscopic and no flavor information of the incident neutrino. Even if this reactions would have been very useful for the large amount of ^{12}C

²In [71] was considered a contamination of Uranium and Thorium of 10^{-17} . In Borexino the lowest ever measured levels of natural contaminants from Uranium and Thorium have been established and are to the order of $10^{-17} - 10^{-18}$.

Reaction	Current	Threshold [MeV]	Cross section [cm^{-2}]
$\nu_e + {}^{12}C \rightarrow {}^{12}N + e^-$ ${}^{12}N \rightarrow {}^{12}C + e^+ + \nu_e$ β^+ : $\tau = 11.0$ ms	CC	17.34	28.7×10^{-44} @ 20 MeV
$\bar{\nu}_e + {}^{12}C \rightarrow {}^{12}B + e^+$ ${}^{12}B \rightarrow {}^{12}C + e^- + \bar{\nu}_e$ β^+ : $\tau = 20.2$ ms	CC	13.37	71.1×10^{-44} @ 20 MeV
$\nu_x + {}^{12}C \rightarrow \nu_x + {}^{12}C^* + \gamma(15.1 MeV)$ $\bar{\nu}_x + {}^{12}C \rightarrow \bar{\nu}_x + {}^{12}C^* + \gamma(15.1 MeV)$	NC	15.11	30.2×10^{-44} @ 20 MeV 27.9×10^{-44} @ 20 MeV
$\nu_e + {}^{13}C \rightarrow {}^{13}N + e^-$ ${}^{13}N \rightarrow {}^{13}C + e^+ + \bar{\nu}_e$ β^+ : $\tau = 862$ s	CC	2.22	8.12×10^{-43} @ $\langle E_{sB} \rangle$
$\nu + {}^{13}C \rightarrow \nu + {}^{13}C^* + e^+ \gamma$	NC	3.68	1.16×10^{-43}

Table 4.1: Detection reactions along with the applying weak current, threshold, the energy dependent cross section (energy in MeV), and the subsequent reaction

in the scintillator and for the large cross section, they are useless for the solar neutrino detection because of the high threshold.

Neutrinos on ${}^{13}C$

As the natural isotopic abundance of ${}^{13}C$ is 1.1 %, a liquid scintillation detector can also exploit neutrino reactions on this isotope.

Albeit event rates are low due to the reduced number of target nuclei³, both the CC reaction of ν_e and the NC inelastic scattering are interesting as their thresholds are low, 2.2 and 3.7 MeV, respectively. Especially the delayed coincidence signal of the CC reaction could be utilized in the detection of solar 8B and SuperNova ν_e .

The advantages in replacing ${}^{12}C$ in scintillator detectors [123] with its isotope ${}^{13}C$, is that this not only makes the detector much more sensitive to charged-current solar neutrino reactions and also enables the determination of the solar neutrino energy, but it also makes it a very efficient detector for neutral-current induced reactions.

4.1.2 Cross section of $\nu + {}^{13}C$ reactions

This very special charged current interactions of neutrino on Carbon permits to an organic liquid scintillator detector to measure the 8B solar neutrino flux by means of the $\nu + e$ charged current interaction with the ${}^{13}C$ nuclei naturally contained in the scintillators.

Here is shown a reliable estimates of the cross section for the neutrinos on ${}^{13}C$ interactions, using a

³In Borexino, even if the natural isotopic abundance is low and so the number of ${}^{13}C$ nuclei is reduced by a factor ~ 100 , there are $1.33 \cdot 10^{29}$ ${}^{13}C$ nuclei in all the inner vessel.

semi-phenomenological effective-operator approach, done in [142,143]. The reactions of our concern are the charged-current induced reaction

$$\nu_e + {}^{13}\text{C} \rightarrow {}^{13}\text{N}(gnd) + e^- \quad (4.5)$$

and the neutral-current induced reaction

$$\nu_e + {}^{13}\text{C} \rightarrow \nu_e + {}^{13}\text{C}^* \quad (4.6)$$

• **charged-current reaction:** $\nu_e + {}^{13}\text{C} \rightarrow {}^{13}\text{N}(gnd) + e^-$

Figure 4.1 illustrates the low-lying nuclear levels relevant to this argument. It is excluded from our considerations negative-parity states with $J \geq \frac{5}{2}$ as well as positive-parity states. The contribution of forbidden transitions leading to these states is negligibly small for the solar neutrino energy region. The effects of forbidden-type transitions operators that interfere with the allowed-type operator, as examined by Bahcall and Holstein, are also quite small for a light nucleus, unless the allowed-type contribution is substantially suppressed for some reasons. The cross section σ for the charged-current reaction

$$\nu_e + {}^{13}\text{C} \rightarrow {}^{13}\text{N}(gnd) + e^- \quad (4.7)$$

or

$$\nu_e + |A\rangle \rightarrow e^- + |B\rangle$$

is given by:

$$\sigma = (2\pi)^4 \int d^3p_e \delta(E_e + E_B - E_\nu - E_A) \times |\langle e^-(p_e); B | H_{eff} | \nu(p_\nu); A \rangle|^2 \quad (4.8)$$

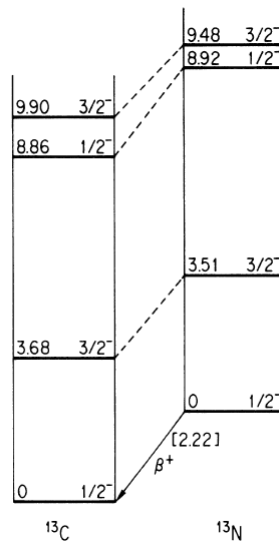


Figure 4.1: Low-lying negative-parity levels in ^{13}C and ^{13}N that can be fed from the ground state via allowed-type transitions, $\Delta J = 1$ or $\Delta\pi = \text{no}$. All the listed levels have isospin $T = \frac{1}{2}$.

where E_ν (E_e) is the neutrino (electron) energy and E_B (E_A) is the energy of the final (initial) state. As of the effective weak interaction Hamiltonian H_{eff} , we start with the effective single particle Hamiltonian. The single-particle Hamiltonian in the allowed-type transition approximation is given by:

$$H_{eff} = -\frac{G}{\sqrt{2}} \cos\theta_C t_+ [f_V iL_4^* + f_A \sigma \cdot L^*] \quad (4.9)$$

with

$$L_\mu^* = -i\bar{\psi}_e \gamma_\mu (1 + \gamma_5) \psi_\nu \quad (4.10)$$

Here, $G \cos\theta_C$ is the weak coupling constant and σ 's are the Pauli spin matrices. The nucleon form factors are $f_V=1.0$ and $f_A=-1.262$. The standard calculation yields:

$$\sigma = \frac{G^2 \cos^2\theta_C}{\pi} p_e E_e F(Z_B = 7; E_e) \times \frac{1}{6(2J_A + 1)} [f_V^2 |\langle B || \tau || A \rangle|^2 + f_A^2 |\langle B || \tau \sigma || A \rangle|^2] \quad (4.11)$$

where the Fermi factor $F(Z_B; E_e)$ is included to take account of the Coulomb distortion effect; the transition matrix elements $\langle B || \tau || A \rangle$ and $\langle B || \tau \sigma || A \rangle$ are reduced in both ordinary and isospin spaces. We have used the fact that all the states shown in Figure 4.1 have isospin $T = \frac{1}{2}$.

In terms of the reduced transition strengths Eq. 4.11 can also be written as

$$\sigma = \frac{G^2 \cos^2\theta_C}{\pi} p_e E_e F(Z_B = 7; E_e) \times \frac{1}{6(2J_A + 1)} \times [f_V^2 B(F) + f_A^2 B(GT)] \quad (4.12)$$

where

$$\begin{aligned} B(F) &= \sum_{M_f, M_i} |\langle J_f M_f | t_\pm | J_i M_i \rangle|^2 \\ &= \frac{1}{6} |\langle B || \tau || A \rangle|^2 \\ B(GT) &= \sum_{M_f, M_i} |\langle J_f M_f | t_\pm \sigma | J_i M_i \rangle|^2 \\ &= \frac{1}{6} |\langle B || \tau \sigma || A \rangle|^2 \end{aligned} \quad (4.13)$$

On the other hand for the β decay $|B\rangle \rightarrow |A\rangle$, there hold the relation:

$$ft = \frac{2\pi^3 \ln 2}{m_e^5 G^2 \cos^2\theta_C} \times \frac{6(2J_B + 1)}{f_V^2 |\langle B || \tau || A \rangle|^2 + f_A^2 |\langle B || \tau \sigma || A \rangle|^2} \quad (4.14)$$

so that:

$$[f_V^2 |\langle B || \tau || A \rangle|^2 + f_A^2 |\langle B || \tau \sigma || A \rangle|^2] = \frac{2\pi^3 \ln 2}{m_e^5 G^2 \cos^2\theta_C} \times \frac{6(2J_B + 1)}{6(2J_A + 1)} \quad (4.15)$$

which allows us to rewrite Eq. 4.11 as:

$$\begin{aligned}\sigma &= \frac{G^2 \cos^2 \theta_C}{\pi} p_e E_e F(Z_B = 7; E_e) \times \frac{1}{6(2J_A + 1)} \times [f_V^2 B(F) + f_A^2 B(GT)] \quad (4.16) \\ &= \frac{2\pi^2 \ln 2}{m_e^5 f_t} p_e E_e F(Z_B; E_e) \frac{2J_B + 1}{2J_A + 1}\end{aligned}$$

where

$$F(Z; E_e) = 2\pi\alpha_{EM} Z \frac{E_e - 2.22 + m_e}{\sqrt{(E_e - 2.22 + m_e)^2 - m_e^2}} \times \frac{1}{1 - \exp\left(\frac{-2\pi\alpha_{EM} Z (E_e - 2.22 + m_e)}{\sqrt{(E_e - 2.22 + m_e)^2 - m_e^2}}\right)} \quad (4.17)$$

So is possible to determine $\sigma[^{13}\text{C} \rightarrow ^{13}\text{N}(g.s.)]$ from the f_t value for $^{13}\text{N}(g.s.) \rightarrow ^{13}\text{C}(g.s.)$ in a model-independent manner.

The fact that the β decay $^{13}\text{N}(g.s.) \rightarrow ^{13}\text{C}(g.s.)$ is a super allowed transition with $\log(ft)^{exp} = 3.667 \pm 0.001$ leads to a rather large cross section for the reaction $\nu_e + ^{13}\text{C} \rightarrow ^{13}\text{N}(gnd) + e^-$. The substitution of $(ft)^{exp}$ into Eq.(4.17) yields:

$$\langle \sigma[^{13}\text{C} \rightarrow ^{13}\text{N}(g.s.)] \rangle = 8.57 \times 10^{-43} \text{cm}^2 \quad (4.18)$$

The symbol $\langle \sigma \rangle$ stands for the cross section averaged over neutrino spectrum from the ^8B β decay. We remark that, due to the threshold energy $E_{th} = 2.2$ MeV, only solar neutrinos from the ^8B decay are relevant in this case.

- **neutral-current reaction:** $\nu_e + ^{13}\text{C} \rightarrow \nu_e + ^{13}\text{C}^*$

This cross section is obtained also through a semi-phenomenological effective-operator approach [142, 143] and it has an uncertainty of $\sim 30\%$:

$$\langle \sigma[^{13}\text{C} \rightarrow ^{13}\text{C}(3.68\text{MeV})] \rangle = 2.58 \times 10^{-43} \text{cm}^2 \quad (4.19)$$

		Final states in ^{13}N			
Charged current reaction	$\frac{1}{2}^- (g.s.)$	$\frac{3}{2}^- (3.51\text{MeV})$	$\frac{1}{2}^- (8.92\text{MeV})$	$\frac{3}{2}^- (4.98\text{MeV})$	
CK	9.10×10^{-43}	5.83×10^{-43}	2.2×10^{-45}	5.3×10^{-46}	
rescaled	8.02×10^{-43}	<u>2.62×10^{-43}</u>	<u>9.9×10^{-46}</u>	<u>2.3×10^{-46}</u>	
direct	<u>8.57×10^{-43}</u>				
		Final states in ^{13}C			
Neutral current reaction	$\frac{1}{2}^- (g.s.)$	$\frac{3}{2}^- (3.68\text{MeV})$	$\frac{1}{2}^- (8.86\text{MeV})$	$\frac{3}{2}^- (9.90\text{MeV})$	
CK		2.58×10^{-43}	3.3×10^{-45}	6.2×10^{-46}	
rescaled		<u>1.16×10^{-43}</u>	<u>1.4×10^{-45}</u>	<u>2.7×10^{-46}</u>	

Table 4.2: Cross sections for $\nu + ^{13}\text{C}$ reactions in unit of cm^2 , averaged over the β -decay neutrino spectrum. The label ‘‘CK’’ corresponds to the result of the shell-model estimate. The label ‘‘rescaled’’ gives the estimate obtained with the use of the rescaled reduced matrix element $\langle B || \tau \sigma || A \rangle_{resc}$ [124], and the label ‘‘direct’’ means the result obtained directly from equation (4.17). The underlined entries are the best estimate. Values taken from [124].

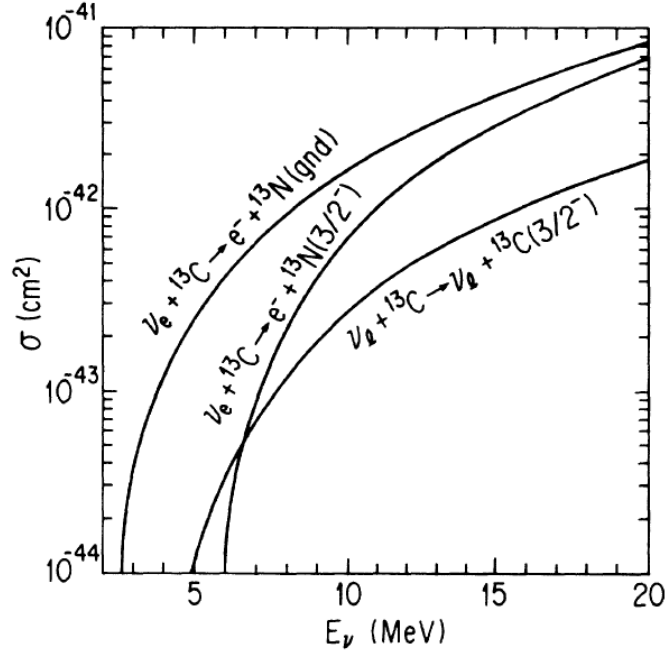


Figure 4.2: Cross section for the charged-current reaction $\nu_e + {}^{13}\text{C} \rightarrow {}^{13}\text{N}(gnd) + e^-$ and the neutral current reaction $\nu_l + {}^{13}\text{C} \rightarrow \nu_l + {}^{13}\text{C}^*$ as a function of the incident neutrino energy E_ν . Plot from [124].

In Table 4.2 are shown the cross sections for $\nu + {}^{13}\text{C}$ reactions in unit of cm^2 , averaged over the β -decay neutrino spectrum with the different methods used to estimate them. In Fig. 4.2 is shown how the cross section of these interaction changes with respect the energy of the neutrino incoming. There are promising consequences of this new estimates on ${}^8\text{B}$ solar neutrino detection, using the latest estimate of the total flux of ${}^8\text{B}$ given in [47]:

$$\phi_{\nu_e}({}^8\text{B}) = 5.58 \times 10^6 \text{cm}^{-2}\text{s}^{-1} \quad (4.20)$$

1. Considering the charged-current induced reactions, the transition between the ${}^{13}\text{N}$ ground state can be monitored by the β decay back to ${}^{13}\text{C}(g.s.)$. On the other hand the final state in the ${}^{13}\text{C}(g.s.)$ is unstable against proton emission ($E_p = 1.57$ MeV) which can also be detected. Since contributions of other states are negligible, it is consider the sum of the transitions leading to the lowest of the two states in ${}^{13}\text{N}$ as available signals for the CC reactions due to solar neutrinos, as shown in Table 4.2.

Is recalled that the cross section for the ground-state transition has been obtained directly from the β -decay data and has a little uncertainty, whereas the cross section for ${}^{13}\text{C}(g.s.) \rightarrow {}^{13}\text{N}(\frac{3}{2}^-; E_x = 3.51 \text{ MeV})$ has a typical ambiguity of $\sim 30\%$.

Combining the charged-current events leading to the lowest two states in ${}^{13}\text{N}$ ($8.57 \times 10^{-43} + 2.62 \times 10^{-43}$), is expected, corresponding to $\langle \sigma \rangle = 1.12 \times 10^{-42} \text{cm}^2$, 7870 events per kiloton yr for a ${}^{13}\text{CH}_2$ detector. The uncertainty in this event rate is expected to be $\sim 10\%$. Comparing this number with 1680 electron recoil events per kiloton yr from $\nu_e e^- \rightarrow \nu_e e^-$ for a cutoff recoil electron energy 3.5 MeV, is possible to note that one has 5-8 times more events with a ${}^{13}\text{CH}_2$ detector than with the usual ${}^{12}\text{CH}_2$ detector, where ${}^{12}\text{C}$ doesn't play a role as an active target.

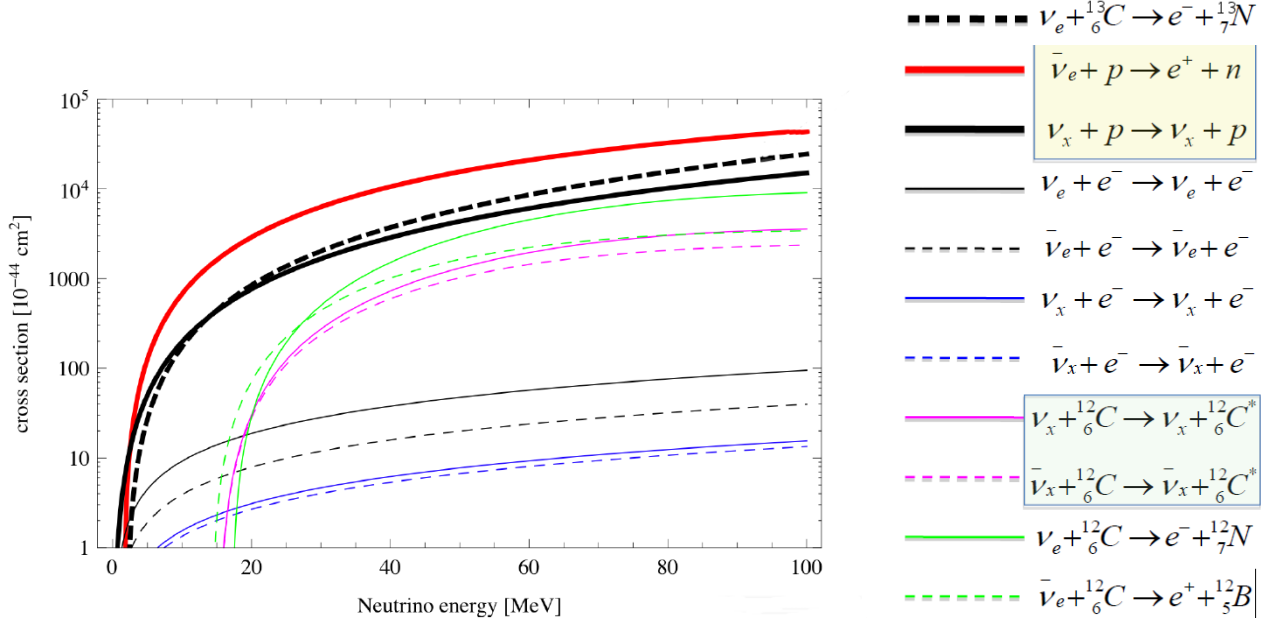


Figure 4.3: Neutrino interaction channels and cross sections. Fig. from [144].

- Regarding the neutral-current interaction, this calculation gives for the transition to the $^{13}\text{C}(\frac{3}{2}^-; E_x = 3.68\text{MeV})$ state $\langle\sigma\rangle = 1.16 \times 10^{-43}\text{cm}^2$ which yields 860 events per kiloton yr in a $^{13}\text{CH}_2$ detector. The uncertainty of this estimate is $\sim 30\%$. The transition can be identified by the mono-chromatic γ ray emitted in the transition back to the ground state.

Only $\frac{3}{2}^-$ level needs to be considered here since the excitations of the other levels are negligible as shown in Table 4.2 because are at the order of 10^{-45} - 10^{-46} . Thus the $^{13}\text{CH}_2$ detector can be highly promising as a neutral-current detector.

Even if the natural abundance of ^{13}C is low, ^{13}C contained in a currently operating large $^{12}\text{CH}_2$ scintillator may provide useful target for measuring the neutral current reactions once the detector threshold is sufficiently lowered.

In Fig. 4.3 are shown for comparison all the cross sections for the neutrinos interaction channels in an liquid scintillator detector. Is possible to note the cross section for neutrino CC interaction on ^{13}C , the thick dotted black line, at solar neutrino energies, is higher by a factor ~ 1 -2 that the one of neutrino scattering on electron, and it becomes also higher at higher energies.

In pink and green are shown the cross sections of neutrinos on ^{12}C , higher that neutrino scattering on electron but at higher energy because of the threshold, that can be useful for SuperNova neutrino detection. The interaction channel that has the higher cross section, not only at solar neutrino energies, is the inverse beta decay (red thick line) through which geo-neutrinos $\bar{\nu}_e$ are detected Borexino.

4.1.3 Neutrino interactions on ^{13}C

A pictorial view of the detection reaction through which neutrinos from ^8B are detected via CC interaction on ^{13}C is shown in Fig. 4.4.

As ^{13}C is a stable isotope of Carbon with a natural isotopic abundance $I=1.07\%$, a small amount of ^{13}C is, thus, naturally present in organic liquid scintillators and can be used as a target for neutrino detection. The relevant detection process in our discussion is the charged current (CC) transition to ^{13}N ground state:



The reaction threshold is $Q = 2.22 \text{ MeV}$ and, thus, only ^8B solar neutrinos are detectable. In

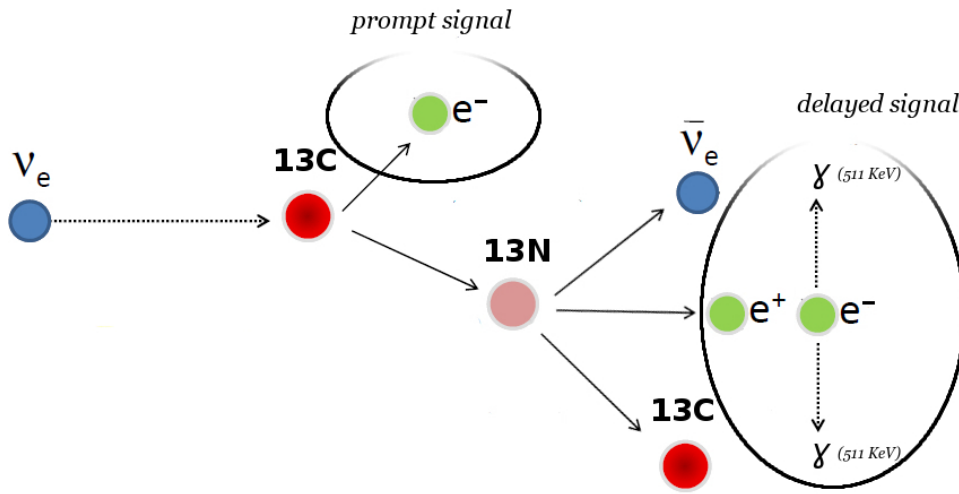


Figure 4.4: Pictorial view of the neutrino charged-current interaction on ^{13}C in liquid scintillator. It is observed by a prompt signal from the electron and a delayed coincidence of the positron annihilation from the charged current (CC) transition to ^{13}N ground state.

liquid scintillators one observes the electron produced in the final state with a visible energy which, neglecting the detector energy resolution, is simply equal to the electron kinetic energy T_e : $E_{\text{prompt}} = T_e = E_\nu - 2.2 \text{ MeV}$

The cross section of reaction (4.21) is known with great accuracy, since it has been deduced from the decay time of ^{13}N as shown in Equation (4.17). One has:

$$\sigma(E_\nu) = \frac{2\pi \ln 2}{m_e^2 \cdot ft} p_e E_e F(Z, E_e) \quad (4.22)$$

By averaging the cross section over the ^8B neutrino spectrum on the [3,16] MeV energy region, one obtains $\langle \sigma \rangle = 8.998 \times 10^{-43} \text{ cm}^2$, which is about one order of magnitude larger than the cross section of $\nu_e e^- \rightarrow \nu_e e^-$ scattering.

The peculiarity of process is that it can be monitored by looking for the delayed coincidence with the positron emitted in the ^{13}N decay:



which occurs with $\sim 99.8\%$ branching ratio (0.2% of ^{13}N nuclei undergo electron capture) and a decay time $\tau = 862.6$ s.

In this case, in a liquid scintillator, the visible energy is the sum of the positron kinetic energy and the energy released in e^+e^- annihilation, so that the delayed events have a continuous energy spectrum in the range [1.02,2.22] MeV.

Moreover, in the absence of macroscopic motions in the detector, the ^{13}N nucleus essentially does not move from its original position. The expected displacement due to recoil and diffusion during the decay time τ is, indeed, smaller than a scintillator detector, as Borexino, spatial resolution, $\sigma \sim 10$ cm. This means that the prompt event produced by the reaction and the delayed event produced by the decay have to be observed essentially in the same position. This condition, as we will see in the following sections, is extremely effective in reducing the background.

In Borexino also the other interaction channels of low energy neutrinos with ^{13}C can, in principle, be considered, as mentioned in the section above. One of this is the CC transition to ^{13}N excited states. For solar neutrinos, only the lowest excited state (at 3.51 MeV) could be of practical importance. The cross section for this process is about 30% of that for the ground state and it is calculated theoretically with an uncertainty at the level of 30 - 40% [124]. However, the $^{13}\text{N}^*$ (3.51MeV) decays almost immediately to $^{12}\text{C}+p$ with almost 100% branching ratio [145]. As a consequence, it cannot be discriminated by the coincidence with the delayed events in (4.23).

The other relevant process is the neutral current (NC) transition: $\nu_x + ^{13}\text{C} \rightarrow \nu_x + ^{13}\text{C}^*$. Here, only the excited state $^{13}\text{C}^*$ (3.68 MeV) is relevant and the excitation to other levels has negligible cross section. The cross section for this process, averaged over the ^8B neutrino spectrum, is $\langle\sigma_{NC}\rangle = 1.16 \times 10^{-43}\text{cm}^2$ and it is affected by about 30 - 40% uncertainty. The process is in principle very interesting since it can give a measure of the total ^8B flux and can be also tagged by a monochromatic γ -ray emission back to the ground state. However, the great uncertainty and the low cross section make this process hard to be competitive with the NC measurement made by SNO.

In this analysis, we will focus on the information which can be obtained from reaction (4.21), which seems more interesting having a larger and much better known cross section, and the advantage of the delayed detection tagging with the ^{13}N decay.

4.2 The ^8B solar neutrino flux

As described in Section 1.2.2, ^8B solar neutrinos are produced in the Sun at the end of the pp chain through reaction:



The calculation of the ^8B solar neutrino spectrum dates back to 1964, when it was pointed out [146] that the usual β -decay allowed spectrum should be averaged over the intermediate 2^+ states of ^8Be ,

as derived by the subsequent alpha decay $^8\text{Be}(2\alpha)$ [147], see Fig 4.5.

The calculation on the spectrum has further continually improved using experimental data and theoretical calculations and in [147] are also included the maximum uncertainties (± 3 effective standard deviations) that can affect the best estimates spectrum. In Fig. 4.6 it is shown the best-estimate (standard) ^8B neutrino spectrum λ , together with the spectra λ^\pm allowed by the maximum ($\pm 3\sigma$) theoretical and experimental uncertainties.

4.2.1 ^8B neutrino signal

A neutrino of energy E_ν interacting with ^{13}C through reaction (4.21) produces an electron with kinetic energy $T_e = E_\nu - Q$.

The rate R_ν of prompt events (per unit mass) produced by ^8B solar neutrinos in the energy window $[T_{e,1}, T_{e,2}]$ is thus simply given by:

$$R_\nu = n_{^{13}\text{C}} \Phi \int_{T_{e,1}+Q}^{T_{e,2}+Q} \sigma(E_\nu) \lambda(E_\nu) P_{ee}(E_\nu) dE_\nu \quad (4.25)$$

where:

$\Phi = 5.58 \times 10^6 \text{cm}^{-2}\text{s}^{-1}$ is the boron neutrino flux [47],

$\lambda(E_\nu)$ is the boron neutrino spectrum [148],

$\sigma(E_\nu)$ is the interaction cross section (Equation 4.17),

$P_{ee}(E_\nu)$ is the electron neutrino survival probability,

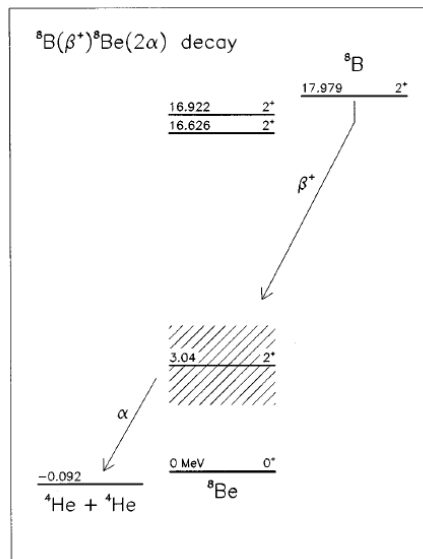


Figure 4.5: Energy levels in the $^8\text{B}(\beta^+) ^8\text{Be}(2\alpha)$ decay chain.

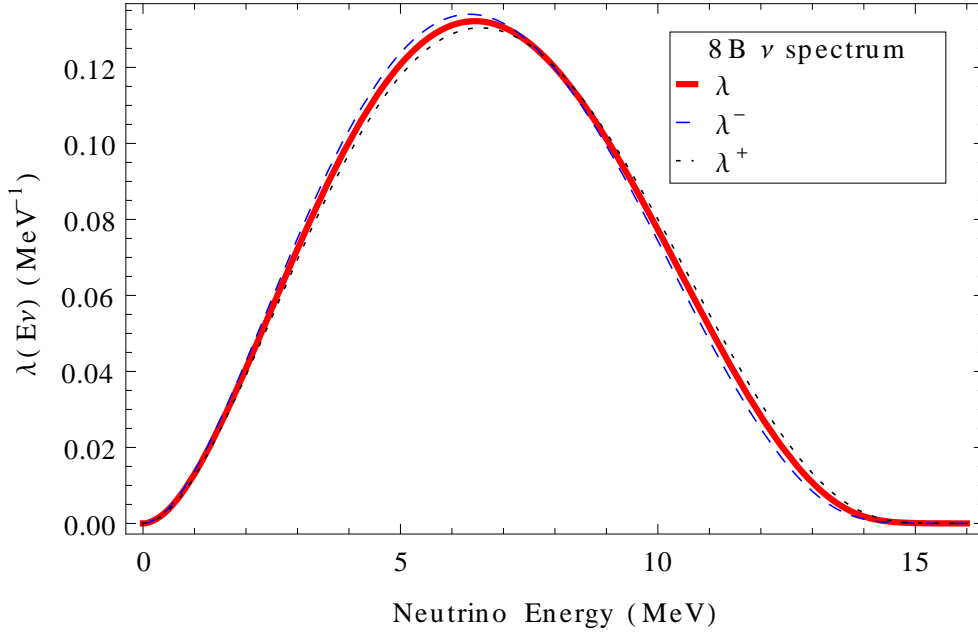


Figure 4.6: The best-estimate (standard) ^8B neutrino spectrum λ , together with the spectra λ^{pm} allowed by the maximum ($\pm 3\sigma$) theoretical and experimental uncertainties. Data from [38].

$n_{13\text{C}}$ is the number of ^{13}C atoms per unit mass, which depends on the scintillator chemical composition:

$$n_{13\text{C}} = N_A I \sum_k f_k \frac{X_k}{\mu_k} \quad (4.26)$$

where $I = 1.07 \times 10^{-2}$ is the isotopic abundance of ^{13}C , $N_A = 6.02 \times 10^{23} \text{mol}^{-1}$ is the atomic mass unit, f_k is the mass fraction of the k -th component into the scintillator, X_k the stoichiometric coefficient of Carbon in the molecule, and μ_k is the molecular mass of the k -th molecule.

In Fig. 4.7 we show the function $\varrho(E_\nu) \propto P_{ee}(E_\nu)\lambda(E_\nu)\sigma(E_\nu)$ (normalized to unity) which gives the relative contribution of neutrinos of different energies to the total signal from reaction (4.21). The solid line is obtained in the assumption of an undistorted ^8B neutrino spectrum (which can be intended as the non oscillatory scenario or a constant suppression of ν_e). The dashed line is obtained in the assumption of $\nu_e \rightarrow \nu_{\mu,\tau}$ flavor transitions for the following oscillation parameters which are the current best fit in global analysis in [25]:

$$\begin{aligned} \delta m^2 &= 7.69 \times 10^{-5} \text{eV}^2 \\ \sin^2 2\theta &= 0.86 \end{aligned} \quad (4.27)$$

The electron neutrino survival probability has been calculated taking into account the Mikheyev-Smirnov-Wolfenstein (MSW) effect in the Sun (for simplicity we have not considered the oscillations in the Earth matter). Neglecting the detector energy resolution, the function $f(T_e) \equiv \varrho(T_e + Q)$ also gives the spectral distribution of solar neutrino events, since detection reaction kinematics

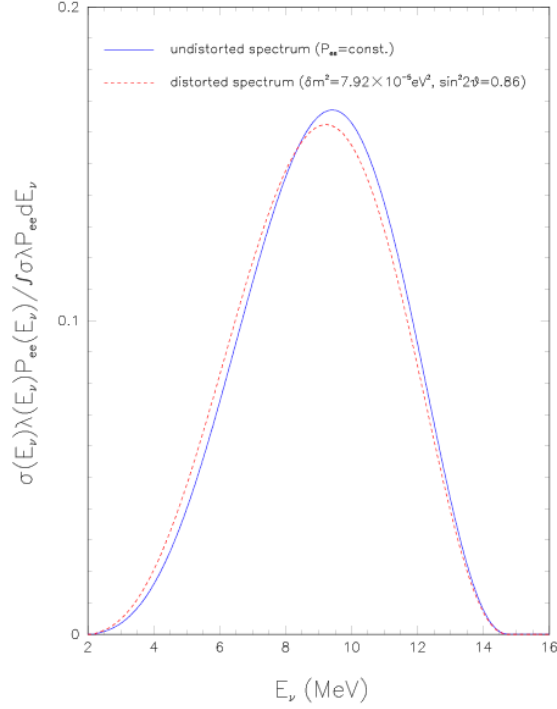


Figure 4.7: Relative contribution of neutrinos of different energies to the total signal from reaction 4.21. Straight line: undistorted ^8B neutrino spectrum (constant P_{ee}). Dashed line: $m^2 = 7.69 \times 10^{-5} \text{eV}^2, \sin^2 2\theta = 0.86$. [71]

implies a one-to-one relation (i. e., $T_e = E_\nu - Q$) between the electron and neutrino energies.

The event spectrum is, in principle, extremely sensitive to a possible deformation of parent solar neutrino spectrum. In particular, the differences between the two curves in Fig. 4.7 directly reflect the behavior of the electron neutrino survival probability in LMA scenarios. Namely, the rise of the LMA spectrum (dashed line) with respect to the standard case (solid line) below $E_\nu \sim 7$ MeV ($T_e \sim 5$ MeV in terms of electron energy) is due to the transition from vacuum averaged neutrino oscillations at small energies to purely adiabatic transitions at large energies. The observation of this feature would be very important as a final confirmation of matter effect in solar neutrino oscillations. However, it will be extremely hard to observe it in the present detectors, due to the smallness of the expected event rates.

4.2.2 Event rate expected in Borexino and Kamland

Is possible to calculate the neutrino events rates with the equation (4.25) expected in Kamland and Borexino scintillator in the energy range $[T_{e,1}, T_{e,2}] = [3, 16]$ MeV assuming the oscillation parameters in (4.28). The part of the ^8B spectrum with energy > 3 MeV is shown in Fig. 4.8 and is 91%..

Borexino

Borexino is composed fo 100% of pseudocumene, so the number of target nuclei of ^{13}C in 1kton will be:

$$n_{^{13}\text{C}} = N_{AI} \sum_k f_k \frac{X_k}{\mu_k} = 1.07 \cdot 10^{-2} \frac{6.02 \cdot 10^{23}}{120.19} 9 \cdot 1000 \cdot 10^6 = 4.82 \times 10^{29} \text{kton}^{-1} \quad (4.28)$$

since the pseudocumene is C_9H_{12} has a molecular mass equal to 120.19 g/mol. It is possible to calculate the rate expected in the energy range [3,16] MeV (the lower bound, as will be explained in the next Chapter, has been chosen to reduce the background from U-Th contamination):

$$R_\nu[3, 16] = n_{^{13}\text{C}} \Phi \int_{3+2.2}^{16+2.2} \sigma(E_\nu) \lambda(E_\nu) P_{ee}(E_\nu) dE_\nu = 23.83 \text{ counts} \cdot \text{kton} \text{y}^{-1} \quad (4.29)$$

The counting rates will be further reduced by the cuts, essential to reduce the background. However, the background levels are extremely low so that it will be possible to extract the solar neutrino signal with a reasonable uncertainty.

Using the Borexino scintillator, that is composed of 100% of pseudocumene, the rate of events is strongly suppressed respect to charged-current interactions, by an order of 100 times from the small amount of ^{13}C present in the scintillator. The expected count rate from solar neutrinos CC interactions on ^{13}C in the energy windows [3, 16] MeV, considering for the analysis only the Fiducial Volume, 100 tons of scintillator, is :

- $R_{^{13}\text{C}}^{ST} = 6.66 \pm 0.73$ counts/100tons/year in the non-oscillatory scenario,
- $R_{^{13}\text{C}}^{OSC} = 2.38 \pm 0.26$ counts/100tons/year in the case of oscillations, taking into account the MSW-LMA solution [25].

In Table 4.3 and 4.4 is reported the number of events expected in Borexino, according to the equation (4.25), listed for different fiducial volumes, and give in count/livetime and in count/year.

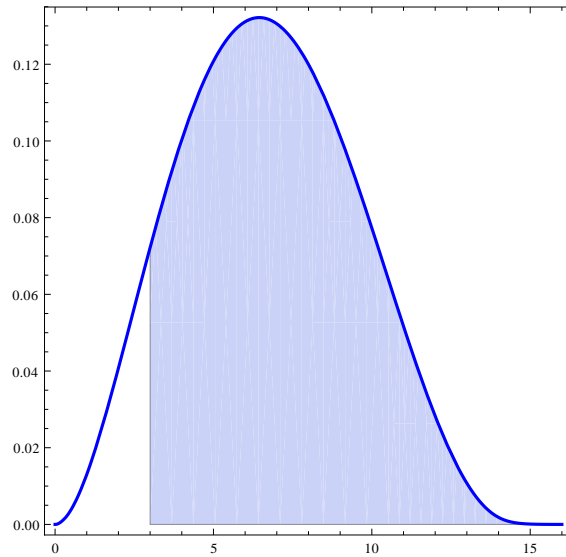


Figure 4.8: Energy spectrum of ^8B , in light blue is shown the part of the spectrum over 3 MeV is $\simeq 91\%$

As is possible to see, clearly, the more mass active is considered the more events are expected, but in Borexino as it will be explained will be chosen for the analysis a fiducial volume of 3.3 m radius for background rejection.

Fiducial mass radius	Fiducial mass [tons]	n C13	expected rate (no oscillation)	expected rate (oscillation)
4.25 m	~ 283	1.36×10^{29}	33.38 ± 4.67 ev/livetime/283t	11.95 ± 1.67 ev/livetime/283t
3.30 m	~ 132	6.36×10^{28}	15.57 ± 2.18 4.67 ev/livetime/132t	5.57 ± 0.78 ev/livetime/132t
3.0 m	$\sim 100.$	4.8×10^{28}	11.8 ± 1.65 ev/livetime/100t	4.22 ± 0.59 ev/livetime/100t

Table 4.3: Number of ^{13}C CC interactions events expected, according to the equation (6.12), listed for different radius fiducial volumes, given in count/livetime, where the livetime is 646.95 and will be used in the measurement.

Fiducial mass radius	Fiducial mass ([tons])	n C13	expected rate (no oscillation)	expected rate (oscillation)
4.25 m	282.97 t	1.36×10^{29}	18.83 ± 2.64 ev/year/283 t	6.74 ± 0.94 ev/year/283 t
3.30 m	132.47 t	6.36×10^{28}	8.78 ± 1.23 ev/year/132 t	3.14 ± 0.44 ev/year/132 t
3.021 m	101.63 t	4.8×10^{28}	6.66 ± 0.93 ev/year/100 t	2.38 ± 0.33 ev/year/100 t

Table 4.4: Number of ^{13}C CC interactions events expected, according to the equation (6.12), listed for different radius fiducial volumes, given in count/year.

Kamland

KamLAND scintillator is composed by 80% of dodecane ($\text{C}_{12}\text{H}_{26}$, with a molecular mass $\mu = 170.33$ g/mol) and 20% of pseudocumene (C_9H_{12} , with a molecular mass $\mu = 120.19$ g/mol), which correspond to

$$\begin{aligned}
 n_{13\text{C}} &= N_{AI} \sum_k f_k \frac{X_k}{\mu_k} \\
 &= 1.07 \cdot 10^{-2} \left(0.2 \frac{6.02 \cdot 10^{23}}{120.19} 9 \cdot 1000 \cdot 10^6 \right) + \left(0.8 \frac{6.02 \cdot 10^{23}}{170.33} 12 \cdot 1000 \cdot 10^6 \right) \\
 &= 4.60 \times 10^{29} \text{ kton}^{-1}
 \end{aligned} \tag{4.30}$$

The expected rate in Kamland is:

$$R_\nu[3, 16] = 22.7 \text{ counts} \cdot \text{kton} \cdot \text{y}^{-1} \tag{4.31}$$

that is, for a target mass of 137 tons and 891 livedays and for an energy $> 5\text{MeV}$:

$$R_\nu[5, 16] = 6.35 \pm 0.7 \text{ counts} \tag{4.32}$$

This value is compatible with the value reported from Kamland in the measurement of the ^8B solar neutrino flux done in [151]. Here, it was used for the analysis a cylindrical fiducial volume, 6-m-high

and 3-m-radius, of 176.4 m^3 that is 137 tons of target mass, since the Kamland scintillator density is 0.78 g/cm^3 . The exposure was 123 kton-days that is ~ 891 days of livetime and the threshold energy is 5 MeV. The estimation done here for the number of events expected in the region of interest, is 5.8 ± 1.4 events.

4.3 The coincidence detection technique

In order to reduce the background, we can take advantage of the time and space coincidence of neutrino events with the positron emitted in the ^{13}N decay. A candidate prompt event will be tagged as signal only if followed by a delayed event in the energy window [1.02, 2.22] MeV, within a time interval $\Delta t = T\tau$ (where τ is the ^{13}N decay time), and inside a sphere of radius Δr from the prompt event detection point (where $\sigma \sim 10 \text{ cm}$ is the typical detector spatial resolution).

The signal event expected rate S is thus depending on the time and space cuts and is given by:

$$S = \text{Rate}_\nu \times \varepsilon(T, R) \quad (4.33)$$

where Rate_ν is from Equation (4.25) and the global efficiency of the coincidence $\varepsilon(T, R)$ is determined by the combined efficiency for the cut in space, $\xi(R)$, and in time, $\eta(T)$:

$$\varepsilon(T, R) = \xi(R) \cdot \eta(T) \quad (4.34)$$

1. The function $\eta(T)$ is simply equal to the probability that the ^{13}N nucleus decays within the time $\Delta t = T\tau$:

$$\eta(T) = 1 - e^{-T} = 1 - e^{-\frac{\Delta t}{\tau}} \quad (4.35)$$

If it is chosen $T=3$ ($\Delta t \simeq 2600\text{s}$), the efficiency of the cut in time is:

$$\eta(T) = 1 - \int_0^{3\tau} \frac{e^{-\frac{t}{\tau}}}{\tau} dt = 0.95 \quad (4.36)$$

2. The function $\xi(R)$ is instead the probability that the prompt event and the delayed event, which are assumed to occur in the same position, are detected at a distance smaller than r ($r = R \sigma$). Modeling the detector spatial resolution with a gaussian function, one obtains:

$$\xi(R) = \frac{\int_0^R dx x^2 e^{-x^2/4}}{\int_0^\infty dx x^2 e^{-x^2/4}} = \text{erf}\left(\frac{R}{2}\right) - \sqrt{\frac{1}{\pi}} R e^{-\frac{R^2}{4}} = 0.79 \quad (4.37)$$

The above equation is valid in the assumption that the displacement between the point where ^{13}N is created and the point where it decays is small with respect to σ . For that to happen, the macroscopic motions in the liquid scintillator have to be sufficiently slow.

If are chosen $R=3$ and $T=3$, the global efficiency is $\varepsilon(T, R)=0.75$. This cut has to be optimized according to each detector performances: for Borexino, as will be shown in next chapter, this cuts

are the optimal, but for other detectors, they could be different.

The expected signal in Borexino after the efficiency cuts are applied is:

$$\text{Borexino : } R_\nu[3, 16] = 17.87 \text{ counts} \cdot \text{ktony}^{-1} \quad (4.38)$$

For Kamland, instead, the delayed energy window has to be restricted to $[E_1, E_2] = [1.3, 2.22]$ MeV in order to reduce the background from ^{210}Bi originated by the decay of ^{210}Pb that can be either produced by build-up due to ^{222}Rn contamination in the liquid scintillator or caused by an intrinsic impurity. This reduces further the efficiency by a factor 0.77 so that the global efficiency will be 0.57.

$$\text{Kamland : } R_\nu[3, 16] = 12.94 \text{ counts} \cdot \text{ktony}^{-1} \quad (4.39)$$

As a final result, the expected signal event rates in Kamland and Borexino are at the level of 10-20 counts·kTy⁻¹. In order to observe such low counting rates, are needed detectors with sufficiently low background levels (and, of course, efficient background rejection). Borexino, as it is possible to see in the next Chapter, satisfy this requirement.

Beyond this global efficiency on the time and space coincidence cuts, has also to be considered the efficiencies on the selection of the energy range for the prompt and the delayed signal (see Chapter 6 for a detailed study), that will further reduce the expected events.

4.4 Backgrounds

The main sources of background for this measurement, and that will be treated in Chapter 5, are:

- Internal background due to U-Th contamination and to contamination from long lived radon daughters out of secular equilibrium with ^{238}U ,
- Cosmogenic background due to muon-induced production of radioactive nuclides, such as ^{11}C , ^{10}C , etc.,
- Elastic ν -e scattering by solar neutrinos.

Since these background sources are well known, in [71] was performed a detailed analysis of their relevance. This is important because it allowed to make a realistic estimate of the expected signal to background ratio. However, they stresses, that the real background level would have been measured directly by the experiments with great accuracy, being the background event rate much larger than the signal event rate both in the prompt and delayed energy window (before space and time cuts are applied).

The detailed calculation of the main background sources done in [71] has shown a big difference in the contribution of each background source to the total background rates (per unit mass) in

KamLAND, Borexino and SNO+⁴.

In Table 6.30 is possible to note the different depth of the three underground locations and the different residual muon flux that Gran Sasso is $1.16 \pm 0.03 \mu \text{ m}^{-2} \text{ hr}^{-1}$ [93, 94].

Therefore, in Kamland and Borexino the cosmogenic background expected is ~ 7 times larger in Kamland than Borexino, while is ~ 93 times lower in SNO+. That is why in Borexino, as will be shown in Chapter 6, the main background source comes from cosmogenic isotopes.

	Depth (m.w.e)	ϕ_μ ($\text{m}^{-2}\text{d}^{-1}$)	$\langle E_\mu \rangle$ (GeV)
Kamioka	2700	230.4	285
Gran Sasso	3800	28.8	320
SNOlab	6000	0.288	350

Table 4.5: Depth, residual muon flux and average muon energy in the three underground locations considered in [71] (see [153] for details).

⁴The SNO+ liquid scintillator composition has still to be decided. For simplicity, is assumed to be the same as Borexino (i. e., 100% pseudocumene).

Chapter 5

Background sources for the ν CC on ^{13}C interactions rate measurement

The background sources for Borexino have already been treated in Section (2.6). In this Chapter are studied, going into more depth, the main backgrounds for the detection of the charged-current interactions on ^{13}C :

- cosmogenic background due to muons and muon induced production of radioactive nuclides such as ^{10}C and ^{11}C ,
- background due to ^{238}U - ^{232}Th contamination (internal and external),
- elastic ν -e scattering by solar neutrinos.

5.1 Muons and cosmogenic isotopes

Underground muons are the remnants of the air showers initiated by the collisions of primary cosmic rays with air nuclei (see Fig. 5.1). In particular muons come from the decay of pions and kaons. We already pointed out that at the LNGS experimental site, which is covered by a $\simeq 1.4$ km thick barrier of dolomite stone corresponding to 3800 meters of water equivalent (m w.e.), the mean muon energy is $320 \pm 4 \pm 11$ GeV and the muon rate is reduced by six orders of magnitude to $1.16 \pm 0.03 \mu\text{m}^{-2}\text{hr}^{-1}$. In Fig. 5.2 the type of muons crossing Borexino in relation to which part of the detector they cross are shown.

5.1.1 Muons

As mentioned in Section 2.6.2, about 10000 muons per day cross Borexino and approximately 4100 of them cross the Inner Detector, generating background signals. Depending on deposited energy and track length of the muon in the buffer and scintillator, there is a small but non-zero probability that a cosmic muon induces a number of photoelectrons comparable to the multi-MeV neutrino

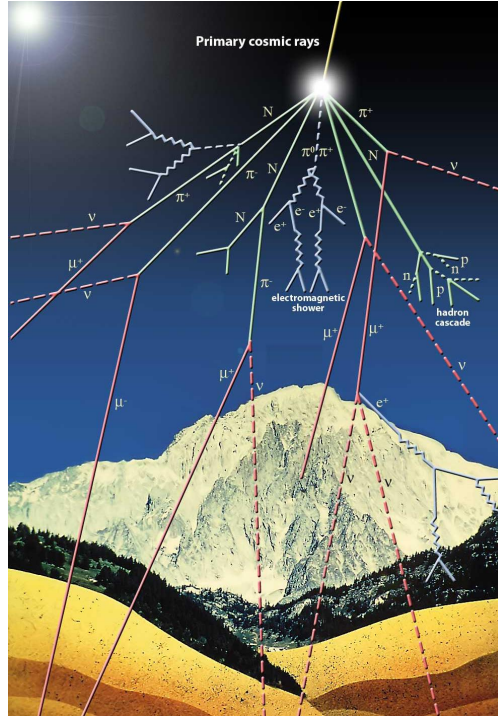


Figure 5.1: Picture representing the interactions of primary cosmic rays, producing secondary cosmic rays. In particular muons are produced by the pion and kaon decays.

charged-current interaction on ^{13}C of interest for this analysis, and is mistaken for a point-like scintillation event.

Due to the high mean energy, most of the cosmic muons reaching an underground muon detector will simply pass through it. It can be shown that only 1-2% of the muons are stopped in a detector the size of Borexino [78]. In any case, a muon deposits a considerable amount of energy when passing the scintillator. The visible output will even increase if a hadronic shower is generated.

Muons, in fact, produce first Čerenkov light in the water tank and then cross the buffer depositing around 2 MeV/cm. If the deposit is in the scintillator, 2 MeV corresponds to $\simeq 1000$ p.e. detected. A muon cover in media 6 m in the Inner Vessel, releasing around 1200 MeV. Instead muon that crosses the buffer produce a visible energy of 10% less respect to the Inner Vessel, due to the presence of the quencher.

Thus, a precise study of the background above 3 MeV in Borexino requires very efficient rejection of muon events and an accurate estimate of the muon tagging efficiency.

As it has been mentioned in the detector description, the Borexino Water Tank is instrumented with 208 PMTs to serve as a muon veto. If an Inner Detector (ID) event coincides in time with an Outer Detector (OD) trigger (i.e. more than 6 PMTs in the Water Tank are hit within a 150 ns window), then the event is tagged as a muon and rejected.

Since the rate of observable neutrino events in the innermost 100 tons of the Borexino scintillator is $\simeq 50$ events/day, the detector was equipped with a muon veto system which was designed to reach a muon detection efficiency higher than 99.99% as published in [80].

The residual muon rate, due to the combined inefficiency of the two tagging systems, taking into

account the fact that the two detectors are independent, is $(4.5 \pm 0.9) \times 10^{-4}$ muons/day/100 t [57] and is a negligible background for the analysis.

The identification of muons is based on the complementarity between outer and inner detectors, as well discussed in [80]. In particular, different methods of muon identification have been studied concerning both the Outer Detector and the Inner Detector:

1. **Outer Detector Flags:** the Outer Detector (OD) muon tags search for an increase in OD PMT activity above usual dark noise fluctuations; they operate at two different stages of data processing:
 - **Muon Trigger Board (MTB):** it is a hardware trigger of the OD, given by a significant increase in number of hits in a time span comparable to the transit time of a muon. The threshold is set to 6 PMTs firing within a time-gate of 150 ns;
 - **Muon Crate Flags (MCR):** it is an offline software trigger based on the acquired OD data. Its trigger condition is a slight refinement of the MTB: two subsets of PMTs are regarded separately, distinguishing between hits at PMTs mounted on the Stainless Steel Sphere and PMTs mounted on the floor. The trigger condition is met if 4 PMTs of either subset fired within 150 ns.
2. **Inner Detector Flags (IDF):** for the Inner Detector (ID) we observe that typical muon pulses feature longer rise and decay times than neutrino-like scintillation events of comparable energy, since a muon crossing the buffer needs up to 45 ns to deposit all its ionization energy. In addition, the number of detected photons is several orders of magnitude above the usual light output of point-like events, prolonging the signal substantially by generating large

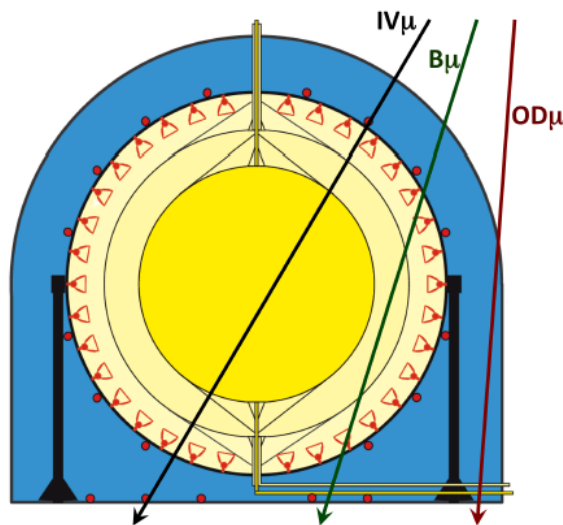


Figure 5.2: Pictorial view of muons crossing Borexino. The muons crossing only the Outer Detector are abbreviated as $OD\mu$'s. Muons traversing the Inner Detector ($ID\mu$'s) are further distinguished in Inner Vessel-crossing muons ($IV\mu$'s) only Buffer-crossing muons ($B\mu$'s)..

amounts of PMT after pulses. Pulse Shape Discrimination (PSD) can therefore be used to identify muons.

The efficiencies of the available muon tags were investigated using two approaches. First, samples of muon events were selected independently of any tagging flag and have been used to find directly the identification efficiencies. Second, each flag has been tested against a muon sample selected by either of the remaining two flags. The overall Borexino muon identification efficiency reaches 99.99% as published in [80]. For a description of the muon flags variable used in the code see Appendix F.

5.1.2 Cosmogenic isotopes

Muons and particles in muon showers may collide with atomic nuclei in the detector, producing hadrons such as pions and neutrons. In muon spallation, an incoming μ interacts with a nucleus via an exchange of a virtual photon. The nucleus subsequently emits neutrons (or pions). It can also happen that a real photon undergoes photo-absorption and neutrons or pions are subsequently emitted. Thus, the results of a muon spallation are radioactive isotopes and neutrons.

In Fig. 5.3 two Feynman diagrams depicting muon spallation processes are shown. A detailed description of the theoretical models describing the muon spallation can be found in [154].

The atomic nuclei which interact with the muon/muon shower particles under emission of nucleons may become radioactive. In organic liquid scintillators (LS), energetic muons and subsequent showers interact mostly with ^{12}C generating neutrons and radioactive isotopes that have different production rates, decay modes, lifetimes and Q-values. The most relevant in Borexino are carbon isotopes ^{11}C , ^{10}C and ^9C , the boron isotopes ^{11}B and ^8B , the beryllium isotopes ^{11}Be and ^7Be , the Lithium isotopes ^{11}Li and ^9Li and the helium isotopes ^8He and ^6He .

The decays of cosmic ray induced radionuclides can mimic different types of neutrino signal, depending on the covered energy range and on the production rate. In order not to overwhelm the

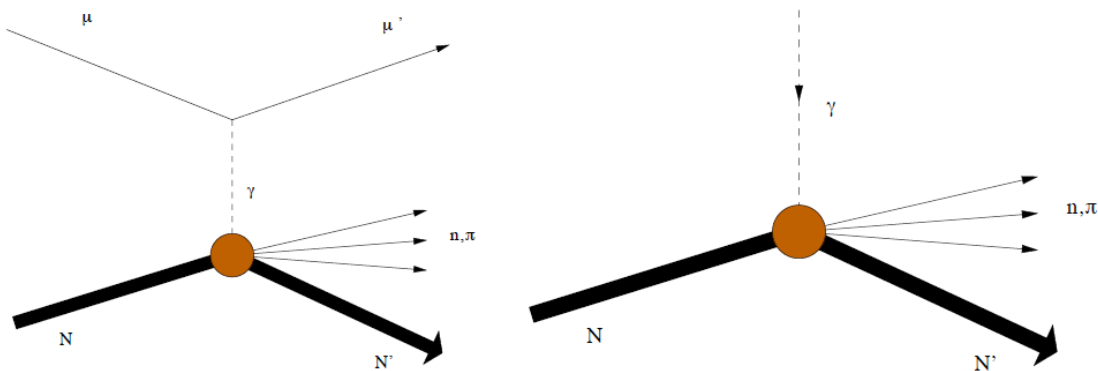


Figure 5.3: Feynman diagrams depicting muon spallation (left) and photo-absorption (right). In panel muon spallation an incoming muon exchanges a virtual photon with a nucleus. In the photo-absorption a real photon is absorbed by the nucleus. The nucleus subsequently emits neutrons or pions [154].

signal of neutrino, different methods and strategies to reject cosmogenics have to be applied, depending on the energy range of the neutrino concerned the analysis. Regarding the charged-current interactions on ^{13}C , the main important backgrounds that have to be taken into account are from ^{11}C , ^{10}C and ^{11}B . In fact, in the case of the other radionuclides with short lifetimes, the radioisotopes can be simply rejected by vetoing the entire detector over a time period of several lifetimes, as will be explained in the next Chapter.

Most neutrons and radioactive isotopes do not come directly from muon-nucleus spallation reactions, but from the muon-initiated hadronic and electromagnetic cascades. These neutrons spread away from the primary muon track, thermalizing slowly, and finally get captured by protons or other nuclei (see for example [153] for ^{11}C production mechanisms).

Table (5.1) presents a list of expected comogenics isotopes and their properties produced by muons in Borexino. As it is possible to note most of the muon-induced contaminants have a lifetime < 2 s. The expected rate quoted are taken from [57], obtained there by scaling the production rates (R^0) measured by Kamland [155] with:

$$R = R^0 \left(\frac{E_\mu}{E_\mu^0} \right)^\alpha \frac{\Phi_\mu}{\Phi_\mu^0} \quad (5.1)$$

where E_μ and Φ_μ are the Borexino mean muon energy ($320 \pm 4_{stat} \pm 11_{sys}$ GeV) and flux ($1.16 \pm 0.03 \text{ m}^{-2}\text{hr}^{-1}$) and E_μ^0 (260 \pm 4 GeV) and Φ_μ^0 ($5.37 \pm 0.41 \text{ m}^{-2}\text{hr}^{-1}$) are the corresponding Kamland values. α is a scaling parameter to relate cosmogenic production rate at different mean energies

Isotopes	τ	Q [MeV]	Decay	Primary process	Expected rate [cpd/100t]	Fraction > 3 MeV	Expected Rate > 3 MeV [cpd/100t]
Short lived ($\tau \leq 2$ s)							
^{12}B	0.03 s	13.4	β^-	$^{12}\text{C}(n, p)$	$1.41 \pm 0.04^*$	0.886	1.25 ± 0.03
^8He	0.17 s	10.6	β^-	$^{12}\text{C}(\pi^-, ^3\text{H})$	$0.026 \pm 0.012^*$	0.898	0.18 ± 0.03
^9C	0.19 s	16.5	β^+	$^{12}\text{C}(\pi^+, ^3\text{H})$	$0.096 \pm 0.031^*$	0.965	0.18 ± 0.03
^9Li	0.26 s	13.6	β^-	$^{12}\text{C}(\pi^-, ^3\text{He})$	$0.071 \pm 0.005^*$	0.932	0.18 ± 0.03
^8B	1.11 s	18.0	β^+	$^{12}\text{C}(\pi^+, ^2\text{H}^2\text{H})$	$0.273 \pm 0.062^*$	0.938	0.6 ± 0.08
^6He	1.17 s	3.5	β^-	$^{12}\text{C}(n, 2p^3\text{He})$	NA	0.009	0.6 ± 0.08
^8Li	1.21 s	16.0	β^-	$^{12}\text{C}(n, p\alpha)$	$0.40 \pm 0.07^*$	0.875	0.6 ± 0.08
Long lived ($\tau \geq 2$ s)							
^{11}Be	19.9 s	11.5	β^-	$^{12}\text{C}(n, 2p)$	$0.035 \pm 0.006^*$	0.91	0.032 ± 0.006
^{10}C	27.8 s	3.6	β^+	$^{12}\text{C}(\pi^+, np)$	$0.54 \pm 0.04^*$	0.012	0.0065 ± 0.005
^{11}C	29.4 min	2.0	β^+	$^{12}\text{C}(\gamma, n)$	28.5 ± 0.073 [59]	0.84	0.0
^7Be	76.9 d	0.9	β^+	$^{12}\text{C}(\gamma, n\alpha)$			

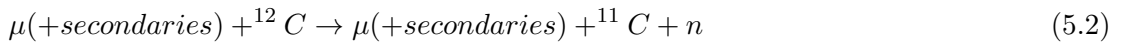
Table 5.1: Expected muon-induced contaminants in Borexino. The Expected rate (*) quoted are taken from [57].

of the incoming muon flux.

The cosmogenically-produced isotopes most relevant for neutrinos CC interaction rate on ^{13}C in Borexino are:

- ^{11}C : (β^+ , $Q_b = 1.982\text{MeV}$, $T_{1/2} = 20.30\text{min}$, $Z = 6$, $N = 5$)

^{11}C production in underground detectors is triggered by the residual flux of high energy muons passing through the organic scintillator. The rate of the process is a function of the location and depth of the experiment. It is produced by numerous channels in Borexino with the most common channel being $^{12}\text{C}(\gamma, n)^{11}\text{C}$ [153], so in 95% of the cases a neutron is also produced in the final state.



The free neutron travels a range of a few dozen cm until it is fully thermalized in the scintillator. After $\simeq 254 \mu\text{s}$ the neutron is captured on Hydrogen, emitting a characteristic 2.22 MeV γ :



The resulting ^{11}C atom has a half life of 20.38 minutes and decays by positron emission to ^{11}B .



The positron released has a maximum energy of 0.96 MeV, which gets calorimetrically summed with the two 511 keV annihilation gamma-rays that are released when the positron finally annihilates with an electron. The total visible energy resulting from this decay is then [1.02,1.98] MeV.

The ^{11}C rate measured by Borexino was expected to be 15-17 counts per day in the fiducial volume ([152, 153]), however, Borexino measures a rate about 50% higher at 28.5 ± 0.77 counts per day in the 100 ton fiducial volume [59]. It is postulated that this discrepancy is due to the underestimation of high multiplicity neutron events [156] and ^{11}C production by (n,2n) reactions. It is worth noting that the KamLAND collaboration sees the same discrepancy in the ^{11}C production rate that is visible in Borexino (albeit at a different depth) [155]. Another important aspect about ^{11}C , is that in Borexino the presence of this very high rate for ^{11}C makes any pep or CNO neutrino analysis impossible if the ^{11}C cannot be tagged, as its rate is roughly an order of magnitude larger than the expected pep flux, and about five times larger than the expected CNO flux.

The charge spectrum of ^{11}C is shown in Fig. 5.4, the percentage of the spectrum in [1.02,2.22] MeV is 84%, so that the backgrounds events expected from ^{11}C is:

$$R(^{11}\text{C}) = 23.97 \pm 0.61 \text{ cpd/100t} \quad [1.02,2.22] \text{ MeV}$$

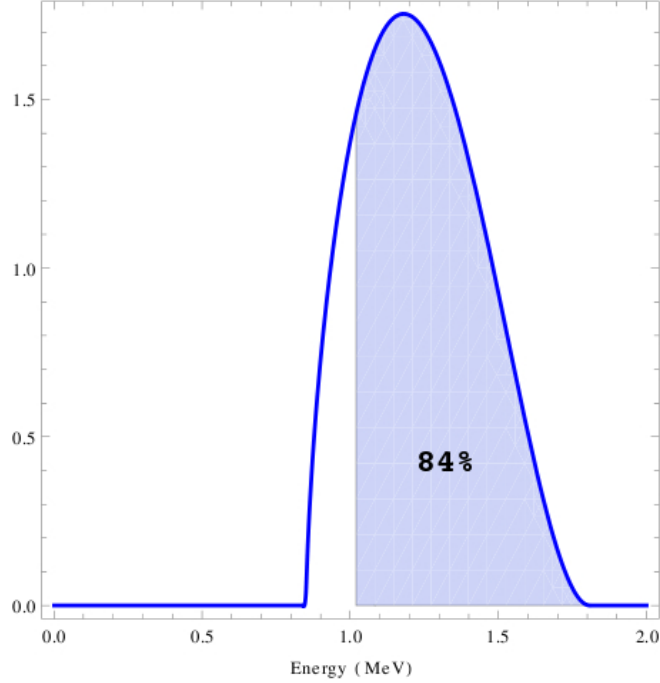


Figure 5.4: ^{11}C charge spectrum. The fraction in the energy range [1.01,2.22]MeV is 84%.

In almost all cases, ^{11}C is produced along with a neutron, so, this make feasible in principle a three-fold coincidence (TFC) between the parent muon, the signal from capture of the free neutron, and β^+ from the ^{11}C decay. This method consist in detecting the ^{11}C decay linking the following three signals as depicted in Fig. 5.5:

- prompt muon signal: detection of a muon or a muon shower crossing the detector as in (5.2). A muon-trigger opens a neutron-trigger gate for the search of subsequent neutron capture events following the creation of radioisotopes like ^{11}C .
- first delayed signal: neutrons that are emitted in the reaction (5.3) are thermalized and finally captured with a characteristic mean capture time of $\sim 254\mu\text{s}$ on hydrogen, resulting in the formation of a deuterium nucleus $n + H \rightarrow D + 2.22\text{MeV}$. The 2.22 MeV gamma has have a strong time correlation with the parent muon and is spatially close to the track of the muon and to the decaying ^{11}C nuclei.
- second delayed signal: ^{11}C atoms, which are created along the muon track, undergo β^+ decays with a mean lifetime of $\tau=29.4$ min:

$$^{11}\text{C} \rightarrow ^{11}\text{Be} + e^+ + \nu_e + 0.960\text{MeV}.$$

The total energy released in the detector by the decay and the instantaneously following positron annihilation is between 1.02 and 1.98 MeV. Herein, the β^+ spectrum is typically shifted to lower energies due to quenching effects of the scintillator. In the case of the Borexino scintillator, the ^{11}C β^+ spectrum begins at ~ 0.84 MeV already.

After each muon-induced neutron detection, the TFC method defines a set of potential ^{11}C candidates within a time delay dt from the detected muon/neutron and inside a sphere of

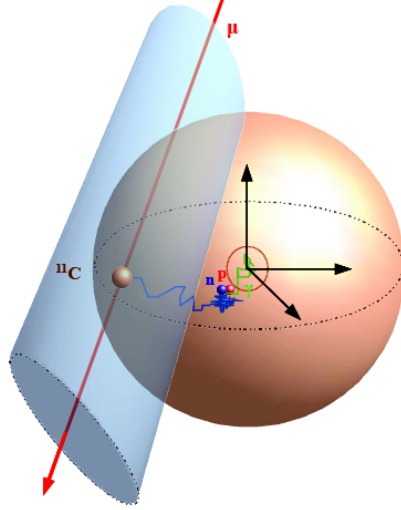


Figure 5.5: Schematic representation of the threefold coincidence (TFC) method.

radius dr placed around the barycenter of the 2.22 MeV γ rays. It is important to note that not only real ^{11}C decays are tagged, but also events (including neutrinos) which accidentally fulfill the TFC tagging conditions. That is why it is important to select the optimal TFC space and time cuts, leading to a larger fraction of real ^{11}C decays than of accidental coincidences to be discarded.

This method allows to tag only ^{11}C production events by muons and muon showers that release at least one neutron, but there are also channels that do not release neutrons and escape the TFC method: $^{12}\text{C}(p,d)^{11}\text{C}$ and $^{12}\text{C}(\pi^+, \pi^0 + p)^{11}\text{C}$, these channels are referred to as *invisible channels*. According to FLUKA simulations the invisible channels contribute to $\sim 5\%$ of the total ^{11}C production [153].

The second problem of the TFC methods is that there is a big fraction of livetime lost, almost $\sim 50\%$, that is one of the reasons why the Three Fold Coincidence technique is not used in this thesis. In fact, the signal event rate expected from CC interactions on ^{13}C is very small and we need as much statistic as possible.

- ^{10}C : (β^+ , $Q_b = 3.648\text{MeV}$, $T_{1/2} = 19.25\text{sec}$, $Z = 6$, $N = 4$)

^{10}C has a lifetime which is considerably longer than the short-lived cosmogenic isotopes (27.8 s) and its production is mostly through visible neutron channels: its primary production process, $^{12}\text{C}(\pi^+, np)$, as shown in Table 5.1, has a neutron in the final state and the fraction of ^{10}C produced in visible channels as measured by KamLAND is $90.7 \pm 5.5\%$.

The decay of ^{10}C proceeds via positron emission to ^{10}B



The positron has an endpoint energy of 1.9 MeV, followed by the two annihilation gammas, and also a 718 keV γ (98.5% branch) due to the decay into an excited state of ^{10}B , the total energy visible in the decay lies in the range [1.74,3.65] MeV. These events can also be

determined via a coincidence with one or two neutrons and the β^+ .

The theoretical rate for ^{10}C calculated in [152] is 2.0 ± 0.2 counts per day in the 100 ton fiducial volume; however, unpublished spectral fits indicate a rate of roughly double this number, this can also be attributed to an underestimation of high neutron multiplicity events described above. In Fig. 5.6 is shown the spectrum of ^{10}C and the backgrounds events expected from ^{10}C are:

$$R(^{10}\text{C}) = 0.0054 \pm 0.0004 \text{ cpd}/100\text{t} \quad [3,16] \text{ MeV}$$

$$R(^{10}\text{C}) = 0.208 \pm 0.015 \text{ cpd}/100\text{t} \quad [1.022,2.22] \text{ MeV}$$

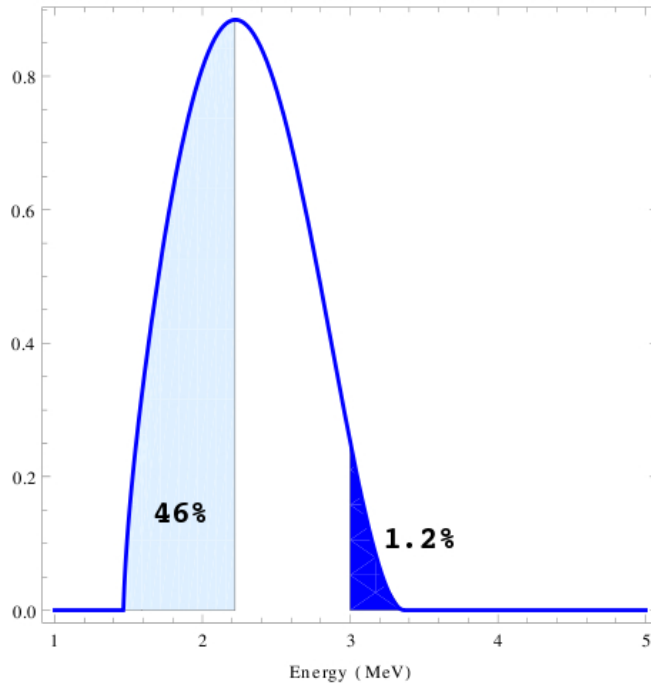


Figure 5.6: ^{10}C charge spectrum. The fraction in the energy range [1.01,2.22]MeV is 1.2% and in the energy range [3,16]MeV is 46%.

- ^{11}Be (β^- , $Q_b = 11.506\text{MeV}$, $T_{1/2} = 13.81\text{sec}$, $Z = 4$, $N = 7$)

^{11}Be is also a product of a muon spallation on ^{12}C , and it decays with a meanlife $\tau=27.8$ via positron emission according to the relation:



This isotope is more difficult to measure since it is not correlated with any other event. In Fig. 5.7 is shown the ^{11}Be charge spectrum expected in Borexino: the backgrounds events expected in the energy range [3,16] MeV:

$$R(^{11}\text{Be}) = 0.025 \pm 0.004 \text{ cpd}/100\text{t} \quad [3,16] \text{ MeV}$$

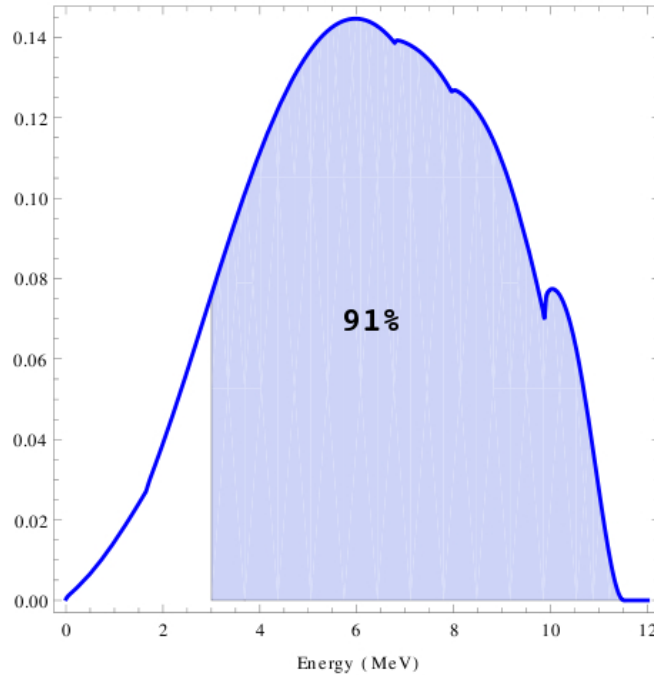


Figure 5.7: ^{11}Be charge spectrum in Borexino. The fraction in the energy range [3,16]MeV is 91%.

- ^7Be

It is produced by muon-induced disintegration of ^{12}C . Once produced, the ^7Be decays by electron capture to ^7Li with a half life of 53.12 days and a Q value of 861 keV. In almost 90% of the cases, the decay goes directly to the ground state of ^7Li and is effectively invisible since the decay energy partitions almost completely to the neutrino, however, in 10.5% of the decays, the transition is to an excited state of ^7Li which de-excites by emitting a 478 keV γ . The long half life and large cross section also dictated that the scintillator spend as little time as possible above ground on its way from the chemical plant where it was produced in Sardinia to the underground labs. In the end, this isotope has not yet been directly observed in Borexino. This isotope is not a background for these analysis since its β^+ spectrum (Q=0.9 MeV) is below the threshold both for the prompt and the delayed signals.

- A handful of other short lived ($t_{1/2} < 2$ s) isotopes as shown in Table 5.1. Saturation of the electronics after a muon precludes the ability to specifically detect some of the shorter lived isotopes like ^{12}B and ^{11}Li . The very high beta decay endpoints of these isotopes do make them the only source of background for the high energy ^8B neutrino analysis. Their removal from the data set is possible by simply vetoing the detector for a time period of five seconds after each muon that crosses the stainless steel sphere [57].

Cosmogenic neutrons

As already explained, muons going through the Inner Vessel can interact with nuclei in the matter and produce neutrons. The neutrons produced in the scintillator are captured on protons with a mean capture time of $\sim 254 \mu\text{s}$, producing a γ with energy of 2.22 MeV. While

the neutrons crossing the Inner Vessel are rejected vetoing the detector for a time period of five seconds after each muon that crosses the IV, to reject neutrons produced in water, we applied a second 2 ms veto after each muon crossing the Water Tank only and called “external muons” as depicted in Fig. 5.2. The rejection efficiency for neutrons produced in water is 0.9996 [57].

5.2 ^{238}U - ^{232}Th contamination

Gamma ray backgrounds from natural radioactivity are a great challenge for a low background detector as Borexino. The background drops sharply over 3 MeV as the highest energy γ -ray with a large branching ratio from natural radioactivity is the 2.614 MeV from ^{208}Tl , which leads to a large flux of radiation from the PMTs and the Stainless Steel Sphere into the Borexino Inner Vessel.

Above 3 MeV, the sources of radioactive background are β decays of ^{214}Bi (^{238}U chain, $Q=3.272$ MeV) and ^{208}Tl (^{232}Th chain, $Q=5.001$ MeV), which are residual contaminants in the liquid scintillator and may also originate from ^{222}Rn and ^{220}Rn emanated by the nylon. γ -rays from ^{214}Bi extend up to 3.23 MeV but the total branching ratio for these decays is small ($I_g < 0.1\%$).

5.2.1 ^{238}U - ^{232}Th internal contamination

Intrinsic radioactivity is mostly due to radio-isotopes belonging to the natural ^{238}U and ^{232}Th chains present in the scintillator itself. ^{238}U and ^{232}Th contamination in the Borexino scintillator contributes above 3 MeV through ^{214}Bi ($Q=3.27\text{MeV}$) and ^{208}Tl ($Q=5.001\text{MeV}$).

These heavy-element decay chains each produce ten or more isotopes with different energies and particle types.

Since the liquid scintillator in Borexino, as described in Section 2.5.1, represents the detector active volume, it has been accurately selected and purified with the techniques explained in Section 2.5.3, in order to have a contamination of ^{238}U and ^{232}Th of the order of 10^{-16}g/g , which corresponds to a signal to background ratio of about 1 in the solar ^7Be region.

Borexino, as pointed out in section 2.6, can tolerate concentrations of these elements not much greater than 10^{-16}g/g , therefore the lowest ever measured levels of natural contaminants from Uranium and Thorium have been established:

- concentration of ^{238}U : $(1.6 \pm 0.1) \times 10^{-17}\text{g/g}$.
- concentration of ^{232}Th : $(6.8 \pm 1.5) \times 10^{-18}\text{g/g}$.

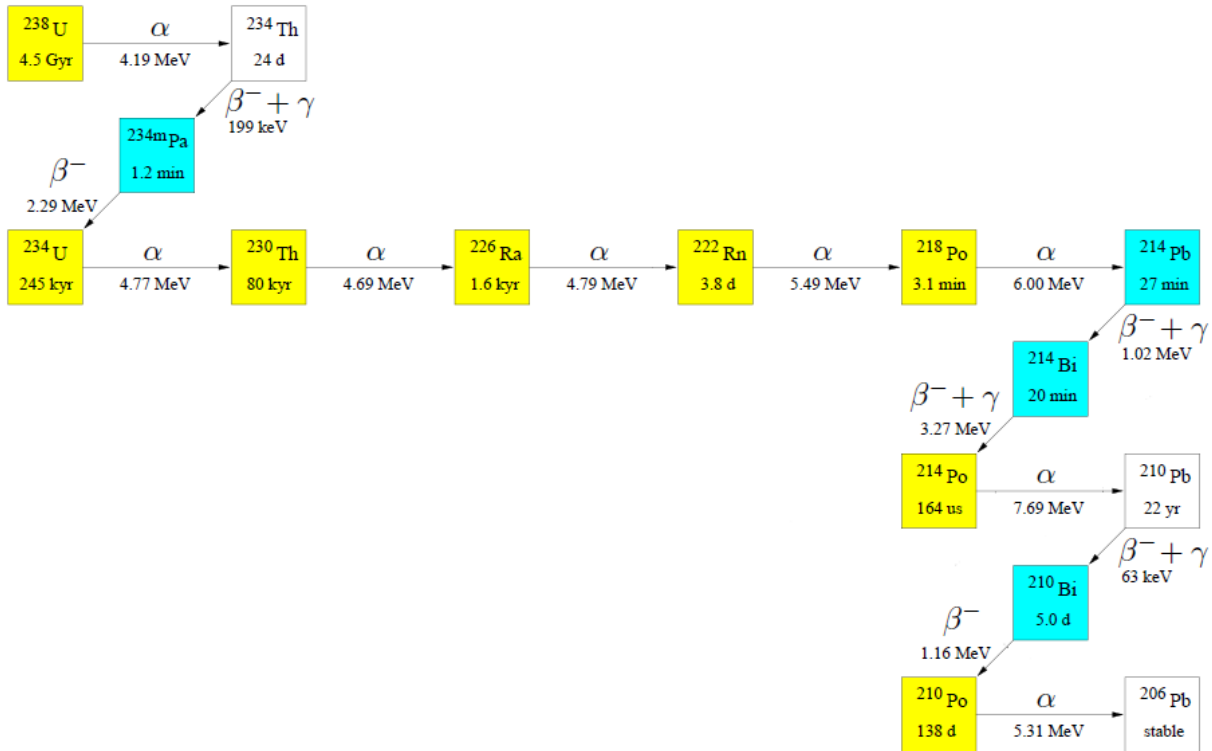


Figure 5.8: The decay series of ^{238}U . The bulk of the contamination present in the inner vessel is in the form of the radioactive gas ^{222}Rn and its daughters.

^{238}U decay chain

The ^{238}U decay chain is a set of 15 decays which transform ^{238}U to ^{206}Pb , several different branches are possible along the way as can be seen in Figure 5.8.

The inner and outer buffers shield the inner-vessel from the vast majority of the radiation originating from Uranium which may be embedded in the construction materials of the detector, and thus, to a good approximation, the signals seen from this chain originate in the inner-vessel. The purification skids, especially the particulate filters, reduce the number of suspended heavy elements in the inner-vessel to a practically negligible level.

The bulk of the inner-vessel contamination attributable to ^{238}U is due to the first gaseous and long-lived ($\tau_{1/2} = 3.8$ days) isotope of ^{222}Rn . Radon introduced during filling has undergone many mean lives since the original operations, therefore, any radon still present in the inner vessel is a product of the emanation of radium in or on the inner-vessel surface (there is also some contribution from the diffusion of Radon present in the inner-buffer through the inner-vessel).

In Borexino, the concentration of ^{238}U cannot be measured directly. Instead, among this very long list of decays, there are two which occur in rapid succession and afford a very efficient means of tagging these two isotopes, and therefore the chain (at least as far back as radon): the fast ^{214}Bi - ^{214}Po delayed coincidences.

^{214}Bi decays (β^- , $Q=3.272$ MeV), releasing a β , and often one or more γ 's. The result of this

decay is an atom of ^{214}Po (α , $Q=7.69$ MeV, $\tau_{1/2}=164.3$ μs) with a half life of 164.3 μs , which then decays by α emission to ^{210}Pb with a high Q value of 7.833 MeV.

^{214}Bi events can be detected by looking for $\beta - \alpha$ delayed coincidence ($\tau=236$ μs) between ^{214}Bi and ^{214}Po . In particular, we search of the coincidences selecting events falling in a time window between 20 μs and 1.4 ms with a spatial separation $<1.5\text{m}$ (efficiency = 1) a cut on the Gatti parameter (see Section 3.3.2). The ^{214}Po α -decays are quenched, so they are selected in the energy range [0.3,1.2] MeV (efficiency = 1).

$$\tau = 236\mu\text{s} \tag{5.7}$$

$$^{214}\text{Bi} \xrightarrow{\beta_{3.2\text{MeV}}} ^{214}\text{Po} \xrightarrow{\alpha_{\sim 700\text{KeV}}} ^{210}\text{Pb}$$

Then, the ^{238}U concentration is deduced from the number of counted ^{214}Bi - ^{214}Po coincidences. Assuming secular equilibrium the Borexino collaboration measured a concentration of $(1.6 \pm 0.1) \times 10^{-17}$ g/g, which is by one order of magnitude lower than the specification.

It is worth noting that the ^{214}Bi - ^{214}Po coincidences provide good reference distributions for particle- and energy-dependent α/β discrimination variables like the Gatti parameter (see Section 3.3.2 and Fig. 3.8).

It has been found in [57] a contamination of ^{214}Bi over 3 MeV:

$$(1.1 \pm 0.4) \cdot 10^{-4} \times 10^{-2} \text{ cpd/100t.}$$

that can be considered negligible for this measurement.

In Fig. 5.9 is possible to note that during the operations on the scintillator, like the water Extractions, the Radon count rate increases and then decreases in few days after the end of the operations, since ^{222}Rn decays with a half-life of 3.8 days.

^{232}Th decay chain

A representation of the decay sequence of ^{232}Th is given in Fig. 5.10.

The concentration of ^{232}Th in the scintillator is estimated via the determination of ^{212}Bi - ^{212}Po delayed coincidences: ^{212}Bi decays ($Q_{\beta}=2.254$ MeV; Branching ratio (BR): 64.06%) to ^{212}Po , ^{212}Po ($\tau=299$ ns) to stable ^{208}Pb . This is more than one order of magnitude below the specification.

The ^{212}Bi decays by emitting a β with a Q value of 2.254 MeV in a 64.06% branch (the other 35.94% of the time, it decays by emitting a 6.207 MeV α to ^{208}Tl). The resulting ^{212}Po lives for a very short time and decays to stable ^{208}Pb with the emission of a 8.954 MeV α . This coincidence is slightly more difficult to tag due to the short meanlife of the ^{212}Po isotope of 432.8 ns because over 97% of the coincidences will occur inside of the same trigger gate, thus the efficiency of the clustering algorithm must be included in calculating the overall efficiency of these cuts.

^{212}Bi - ^{212}Po events are selected in a time window between 400 and 1300 ns, with an efficiency of 0.35, and requiring a maximum spatial distance between the two events of 1 m (efficiency= 1). ^{212}Bi and ^{212}Po are selected in [20-1200] p.e. (efficiency = 1) and [420-580] p.e. (efficiency = 0.93)

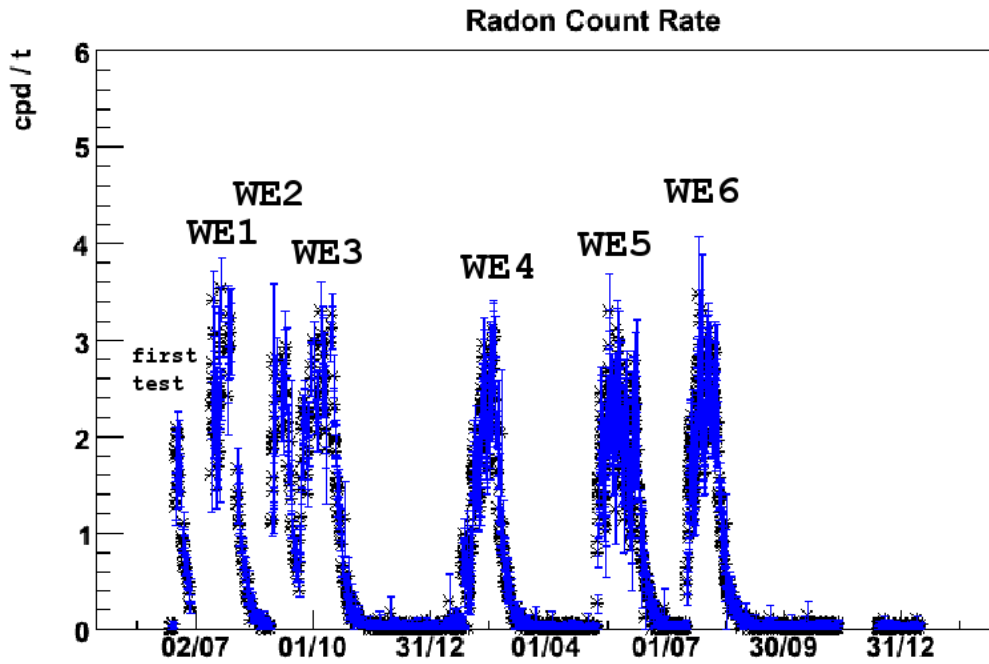


Figure 5.9: Radon count rate increasing during the WE operations on the detector. In the figure the various WE campaigns are indicate.

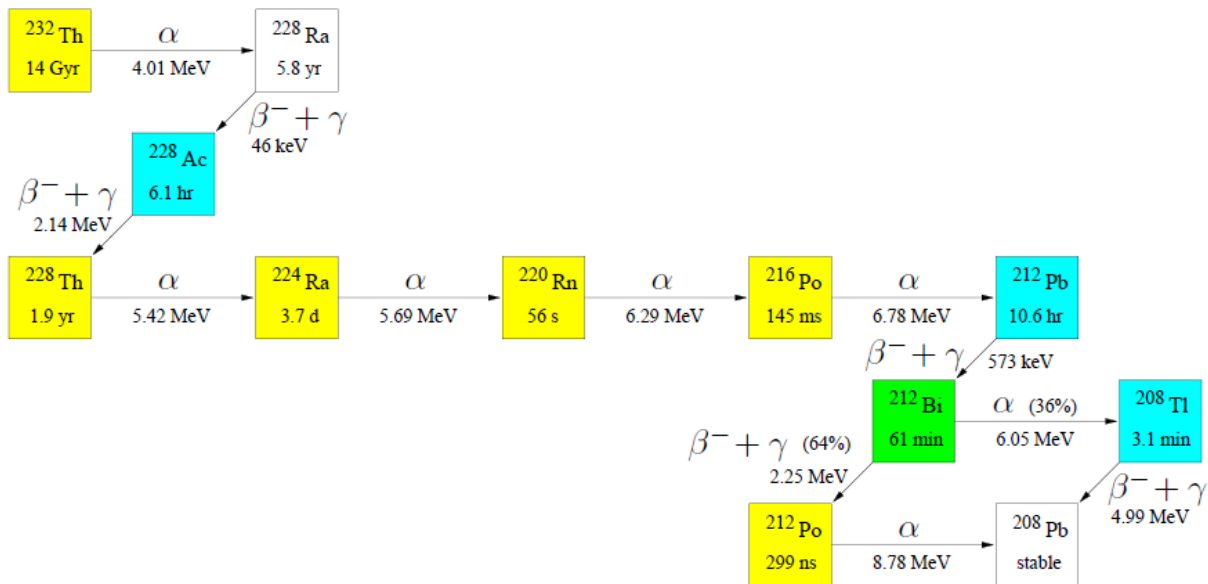


Figure 5.10: The decay series of ^{232}Th .

energy regions, respectively. α 's from ^{212}Po are strongly quenched in the Borexino scintillator. The corresponding quenched energy can be estimates from the ^{210}Po and ^{214}Po peaks. The ^{212}Bi - ^{212}Po coincidences are detected with the delayed coincidence:

$$\tau = 432.8 \text{ ns} \quad (5.8)$$

$$^{212}\text{Bi} \xrightarrow{\beta, 2.25 \text{ MeV}} ^{212}\text{Po} \xrightarrow{\alpha, \sim 800 \text{ KeV}_{eq}} ^{208}\text{Pb}$$

Assuming secular equilibrium, the concentration of ^{232}Th turned out to be $(6.8 \pm 1.5) \times 10^{-18}$ g/g.

Among the many isotopes in the ^{232}Th decay chain there is the particularly troublesome ^{208}Tl , and that will be the reason for the energy threshold setted at 3 MeV in the analysis concerning this thesis this thesis.

^{208}Tl , produced in the 36% branch of the decay of ^{212}Bi , has a mean life of 3.1 minutes, and decays by β emission with a Q value of 5.001 MeV. In the decay process, several gammas are released, most notably one with an energy of 2.614 MeV, the very highly-penetrating gamma ray of concern in the ^8B analysis.

The rate of this background from internal contamination can be estimated by counting the ^{212}Bi - ^{212}Po coincidences, as just explained, and knowing the ^{208}Tl branching ratio.

It has been found in [57] an internal contamination of ^{208}Tl over 3 MeV:

$$(8.4 \pm 2.0) \times 10^{-2} \text{ cpd/100t.}$$

However, even ^{232}Th isotopes outside of the inner vessel will produce ^{208}Tl γ 's that will produce a signal in the inner vessel. The degree to which the buffer shields these events was the subject of a dedicated campaign with a ^{228}Th (a parent of ^{208}Tl) source inserted at the radius of the PMTs (6.35 m) using the external source insertion system done in July of 2010 and in November 2011 and treated in Section 3.5.

5.2.2 External ^{208}Tl

2.615 MeV γ rays originating from decays of the ^{232}Th daughter nuclide ^{208}Tl , mainly contribute to the external background. The 2.615 MeV γ rays are the highest energetic photons released from naturally occurring radioactive decays. Radioactive decays and nuclear interactions in the buffer, the photomultiplier tubes (PMT), the light concentrators, the Stainless Steel Sphere (SSS) and from the environment emit highly energetic γ rays and neutrons which can penetrate the buffer layers, producing a signal in the fiducial volume. A discrimination of these signals looking at the fast coincidences from ^{212}Bi - ^{212}Po decays is not possible as opposed to the internal contamination by ^{232}Th .

The energy spectrum of the external background has a peak around 2.6 MeV and decreases to lower energies. The rate of the events also decreases for smaller fiducial volumes but is still visible within a spherical fiducial volume with radius $R < 2.5$ m (see Fig. 5.11).

If is applied a strong radial cut, is reduced not only the external background, but also the statistics on the data set; instead, if a larger volume is considered, i.e. more statistics, then more external background is present. That is why is necessary to know the spectral shape of the external background, studied in the next section using the data from the external calibration campaign.

Data from external calibration campaign

As shown in Chapter 4 the main reason for the 3 MeV threshold for these analysis is the peak at 2.6145 MeV from ^{208}Tl . It is possible to use data from the external source calibrations for the selection of the cut for the prompt event energy in this analysis, in order to exclude all the spectrum from external background.

The external calibration was performed using a custom-made ^{228}Th , selected since it is long-lived (half life: 1.9 y) and one of its daughter nuclides, ^{208}Tl , emits the characteristic 2.61 MeV γ -rays dominating the external background observed in Borexino. During the first external calibration campaign the ^{228}Th source was deployed in two positions close to the SSS on outside surface, one in the upper and one in the lower hemisphere of the detector.

To reconstruct the spectrum were used the calibration runs in both the position and for background estimation some normal runs before the calibration campaign. Final source and normal runs spectra above are shown in Fig. 5.12. On both data sets standard ^7Be cuts (taken from [158]) were applied. All presented spectra are in the variable **normalized charge**, corrected with the geometrical function studied in [118] in order to eliminate difference in the detector's response for the northern and southern source positions).

The plot in Fig. 5.13 is obtained subtracting the spectra without source to the source spectra (source-k*normal histogram), where $k = 2.10064$ is the normalization coefficient calculated with live times for the spectra.

The histogram was fitted with a gaussian, for the peak, and 3 exponential for the tail [157]. From

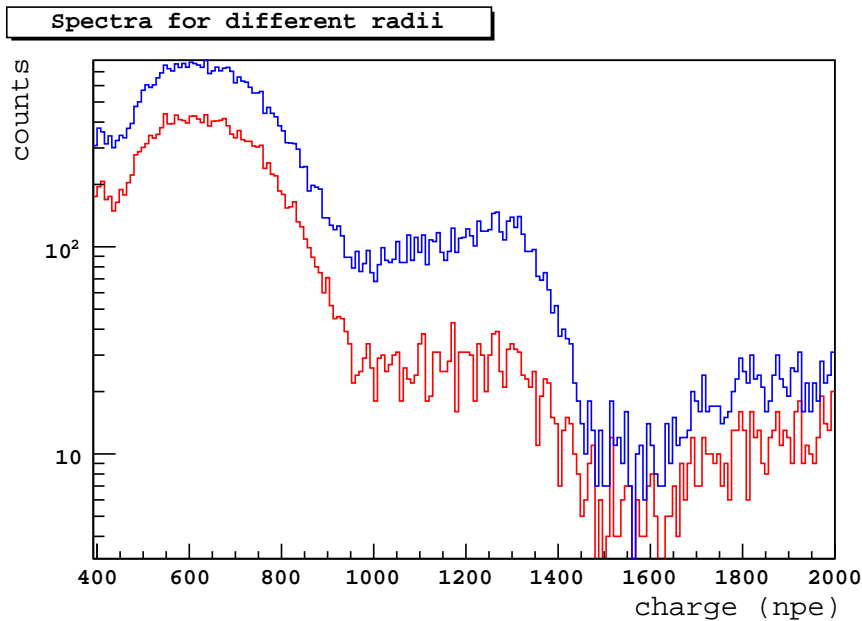


Figure 5.11: Radial dependence of the external background: the spectra of events contained in a fiducial volume with radii $R < 2.5$ m, in red, and $R < 3.0$ m, in blue, are compared. As it is possible to note the Thallium peak around 1250 npe is still present for a radius of 2.5 m.

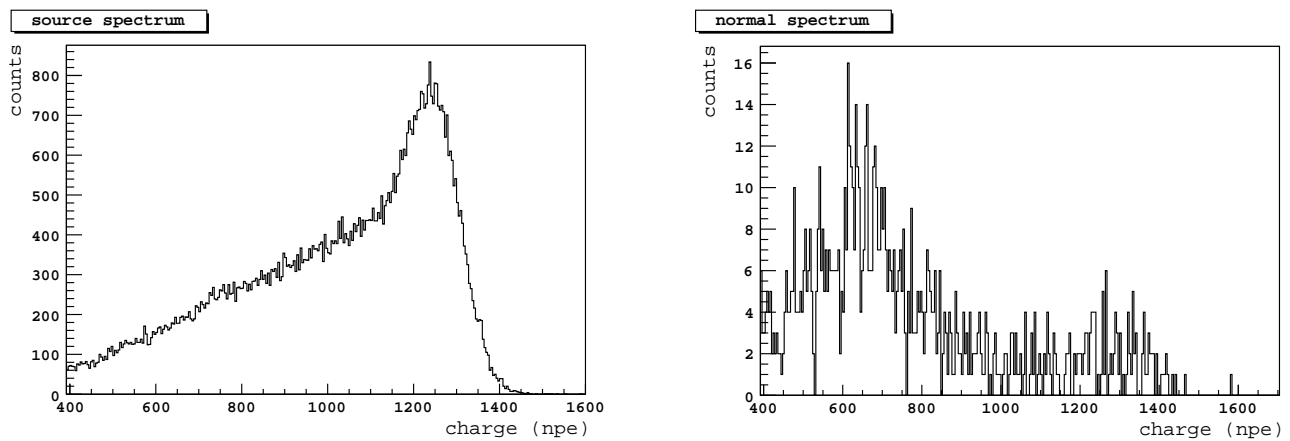


Figure 5.12: Energy spectra with the source and without the source: on the left is the spectrum for normal runs 13437-13552 for background estimation (15.15 days of live time) and on the right is the spectrum for the source calibration runs 13621-13749 with the stable data taking, both positions northern and southern (6.16 days of live time) are included.

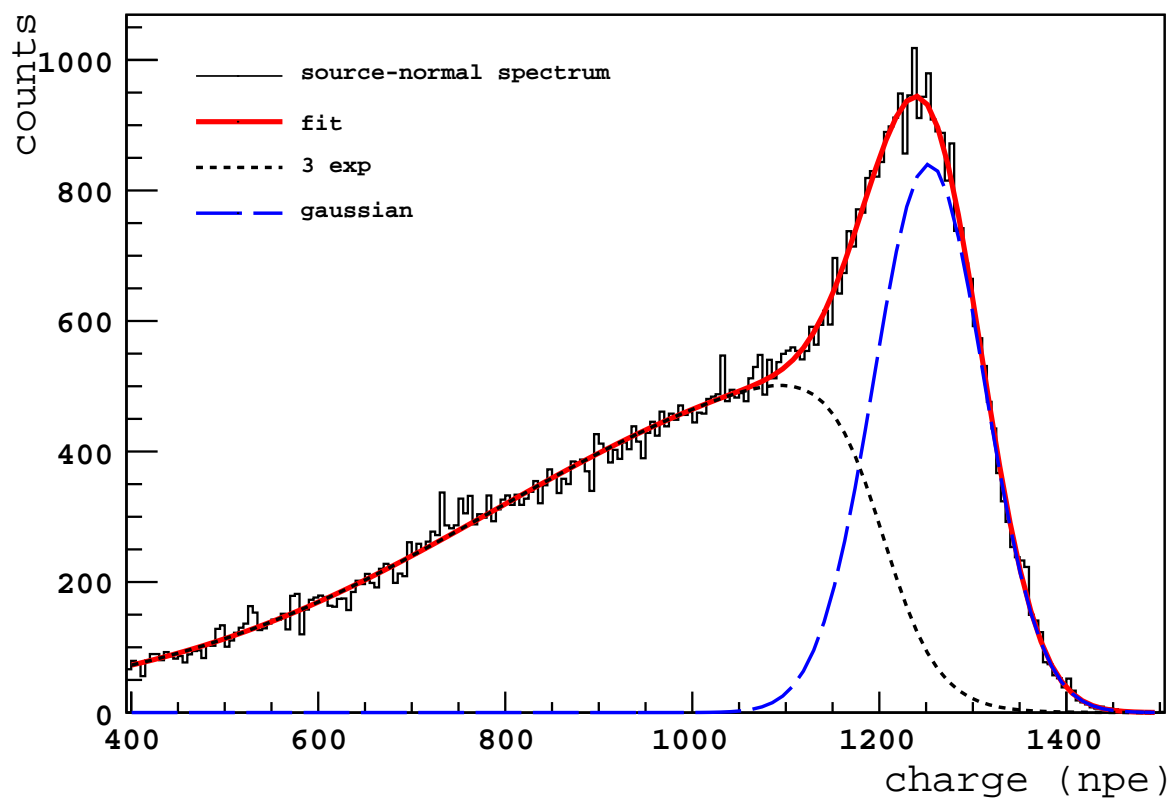


Figure 5.13: Energy spectrum induced by the external ^{228}Th source placed in the northern and southern hemisphere of the Borexino detector.

the fit was obtained:

- $\bar{x} = 1252.9 \pm 6.76$ p.e.
- $\sigma = 59.15 \pm 2.18$ p.e.

The energy of the peak is 2.6145 MeV, so that:

$$\frac{(1252.9 \pm 6.76) \text{ p.e.}}{2.164533 \text{ MeV}} = 479.21 \pm 2.59 \text{ p.e./MeV} \quad (5.9)$$

is the Light Yield obtained, compatible with the result of the $\text{LY} = 478.47$ from the $^{241}\text{Am}^9\text{Be}$ calibration [118].

The gaussian fitting the peak is:

$$f_{x,\sigma}(x) = \frac{1}{59.15\sqrt{2\pi}} e^{-\frac{1}{2}\left(\frac{x-1252.9}{59.25}\right)^2} \quad (5.10)$$

As will be explained in the next section, the energy threshold for this detection will be set at 3 MeV. If it is taken $\text{LY} \simeq 480$, an energy of 3 MeV corresponds to ~ 1440 npe. The percentage of the Thallium peak that is not cut out with 1440 npe threshold is $\sim 0.07\%$.

5.3 Solar neutrinos

Above 2.22 MeV the detector is exposed to neutrinos from ^8B that mainly scatters on the electron via elastic scattering interactions and they are a background for the measurement of charged-current interactions on the rare atoms of ^{13}C .

The internal background due to the elastic scattering of solar neutrinos on electrons has been evaluated assuming $\nu_e \rightarrow \nu_{\mu\tau}$ flavor oscillations with this oscillation parameters [25]:

$$\delta m^2 = 7.6 \times 10^{-5} \text{ eV}^2 \quad \sin^2 2\theta = 0.87 \quad (5.11)$$

and the cross section in equation (2.4). The cross section averaged on the energy range [2.22,16]

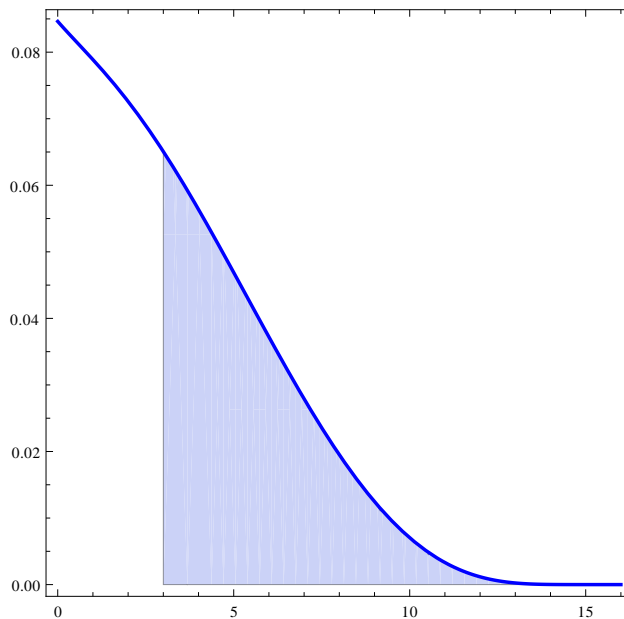


Figure 5.14: Recoil electron spectrum expected in Borexino from solar neutrinos from ^8B . It is highlighted the region over 3 MeV that is 53% of the whole spectrum expected.

MeV is:

$$\langle\sigma\rangle = 8.57 \times 10^{-43} \text{cm}^2 \quad (5.12)$$

but since as it will be explained in the next section, is necessary to raise the threshold for this analysis because of the external background, the cross section averaged on [3.16] MeV becomes:

$$\langle\sigma\rangle = 8.99 \times 10^{-43} \text{cm}^2 \quad (5.13)$$

and the backgrounds events expected in the prompt window signal in the energy range over 3 MeV are: **0.24 ± 0.033 cpd/100t**.

In Fig. (5.14) is shown the recoil electron spectrum expected in Borexino from solar neutrinos from ${}^8\text{B}$.

5.4 Expected Background in prompt and delayed windows

According to the studies just done, in Table (5.2) all the main backgrounds for this measurement in prompt and delayed windows are shown. In the second column it is reported the background event rates (given in counts per day in 100 tons) expected in Borexino [57] for the energy windows considered; in the third column the percentage of this spectrum in the energy window we consider, that is [3,16] MeV for the prompt signal and [1.02,2.22] for the delayed one.

In the last two columns are shown the rate in the energy window we consider given in counts per day in 100 tons, and in counts per day in 132 tons; this latter will be the active target mass used in the analysis.

It is worth to note that in the delayed window the background is almost all due to ^{11}C .

Background in prompt window	Rate [cpd/100t]	Fraction [3,16] MeV	Rate [3,16] MeV [cpd/100tons]	Rate [3,16] MeV [cpd/132tons]
^8B (solar n)	0.49 ± 0.05	0.53	0.24 ± 0.034	0.32 ± 0.044
^{11}Be	0.035 ± 0.006	0.91	0.025 ± 0.033	0.033 ± 0.006
^{10}C	0.54 ± 0.04	0.012	0.0054 ± 0.0004	0.007 ± 0.0005
^{208}Tl			0.084 ± 0.02	0.11 ± 0.03
^{214}Bi			$(1.1\pm 0.4)\cdot 10^{-4}$	$(1.45\pm 0.5)\cdot 10^{-4}$
Background in delayed window	Rate [cpd/100t]	Fraction [1.02,2.22] MeV	Rate [1.02,2.22] MeV [cpd/100tons]	Rate [1.02,2.22] MeV [cpd/132tons]
^{11}C	28.5 ± 0.73	0.841	23.97 ± 0.61	31.64 ± 0.81
^{10}C	0.54 ± 0.04	0.461	0.208 ± 0.015	0.27 ± 0.02
U+Th			negligible	
^{210}Bi			negligible	

Table 5.2: In this table is shown the background in prompt and delayed windows: in the second column is reported the background event rates (given in counts per day in 100 tons) expected in Borexino for the energy windows considered. In the last two columns are shown the rate in the energy window we consider given in count per day in 100 tons, and in count per day in 132 tons, that will be the active target mass used in the analysis.

Chapter 6

Measurement of the neutrino CC interactions rate on ^{13}C in Borexino

6.1 Outline

In this Chapter we present the analysis based on Borexino data collected between December 2007 and May 2011.

First of all is presented the technique to select the neutrino candidates (Section 6.2), the data set, the livetime definition (Section 6.3) and the target volume used in the analysis (Section 6.4).

In Section 6.5 with a MonteCarlo are studied the selection cuts used and their efficiencies.

Then, the expected CC interaction rate in Borexino is calculated, in the Solar Standard Model and neutrino oscillation framework (LMA-MSW), and is calculated the rate of accidental background expected when are taken into account the coincidence criteria (Section 6.6).

In Section 6.7 and 6.8 are reported the steps done to select the candidates with $E > 3$ MeV and is done a study on the accidental and correlated background that brings us to to perform the measurement with a threshold of 4 MeV and the results are shown in Section 6.9.

6.2 Event selection technique

The candidates are selected based on energy, position, and time cuts chosen to maximize the efficiency for observing the charged-current interaction on ^{13}C , described in Chapter 4, while minimizing backgrounds, studied in Chapter 5.

In the region above 2.22 MeV we expect background from cosmogenic events produced by cosmic ray muons as ^{10}C and ^{11}Be and radioactivity from ^{208}Tl and ^{214}Bi both internal and external. The only solar neutrinos that have enough energy to produce charged-current interactions above 2.22 MeV are ^8B and hep neutrinos (as shown in Fig 1.7). The solar ^8B flux is $5.58 (1 \pm 0.14) \times 10^6 \text{ cm}^{-2}\text{s}^{-1}$ while the solar hep flux is $8.04 (1 \pm 0.30) \times 10^3 \text{ cm}^{-2}\text{s}^{-1}$ in the standard solar model GS98. The expected total ^8B neutrino rate in Borexino is ~ 0.5 counts/day/100 tons, while the hep rate

is $\sim 4 \times 10^{-4}$ counts/day/100 tons, which is too small for a statistically significant observation. As discussed in Chapter 4, in Borexino it is possible to detect neutrinos by the charged-current reaction:

$$\nu_e + {}^{13}\text{C} \rightarrow {}^{13}\text{N}(gnd) + e^- \quad E_\nu = T_e + 2.22 \text{ MeV} \quad (6.1)$$

with energy threshold of 2.2 MeV, and the delayed decay of ^{13}N :

$${}^{13}\text{N} \rightarrow {}^{13}\text{C} + e^+ + \nu_e \quad \tau = 862.6 \text{ s} \quad (6.2)$$

with lifetime ~ 15 minutes giving a signal in the energy range [1.02,2.22] MeV .

This reaction makes two correlated signals. The first signal, prompt, is made by the electron. The second signal, delayed, is made by the positron and two 0.511 MeV gamma ray particles generated by the annihilation of the positron as depicted in Fig. 4.4.

These correlated signals are tagged by means of delayed coincidence method. We search pairs of signals that occur within a certain interval (~ 3 times the ^{13}N decay time) and within short distance (order of tens of centimeters). Cosmic muons are a major source of backgrounds, they not only generate unstable isotopes, but also disturb the detector for a certain span. So we decided to veto the detector for a period after each muons crossing the detector.

In order to perform background reduction and fiducialization (i.e. selection of an active spatial region of the detector where the background is low and well understood in order to maximize the neutrino interaction signal) it is necessary to reconstruct precisely the energy and the position of each particle interaction that occurs in the detector. This is done choosing the adequate energy variable for this energy range and the position reconstruction algorithm described in Section 3.3.

6.3 Data set definition and livetime

Borexino has been taking data since May 15th of 2007. In this study the data taken from December 2007 up to May 2011 are used (validated runs 6444-16028). The runs before December 2007 were not used, since the Outer Detector (OD) trigger (Muon Trigger Board) that serves as muon veto was not yet cabled.

Only runs that fell within the given time periods and passed the standard validation checks were included in the analysis. There are several levels of data filtering and validation before proceeding with the final data analysis. As a first step of filtering, all runs with electronics problems (such as flashing PMTs, broken channels, electric power failure, etc.) and runs where the outer detector was off for any reason, were excluded. Runs accepted by the validation procedure were selected as “good runs” and only these runs were used in this analysis.

The Borexino data validation procedure is a major step which aims to verify that the data collected during the run, are acceptable for the physics analysis. According to this procedure, a run should: contain more then 30000 raw events, the event rate should be stable, the number of functional laben channels (see section 3.1) between the beginning and the end of the run should not differ by

more than 100 channels (since during a run some laben channels become disabled from the data taking). The trigger rate and the number of live channels (PMTs) are checked by the validation procedure as well.

The livetime for each run is calculated by taking the difference in time between the first and last valid trigger. The time of each trigger is obtained from a GPS clock and care is taken to avoid problems with changes due to daylight savings. The total livetime of the data taking period before any event selection cuts is :

$$\text{livetime} = 985.672 \text{ days}$$

The uncertainty of the GPS clock compared to the total length of the data taking period is negligible.

6.3.1 Filter framework and DSTs

The creation of the DST (Data Summary Tape) root files is the last step of the selection as explained in Section 3.3. They represent a flexible approach able to reduce the processing time and simplify the physical analysis. They are lightened version of the initial root data files produced by the reconstruction codes, for example, events with a number of hits ≤ 75 that are mainly very low energy ^{14}C events are not present in the DSTs.

This analysis is implemented on a code within the `bx.filter` project (an engine to loop over events on files that are given as input, i.e. a text list of DST). The code runs on the version `cycle14` DSTs of the data decoding program. The cuts used to generate the DSTs are listed in Appendix E.

6.3.2 Water Extraction runs removal

During the study on the various optimal cuts for the selection of the candidates based on energy, time and position, it was discovered that, during the periods in which was performed the Water Extraction (WE) purification (described in section 2.5.3), there were bunch of signals pairs.

This is shown in Fig. 6.1 and in Fig. 6.2, where we used for selecting the pairs of events, larger cuts than the ones that will be used in the analysis, to study better how the number of candidate events changes as a function of the operation on the detector. Here the energy of the prompt and delayed signal is plotted, expressed in number of photoelectrons (npe) collected by the PMTs according to the Equation (3.3), respect to the run number (the Water Extraction periods are coloured).

This excess of events during the operation on the detector remain also if the threshold of the prompt is raised to 3 MeV as shown in Fig. 6.3. In Fig. 5.9 was already shown the increasing of radon during the Water Extraction periods, so, in order to be sure to have a clean sample data, the runs during the WE and some runs after, ~ 5 days, were excluded from the analysis, to let the ^{222}Rn decay since its half-life is 3.8 days.

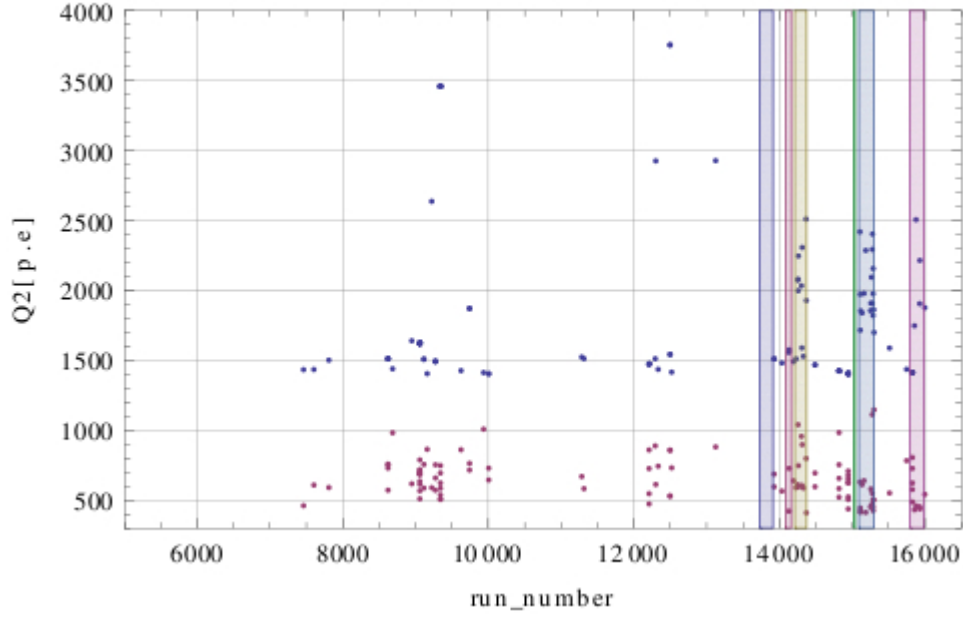


Figure 6.1: Scatter plot of the charge of the prompt (blue) and the delayed (red) signals with respect to the run DAQ number applying the following cuts for the selection: the signal prompt is selected to have energy > 2.9 MeV ($Q_{prompt} > 1400$ npe), the signal delayed is select to have energy in $[1.02, 2.22]$ MeV (400 npe $< Q_{delayed} < 1200$ npe), the distance between the prompt and the delayed to be $\Delta R < 50$ cm, and the time difference between the prompt and delayed to be $\Delta T < 2600$ s. (WE periods are colored).

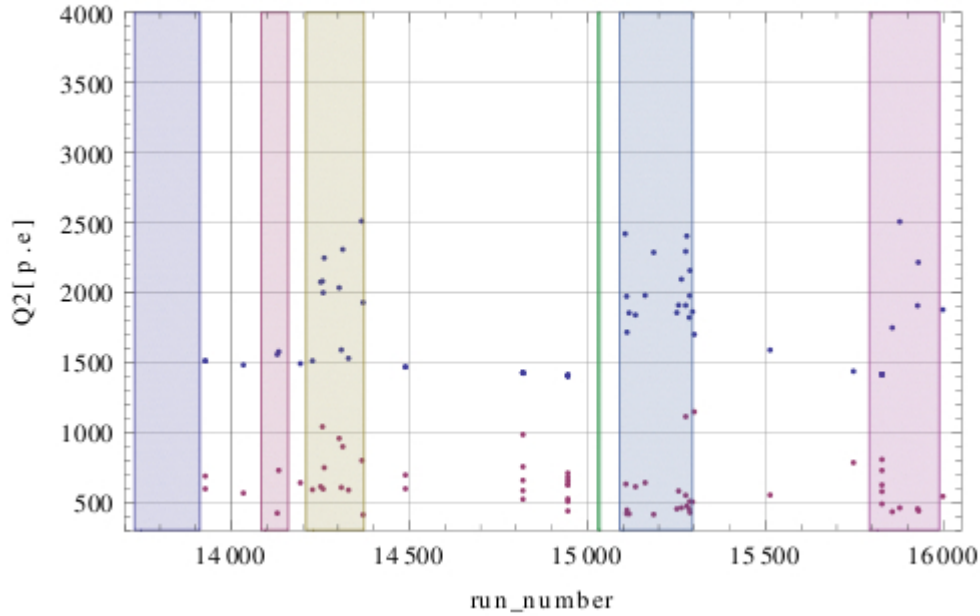


Figure 6.2: This is the enlargement of Fig. 6.1.

The livetime after the exclusion of the Water Extraction periods is:

$$\text{livetime (no WE runs)} = 874.45 \text{ days}$$

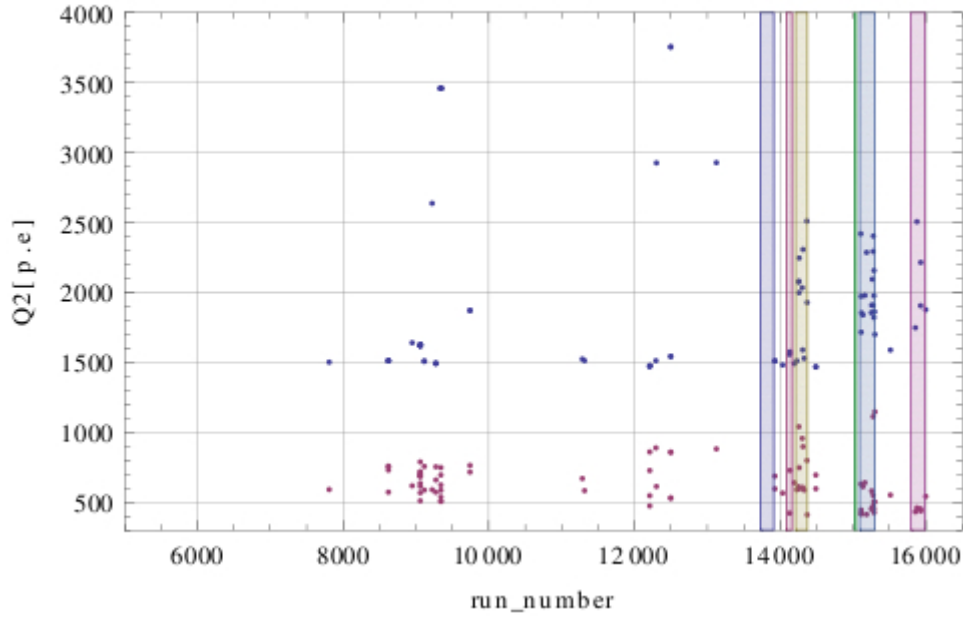


Figure 6.3: Scatter plot of the charge of the prompt (blue) and the delayed (red) signals with respect to the run DAQ number applying the following cuts for the selection: the signal prompt is selected to have energy > 3 MeV ($Q_{prompt} > 1440$ npe), the signal delayed is select to have energy in $[1.02, 2.22]$ MeV (400 npe $< Q_{delayed} < 1200$ npe), the distance between the prompt and the delayed to be $\Delta R < 50$ cm, and the time difference between the prompt and delayed to be $\Delta T < 2600$ s. (WE periods are colored).

6.3.3 Muons and cosmogenics rejection

As already mentioned in Chapter 5, cosmic ray muons and radioactive cosmogenic isotopes produced by muon spallation on ^{12}C nuclei of the scintillator are potential background contribution to low-energy underground experiments searching for and detecting rare events associated with neutrino interactions, like neutrinos CC interactions on ^{13}C . In particular, cosmogenic isotopes contribute to the background through their decays (up to about 20 MeV, see Table 5.1) and neutrons can be captured on nuclei emitting a gamma rays.

As already underlined, a key element for the Borexino experiment is the suppression of the background induced by the residual cosmic muons. A high-efficiency veto and geometrical reconstruction of these muons is mandatory for an identification of cosmogenic backgrounds based on time and space coincidences with the parent muon.

Muon rejection

In Fig. 6.4 the energy spectrum above 3 MeV in the whole Borexino vessel is shown; the number of events in 645.95 livedays is 267947 which corresponds to a rate of ~ 400 cpd/278 t. The expected rate for CC ^8B solar neutrino interaction on ^{13}C , in the Solar Standard Model and neutrino oscillation framework (LMA-MSW), is about 6.74 cpy/278 t above 3 MeV (see Table 4.4).

This shows how challenging is the task of the measurement of the neutrino CC interaction rate on ^{13}C . In order to extract the CC neutrino candidates we have to perform an accurate reduction of

all the backgrounds described in Chapter 5.

The methods that permits the identification and then rejection of muons have already been discussed in Section 5.1.1. In the samples, the selected events identified and rejected as muons are:

3930051 internal muons

2558830 external muons

After the subtraction of the muons the number of events with $E > 3$ MeV reduces to 30761 which corresponds to a rate of ~ 48 cpd/278 t as it is shown in the blue plot in Fig. 6.4.

Cosmogenic isotopes rejection

As studied in Chapter 5, surviving cosmic muons can interact with ^{12}C nuclei of the scintillator, through spallation interaction. The final state is usually composed by unstable nuclei and free neutrons. The first can decay in β mode, and therefore simulate the neutrino interaction, and the latter, after thermalization, will be captured by ^1H or ^{12}C nuclei, emitting a 2.22 MeV or a 4.94 MeV gamma, respectively. Both the spallation final state products can thus mimic the neutrino events in liquid scintillator.

The rejection of cosmic muon products has been performed in different ways, depending on the cosmogenic nature: fast cosmogenic isotopes or cosmogenic neutron captures.

- **Fast cosmogenic veto:** Table 5.1 report a list of expected cosmogenic isotopes produced by muons in Borexino. There are a few that have a decay time < 2 seconds, so, in order to suppress them as a possible background, 5 s dead-time is applied after each muon passing the ID. Since in Borexino the muon rate is ~ 4300 muons/day, this cut gives a dead time of \sim

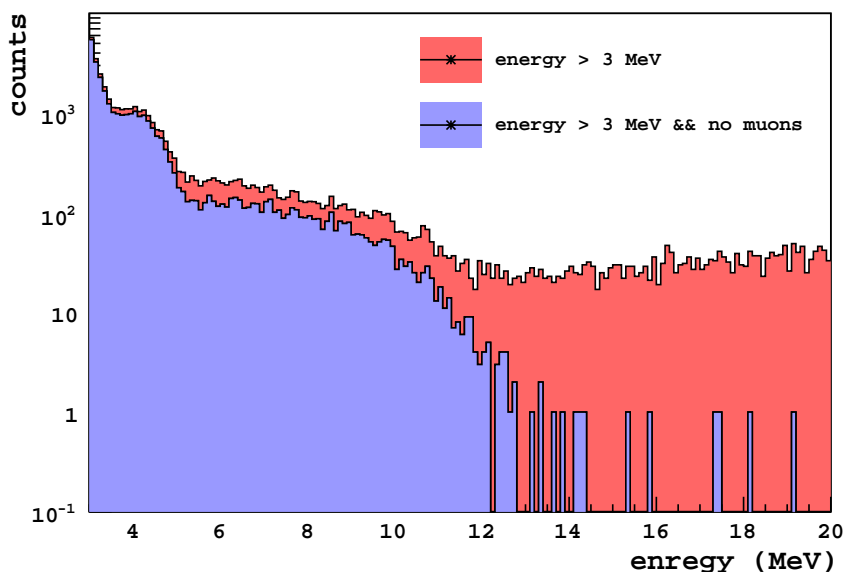


Figure 6.4: Energy spectrum of Borexino events above 3 MeV for the period between December 2nd 2007 and May 29th 2011 in all the inner vessel with (267947 events) and without muons (30761 events).

25%. This fast cosmogenic veto rejects neutrons produced in the scintillator or in the buffer by muon spallation with 99.99% efficiency [80].

- **Cosmogenic neutron veto:** To reject neutrons produced in water which could penetrate to the Inner Detector and mimic the neutrino signal, we applied a second 2 ms veto after each muon crossing the Water Tank only.

2 ms veto corresponds to 7.8 times the neutron live time in the scintillator ($\tau \simeq 256 \mu\text{s}$), and so that the rejection efficiency for neutrons produced in water is 99.96% [80].

The application of the fast cosmogenic veto and the cosmogenic neutron veto reduces the event rate but it also reduce the livetime of 256.34 days (26% of live data taking time), so that the final livetime used in the analysis is:

$$\text{livetime (after muon cut)} = 874.45 \text{ days} - 227.23 \text{ days} = 646.95 \text{ days}$$

6.4 Target volume selection

Here we explain the criteria to choose the *fiducial volume* or the active target mass for this measurement. A fiducial volume is the region at the center of the active volume of the detector in which radioactive background is well known or expected to be at a minimum. The discrimination

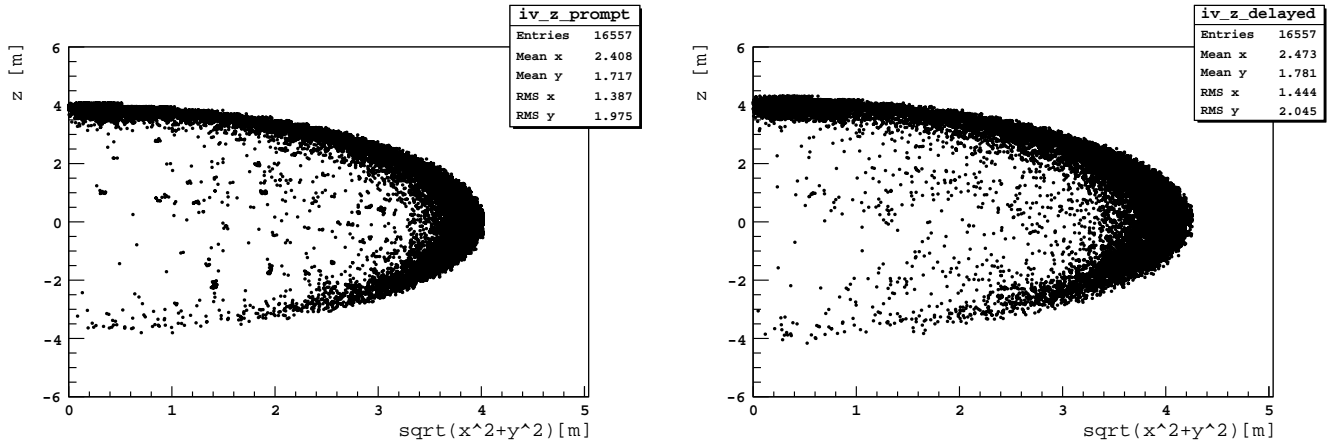


Figure 6.5: The vertex distribution of the prompt signal (Left) and delayed signal (Right) if are selected prompt signal with $Q > 1000$ npe (~ 2 MeV) and delayed signal with $400 \text{ npe} < Q < 1200$ npe ([1.01, 2.22] MeV) without the fiducial volume cut. The regions with event rates higher than other regions are seen at around $Z \sim 4.25$ m and at around IV surfaces, $R \sim 4.25$ m. The charge spectrum of this events is shown in Fig. 6.6.

between events belonging to the fiducial and to the non-fiducial regions is performed by means of software implementation (reconstruction code) of an algorithm (reconstruction algorithm) based on a photon time-of-flight method, which assigns to each single event a reconstructed position, either inside or outside the fiducial volume as explained in Section 3.3.

While neutrino events are distributed uniformly throughout the detector, accidental backgrounds are mainly concentrated near the Inner Vessel surface, where the rate of events from the vessel

contaminants and external radioactivity is high. This excess is illustrated by the bright regions in Fig. 3.6.

In the plot in Fig. 6.5, it is done a selection of the signals prompt and delayed with $Q_{prompt} > 1000$ npe ($E_{prompt} \gtrsim 2$ MeV) and $R_{prompt} < 4.25$ m, in order to show the big contamination from the external background both in the prompt energy window and in the delayed¹.

This contamination remains also if the energy threshold for the prompt event is raised at 1440 npe (3 MeV) as shown in Fig. 6.7. Therefore it is necessary to perform a radial cut in order to remove the external background mostly due to the 2.61 MeV gammas from ^{208}Tl contamination on the

¹It is plotted z versus $\sqrt{x^2 + y^2}$ for the prompt and delayed event.

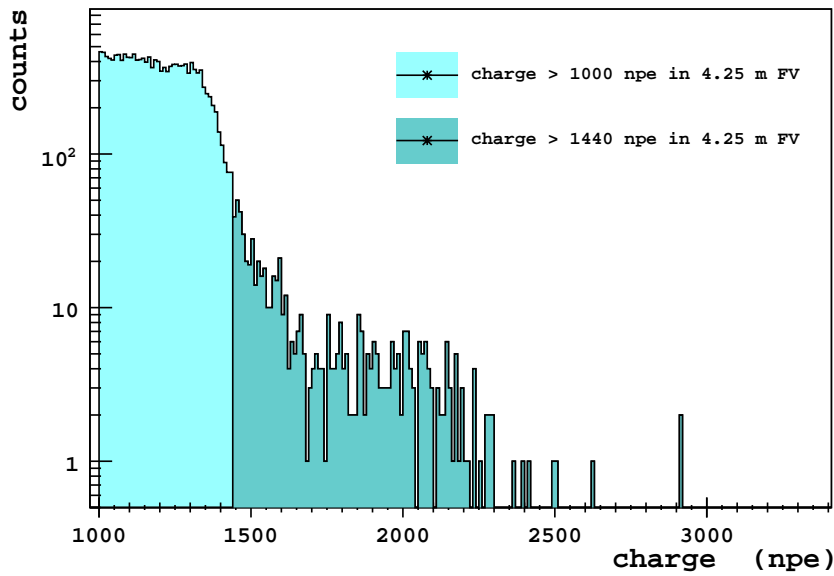


Figure 6.6: Charge spectrum of the selected prompt signals with a fiducial volume of radius of 4.35. It is visible the external ^{208}Tl peak around 1250 npe.

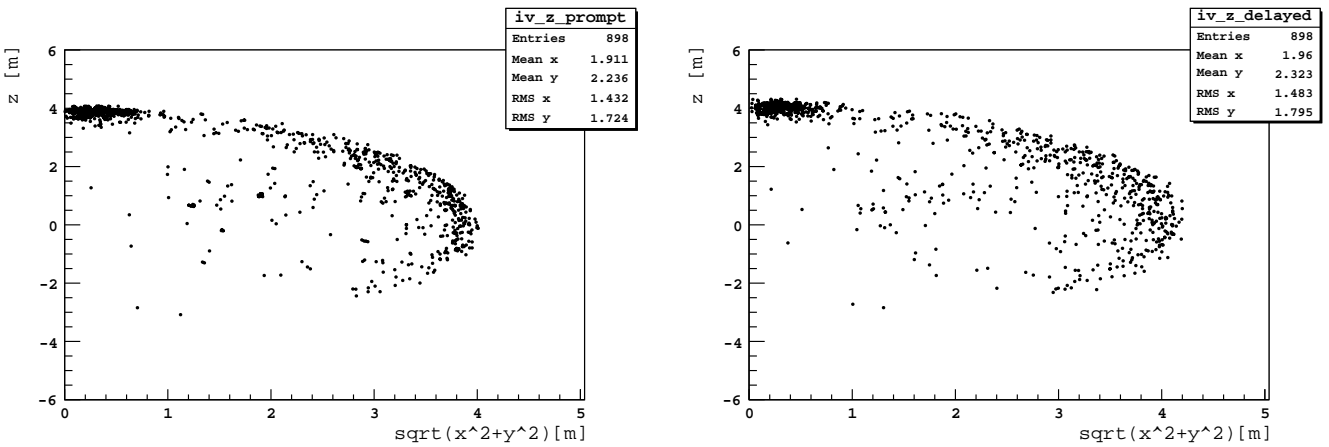


Figure 6.7: The vertex distribution of the prompt signal (Left) and delayed signal (Right) if are selected prompt signal with $Q > 1440$ npe (~ 3 MeV) and delayed signal with 400 npe $< Q < 1200$ npe ([1.01, 2.22] MeV) without the fiducial volume cut. The regions with event rates higher than other regions are seen at around $Z \sim 4.25$ m and at around IV surfaces, $R \sim 4.25$ m.

photomultipliers (PMTs) that can reach the detector core and mimic the neutrino signals. In Fig. 6.6 the charge spectrum of the events shown in Fig. 6.5 and 6.7 is plotted.

Since it is known that the shape of the nylon vessel that contains the scintillator has changed during time, due to operations on the detector, and we know that also the radioactive decays from the vessel itself are a source of background, we have to study if is needed a dynamical selection of the fiducial volume that takes into account how the shape changes in time.

In Fig. 6.8 are overlapped the shapes of the vessel during time according to the study performed in [76].

Nevertheless, it is shown in [159] that the radial distribution of the external gamma-rays does not depend on the vessel shape neither in the South nor in the North hemisphere for radii < 3.5 m, and the attenuation length for gammas is the same for all the ^{208}Tl sources, (PMTs, concentrators and the vessel) and is $\lambda=(25.6 \pm 0.4)$ cm from Geant4 simulations.

As shown in Fig. 6.9, the shape of the vessel moves from the original position (4.25 m) between

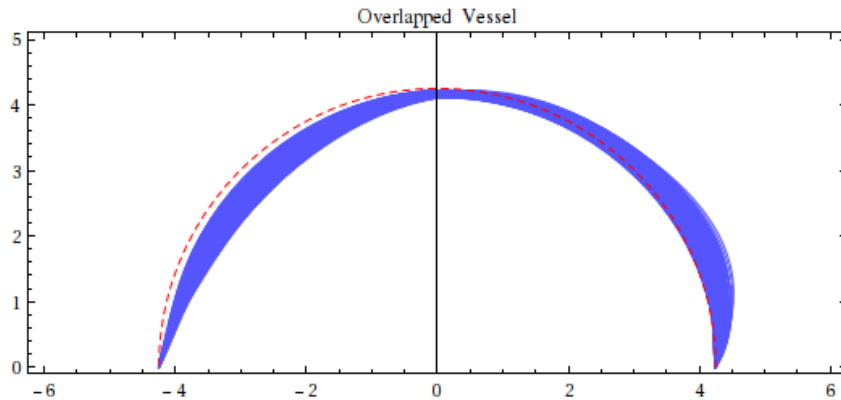


Figure 6.8: Overlapped vessel shape [76]. The red dotted line indicates the 4.25 m radius sphere. Here are shown the z coordinates on the x axes and $\sqrt{x^2 + y^2}$ on the y axes.

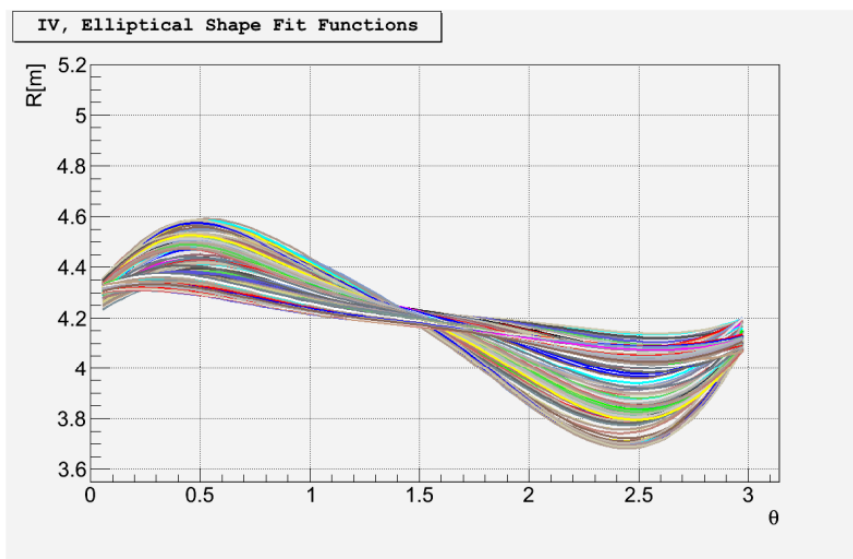


Figure 6.9: Overlapped vessel shape in the period 2007-2011 [77]. As is possible to note the vessel moves from its original position (4.25 m) in between 3.7 and 4.6 m.

3.7 m and 4.6 m. This means that if we choose a fiducial volume of 3.30 m radius the gammas from the vessel are attenuated by a factor $\sim 80\%$ - 100% and it is a good compromise to get enough statistics and at the same time to reject already most of the external background over 2 MeV.

In order to remove the regions of high backgrounds at large radii from the analysis, a fiducial volume cut is applied in which neutrino candidate are required to have a reconstructed distance from the center of the detector < 3.30 m. The radial fiducial volume cut is applied to both the prompt and delayed signals.

Choosing a fiducial volume of radius < 3.30 m, the systematic error on the event position reconstruction is estimated by the reconstruct position shift from the nominal around the edge of the fiducial volume in the same charge region as the data analysis, for charge bigger then 1440 npe in $^{241}\text{Am}^9\text{Be}$ calibration data [160]. The average value of the position shift is 3 cm, so that:

$$\frac{\Delta V}{V} = \frac{\frac{4}{3}\pi R^2 \Delta R}{\frac{4}{3}\pi R^3} = 3 \frac{\Delta R}{R} \quad (6.3)$$

if the position shift is 3 cm, the error on the fiducial volume determinations is at the order of 3%:

$$\Delta R = 3 \text{ cm} \implies \frac{\Delta V}{V} = 3\% \quad (6.4)$$

6.5 MonteCarlo simulation and efficiencies

To recall the step in the coincidence method technique:

1. The first selection criteria is requiring that the energy deposited by the first signal is $Q_{prompt} \geq 1000$ npe (~ 2 MeV), taking into account the Q-value ($Q = 2.2$ MeV) of the reaction and the LY in Borexino $\simeq 480$ pe/MeV. This threshold is raised up to 1440 npe (3 MeV) for the external background removal and in the analysis will be used a threshold of 1920 npe (4 MeV). The 3-4 MeV part will be used for background studies.
2. Impose that the energy of the second signal is between $[1.02, 2.22]$ MeV, that is, choosing a wider window, asking that $400 \text{ npe} \leq Q_{delayed} \leq 1200 \text{ npe}$
3. apply the space and time coincidence criteria requiring:
 - (a) that the distance between the prompt and the delayed signal is $\Delta r \leq 30$ cm (diffusion is considered negligible in Borexino)
 - (b) that the coincidence time between the two signals signals is $2 \text{ ms} \leq \Delta t \leq 2587.8 \text{ s}$ (the lower limit eliminates fast coincidences while the upper limit is chosen to be three times the ^{13}N decay time).

In order to study the optimal cuts for minimizing the background and at the same time maximizing the efficiency for detecting the signal, we developed a dedicated Montecarlo simulation.

The Geant4-based Borexino Monte Carlo code (MC) [161] together with the code that simulates

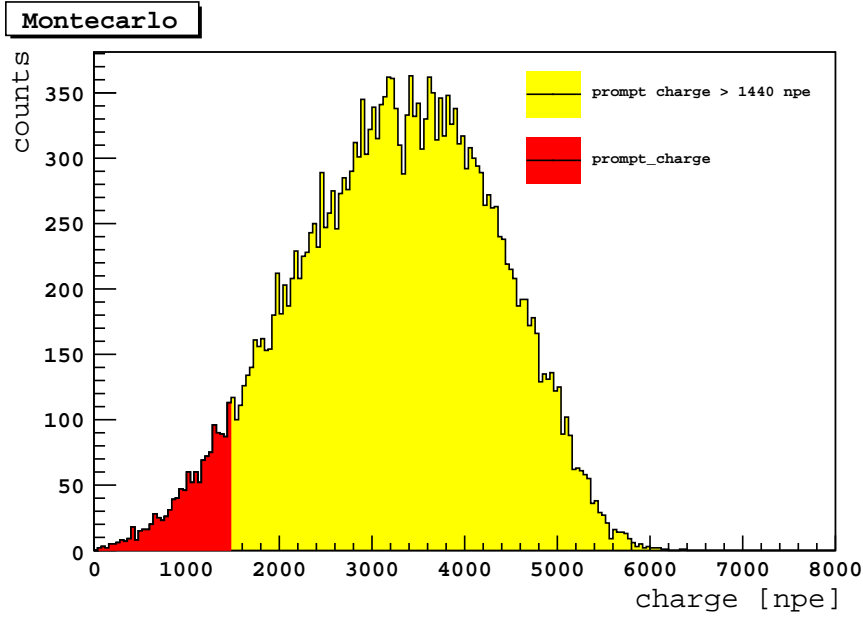


Figure 6.10: Simulated spectra for the prompt signal. In yellow is highlighted the part of the spectrum considered if is chosen $Q_{prompt} > 1440$ npe (3 MeV), it is the 94.98% of the expected spectrum.

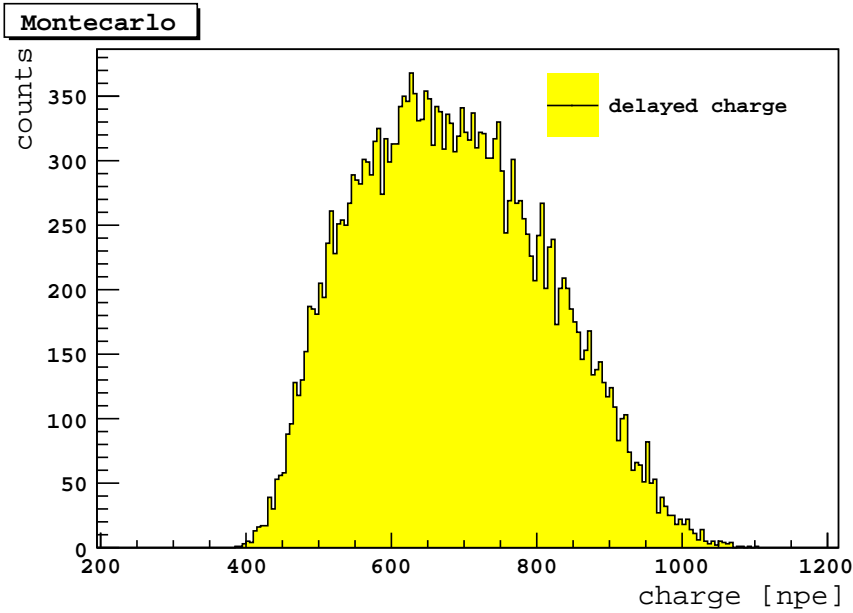


Figure 6.11: Simulated spectra for the delayed signal. As is possible to note with the energy window chosen for the delayed signal ($400\text{npe} < E_{delayed} < 1200\text{npe}$), the percentage of the expected spectrum rejected is almost zero (99.98% between $[400,1200]\text{npe}$).

the detector electronics were tuned on the basis of the calibration campaigns discussed in Section 3.5. We simulate the expected CC interactions on ^{13}C in Borexino. The expected spectrum for the prompt and the delayed signal were used as input to the MC code in order to simulate the detector response to the neutrinos interactions.

The MC generated spectra for the prompt event on ^{13}C and for the delayed decay of ^{13}N are

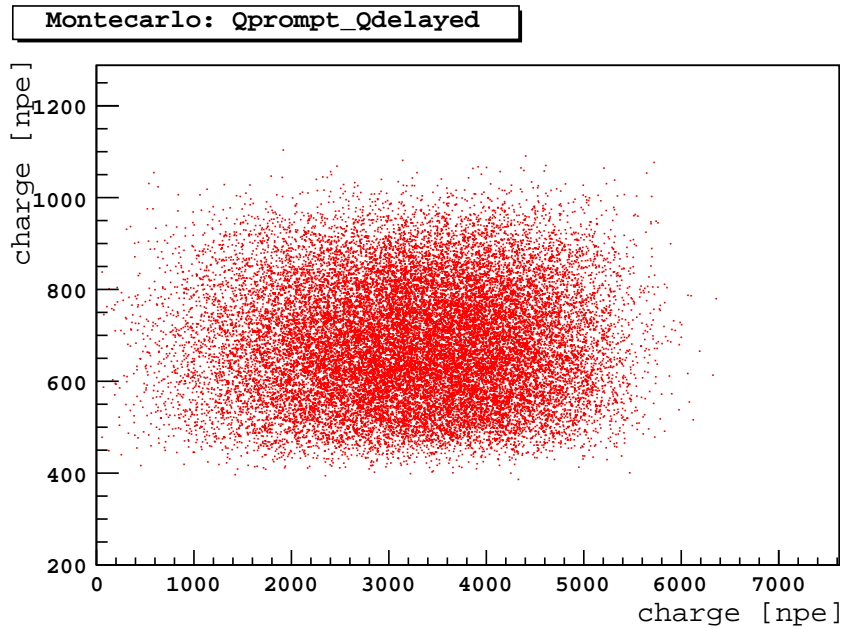


Figure 6.12: Scatter plot of the energy of the prompt event with respect to the energy of the delayed event.

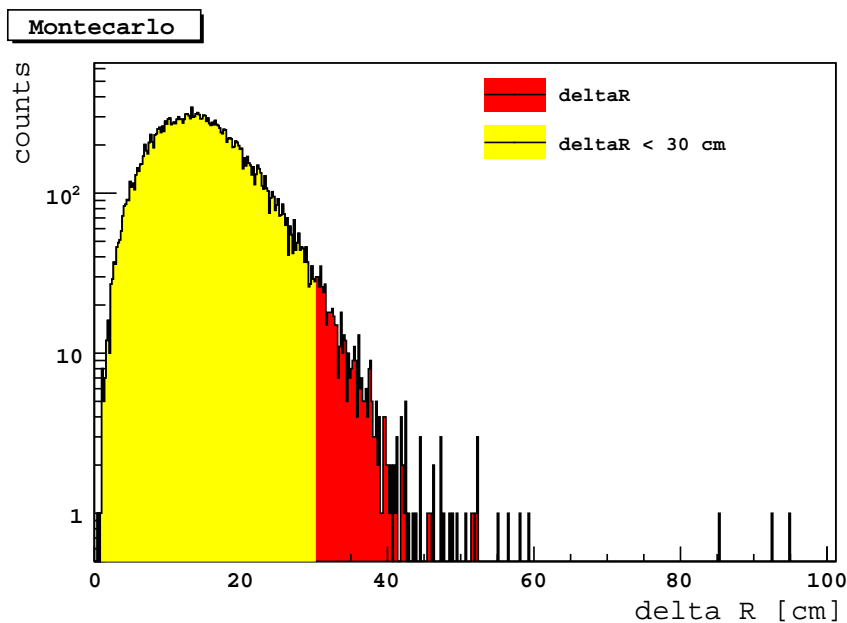


Figure 6.13: Simulated spatial distribution between prompt and delayed signal. If is chosen $\Delta R < 30$ cm the efficiency pf the cut is 97.35%.

shown in Fig. 6.10 and 6.11 as a function of the charge Q , collected by all PMTs and expressed in photoelectrons (npe). In Fig. 6.12 is shown the scatter plot of the charge of the prompt with respect to the charge of the delayed event: is the distribution expected from the Montecarlo obtained by simulating 50000 events in the fiducial volume. While the simulated spatial distribution between the prompt and the delayed signal is shown in Fig. 6.13.

From the montecarlo we find:

- efficiency for the cut in the prompt energy, $Q_{prompt} > 1440$ npe ($E_{prompt} > 3$ MeV): 94.98%

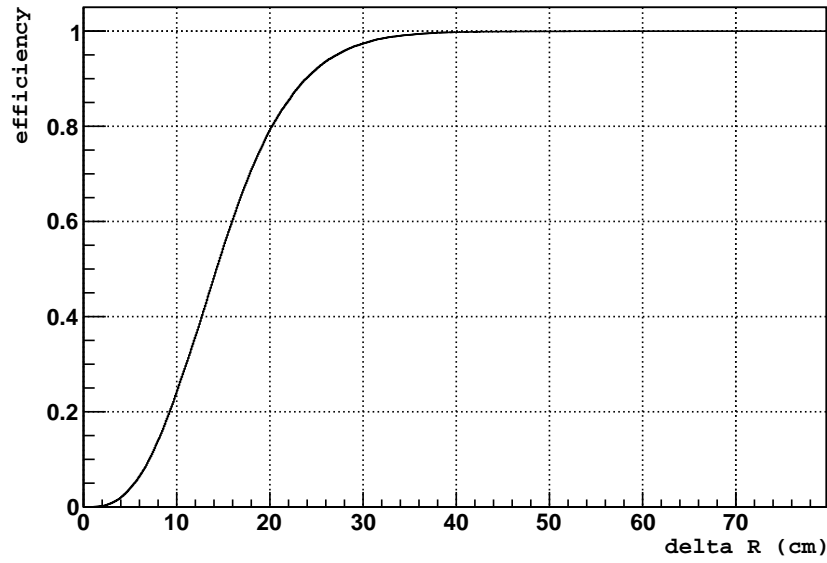


Figure 6.14: Behaviour of the efficiency of the spatial cut, i.e. the distance between the prompt and the delayed signals.

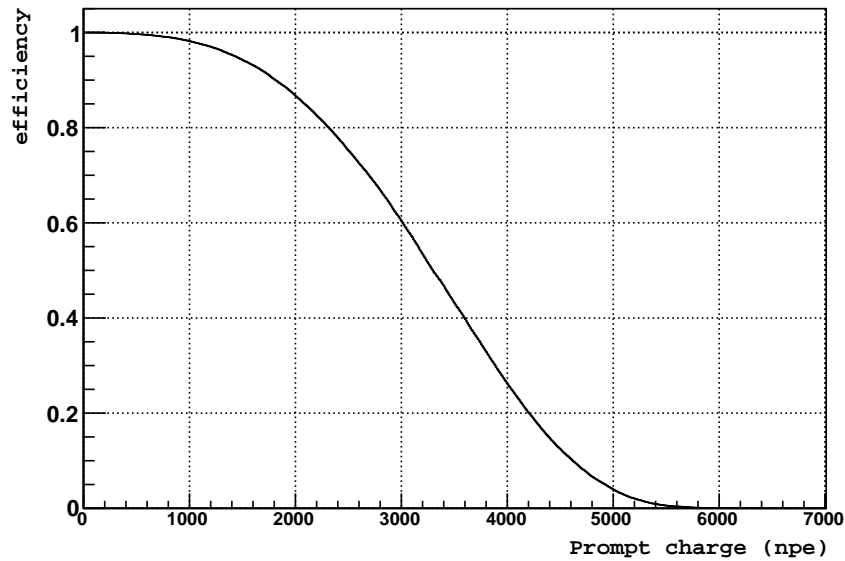


Figure 6.15: Behaviour of the efficiency of the cut on the prompt charge.

- efficiency for the cut in the delayed energy, $400npe < Q_{delayed} < 1200npe$ ($1.02MeV < E_{delayed} < 2.22MeV$): 99.98%
- efficiency for the cut in space ΔR , $\Delta R < 30$ cm: 97.35%

We also have to consider the efficiency of the time cut:

- cut in time ΔT , 0.002 s $< \Delta T < 2587.8$ s:

$$\int_{0.002}^{2587.8} \frac{e^{-\frac{t}{862.6}}}{862.6} dt = 95.02\% \quad (6.5)$$

The global efficiency obtained from the efficiencies of all these cuts is 87.84%, see Table 6.1. In Fig. 6.14 and 6.15 is shown respectively how the behaviour of the efficiency of the ΔR cut and of the energy prompt threshold cut.

In the following are shortly described the cuts chosen on the basis of the efficiencies studied.

Prompt energy analysis threshold

The kinematic threshold for the charged-current (CC) transition to the ^{13}N ground state

$$\nu_e + {}^{13}\text{C} \rightarrow {}^{13}\text{N}(gnd) + e^- \quad (6.6)$$

is 2.2 MeV, therefore that with this channel it is possible to detect only neutrinos with $E > 2.22$ MeV. For a light yield in Borexino of $\simeq 480$ npe/MeV as shown in Section 3.3.2, this threshold corresponds to a charge of $\simeq 1000$ npe. Since we want to avoid the background coming from the 2.614 MeV γ -rays from the β -decay of ^{208}Tl the threshold for the prompt signal is set to be $E > 3$ MeV:

$$\implies Q_{prompt} > 1440\text{npe} \quad (6.7)$$

Energy cut on the delayed signal

For the delayed signal:

$${}^{13}\text{N} \rightarrow {}^{13}\text{C} + e^+ + \nu_e \quad (6.8)$$

the visible energy is the sum of the positron kinetic energy and the energy released in e^+e^- annihilation, for this reason delayed events have a continuous energy spectrum in the range [1.02,2.22] MeV:

$$\implies 400\text{npe} < Q_{delayed} < 1200\text{npe} \quad (6.9)$$

Time correlation

The ^{13}N that subsequently decays has a $\tau = 862.6$ s, around 15 minutes, so we choose the time cut to be $3\tau = 2587.8$ s (as highlighted in Fig. 6.16) so that the percentage of events lost is $\sim 5\%$:

$$1 - \int_{0.002}^{2587.8} \frac{1}{\tau} e^{-\frac{t}{\tau}} dt = 4.98\% \quad (6.10)$$

Space correlation

An extremely effective condition in reducing the background, as explained in section 4.1.3, is that, in the absence of macroscopic motions in the detector, the ^{13}N nucleus essentially does not move from its original position: the expected displacement due to recoil and diffusion during the decay time τ is smaller than the scintillator detector spatial resolution, $\sigma \sim 10$ cm at ~ 1 MeV. This means that the prompt event produced by the reaction and the delayed event produced by the decay have to be observed essentially in the same position.

The ΔR Cut ($\Delta R < 0.3$ m), that we choose to be $\simeq 3$ times the detector spatial resolution, is designed to select spatially correlated prompt and delayed event-pairs.

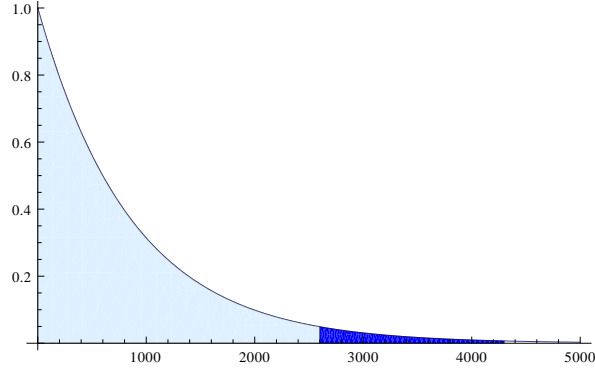


Figure 6.16: Decay time of ^{13}N , the light blue part highlight the 3τ of ^{13}N .

Selection cut	Efficiency
$E_{prompt} > 1440 \text{ npe}$	0.9498
$400\text{npe} < E_{delayed} < 1200\text{npe}$	0.9998
$\Delta R < 30$	0.9735
$0.002 \text{ s} < \Delta T < 2600\text{s}$	0.9502
	0.8784

Table 6.1: Cuts efficiencies.

6.6 Expected signal and background rate

6.6.1 Expected and effective signal

Now that the efficiencies have been calculated, we can calculate the signal event expected rate S , that is given by:

$$S = R_\nu \times \varepsilon \quad (6.11)$$

where ε is the the global efficiency that is the combined efficiency for all the cuts. For estimating the expected rate, we have to consider also the efficiency of the determination of the fiducial volume that is 97% as already pointed out in Section 6.4. The global efficiency becomes:

$$\varepsilon = 85.21\%.$$

The number of signal events R_ν as a function of threshold of prompt events (per unit mass) produced by ^8B solar neutrinos in the energy window $[T_{e,1}, T_{e,2}]$ is given by (see equation (4.25)):

$$R_\nu = n_{13C} \Phi \int_{T_{e,1}+Q}^{T_{e,2}+Q} \sigma(E_\nu) \lambda(E_\nu) P_{ee}(E_\nu) dE_\nu \quad (6.12)$$

where :

- $\Phi = 5.58 \times 10^6 \text{ cm}^{-2} \text{ s}^{-1}$ is the boron neutrino flux [47],

- $\lambda(E_\nu)$ is the boron neutrino spectrum, see section 4.2,
- $\sigma(E_\nu)$ is the interaction cross section, see section 5.3,
- $P_{ee}(E_\nu)$ is the electron neutrino survival probability,
- $n_{^{13}\text{C}}$ is the number of ^{13}C atoms per unit mass, which depends on the scintillator chemical composition, as already calculated in section 4.2.1 :

$$n_{^{13}\text{C}} = I \cdot N_A \sum_k f_k \frac{X_k}{\mu_k} \quad (6.13)$$

The fiducial volume considered for this measurement is a sphere of radius 3.30 m, that correspond to a mass of ~ 132 ton and the number of ^{13}C atoms is: $n_{^{13}\text{C}} = 6.36 \times 10^{28}$.

For a detection threshold on the prompt event of 3 MeV, are expected:

$$Rate_{expected}(^{13}\text{C}) = 5.57 \pm 0.78 \text{ events/livetime/132t.} \quad (6.14)$$

Now we have to correct the expected rate through equation (6.11) for taking in consideration the efficiency, and we obtain that the effective expected rate is:

$$Rate_{effective}(^{13}\text{C}) = 4.75 \pm 0.66 \text{ events/livetime/132t} \quad (6.15)$$

The number of signal events expected and effective against the detection threshold is plotted in 6.17.

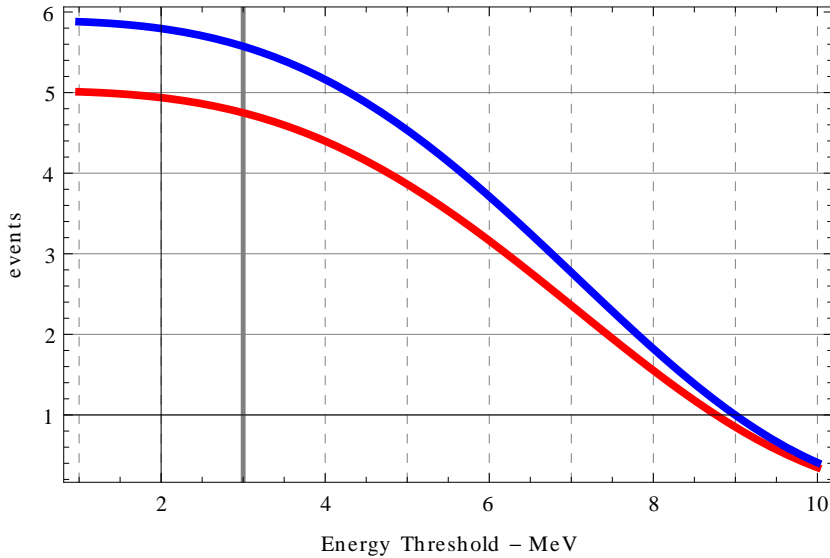


Figure 6.17: Number of signal events expected (Blue) and effective (Red) against the detection threshold, given in events/livetime/132t. For a cut on the energy of the prompt signal at 3 MeV are expected 5.57 ± 0.78 events/livetime/132t which becomes 4.75 ± 0.66 events/livetime/132t taking into account the efficiency.

Background in prompt and delayed windows

In Chapter 5 we studied the background sources in the Region Of Interest (ROI) for the neutrino CC interaction on ^{13}C , and in Table (5.2) is reported the contribution of each main background source in the prompt and in the delayed energy window.

From those values, we calculate in Table 6.2 the rate of expected and measured background: in the second column it is reported the number of background events expected in the prompt window in all the livetime, while in the last column it is shown the rate of background events in the prompt energy window after the coincidence criteria are applied and it is taken in account the efficiency.

This is obtained by considering that the probability to have a background event in the delayed energy window when space and time cuts are applied is simply equal to the average number of delayed background events during the time interval $\Delta t = n_t \tau$ and inside the spherical volume $V = (4/3)\pi(R\sigma)^3$, being this number much smaller than one (where σ is the detector spatial resolution and $\Delta r = R\sigma$)

The rate of fake coincidences B is thus given by

$$B_{effective} = B_{prompt} B_{delayed}(\Delta t) \left(\frac{4}{3} \pi (\Delta r)^3 \rho \right) \quad (6.16)$$

where B_{prompt} and $B_{delayed}$ are the prompt and delayed background rates (per unit mass), ρ is the liquid scintillator density (equal to $\rho = 0.88 \text{ g/cm}^3$ for the Borexino scintillator), $\Delta r = 30 \text{ cm}$ and $\Delta t = 3 \times 862.6 \text{ s}$.

It is possible to see that, despite of the large number of background events in the prompt and delayed energy window, the fake coincidences are rare, and lower than the expected signal. The

	Expected rate in prompt window counts/lt/132t	Effective rate in prompt window counts/lt/132t
Background		
^8B (solar n)	204.95±28.69	0.19±0.027
^{11}Be	21.18±3.63	0.02±0.003
^{10}C	4.62±0.34	0.004±0.0002
^{208}Tl	71.73±17.08	0.068±0.016
^{214}Bi	0.09±0.03	negligible
TOTAL	302.58±33.59	0.29±0.032
Signal		
^{13}C	5.57±0.78	4.75±0.66

Table 6.2: Expected and measured background [counts/livetime/132 tons].

number of expected accidental coincidences is:

$$Rate_{accidentals} = 0.29 \pm 0.032 \text{ events/livetime/132t} \quad (6.17)$$

and the signal to background rate is :

$$\frac{S}{B} \simeq 16.4 \quad (6.18)$$

6.7 Data reduction

To select prompt and delayed events associated with the neutrino interaction on ^{13}C , the first step is to select a clean data set, and then apply space and time coincidences.

Within the Echidna framework the energy variable we use for this analysis is the **Normalized Charge**, it gives the charge of an event in number of photoelectrons (npe) because, as explained in Section 3.3.2, this variable is more adequate in the analysis of events of which scintillation light deposited in the detector lies above 1 MeV, this because it has a wider dynamical range and follows an almost linear behavior at least above ~ 2 MeV.

Since the selection method for the neutrinos CC interactions on ^{13}C is based on the coincidence technique, the first step in this analysis is the data reduction in order to obtain two clean set of events, one for the prompt signal ($E > 3$ MeV) and one for the delayed one ($1.02 < E < 2.22$ MeV). It is reported also the number of events in a sample with energy over 4 MeV for the prompt event because it will be the threshold used for the analysis. The region between 3 and 4 MeV will be used for the estimation and rejection of the correlated background.

This selection of events is divided in 5 categories of cuts:

1. General: where basic requirements are asserted, like:
 - trigger type equal to 1. This means selecting signals that have been acquired with the Inner Detector read-out tagged as *neutrino trigger* as explained in Section 3.1.3 and that are not neutrons.
 - one cluster events. As explained in Section 3.3.1, a *cluster* is collection of the hits from PMTs that are identified as belonging to the scintillation event. The events with more than one cluster are rejected because they can be for example fast coincidences from radioactive background or neutron trigger.
2. Muons: where muons and cosmogenics with short τ are vetoed. The muon cuts eliminate muons, spallation neutrons, and short lived radioactive backgrounds generated by muons.
 - remove internal muons according to the flags listed in Section 6.3.3,
 - remove all events in a 5 s time window after each internal muon,
 - remove external muons, i.e. muons crossing only the Water Tank,
 - remove all events in a 2 ms time window after each external muon.
3. Fiducialization: selection on the reconstructed radius to reduce the background:

$$R_{prompt} < 3.30 \text{ m and } R_{delayed} < 3.30 \text{ m.}$$
4. Charge: selection on the energy window for the prompt and the delayed event:

$$Q_{prompt} > 1440 \text{ npe } (\sim 3\text{MeV}),$$

$$400 \text{ npe} < Q_{delayed} < 1200 \text{ npe } (\sim [1.02, 2.22]\text{MeV}).$$

After the subtraction of the muons and of all the events in 5 s after each internal muon and 2 ms after each external muon the number of events is:

\Rightarrow 613 events with $Q > 1440$ npe (299 events with $Q > 1920$ p.e)

\Rightarrow 41658 events with $400 \text{ npe} < Q < 1200$ npe

In Fig. 6.18 and 6.19 are shown the charge spectra of the samples selected, while in Fig. 6.20 and

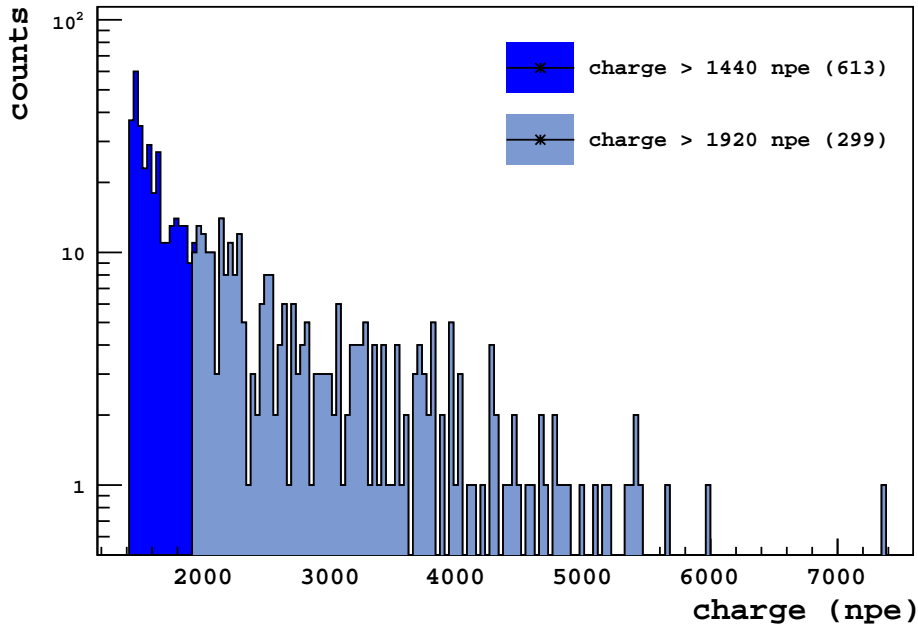


Figure 6.18: Charge spectrum of the sample with $Q > 1440$ npe (~ 3 MeV) . and the sample with $Q > 1920$ npe (~ 4 MeV).

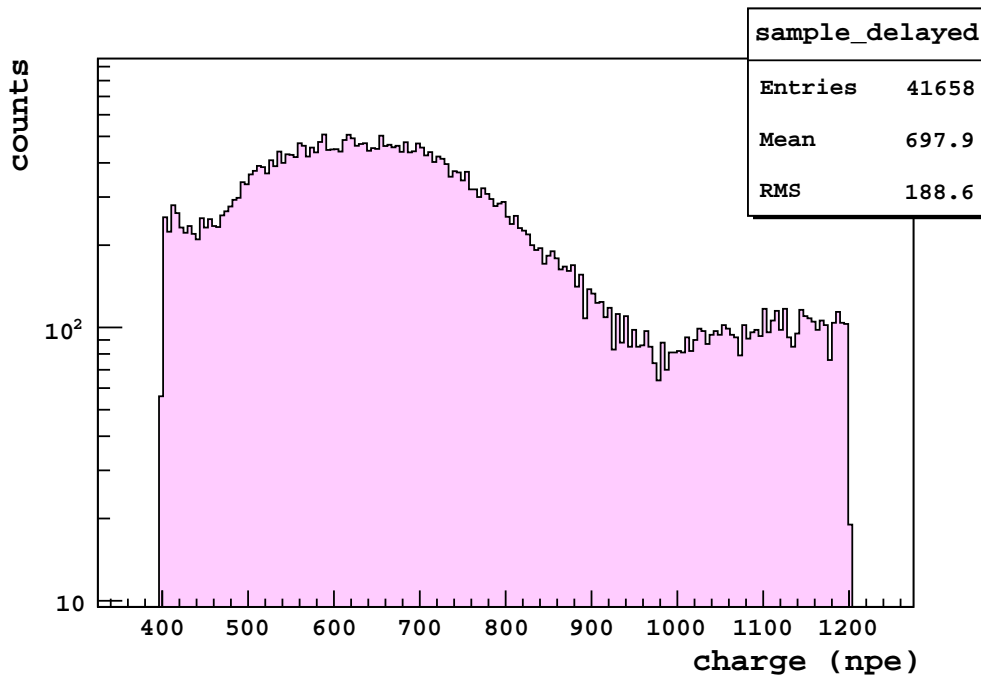


Figure 6.19: Charge spectrum of the sample with $400 \text{ npe} < Q < 1440$ npe.

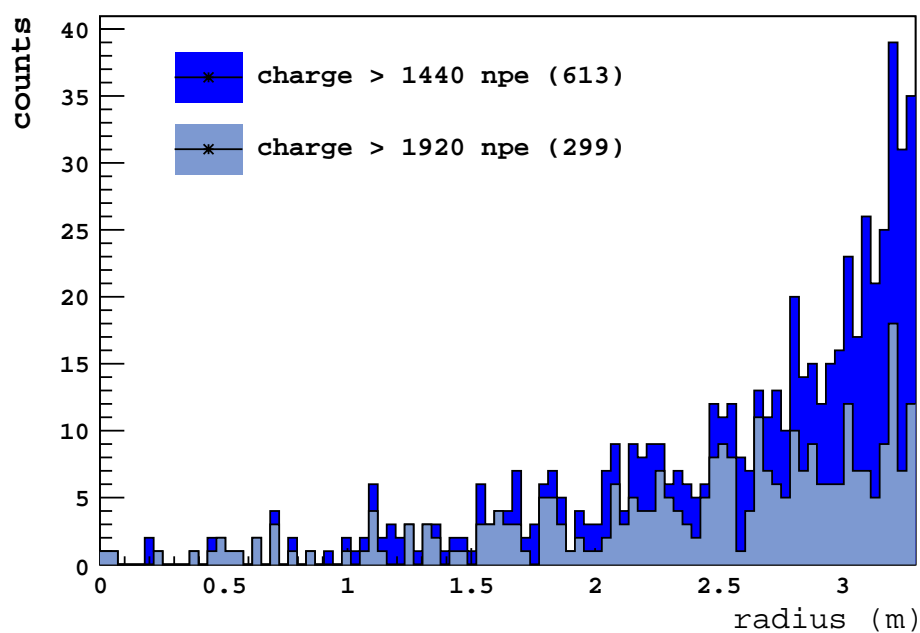


Figure 6.20: Radial distribution of events in the 3.3 m radius sphere and with charge [400,1200] npe.

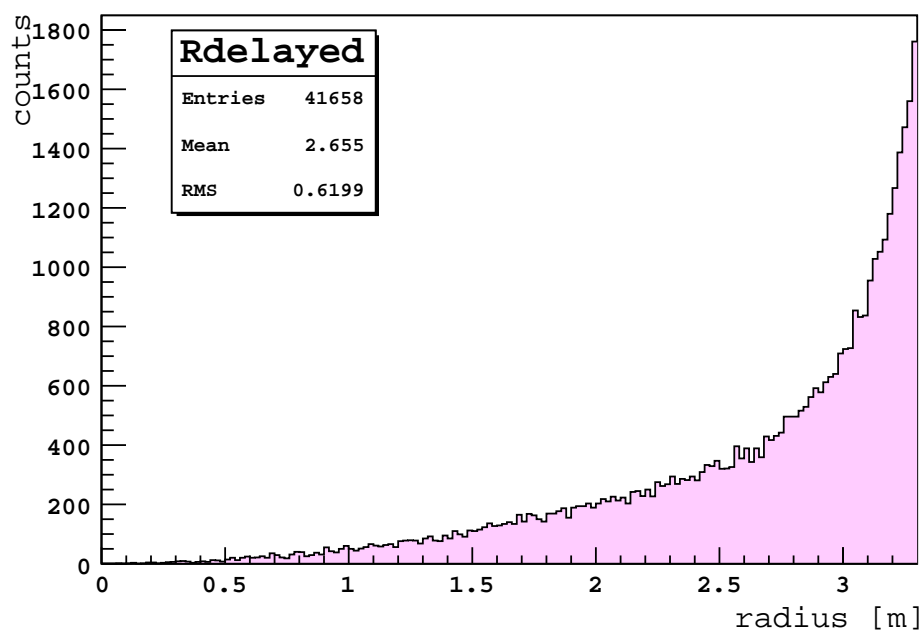


Figure 6.21: Radial distribution of events in the 3.3 m radius sphere and with charge (400,1200) npe

6.21 are shown the radial distribution of the selected events that will be used as input in the toy Montecarlo describes in Section 6.8.

6.8 The space-time coincidence technique

In order to reduce the background, we can take advantage of the time and space coincidence of the neutrino events with the positron emitted in the ^{13}N decay. A signal prompt event is tagged as candidate if it is followed by a delayed event in the energy window $[1.02, 2.22]$ MeV, within a time interval $\Delta t = 3\tau$ (where τ is the ^{13}N decay time), and inside a sphere of radius Δr centered on the prompt event detection point ($\Delta r \sim 3$ times the Borexino spatial resolution).

Cut	Rate [counts/livetime/132t]
1) $E_{prompt} > 1440$ npe	267947
2) $R < 3.3$ m	83543
3) no μ + tt1 + muon cuts + 1cluster	3046
4) $400\text{npe} < E_{delayed} < 1200\text{npe}$ in $0.002 \text{ s} < \Delta T < 2587.8\text{s}$	426
5) $\Delta R < 30$ cm	12

Table 6.3: Data reconstruction steps: the reduction of the candidates through the application of the listed cuts.

In Table 6.3 and Fig. 6.22 and 6.23, the data reconstruction steps for the prompt events are shown: the reduction of the candidates through the application of the listed cuts.

- 1) The starting sample consists of events with energy > 3 MeV (1440 npe) in all the Inner Vessel;
- 2) then the radial cut is applied, i.e. only events in a 3.30 m radius sphere are selected;
- 3) then the basic assumptions are requested: the number of cluster is one (see Section 3.3.1), the trigger type is one and finally the muon and after muon cuts are applied.
- 4)+5) The last steps consists in selecting candidates with a delayed signal in the proper energy region and to ask that they are spatial and time correlated.

It is worth to note that the very effective cut for rejecting the background in between the coincidence criteria is the space cut that reduced the candidates prompt from 426 to 12.

The analysis performed in such a way selects 12 prompt candidates. In Fig. 6.24 the charge distribution of the prompt events (left) and of the delayed ones (right) is shown.

A fraction of these events show a characteristic multiplicity, that is a prompt followed by more delayed signal. We define *multiplicity index* the number of delayed signals after a prompt is selected. Out of 12 candidates we measure 3 events with multiplicity equal to 3,4 and 5 (the candidates found are listed in Appendix G.)

In Fig. 6.25 it is shown an example of a prompt signal and two delayed events that fall in the same space-time window from the prompt. We know that the neutrino on ^{13}C signal must have multiplicity equal to one, so we want to investigate the nature of the background of events with multiplicity larger than one.

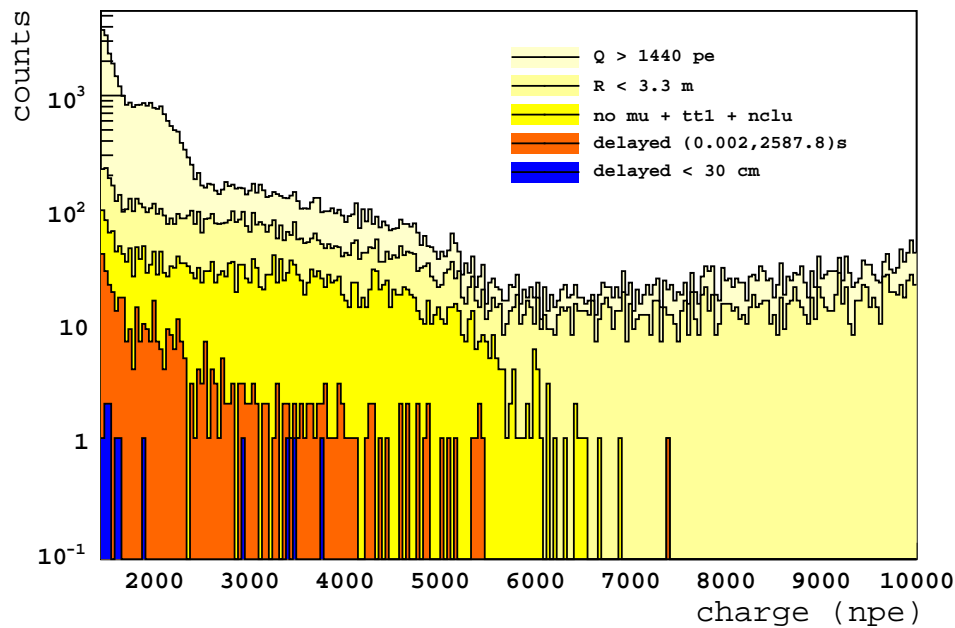


Figure 6.22: Data reconstruction steps: the reduction of the candidates prompt signal through the application of the cuts listed in Table 6.3. In the plot is shown: the charge spectrum of 267947 events with $Q > 1440$ npe, of the 83543 events with only the FV cut (light yellow), of the 3046 events applying the muon cuts and the general requirements (yellow), and (orange) the 426 events that have a delayed events in the time gate. The 12 events found applying also the space cuts are shown in blue.

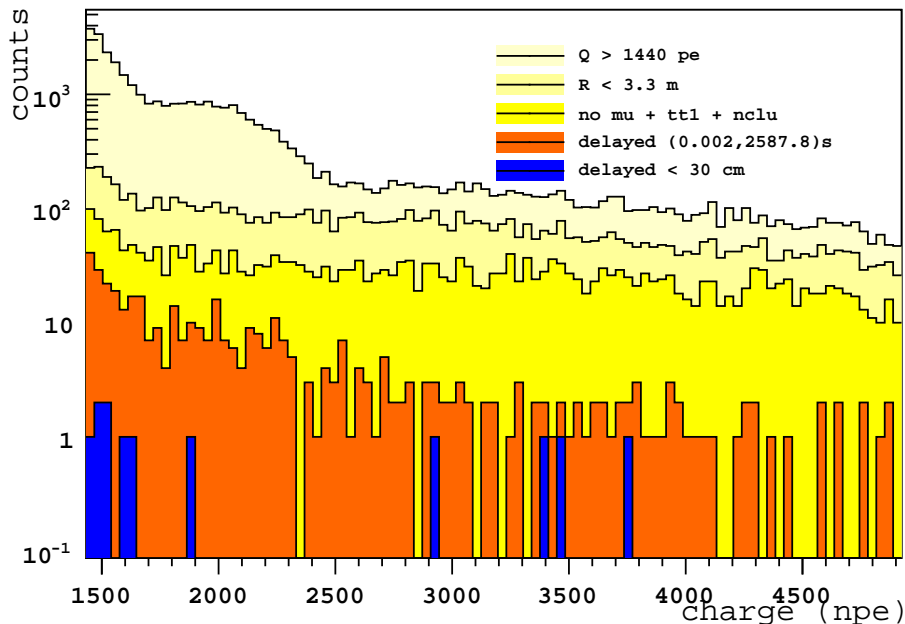


Figure 6.23: Enlargement of Fig. 6.22, as is possible to note the space cut is very effective in reducing the background, as shown by the reduction of events from the orange plot to the blue.

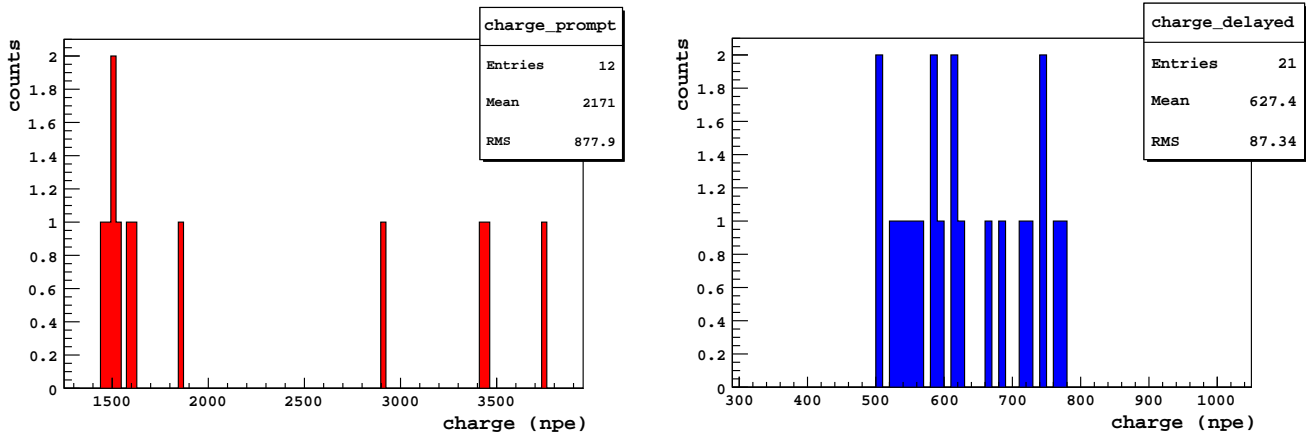


Figure 6.24: Charge distribution of the 12 prompt events (left) and of the delayed ones (right). Since the candidate found are 12, and three of them with multiplicity equal to 3,4 and 5 instead of one, the number of entries in the delayed charge spectrum is 21. In Appendix G are listed the candidates found.

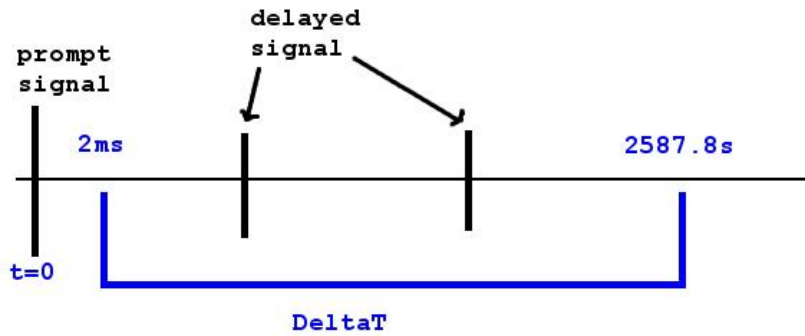


Figure 6.25: Example a prompt signal and two candidates delayed signals that fall in the same space-time window from the prompt.

6.8.1 Accidental coincidences and multiplicity cut

The background for this measurement can come from either uncorrelated or correlated signal pairs:

- Uncorrelated background is a result of random coincidences between two independent processes which just happen to fake the signature of the interaction of the neutrino with the ^{13}C , for example a signal from internal ^{208}Tl contamination in the prompt energy window and a signal from ^{11}C beta-decay in the delayed energy window. Usually the event selection by the delayed coincidence technique significantly reduces the uncorrelated background events. But some events can remain as accidental background events, this are randomly correlated events from the uncorrelated signal. Such signals are called accidental coincidences.
- Correlated background is from interactions producing both a prompt and a delayed signal, which can be mistaken for an interaction of a neutrino on ^{13}C plus the decay of the ^{13}N . As already mentioned is due to burst of cosmogenics produced by a single muon, for example ^{11}C , ^{10}C and ^{11}Be .

A toy Montecarlo

Since some of the selected candidate signal pair show a multiplicity larger than one, we want to estimate the probability that two accidental signals fall in the coincidence cuts, in our case that the delayed signal occurs in a time window between 2 ms and 2587.8 s from the prompt event time and in a sphere of radius 30 cm for the prompt position. For this purpose we developed a dedicated Montecarlo simulation.

We generate in the toy MC $\sim 10^7$ delayed events, spatially distributed in a 3.3 m radius sphere, following the radial distribution of the delayed events shown in Fig. 6.26 obtained from the data, see Section 6.7.

The generated delayed events are also distributed in time with a rate equal to:

$$Rate = \frac{n_{ev}}{LT} = \frac{41658}{646.95} = 71.35 \text{ ev/day} \quad (6.19)$$

where $n_{ev} = 41658$ is the number of events in the energy range [1.02,2.22] MeV, selected in Section 6.7, and $LT=646.95$ days is the livetime.

In particular, assuming all the events uniformly distributed in 646.95 days of livetime, the average number of events in a time window of 2587.8 s is:

$$\langle ev \rangle = \frac{n_{ev}}{LT} \cdot \Delta T = \frac{41658}{646.95 \cdot 86400[s]} \cdot 2587.8[s] = 1.928 \pm 0.009 \text{ ev}/2587.8\text{s} \quad (6.20)$$

where $\Delta T = 2587.7$ s is the time window.

On this set of simulated events we generate N prompts and we apply the space-time selection cuts.

The mean value of events that satisfy both the space and time cut (Fig. 6.27) is equal to:

$$\Rightarrow \mu = 1.078 \cdot 10^{-3} \text{ ev/gate.}$$

The probability $P(\geq 1)$ to have at least one event per gate is:

$$P(\geq 1) = 1 - e^{-\mu} = 1.077 \cdot 10^{-3} \quad (6.21)$$

If we multiply this probability for the number of time we open the gate (613 times, i.e. the number of prompts), we obtain the expected number of accidental events in the livetime:

$$N_{acc} = 1.078 \cdot 10^{-3} \times 613 = 0.66 \pm 0.027 \text{ events/livetime} \quad (6.22)$$

This is the number of accidental background signal with a multiplicity equal or larger than one. The number of candidates found with multiplicity > 1 is three, therefore, we conclude that it is not possible that these events are classified as accidental background.

6.8.2 The correlated background from cosmogenic isotopes

In Section 5.1.1 we already discuss the production of radioactive isotopes and we know that cosmogenic nuclei are often produced with high multiplicity if created in hadronic showers produced by muons. We can demonstrate with the following calculation that the background that has multiplicity larger than one is not accidental but is correlated, and in this way we can reject most of

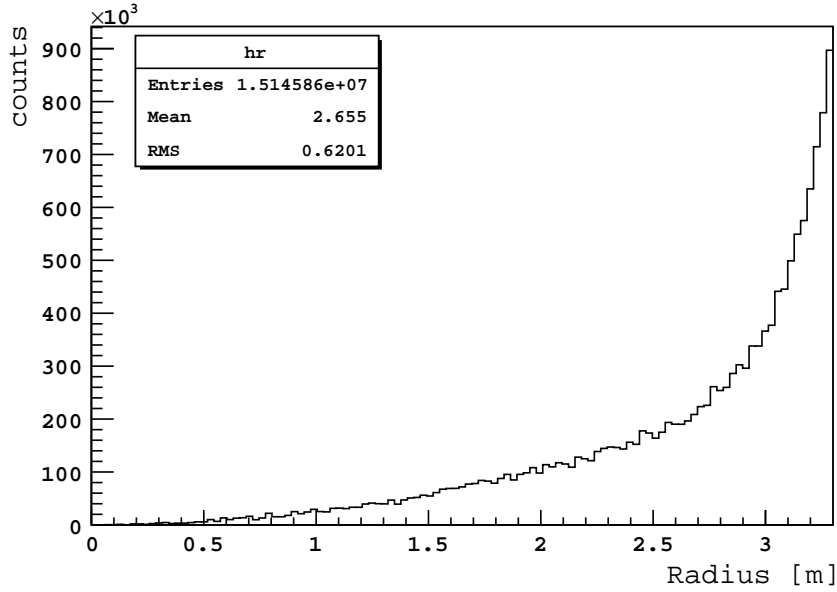


Figure 6.26: Radial distribution of the MC generated delayed events in a radius 3.3 m sphere, taken from data (see Fig. 6.21)

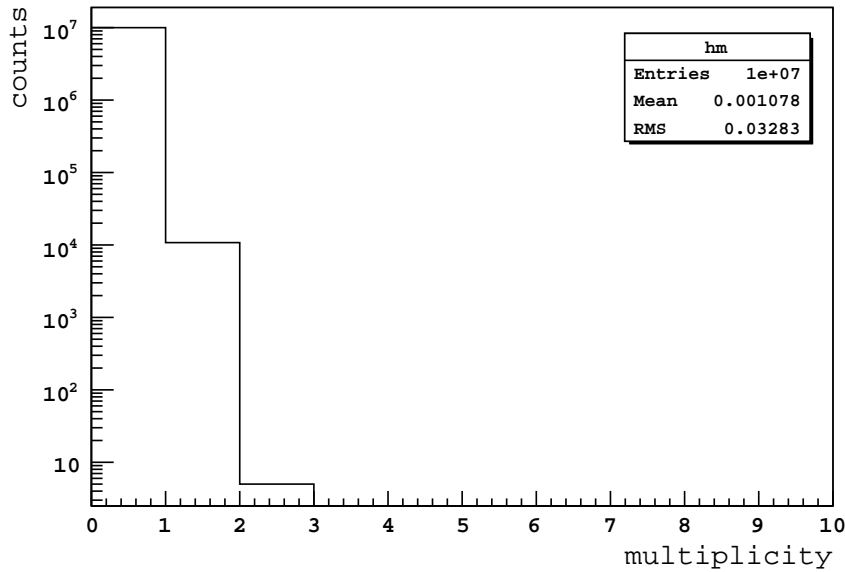


Figure 6.27: Multiplicity of events, i.e. average number of events, that satisfy both the radial and time cut, the mean value is $1.078 \cdot 10^{-3}$ events/gate.

it with a cut that we call *multiplicity cut*.

First, we have to demonstrate that the probability to have more than one accidental background in the delayed gate is negligible.

Assuming all the backgrounds as accidentals we can calculate the probability $P(\geq 2)$ to have at least 2 events per gate equal to:

$$P(\geq 2) = 1 - e^{-\mu} - \mu e^{-\mu} = 5.8 \cdot 10^{-7} \quad (6.23)$$

being $\mu = 1.078 \cdot 10^{-3}$ ev/gate the average number of events satisfying time and space cuts (Fig. 6.27).

If we multiply this probability by the number of times we open the window (613), we obtain the number of accidental events with multiplicity ≥ 2 in the livetime:

$$N_{acc} = 5.8 \cdot 10^{-7} \times 613 = (3.56 \pm 0.144) \cdot 10^{-4} \text{events/livetime} \quad (6.24)$$

We can set that the number of accidentals with multiplicity larger than one is negligible, therefore we have shown that this signals have to come from correlated background.

This background is probably due to bursts of cosmic radioactive nuclei following a muon created in hadronic showers. We remove these events with a cut that we call *multiplicity cut*.

In order to calculate the inefficiency of this cut we have to demonstrate that we are not rejecting neutrinos: being conservative and assuming that in the livetime 10 signal of neutrinos on ^{13}C are expected, we calculate the average number of neutrino candidates in the gate to be:

$$\langle ev_{13C} \rangle = \frac{ev_{13C}}{LT} \cdot \Delta T = \frac{10}{646.95 \cdot 86400[\text{s}]} \cdot 2587.8[\text{s}] = (4.6 \pm 1.5) \cdot 10^{-4} \text{events/gate} \quad (6.25)$$

where $ev_{13C} = 10$ is the number of neutrino CC events expected, $\Delta T = 2587.7$ s is the gate time window, and $LT = 646.95$ days the livetime.

The probability $P(\nu)$ that more than one event of ^{13}C falls in the same time window is:

$$P(\geq 1) = 1 - e^{-\mu} - \mu e^{-\mu} = 1.07 \cdot 10^{-7} \quad (6.26)$$

Finally the number of neutrino events that falls in the space-time window is:

$$N_{13C} = 1.07 \cdot 10^{-7} \times 613 = (6.56 \pm 0.26) \cdot 10^{-5} \text{events/livetime} \quad (6.27)$$

that is negligible.

Therefore we can set the efficiency of this *multiplicity cut* equal to 1 and conclude that a cosmogenic correlated background is present in the delayed window.

Now lacks only to evaluate the probability to detect a neutrino signal plus an accidental background in the delayed event gate, that can give the signal with multiplicity ≥ 2 . For example if the signal shown in Fig. 6.25 is composed by one real candidate (prompt+delayed) and one accidental in the delayed window.

Since the probability to have in the same gate more than one event of neutrino is much more smaller than the probability to have in the same gate 2 accidental backgrounds, we can conclude that also the mixed probability is negligible:

$$P_{\nu}(\geq 1)P_{BKG}(\geq 1) \ll P_{BKG}(\geq 1) \ll 1 \quad (6.28)$$

since from Equation (6.26) and (6.21):

$$P_{\nu}(\geq 1)P_{BKG}(\geq 1) = 1.07 \cdot 10^{-7} \times 1.077 \cdot 10^{-3} = 1.15 \cdot 10^{-10} \quad (6.29)$$

This correlated background come from cosmogenics. As shown in Table 5.2, there are two cosmogenic isotopes which can give a fake prompt signal with $E > 3$ MeV: ^{11}Be and ^{10}C . A muon crossing the IV can create one of these two isotopes from spallation on ^{12}C . The beta decays of one of these two isotope can mimic a prompt ^{13}C signal since they are not rejected with a 5 seconds vetoed time after a muon. The muon can produce nearby also ^{11}C atoms that β^+ decay and its energy range perfectly match the ^{13}C delayed signal.

We studied the distribution of the time distance between a prompt and a delayed candidate, shown in Fig. 6.28, in the case we enlarge the coincidence space-time cuts. Here we look for a delayed signal in $\Delta T = 7200$ s from the prompt one and in a sphere of radius 80 cm centered in the prompt position. Fitting the distribution with an exponential plus a zeroth order polynomial we obtain a decay time of ~ 30 minutes that is in agreement with the decay time of ^{11}C .

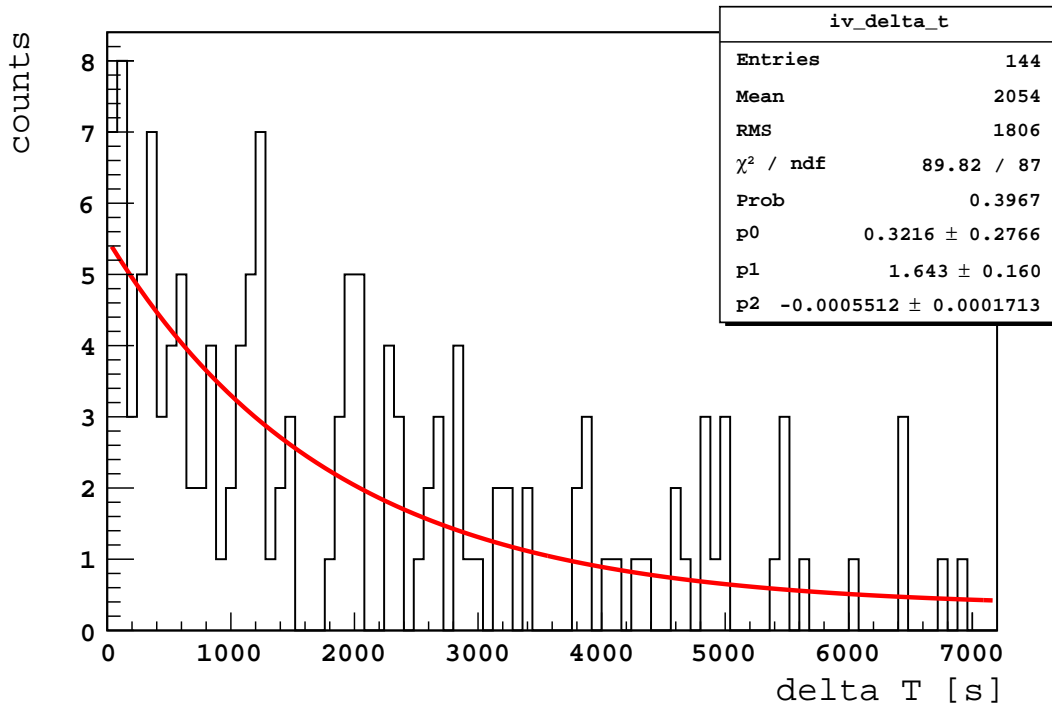


Figure 6.28: Time distribution of ΔT between prompt and delayed events in $\Delta T=7200$ s and in a sphere with radius 80 cm. Fitting it with an exponential plus a zeroth order polynomial we obtain a decay time of ~ 30 minutes that is in agreement with the decay time of ^{11}C .

6.9 Selected candidates over 4 MeV

To be conservative we decided to rise the threshold for the prompt event: $Q_{prompt} > 1920 \text{ npe}$ ($\sim 4 \text{ MeV}$) since, as shown in Fig. (6.29), the efficiency of this cut is not changing considerably, and in this way we reject the background in the prompt window from ^{10}C that has a Q-value of 3.53 MeV.

After applying all the cuts listed in 6.4, in the whole period from December 2007 to May 2011 we find 3 neutrino CC interaction on ^{13}C candidates. The efficiency for the cut in energy for the prompt event becomes 88.20%, leading to a combined efficiency for all the cuts of 81.57% as resumed in Table 6.4.

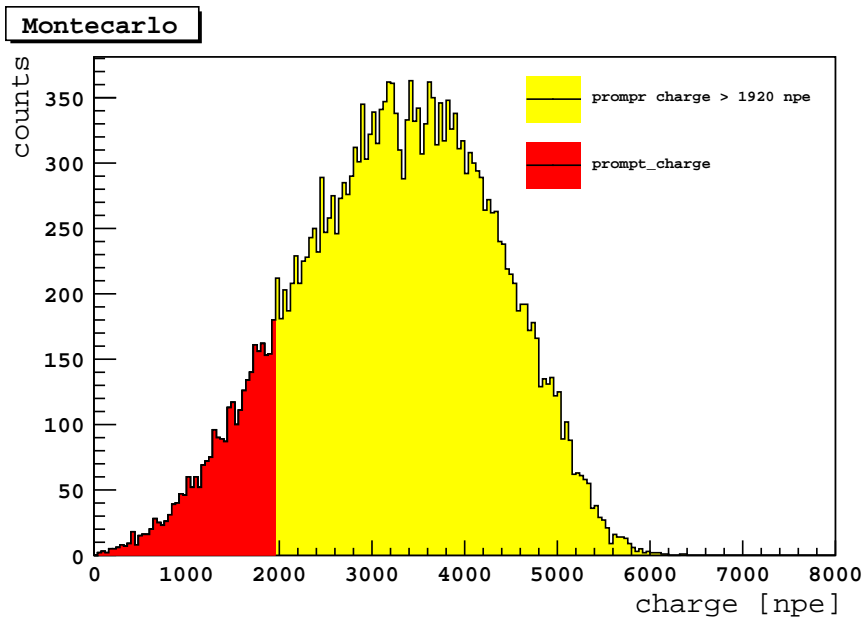


Figure 6.29: Simulated spectra for the prompt signal. In yellow is highlighted the part of the spectrum considered if is chosen $Q_{prompt} > 1920 \text{ npe}$ (5 MeV), it is the 88.20% of the expected spectrum.

Selection cut	Efficiency
$E_{prompt} > 1920 \text{ npe}$	0.882
$400\text{npe} < E_{delayed} < 1200\text{npe}$	0.9998
$\Delta R < 30$	0.9735
$0.002 \text{ s} < \Delta T < 2600\text{s}$	0.9502
multiplicity cut	~ 1
	0.8157

Table 6.4: Cuts efficiencies.

Expected signal and background rate over 4 MeV

In Table 6.5 we report the contribution of each main background source in the prompt and in the delayed energy window if the threshold is raised up to 4 MeV. As it is possible to note, in comparison with the Table 5.2, the background from ^{10}C in the prompt window is rejected and the other backgrounds are reduced.

In Table 6.6 it is shown the rate of expected and measured signal and background if the threshold for the prompt is set at 4 MeV calculated according to Equation (6.16): in the second column is reported the number of background events expected in the prompt window while in the last column we show the rate of background events in the prompt energy windows after the coincidence criteria are applied and the efficiency is taken in account.

Background in prompt window	Rate [cpd/100t]	Fraction [4,16] MeV	Rate [4,16] MeV [cpd/100tons]	Rate [4,16] MeV [cpd/132tons]
^8B (solar n)	0.49 ± 0.05	0.40	0.18 ± 0.03	0.24 ± 0.033
^{11}Be	0.035 ± 0.006	0.82	0.022 ± 0.004	0.029 ± 0.005
^{10}C	0.54 ± 0.04	0.0	0.0	0.0
^{208}Tl			0.011 ± 0.002	0.016 ± 0.003
^{214}Bi			0	0

Background in delayed window	Rate [cpd/100t]	Fraction [1.02,2.22] MeV	Rate [1.02,2.22] MeV [cpd/100tons]	Rate [1.02,2.22] MeV [cpd/132tons]
^{11}C	28.5 ± 0.73	0.841	23.96 ± 0.61	31.64 ± 0.81
^{10}C	0.54 ± 0.04	0.461	0.208 ± 0.015	0.27 ± 0.02
U+Th			negligible	
^{210}Bi			negligible	

Table 6.5: In this table is reported the background in prompt and delayed windows: in the second column is reported the background event rates (given in counts per day in 100 tons) expected in Borexino for the energy windows considered. In the last two columns are shown the rate in the energy window we consider given in count per day in 100 tons, and in count per day in 132 tons. The main difference from Table 5.2 is the rejection of the background from ^{10}C in the prompt window.

6.9.1 Selected candidates

We select with these cuts 3 candidates. Since real and accidental coincidences are indistinguishable, the number of signal events N_S has to be obtained from the difference between the total number of observed events N_T and the number of background events N_B :

$$N_S = N_T - N_B \quad (6.30)$$

From (6.21) the probability to have an accidental background is:

$$P(\geq 1) = 1 - e^{-\mu} = 1.077 \cdot 10^{-3} \quad (6.31)$$

	Expected rate in prompt window counts/lt/132t	Effective rate in prompt window counts/lt/132t
Background		
^8B (solar n)	153.71 ± 21.52	0.15 ± 0.02
^{11}Be	19.06 ± 3.27	0.0018 ± 0.003
^{10}C	0	0
^{208}Tl	9.39 ± 1.7	0.009 ± 0.002
^{214}Bi	0	0
TOTAL	182.17 ± 21.83	0.17 ± 0.034
Signal		
^{13}C	5.16 ± 0.72	4.08 ± 0.57

Table 6.6: Expected and measured background [counts/livetime/132 tons] if the threshold for the prompt signal is 4 MeV.

The number of times we open the space-time gate, for prompts with energy > 4 MeV, is 299 as shown in Fig. 6.18, so that the number of accidental background is:

$$N_{acc} = 1.078 \cdot 10^{-3} \times 299 = 0.32 \pm 0.019 \text{ events/livetime/132t} \quad (6.32)$$

So the number of signal events is:

$$N_S = N_T - N_B = 3 - 0.32 = 2.68 \text{ events/livetime/132t} \quad (6.33)$$

If is taken in account the efficiency this becomes:

$$\frac{2.68}{\varepsilon} \pm \frac{\sqrt{2.68}}{\varepsilon} = \frac{2.68}{0.8157} \pm \frac{\sqrt{2.68}}{0.8157} = 3.28 \pm 2.0 \text{ events/livetime/132t} \quad (6.34)$$

So in conclusion we have measured 3.28 ± 2.0 events/livetime/132t. The present result is limited by the statistic, although it is in agreement with the predicted value of 5.16 ± 0.72 counts/lt/132t. Due to the large error we prefer to quote an upper limit on the number of neutrinos CC interactions on ^{13}C in Borexino at 3σ :

$$N(^{13}\text{C}) < 9.28 \text{ events/livetime/132t} (99.73\% \text{ CL}) \quad (6.35)$$

The discrepancy between the expected accidental background rate from Table 6.6 (0.17 ± 0.034 ev/livetime/132t) and the background rate obtained in Equation (6.32) with the MonteCarlo toy in which we use as input the real data distribution (0.32 ± 0.019 events/livetime/132t) can be explained considering that the application of the multiplicity cut rejects only correlated background with multiplicity equal or larger than 2, but some correlated background with multiplicity = 1 can remain and is indistinguishable from the real CC signal.

Muon depth/intensity relation

From this analysis we have shown that the main background for the neutrino CC detection is of cosmogenic origin, in particular it comes from the troublesome ^{11}C $\beta+$ decay spectrum that perfectly matches the ^{13}N decay energy range. A possibility to reduce/eliminate this source of background is to place a detector at larger depth.

In Fig. 6.30 it is shown how the muon intensity changes versus depth: the intensity of the muon flux between the Borexino experiment that is located under 3800 m.w.e. of rock and the SNOlab situated at 6000 m.w.e. differs by $\sim 10^2$.

In Table 6.7 the number of expected ^{11}C events in Borexino, Kamland and at SNOlab site is reported: the ^{11}C production rate at SNOlab is expected to be 10 times less than in Borexino and are expected in SNO+ ~ 70 muons per day crossing the detector.

It is important to remember, as already pointed out in Section 5.1.2, that this expected ^{11}C rate calculated in [153] to be ~ 15 count per day in Borexino was then measured to be about 50% higher. Nevertheless, even if we consider a doubled ^{11}C production rate at SNOlab site of ~ 0.30 cts/d 100tons, it is still 100 times less than in Borexino.

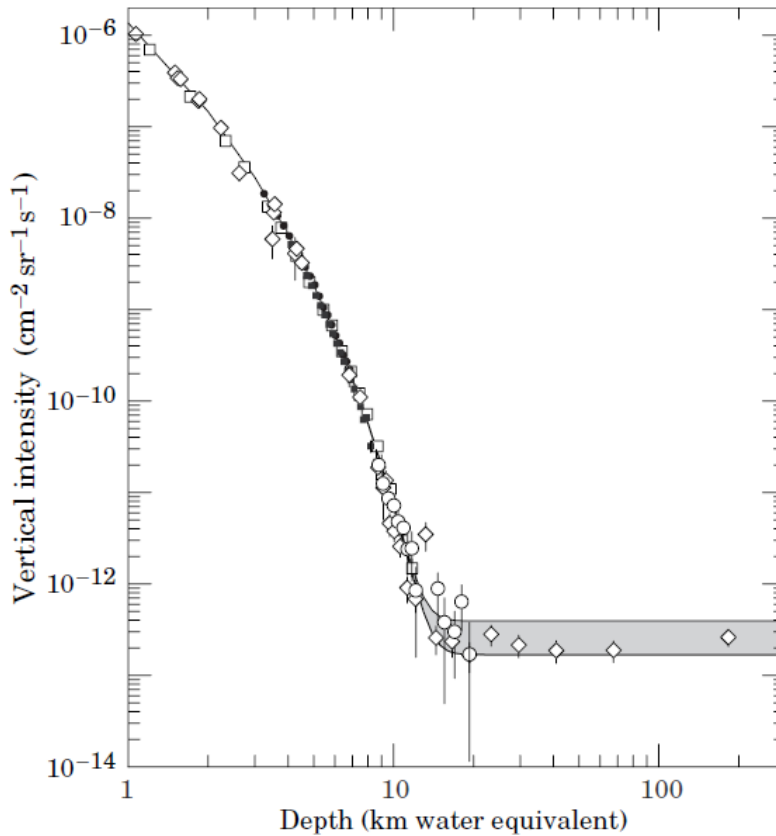


Figure 6.30: Vertical muon intensity vs depth (1 km.w.e.= 10^5 g cm^{-2} of standard rock). The experimental data are from: \diamond : the compilations of Crouch [162], \square Baksan [163], \circ : LVD [164], \bullet : MACRO [27], \blacksquare : Frejus [165]. The shaded area at large depths represents neutrino-induced muons of energy above 2 GeV. The upper line is for horizontal neutrino-induced muons, the lower one for vertically upward muons [166].

	Depth (m.w.e) (m.w.e)	ϕ_μ (μ/m^2h)	$\langle E_\mu \rangle$ (GeV)	N (cts/d 100tons)	P (cts/d 100tons)
Kamland	2700	9.6	285	300	107
Borexino	3800	1.2	320	40	15
SNOlab	6000	0.012	350	0.43	0.15

Table 6.7: Depth (D), residual muon flux (ϕ_μ), average muon energy ($\langle E_\mu \rangle$), neutron capture rate (N), and expected ^{11}C production rate (P) at KamLAND, Borexino, and SNOlab. Table from [153].

Conclusions

In this dissertation we report the results of the measurement of the solar neutrinos charged-current (CC) interaction rate on ^{13}C in Borexino in a period of 646.95 days of livetime using data from December 2007 to May 2011. The main goal of the analysis is to perform a feasibility study for this detection channel in a low background liquid scintillator detector such as Borexino. We point out that this study on an operating detector has never been performed yet. For this purpose we have selected a sample of data collected with the Borexino scintillator in a 3.3 m fiducial volume and carried out a detailed study of the predicted signal and expected backgrounds.

The starting point of this study is the work done in [71] where the possibility to detect solar ^8B neutrinos through a coincidence technique using signal from the solar electron neutrino CC interactions with ^{13}C nuclei naturally contained in organic liquid scintillators was discussed. The analysis presented in [71] in 2005, however, is based on background data published in the literature before Borexino became operational in 2007. Borexino data have shown some not expected feature of the ^{11}C cosmogenic background: high multiplicity of muon-induced neutrons with burst production of ^{11}C nuclei. This feature is of particular importance for our study.

In this dissertation the detection strategy for the CC events is based on a space and time correlated signals tagging, where the prompt event is due to the neutrino interaction on ^{13}C with ^{13}N production, and the delayed event by the β^+ ^{13}N decay. The proposed detection process has a threshold of 2.22 MeV and a large and well-known cross section. This threshold allows to make a direct measurement of electron neutrinos from ^8B in the pp-chain with a detection energy lower than that used in past and present solar neutrino experiments. We recall that ^8B solar neutrinos have been detected by CC interactions in SNO and Elastic Scattering in SuperKamiokande, Borexino and KamLAND.

In this dissertation we first present a comprehensive introduction of solar neutrinos, neutrino oscillations, and of the Borexino detector, including, in particular, the data acquisition system, calibrations and MonteCarlo. Then, we perform a detailed calculation of the expected CC interaction rate on ^{13}C in the Solar Standard Model and neutrino oscillation framework (LMA-MSW) to be 2.38 ± 0.33 events/year/100t.

A detailed study on the background expected in Borexino in the energy range of interest is performed as well. This study shows that the signal to expected background ratio is ~ 16 when the correlated events cut is applied. The tagging for interactions on ^{13}C is challenging due to the long correlation time related to the ^{13}N mean-life of 862.6 sec. Moreover, the spectrum of ^{13}N decay overlaps with that of ^{11}C which is a main source of background in Borexino. Therefore, this fea-

sibility study has to face two difficult goals: handle a long correlation time coincidence and veto cosmogenic backgrounds. This latter background can be strongly reduced by a 5 s veto cut after each detected muon crossing the liquid scintillator. Ultimately, the small isotopic abundance of ^{13}C (1%) limits the number of predicted events in the fiducial volume of Borexino.

Moreover, with a dedicated MonteCarlo calculation we have simulated the expected CC interactions on ^{13}C in Borexino and we have performed a study to choose the best energy, time and position cuts in order to select the prompt and delayed correlated pairs, and at the same time to maximize the efficiency for observing the events of interest while minimizing the background.

In the region above 2.22 MeV we expect backgrounds from cosmogenic events produced by cosmic ray-muons and radioactivity from ^{208}Tl and ^{214}Bi both internal and external. In the analysis presented in this dissertation the detection threshold is set at 3 MeV in order to reject the main background source above 2.22 MeV, i.e. the 2.614 MeV gamma-ray from ^{208}Tl from photomultipliers mainly. These gamma-rays can reach an inner 3-m fiducial volume within the scintillator volume and mimic the neutrino signal.

The measurement performed with this threshold shows that the main background for the neutrino CC detection is of cosmogenic origin. In particular, the background is dominated by cosmogenic nuclei produced by muon spallation, as ^{10}C or ^{11}Be followed by a ^{11}C . In fact, a muon crossing the inner vessel can create one of these two isotopes from spallation on ^{12}C . The beta decays of one of these nuclei can mimic a prompt ^{13}C signal since they are not rejected with the 5 seconds veto after each detected muon. The muon can produce nearby also ^{11}C nuclei which decay ($\beta+$) giving a fake delayed signal.

Radioactive isotopes often do not come directly from muon-nucleus spallation reactions, but from the muon-initiated hadronic and electromagnetic cascades. Since in this case they are produced with high multiplicity, we reject most of the correlated background rejecting events with multiplicity larger than one, i.e. a prompt candidate followed by more than one signal in the delayed space-time window. From these studies we decide to perform the measurement with a threshold of 4 MeV in order to reject the ^{10}C background in the prompt energy window and to reduce other background sources.

Since real and fake correlated coincidences are indistinguishable, from this study we can pose a limit of 9.31 events/lifetime/132ton on the neutrinos CC interaction rate on ^{13}C in Borexino at 3σ CL.

A more precise measurement can be done with more statistic, i.e. lifetime. Moreover, more statistic will allow to perform the three fold coincidence technique [153] as a method to reject most of ^{11}C .

In conclusion, in this dissertation we have performed an original work on solar neutrinos CC interactions on ^{13}C nuclei in massive liquid scintillators using Borexino real data. We have shown that such a detection channel can be implemented in future detectors such as SNO+ or LENA. We have also shown how critical is the radiopurity of the scintillator and the possibility to veto and tag cosmogenic backgrounds. At present our result is limited by the statistic.

Appendix A

Counting Test Facility

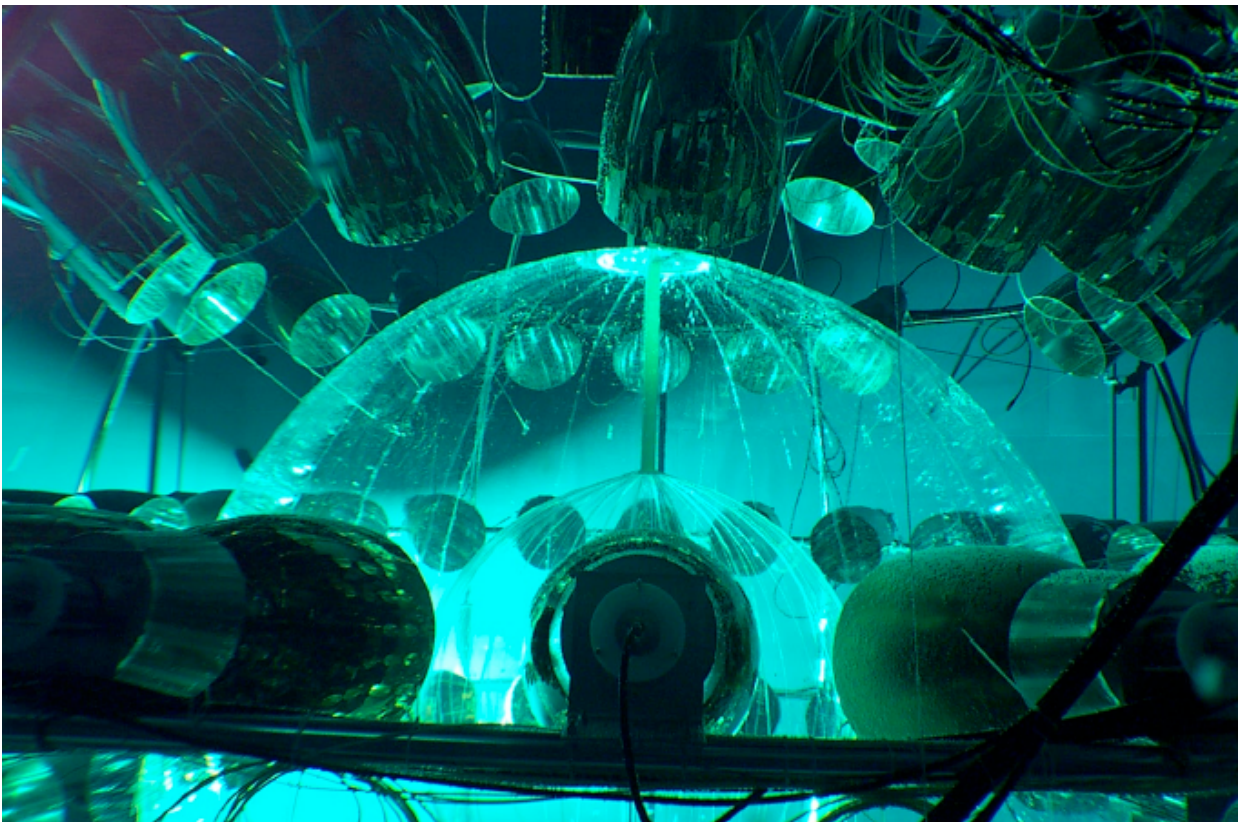


Figure A.1: Counting Test Facility detector.

Appendix B

Radiopurity construction requirements

The main requirements used in the Borexino construction are listed in Table B.1. The Borexino purification plants differ significantly from typical industrial purification plants in that they had to be leak tight to air ($< 10^{-8}$ mbar L/s for He) to prevent the introduction of radioactive gases ^{39}Ar , ^{85}Kr , ^{222}Rn . Dust was a concern after fabrication so they were assembled and cleaned in a low particulate environment (class 100 clean room), with low radon levels to reduce the deposition of radon progeny. The internal surfaces of the purification plants were had to be smooth to eliminate crevasses that would be difficult to clean. They are also rust resistant to prevent the surface layer from oxidizing and flaking off into the scintillator. The stainless steel parts were mechanically polished and electropolished. Those that could not be electropolished were pickled and passivated making them rust resistant and giving them a smooth finish. In addition, the entire system had to be precision cleaned after it was assembled and installed at LNGS. This cleaning involved circulating of a hot detergent solution through the system and a through rinsing. These unusual requirements required a careful selection of pumps, valves, instruments, and other components.

<p>Detector and plants material</p> <ul style="list-style-type: none"> -low intrinsic radioactivity -low radon emanation -chemical compatibility with PC 	<p>Thorn-EMI photomultipliers</p> <ul style="list-style-type: none"> -Low radioactivity Shott borosilicate glass (type 8246) -1.1 ns time jitter for good spatial resolution -(Al) light cones for uniform light collection in the FV -mu-metal shielding for the earth magnetic field -384 PMTs with no cones for muon identification in the buffer region
<p>Pipes, vessel</p> <ul style="list-style-type: none"> -Electropolished -Cleaned with filtered detergents -Pickled and passivated with acids -Rinsing with ultrapure water (class 20-50 MIL STD 1246) 	<p>Leak tightness</p> <ul style="list-style-type: none"> -Leak rate $< 10^{-8}$ atm cc/s -Nitrogen blanketing on critical elements like pumps, valves, big flanges -Double seal metal gaskets
<p>Nylon vessels</p> <ul style="list-style-type: none"> -Good chemical and mechanical strength -Low radioactivity (< 1 count/day/100tons) -Construction in low ^{222}Rn -High purity nitrogen storage 	<p>Clean rooms</p> <ul style="list-style-type: none"> -Mounting rooms in class 100 -Inner detector in class 1.000 -Outer detector in class 100.000

Table B.1: Radiopurity construction requirements.

Appendix C

Pictures of the detector



Figure C.1: A sealed Borexino 8" ETL-9351 PMT fully assembled with light concentrator and mu-metal magnetic shield, ready for installation on the sphere.



Figure C.2: The Borexino Water Tank with its big entrance door (before the construction of BBW and CR1) and The top of the Borexino Water Tank with its "Organ Pipes" (before construction of BBW).

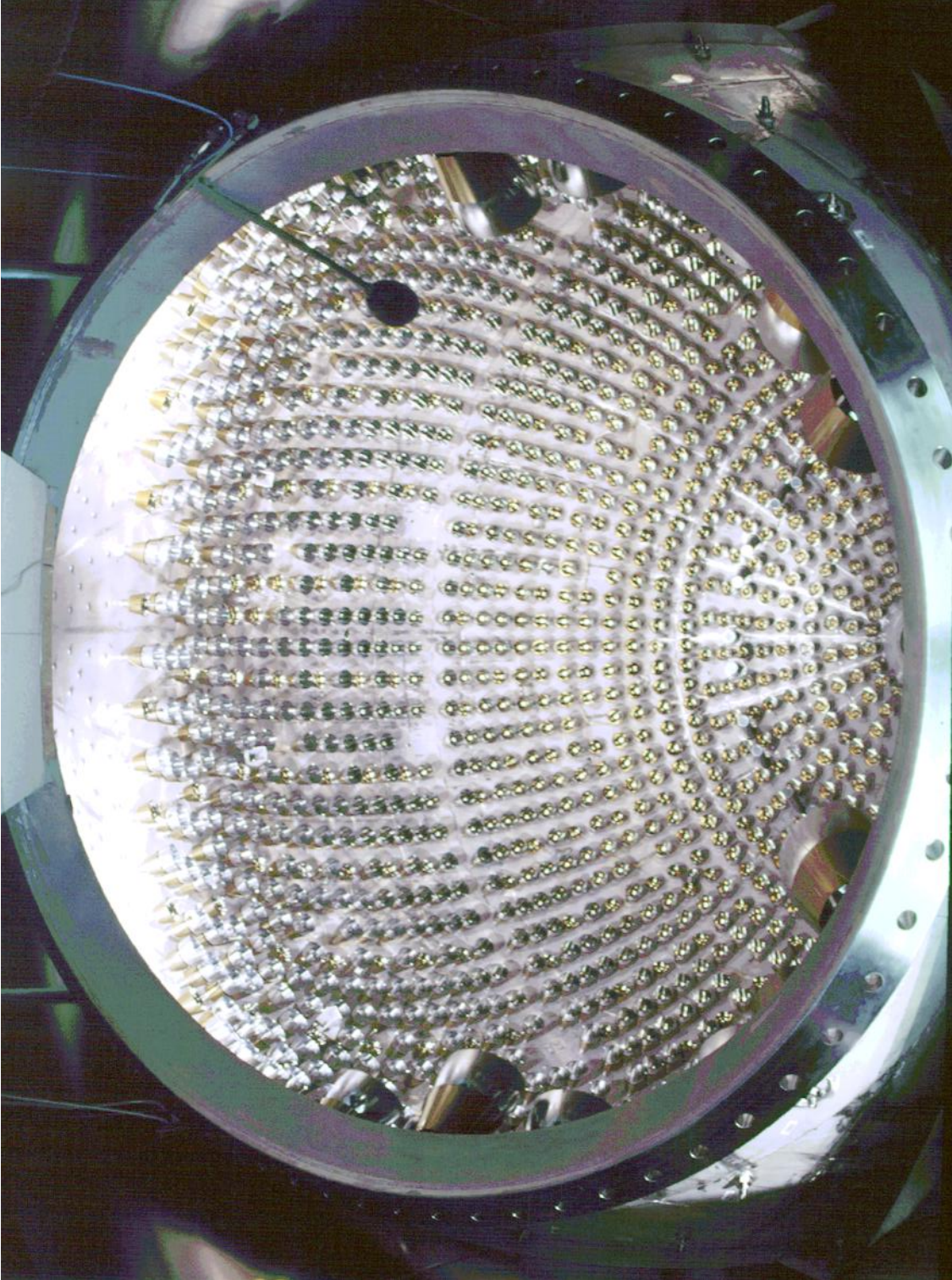
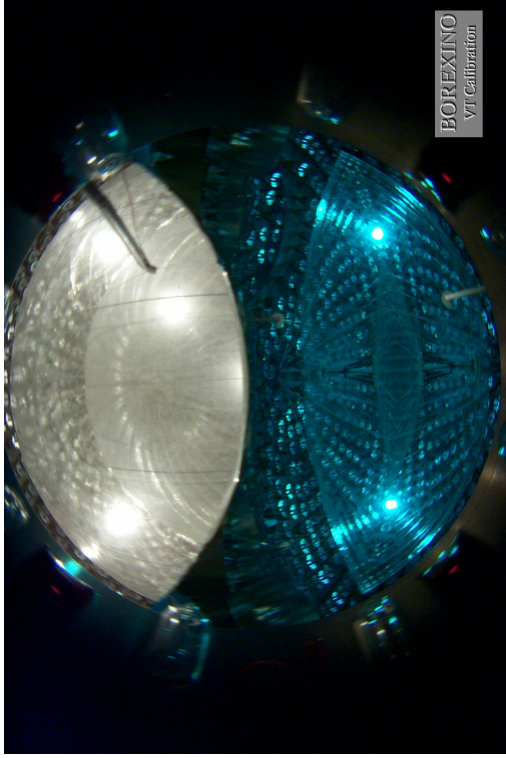
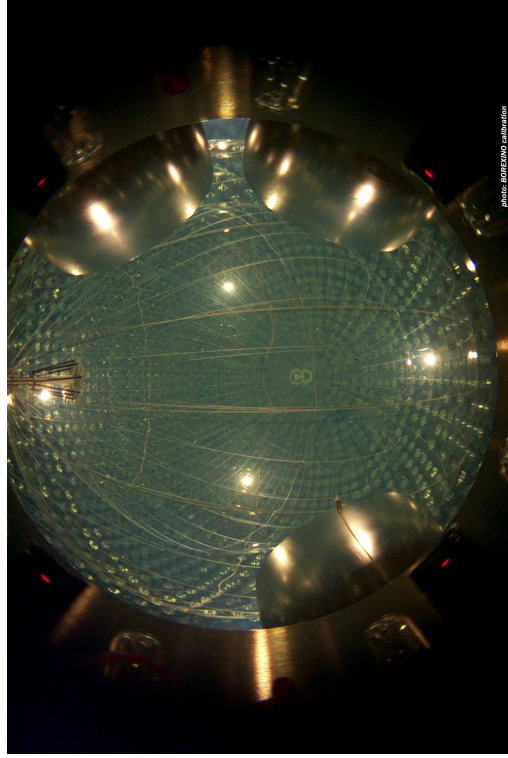


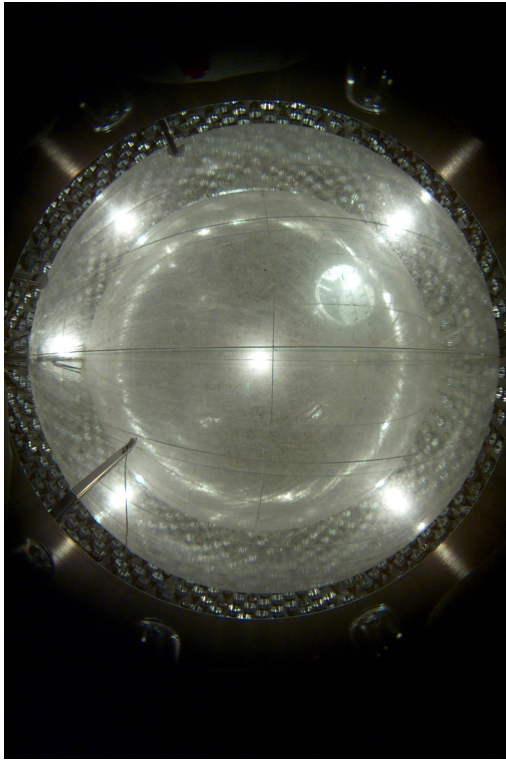
Figure C.3: PMTs on the sphere surface.



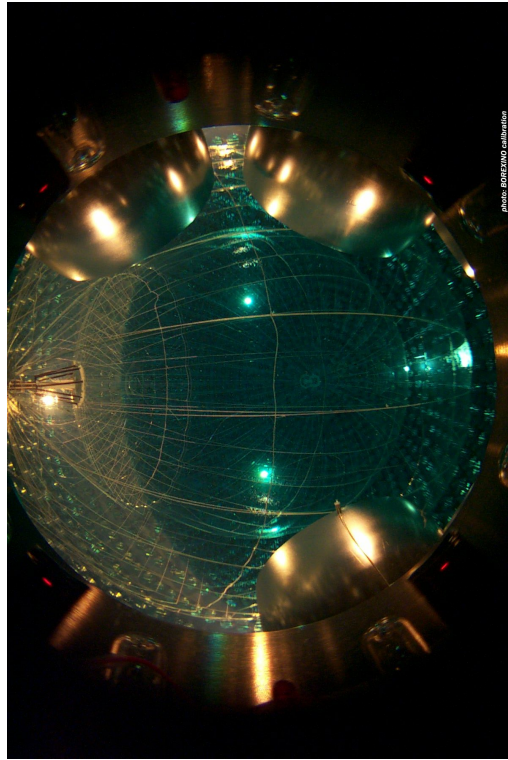
(b) Borexino SSS partially filled with water



(d) Inside view of the Borexino detector: SSS full of scintillator



(a) A view of the Borexino vessels (gas) inflated.



(c) Inside view of the Borexino detector: Water in the SSS (on the bottom) is being replaced by scintillator

Figure C.4: Steps for filling the Borexino detector with pseudocumene.

Appendix D

The scintillator and buffer properties

A liquid scintillation detector measure incident radiation through detection of the emitted scintillation light. The incident radiation excites the scintillator components which then relax to their ground state and sometimes emit light in the process. The emitted light is then detected by the PMTs. Organic liquid scintillators normally consist of an aromatic solvent that is excited by the incident radiation.

Most solvent species have rather a low efficiency for turning their excitation energy into light, and the fluors are added to improve this efficiency. The fluor molecules have higher efficiency for producing light from their excitation energy, so the solvent has to efficiently transfer its energy to the fluor which emits the detected light. Unfortunately not all the light emitted by the fluor is detected: the study of light propagation in liquid scintillator detector is concerned with light production and the journey of the emitted photons from their point of emission until they are detected from the PMTs.

The active target of Borexino are ~ 300 tons of organic scintillator. A lot of measurement were done to find the best solution for the choice of the scintillator. Finally with the CTF data analysis the collaboration decided for a binary mixture of pseudocumene (1,2,4-trimethylbenzene, $C_6H_3(CH_3)_3$), used as a solvent, with PPO (2,5-diphenyloxazole, $C_{15}H_{11}NO$), used as primary fluor on the concentration of 1.5 g/l. The physical properties of PC are listed in Table D.1.

The scintillator optical properties have been widely studied during several laboratory experiments, by using different techniques on small scale sample (few cubic cm^3) and medium scale sample (about 10 liters) by using both ultra-violet light as well as α, β and γ radiation [168, 169]. However only the measurement obtained with the CTF detector allowed a complete characterization of this scintillator solution. Its main characteristics are:

- an high primary photon yield: about 10^4 photons/MeV.

Compared to pure PC, the light yield LY for Borexino was increased by factor ~ 20 for β -like events, leading to an emission of ~ 10.000 photons per deposited MeV. This induces ≈ 500 photoelectrons/MeV in all PMTs of the Inner Detector. The obtained energy resolution scales approximately with $5\% \sqrt{E(\text{MeV})}$.

Chemical name	1,2,4-trimethylbenzene
Molecular structure	$C_6H_3(CH_3)_3$
Molecular weight	120.2
Density	0.876
Index of refraction	1.505
Water solubility	57 mg/l at 20°C
Flash point	48°C

Table D.1: The most relevant physical properties of pseudocumene

- an emission wavelength peak at 430 nm i.e. well above the PMT's sensitivity threshold (~ 350 nm). The emission spectrum of PPO matches the PMT sensitivity, which lies around [350,500] nm, more closely than PC. Fig. D.1 depicts the final emission spectrum of PC+PPO in the concentration used for the Borexino scintillator.

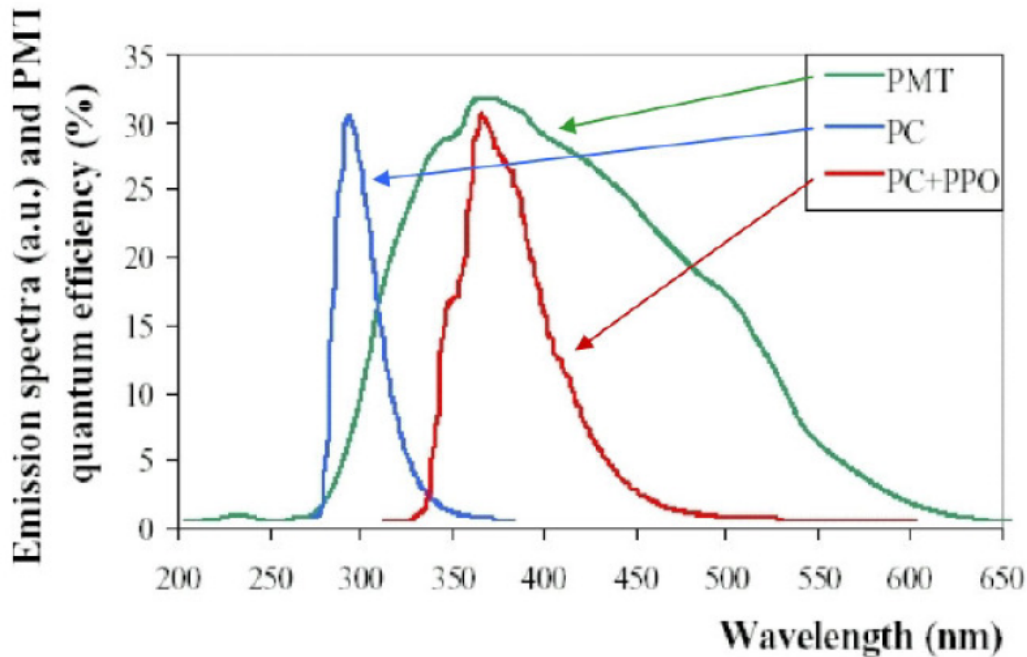


Figure D.1: Fluorescence emission spectrum of pure pseudocumene (blue), pseudocumene plus 1.5 g/l of PPO (red) and the quantum efficiency of the Borexino photomultiplier tubes [81].

- a mean free path length of the light in the scintillator that exceeds 7 m at the peak emission wavelength.
- a short scintillation decay lifetime (≤ 4 ns), as required for a good spatial resolution. A fast de-excitation of the PPO molecules comparable with the time jitter of the PMTs (few ns) allows to reconstruct the position of point-like events in the scintillator using the time-of-flight (TOF) information of the isotropically emitted photons. In an offline modus is possible to reconstruct the positions of events from data to define a so-called fiducial volume (FV): a virtual volumetric software cut that is a powerful tool to reject events reconstructed outside

a given region in the scintillator. This radial cut rejects efficiently events with a deteriorated energy reconstruction and external background events. Another useful application of the position reconstruction algorithms is the tagging of background coincidences in space and time within the scintillator.

- a large difference on the tail of the decay time distributions for α and β excitation modes that allow an efficient α/β discrimination
- an α quenching factor greater than 10 in the energy range 5-6 MeV. This constrains the β equivalent energies for most of the α decays in the uranium chain below 0.5 MeV, and hence below the Compton-like ${}^7\text{Be}$ edge. The energy dependence of the α quenching factor, measured in laboratory, results:

$$Q(E) = 20.3 - E \cdot (1.3 \text{MeV}^{-1}) \quad (\text{D.1})$$

- high radiopurity level (10^{-6} g/g of ${}^{238}\text{U}$ and ${}^{232}\text{Th}$), attainable also on a large mass scale, as shown with the CTF detector

The inactive scintillator that is contained in the inner and outer buffers and is comprised again of pseudocumene, but with the addition of the scintillation quencher dimethylphthalate (DMP) at an initial concentration of 5 g/l. An important fact is that these two solutions have a very small

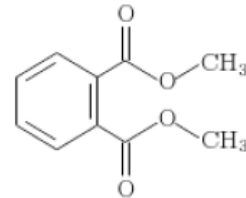
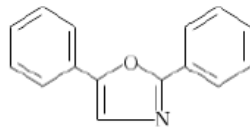
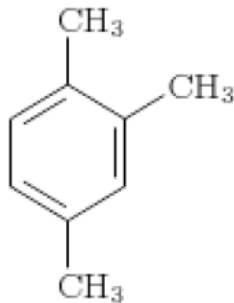


Figure D.2: Pseudocumene

Figure D.3: PPO

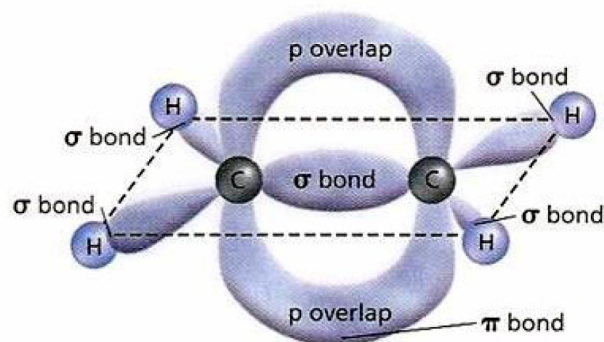
Figure D.4: DMP

density difference (less than one part per thousand), thus, the nylon inner vessel will not be under any considerable strain, assuming a constant and uniform temperature. It is also easier to perform the analysis if the two volumes have the same index of refraction so that the light propagation is easier to model.

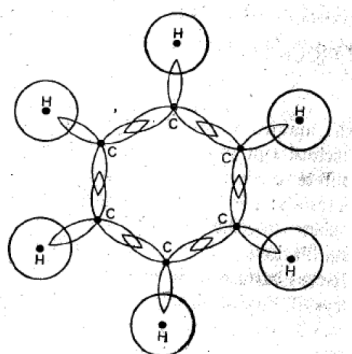
In 2008, a leak was discovered in the Borexino inner vessel and it became necessary to reduce the density difference between the inner vessel and the buffers to as small a level as possible. The purification skids were used in loop-mode to distill out some of the DMP until the average concentration was reduced to a level of 2 g/l. At this level, the DMP is still effective in quenching the scintillation light, but the upward buoyant force on the inner vessel is reduced by a factor of ~ 7 . The lower buoyant force reduces the ΔP across the film at the site of the leak and therefore the leak rate.

Light emission mechanism

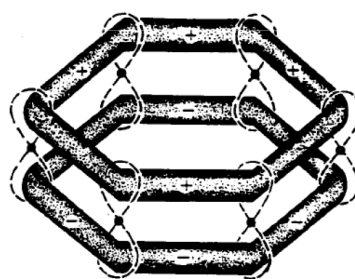
Incident charged particles (e.g. recoiled electrons in scattering processes with neutrinos, β and α particles) losing energy in the PC+PPO medium lead to the ionization and excitation mostly of the PC molecules which are present in larger quantities with respect to PPO ones. The PC ex-



(a) r



(b)



(c)

Figure D.5: Pictorial representation of π and σ bonds between two carbon atoms: (a) is for ethene, but the mechanism is the same in pseudocumene. (b) The σ hybrid orbitals of the carbon atoms of benzene (c) The π -molecular orbitals in benzene: when six carbons come together in a hexagon, each adjacent pair forms a temporary π bond that can travel from carbon to carbon, these bonds that are responsible for producing scintillation light. [84]

cited molecules transfer their energy to the PPO ones and the radiative decay of the PPO excited molecules from the first excited state to the ground state is responsible for the observed fluorescence.

Organic scintillator have a molecular structure made essentially of benzene rings (Fig. D.5 (b) and (c)). In these planar molecules, 2 or 3 valence electrons of the carbon atoms are localized among the atoms themselves in the molecular plane, while the remaining are de-localized in planes parallel to it. They account for the so called σ and π bounds respectively. Transitions among the π energy levels (Fig. D.6) are responsible for the scintillation mechanism, while interactions involving excitation or ionization of σ electrons determine de-excitation or recombination processes where the energy is dissipated thermally, rather than through photon emission.

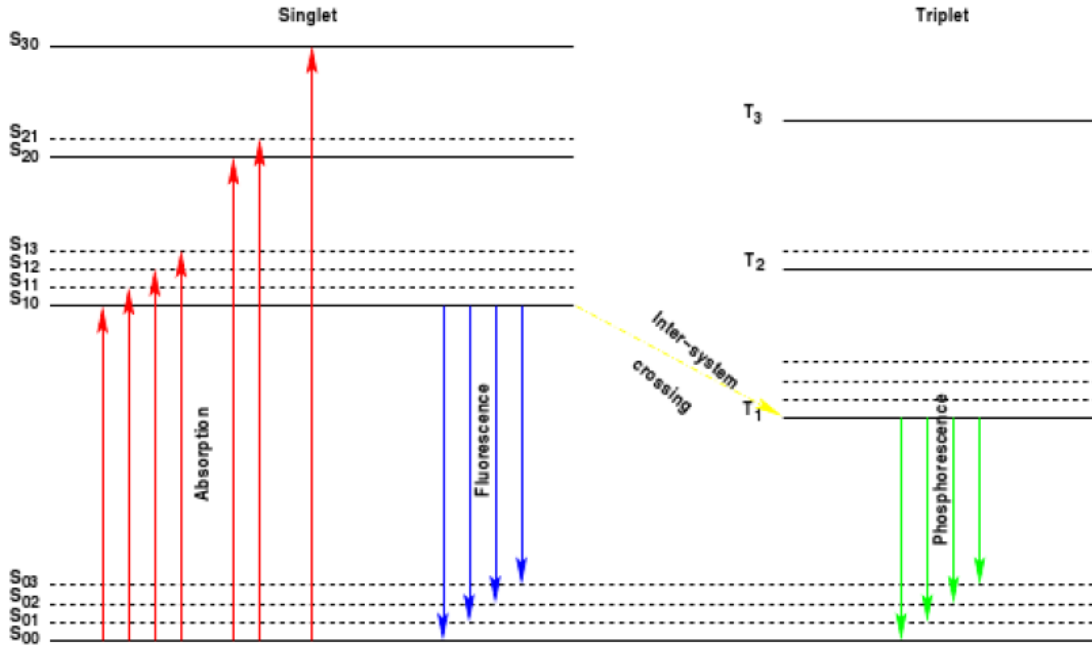


Figure D.6: Energy level scheme for the π electrons of an aromatic hydrocarbon scintillator like pseudocumene. Direct excitation into the triplet states requires a spin-flip of the electron and is thus negligible. The triplet states are populated through molecular recombination as well as transitions from the singlet states via a process known as intersystem crossing [84].

Single state excitation

Singlet states (spin 0) S_0, S_1, S_2, \dots are further subdivided in vibrational states. The energy separation between S_0 and S_1 is $\sim 3-4$ eV, while separation between higher states is progressively smaller and vibrational sub-states separation is of the order of ~ 0.15 eV. At thermal energies (0.025 eV) most of the molecules are therefore in the S_{00} ground state, and when excited to, for instance, S_{12} , will quickly fall back to the S_{10} state in less than a nanosecond.

The energy deposition of a charged particle crossing the medium can determine excitation to any of the singlet states, but the molecule quickly ($\tau_c \simeq 1 \div 10$ ps) moves to S_{10} through non-radiative processes. From S_{10} it de-excites to one of the S_0 states through the so called radiative transition *fluorescence* that accounts for the quick component of the scintillator light response and whose intensity can be described simply as:

$$I = I_0 e^{-t/\tau_s} \quad (\text{D.2})$$

where $\tau_s \simeq 1 - 10$ ns is the characteristic decay time of the singlet state emission and the S_{10} population time was neglected ($\tau_r < 0.5$ ns). The absorption and fluorescence processes are shown by the red and blue arrows respectively in Fig. D.6.

Of particular importance for the efficacy of the scintillation mechanism is the fact that the maximum photon energy emitted in the fluorescence process (from the $S_{10} \rightarrow S_{00}$ transition) is the minimum energy required for the lowest energy absorption process ($S_{00} \rightarrow S_{10}$), therefore, the scintillator is largely, but not completely, transparent to its own light.

Triple state excitation

Population of triplet states (spin 1) can occur in two ways:

1. inter-system crossing from state S1: some singlet states can be converted in triplet states (spin=1) called T_{ij} . The triplet state has a longer mean life compared to the singlet state ($\tau_d \simeq 1 \div 10$ ms) and the emission, called *phosphorescence*, occurs at higher wavelength compared to fluorescence as $E(T_1) < E(T_2)$. Consequently it doesn't play a role in the scintillation process.
2. ionic recombination in higher energy triplet states and successive internal conversion to T1: a pair of molecules in state T_1 can annihilate into a state S_1 and a state S_0 . De-excitation occurs then with the fluorescence spectrum but in times typical of phosphorescence. This phenomenon is known as *delayed fluorescence*. For highly ionizing particles, like α s, characterized by a high specific energy loss dE/dx , ionic recombination and triplet state excitation occur more frequently. These particles can therefore be identified by the higher light emission at long times, see Fig. D.7.

Binary systems

Binary organic mixtures like the one used in Borexino involve a solvent and a solute (fluor), whose molecular levels structure is similar to the solvent but where any level lies at a slightly lower energy. Incoming particles loose energy mostly to solvent molecules, where the primary excitation occurs as well as the energy degradation to states S_{10} and T_{10} . At this point the energy is rather transferred to solute molecules which have a higher scintillation efficiency. For example the addition of PPO in the concentration of 1.5 g/l increases the light output of the pure pc by ~ 20 times, bringing it to the quoted 10000 photons/MeV . Moreover the solute is acting as wavelength shifter in the sense that it has spectral emission that matches more closely the sensitivity of the photomultiplier (Fig. D.1).

The scintillating mixture PC+PPO (1.5g/l) has a light response which can be modeled as a sum of exponential functions:

$$S(t) = \sum_{i=1}^N \frac{q_i}{\tau_i} e^{-t/\tau_i} \quad (\text{D.3})$$

where $N=3$ for β (or $\beta + \gamma$) excitations and $N=4$ for α excitations. Tab. D.2 reports the values of τ_i and q_i measured in laboratory.

The first component accounts for the average PC \rightarrow PPO excitation transfer time as well as the fluorescent de-excitation time of the PPO S_1 state ($\tau_d = 1.6$ ns). In fact increasing the PPO concentration τ_1 decreases to τ_d . Other exponential terms account instead for the more complex delayed fluorescence and result from a parameterization of the light profile studied in laboratory tests. Indeed one of the valuable characteristics of liquid scintillators is the “fast” response, i.e. the high relative weight of the emission occurring at the ns scale, which for Borexino is essential to perform a reliable position reconstruction of the events.

Particle type	τ_1	τ_2	τ_3	τ_4	q_1	q_2	q_3	q_4
$\beta - \gamma$	3.57	17.61	59.50		0.895	0.063	0.042	
α	3.25	13.49	59.95	279.1	0.630	0.178	0.119	0.073

Table D.2: Time constants and relative intensities for the light produced when Borexino scintillator is excited by the types of radiation listed. These values were measured by the CTF [170].

Scintillation efficiency and quenching

There are a multitude of processes by which scintillator molecules may relax to their ground state, only some of which involve the emission of light. Like triplet excitation, non radiative molecular recombination to the ground state is itself a function of the density of ionized molecules, and therefore occurs much more often for those particles with a large value for $\frac{dE}{dx}$. This process, called *ionization quenching*, is responsible for the reduction of the deposited energy down to the energy one actually observes. For α particles in Borexino, the observed number of photons is approximately 10% of that expected from an equal energy β .

The **Scintillation Efficiency** (LY) is defined as the fraction of the incident particle energy that is converted into visible light. Processes leading to non-radiative energy dissipation, such as σ electron excitation and especially ionization, account for scintillation inefficiencies and are generally indicated as quenching effects. Generally LY depends on the particle type (i.e. heavier, more ionizing particles are more quenched) as well as on the energy, though above a given threshold the energy dependency disappears.

The light produced as fluorescence, L , by a particle along its track (from 0 to R , its range) is given by:

$$L = \int_0^R LY \frac{dE}{dx} dx \quad (\text{D.4})$$

where S is the absolute scintillation efficiency and is defined as the fraction of the incident energy actually converted to photons.

If we define a constant B such that $B \frac{dE}{dx}$ is the density of ionized and excited molecules per unit path length, and define another constant k to be the fraction of these ionized and excited molecules that participate in ionization quenching, then we can express equation D.4 as:

$$L = \int_0^R \frac{LY \frac{dE}{dx}}{1 + kB \frac{dE}{dx}} dx \quad (\text{D.5})$$

known as the Birk's formula [83,84], where kB is called the *Birk's parameter* and is treated as a single parameter characteristic of the specific scintillator in use and it must be empirically determined. The experimental determination of kB is not a trivial task: unpublished laboratory measurements indicated $kB = 0.015 \text{ cm/MeV}$, but a modeling of the CTF data seems to indicate $kB \simeq 0.010 \text{ cm/MeV}$.

The light emission processes described have profound consequences in terms of identifying the different types of radiation that cause excitation of the scintillator. The phosphorescence process occurs with a time constant on the order of milliseconds and is irrelevant for the short trigger gates used for Borexino, so we can neglect it. The net result of the competition between fluorescence and delayed fluorescence is a light emission spectrum that is comprised of both processes: the former referred to as the “prompt” component, and the latter the “slow” component.

For highly ionizing particles, like α s, characterized by a high specific energy loss $\frac{dE}{dx}$, ionic recombination and triplet state excitation occur more frequently: this triplet states cause the longer lived component of the scintillation light. A particle which produces a higher density of molecules in the triplet states will yield a track along which there are more collisions between molecules in triplet states, and when they recombine and emit light via delayed fluorescence there will be a larger slow component of the scintillation light.

Therefore, particles with a large $\frac{dE}{dx}$ such as heavy ions, α 's and to some extent protons, can be distinguished from β 's by looking at the relative abundance of light in the tail to that of the entire pulse, known as the *tail-to-total ratio* (TTR).

Fig. D.7 shows the normalized light output of a sample of Borexino scintillator bombarded with α 's and β 's: the larger slow component of the α component is a very important result as it affords a method of tagging them.

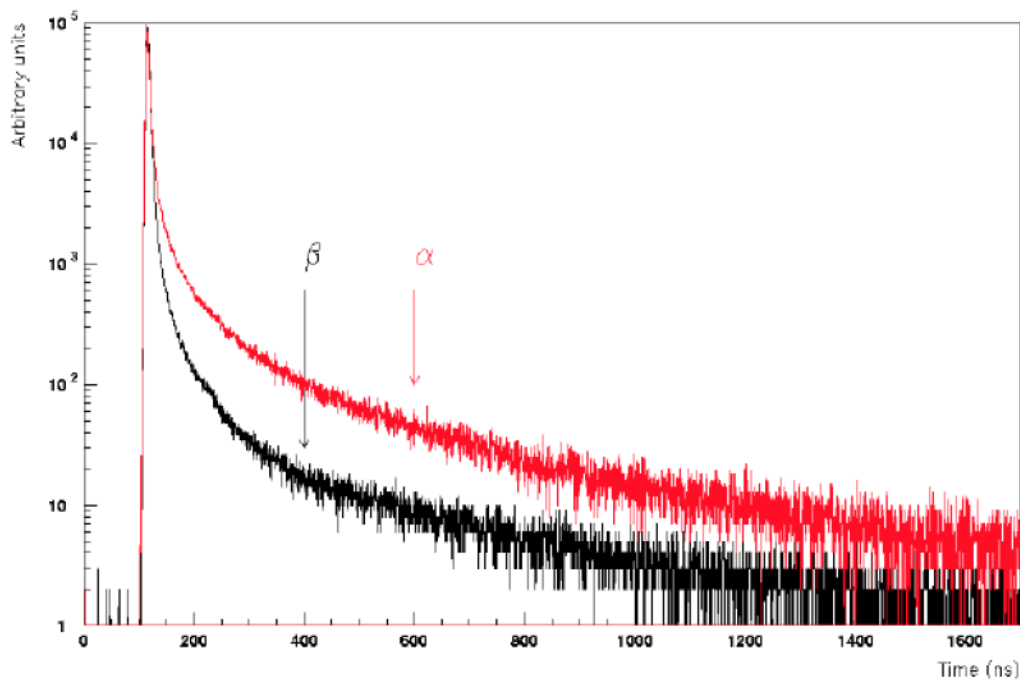


Figure D.7: Normalized scintillation emission spectra from α and β excitation of the Borexino scintillator. The higher density of ionized molecules produced by the α 's causes a higher percentage of light emission via the delayed fluorescence process [82].

- For particles with a small $\frac{dE}{dx}$ such as high energy β 's, equation D.5 reduces to:

$$L = \int_0^R \frac{LY}{kB + (\frac{dE}{dx})^{-1}} dx \approx \int_0^R S \frac{dE}{dx} dx \approx SE \quad (\text{D.6})$$

Thus, in this regime, the light produced is linearly proportional to the energy of the incident particle as expected.

- On the contrary for α particles with a rather large $\frac{dE}{dx}$, the denominator in equation D.5 can be taken to be just $kB \frac{dE}{dx}$ and it reduces to:

$$L = \int_0^R \frac{LY}{kB} dx \quad (\text{D.7})$$

In this regime, we have saturation, and the light output varies linearly with the range of the particle.

A parameter often quoted in describing a scintillator is the quenching factor $Q = L(\beta)/L(\alpha)$, the ratio of luminosity emitted by β and α particles of the same energy. A small scale laboratory test indicates:

$$Q(E_\alpha) = 20.3 - \frac{E_\alpha}{0.77} \quad E_\alpha^{observed} = \frac{E_\alpha}{Q(E_\alpha)} \quad (\text{D.8})$$

where the energy is in MeV and is referred only to the energy of the α particle. The quenching pushes the 5-10 MeV α s of the ^{238}U and ^{232}Th chains down into the Neutrino Window making α/β separation a fundamental background rejection tool.

Propagation of scintillation light

The fluorescence light is attenuated by the PPO itself at lower wavelength values ≤ 360 nm (see Fig. D.8). The PPO quantum efficiency to re-emit this light is $\approx 80\%$, leading to an absorption after few iteration steps or at least to delayed arrivals of the photons on the photo-cathodes of the PMTs. Hence, the fluor concentration has to be balanced between the highest possible light yield and the fastest emission (see next point). The obtained absorption and scattering mean free length at 420 nm (close to the PMT quantum efficiency peak) are 7.8 m and 6.6 m, respectively. For 460 nm the mentioned mean free lengths are 8.2 m and 11.1 m [170]. This leads to a very transparent medium suitable for a large volume detector like Borexino.

Ideally photons emitted in the scintillator should simply propagate in a straight line undisturbed until they reach photomultipliers and this indeed happens to a consistent fraction of them. However the propagation of light in a large volume of scintillator such as borexino has been studied and can be described using the attenuation length $\Lambda(\lambda)$ and the relation:

$$I(x, \lambda) = I_0(\lambda) e^{-\frac{x}{\Lambda(\lambda)}} \quad (\text{D.9})$$

where $I(x, \lambda)$ is the light intensity of a test beam after a path x and I_0 is the intensity at origin. The attenuation length of the borexino mixture at the peak of the emission spectrum is in the 5÷10

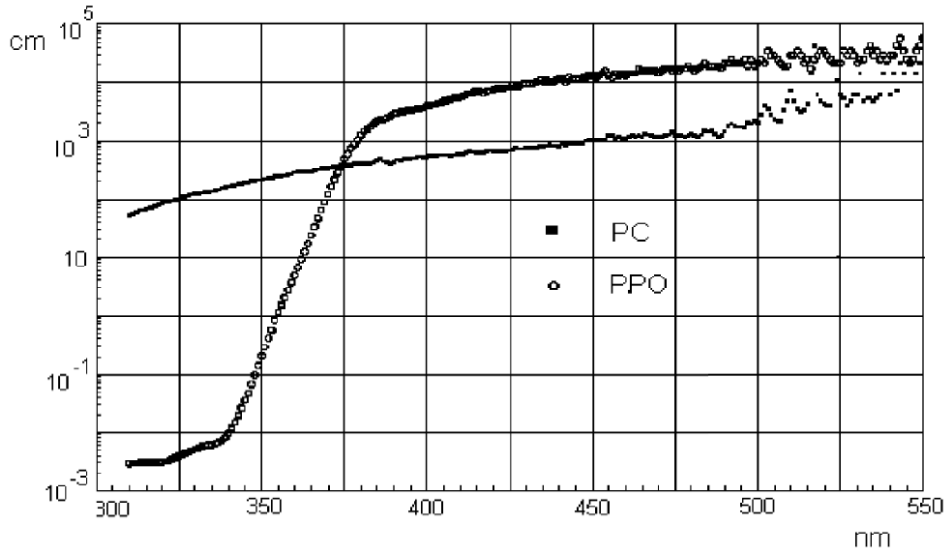


Figure D.8: Attenuation length (in (cm)) of PC and PPO (1.5 g/L) versus wavelength given in (nm) [170].

m range.

Two possible interactions are determinant here:

1. Absorption and re-emission of the light on ppo molecules (*Inelastic Scattering*).
2. *Elastic (Rayleigh) Scattering* on pc molecules.

These effects do not essentially change the light yield of the mixture, but they can make the response somewhat slower.

- **Absorption and re-emission**

Comparing the laboratory measurements of the PPO emission spectrum (Fig. D.1) and the attenuation length of PC and PPO (Fig. D.8), it can be seen how the PPO is able to absorb most of its own emission at small wavelengths ($\lambda < 360$ nm) within a few cm from the emission point. The PPO quantum efficiency in re-emitting the absorbed photon is $\sim 80\%$ and re-emission occurs according to the same emission spectrum. The process can be iterated a few times, until it is re-emitted with a wavelength above the absorption region. Consequently the spectrum is slightly shifted toward red light. Re-emission is isotropic with no correlation with the direction of the absorbed photon, but this does not affect the position reconstruction capability of the detector as the spatial resolution is anyhow larger than the distance between emission and re-emission points. The relevant effect for Borexino is instead the increase of the fast decay constant of the scintillator to about 5ns. So a higher fluor concentration improves the transfer efficiency and therefore the light yield, but at the same time absorption effects can make the time response slower. The PPO concentration for Borexino was an optimized compromise between these two aspects.

- **Elastic scattering**

The lowest transition energy of PC molecules is at about 320 nm, out of the PPO emission spectrum, so absorption on PC molecules is negligible. However above the PPO absorption region ($\lambda > 380$ nm) Rayleigh scattering starts to dominate on absorption and re-emission. The attenuation length for this process is above 1 m so the number of scatters a photon can undergo is limited (in CTF it should rarely be more than 1) and the scattered photons have a $1 + \cos^2(\theta)$ angular dependency, i.e. the usual deflection of the process is not too large. This phenomenon makes trajectories somewhat longer and less linear, limiting to some extent the spatial resolution of the detector.

Appendix E

Cuts to generate DSTs

Listed below are the cuts used to generate the DSTs. The selection is done in 3 chains:

1. NoCluster0 or MuonTrigger or BTBInput
2. NeutrinoTrigger or MuonTrigger or NeutronTrigger
3. No 14C or MultiClusters or Muons or Fast

Each event is passed successively through each chain and any event surviving all the chains is written to the DST. Each element of the chain has a definition as follow:

- NoCluster0: only events with > 1 cluster are kept
- MuonTrigger: only events with trigger type = 2 are kept
- BTBInput: only events with btb inputs & 4 are kept
- NeutrinoTrigger: only events with trigger type = 1 are kept
- NeutronTrigger: only events with trigger type = 128 are kept
- No 14C: only events with charge > 75 or nhits > 75 are kept
- MultiClusters: only events with > 1 cluster are kept
- Muons: is a filter implementing the internal muons identification (using the most updated muon selection criteria), external muons and CNGS muons. For any muon any events in the subsequent 300 ms are identified as muon daughter and kept (if not empty).
- Fast: keeps sequence of events with dt between events < 2 ms

Appendix F

Muon Flags

As ID muons are considered muons having cluster in the laben part of the data (`laben.n_clusters > 0`) and further we call them internal muons. For the muon selection it was user the variable `is_muon_internal_strict`, this variable uses the three following flags in OR (see [167] for a detailed description):

1. Muon Trigger Board (MTB) flag that means that the OD did trigger. 6 PMTs are requested to fire within 150 ns. (`trigger.btb inputs 4 == 1`)
 \Rightarrow `is_muon_mtb ()`;
2. Inner Detector Flags (IDF) that are the energy dependent conditions on the cluster shape as summarized in Table F.1. The analysis uses the mean time of hit time distribution, the time of the first peak identified within a pulse and the Gatti parameter. The shapes of muon pulses depends on their path through the Inner Detector, and therefore on their visible energy deposition. For this reason the discrimination criteria also vary with the visible energy.
 \Rightarrow `is_muon_idf ()`;
3. Muon Crate Flags (MCR) that means that OD data do have a cluster, i.e. presence of data in the Outer Detector, other then dark noise. For this tag 4 PMTs are requested to fire within 150 ns in either half detector. (`muon.has cluster == 1`)
 \Rightarrow `is_muon_mcr ()`;

Nhits range	mean time	peak time (if npeaks >0)	gatti
> 2100	>100 ns	NONE	< 0.55
900-2100	NONE	>30 ns	NONE
100-900	NONE	>40 ns	!(< 0.2 && > 4m)

Table F.1: A set of the energy dependent IDF.

A muons passing only the external Water Tank (external muons) were flagged those muons who did not create a cluster in the laben electronics. For the muon external selection it was user the variable `is_muon_external ()`.

Appendix G

Selected candidates

RUN1	EV1	Q1	Z1	R1	deltat	deltar	RUN2	EV2	Q2	Z2	R2
7809	457687	1500.9	1.87126	2.20104	554.655	29.909	7809	474424	590.484	2.16147	2.48683
8622	244540	1511.16	-0.581499	2.97587	603.316	24.5759	8622	262811	752.486	-0.535018	3.10636
					1207.55	23.6598	8622	281020	729.107	-0.679361	2.99279
					1220.05	27.1016	8622	281410	571.429	-0.477381	3.1298
9059	380397	1621.53	1.06176	2.18806	386.701	27.943	9059	393208	612.778	1.33891	2.32024
					492.498	17.1561	9059	396383	713.131	1.01017	2.28456
					1422.04	24.3432	9059	424547	688.422	0.83627	2.06617
					2375.25	19.1949	9059	454942	509.701	0.881298	2.14638
9342	412066	3458.97	0.629221	1.36509	131.626	11.7917	9342	416095	747.209	0.57603	1.24866
					436.694	12.9425	9342	425519	505.366	0.523487	1.37273
					902.023	20.1721	9342	439747	622.782	0.449823	1.37898
					1818.05	28.669	9342	467743	584.414	0.396714	1.38355
					2075.0	10.7967	9342	475573	537.128	0.574159	1.31901
9742	495681	1870.52	-1.24862	1.84772	2019.83	26.3814	9742	554099	762.732	-1.13727	1.93575
11284	78308	1523.05	-1.77038	2.61545	960.956	9.6811	11284	108276	669.009	-1.75214	2.54538
12209	145050	1473.72	-0.160464	1.52538	376.258	22.877	12209	155270	546.435	-0.325798	1.42494
12301	355042	2925.49	-1.31973	2.65608	358.516	20.531	12301	364915	612.227	-1.52477	2.77175
12498	349450	3754.42	1.55848	2.08266	1873.65	26.9236	12498	404026	529.62	1.61206	2.19461
14029	372053	3417.76	-1.80666	3.14154	2276.48	28.8107	14029	439006	773.911	-1.5302	3.00207
14489	193858	1466.98	1.99135	2.83899	839.765	28.6766	14489	216669	596.097	1.7395	2.63159
15513	26583	1587.84	-2.78399	2.87478	848.259	28.5144	15513	49913	551.124	-2.69588	2.86261

Figure G.1: List of the 12 neutrino CC interaction on ^{13}C candidates. Some variable of the signals are shown, as the RUN number, the event number, the charge Q , the Z coordinate, the Radius, the ΔT and the ΔR . The candidates

Bibliography

- [1] W. Pauli, *Collected Scientific Papers*, Vol. 2, p. 1313, Interscience, New York,(1964).
- [2] F. Reines, C. L. Cowan, F. B. Harrison, A. D. McGuire, and H. W. Kruse, *Detection of the free antineutrino*, *Phys. Rev.*, 117, 159-173, (1960).
- [3] S. M. Bilenky, *Majorana neutrino mixing*, *J. Phys. G*32, R127 (2006), arXiv:hep-ph/0511227.
- [4] B. Kayser, *Neutrino mass, mixing and flavour change*, *Phys. Lett. B*667, 163 (2008), hep-ph/0804.1497.
- [5] C. Amsler et al. (Particle Data Group), *Physics Letters B*667, 1 (2008)
- [6] E. Fermi, *An attempt of a theory of beta radiation*, *Z. Phys.* 88, 161 (1934).
- [7] B.T. Cleveland et al. (The Homestake Collaboration), *Measurement of the solar electron neutrino flux with the Homestake chlorine detector*, *Astrophys. J.* 496, p. 505-526 (1998).
- [8] M. Altmann et al. (The GNO Collaboration), *Complete results for five years of GNO solar neutrino observations*, *Phys. Lett. B*616 174 (2005).
- [9] Y. Ashie et al., *Evidence for an oscillatory signature in atmospheric neutrino oscillation*, *Phys. Rev. Lett.*, vol. 93, p. 101801, 2004, hep-ex/0404034
- [10] B. Pontecorvo, *Jour. Exp. Theoret. Phys.* 34 247 (1958).
- [11] Z. Maki, M. Nakagava, and S. Sakata, *Remarks on the unified model of elementary particles*, *Prog. Theor. Phys.* 28 870 (1962).
- [12] B. Pontecorvo, *Jour. Exp. Theoret. Phys.* 53 1717 (1967).
- [13] L. Wolfenstein, *Neutrino Oscillations in Matter*, *Phys. Rev. D* 17, 2369 (1978);
- [14] S.P. Mikheev and A.Yu. Smirnov, *Resonance Amplification of Oscillations in Matter and Spectroscopy of Solar Neutrinos*, *Sov. J. Nucl. Phys.* 42, 913 (1985);
- [15] Q. R. Ahmad et al., (The SNO Collaboration), *Measurement of Charged Current Interactions Produced by 8B Solar Neutrinos at the Sudbury Neutrino Observatory*, *Phys. Rev. Lett.* 87, 071301 (2001).

- [16] Q. R. Ahmad et al., (The SNO Collaboration), *Measurement of Day and Night Neutrino Energy Spectra at SNO and Constraints on Neutrino Mixing Parameters*, Phys. Rev. Lett. 89, 011301 (2002).
- [17] B. Aharmim et al. (The SNO Collaboration), *Measurement of electron neutrino and total 8B solar neutrino fluxes with the Sudbury Observatory Phase I Data Set*, Phys. Rev. C 75, 045502 (2007)..
- [18] S. N. Ahmed et al., (The SNO Collaboration), *Measurement of the total active 8B solar neutrino flux at the Sudbury Neutrino Observatory with enhanced neutral current sensitivity*, Phys. Rev. Lett. 92, 181301 (2004), nucl-ex/0309004.
- [19] T. Araki et al. (The KamLAND collaboration), *Measurement of Neutrino Oscillation with KamLAND: Evidence of Spectral Distortion*, Phys. Rev. Lett. 94 081801 (2005).
- [20] S. P. Mikheyev and A. Yu. Smirnov, Sov. J. Nucl. Phys. 42, 913 (1985);
L.Wolfenstein, Phys. Rev. D 17, 2369 (1978).
- [21] A.Yu Smirnov, *The MSW effect and Solar Neutrinos*, 11th workshop on Neutrino Telescopes, Venice, March 11-14 2003, (2003); arXiv:hep-ph/0305106
- [22] D. Franco, *The Borexino experiment: test of the purification system and data analysis in the Counting Test Facility*, Ph.D. thesis, Università degli Studi di Milano (2004).
- [23] John N. Bahcall and Carlos Peña-Garay. *A road map to solar neutrino fluxes, neutrino oscillation parameters, and tests for new physics*. Journal of High Energy Physics, 0311:004, 2003.
- [24] G. Bellini et al. (Borexino), *First evidence of pep solar neutrinos by direct detection in Borexino*, 2011 [hep-ex/1110.3230].
- [25] K. Nakamura et al. (Particle Data Group), *Review of Particle Physics*, J. Phys. G 37, 075021 (2010).
- [26] Y. Fukuda et al. (The SuperKamiokande collaboration), *Evidence for oscillation of atmospheric neutrinos*, Phys. Rev. Lett. 81 (1998).
- [27] M. Ambrosio et al., MACRO collaboration, Phys. Rev. D 52, 3793 (1995).
- [28] M.H. Ahn et al. (The K2K collaboration), *Measurement of Neutrino Oscillation by the K2K Experiment*, Phys. Rev. D 74 (2006).
- [29] B. T. Cleveland et al., *Update on the measurement of the solar neutrino flux with the Homestake chlorine detector*, Nucl. Phys. Proc. Suppl. 38, 47 (1995).
- [30] W. Hampel et al., GALLEX collaboration, *GALLEX solar neutrino observations: Results for GALLEX IV*, Phys. Lett. B 447, 127 (1999).

- [31] S. Fukuda et al., Super-Kamiokande collaboration, *Constraints on neutrino oscillations using 1258 days of Super-Kamiokande solar neutrino data*, Phys. Rev. Lett. 86, 5656 (2001), hep-ex/0103033.
- [32] Q. R. Ahmad et al., SNO collaboration, *Direct evidence for neutrino flavor transformation from neutral-current interactions in the Sudbury Neutrino Observatory*, Phys. Rev. Lett. 89, 011301 (2002), nucl-ex/0204008.
- [33] H. Bethe, *Energy Production in Stars*, Phys. Rev. 55, 434-456 (1939).
- [34] A. Zalewska, *Topical questions in the experimental neutrino physics*, Acta Physica Polonica B 34 (11) (2003) 5249.
- [35] V. Kopeikin, *Components of antineutrino emission in nuclear reactor*, Physics of Atomic Nuclei 67 (11) (2004) 1963.
- [36] R. Lopez, et al., *Precision detection of the cosmic neutrino background*, Phys. Rev. Lett. 82 (20) (1999) 3952.
- [37] G. Fiorentini, et al., *Kamland, terrestrial heat sources and neutrino oscillations*, Phys. Rev. B 558 (2003) 15.
- [38] J.N. Bahcall home page, <http://www.sns.ias.edu/~jnb/>
- [39] J. N. Bahcall, M. H. Pinsonneault, and S. Basu, *Solar Models: current epoch and time dependences, neutrinos, and helioseismological properties*, Astrophys. J., 555, 990- 1012, 2001, astro-ph/0010346.
- [40] J. N. Bahcall, Phys. Rev. Lett., 12, 300-302, 1964.
- [41] J. N. Bahcall and M. H. Pinsonneault, Phys. Rev. Lett., 92, 121301, 2004, astro-ph/0402114
- [42] J. N. Bahcall, A. M. Serenelli, and S. Basu, Astrophys. J. Supp. Ser., 165, 400-431, 2006, astro-ph/0511337.
- [43] M. Schwarzschild, *Structure and Evolution of the Stars*, Princeton University Press, 1958.
- [44] Carlo Giunti and Chung W. Kim, *Fundamentals of Neutrino Physics and Astrophysics*.
- [45] J.N. Bahcall, M.C. Gonzalez-Garcia, C. Peña-Garay, Phys. Rev. Lett. 90, 131301 (2003).
- [46] http://www.mpa-garching.mpg.de/~aldos/solar_main.html
- [47] A.M. Serenelli, W.C. Haxton and C. Peña-Garay, *Solar models with accretion. I. Application to the solar abundance problem*, Astrophysical Journal Letters, 743, 24 (2011)
- [48] John N. Bahcall, Aldo M. Serenelli, and Sarbani Basu. *New solar opacities, abundances, helioseismology, and neutrino fluxes*. The Astrophysical Journal Letters, 621, 85-88, March 2005.

- [49] John N. Bahcall and Aldo M. Serenelli. *How do uncertainties in the surface chemical composition of the sun affect the predicted solar neutrino fluxes*. The Astrophysical Journal, 530-542, 2005.
- [50] M. Asplund, N. Grevesse, and A. Sauval, *Cosmic abundances as records of stellar evolution and nucleosynthesis*, vol. 336, p. 25, 2005.
- [51] N. Grevesse and A. Sauval, *Standard solar composition*, Space Science Reviews, vol. 85, no. 1, pp. 161-174, 1998.
- [52] S. Basu and H. M. Antia, *Constraining solar abundances using helioseismology*, The Astrophysical Journal Letters, vol. 606, no. 1, pp. L85-L88, 2004.
- [53] M. Asplund, N. Grevesse, A. J. Sauval, and P. Scott, *The chemical composition of the sun*, Annual Review of Astronomy and Astrophysics, vol. 47, no. 1, pp. 481-522, 2009, astro-ph.SR/0909.0948
- [54] A. Serenelli, *New Results on Standard Solar Models*, arXiv:0910.3690 (2009).
- [55] C. Arpesella et al., *First real time detection of ${}^7\text{Be}$ solar neutrinos by Borexino*, Phys. Lett., vol. B658, pp. 101-108, 2008, astro-ph/0708.2251.
- [56] Peña-Garay, C., Serenelli, A.M., *Solar neutrinos and the solar composition problem*, arXiv:0811.2424 (2008).
- [57] G. Bellini et al. (Borexino Collaboration), *Measurement of the solar ${}^8\text{B}$ neutrino rate with a liquid scintillator target and 3 MeV energy threshold in the Borexino detector*, Phys. Rev. D 82, 033006 (2010).
- [58] B. Aharmim et al. (The SNO Collaboration), *Low Energy Threshold Analysis of the Phase I and Phase II Data Sets of the Sudbury Neutrino Observatory*, Phys. Rev. C 81, 055504 (2010).
- [59] G. Bellini et al. (Borexino Collaboration), *Precision measurement of the ${}^7\text{Be}$ solar neutrino interaction rate in Borexino*, Phys. Rev. Lett. 107, 141302 (2011)
- [60] R.S.Raghavan, S.Pakvasa, *Probing the nature of the neutrino: The boron solar-neutrino experiment*, Phys. Rev. D 37, 849 - 857 (1988).
- [61] C. Arpesella et al. (The Borexino Collaboration), *Borexino at Gran Sasso. Proposal for a real time detector for low energy solar neutrinos*, ed. By I.N.F.N. (1991).
- [62] G. Bellini et al. (The Borexino Collaboration), *Observation of Geo-Neutrinos*, Phys. Lett. B, Vol. 687 (2010).
- [63] G. Bellini et al. (Borexino collaboration), *Study of solar and other unknown anti-neutrino fluxes with Borexino at LNGS*, (2010), arXiv:hep-ex/1010.0029v1

- [64] The Borexino Collaboration, *Absence of day-night asymmetry of 862 keV Be-7 solar neutrino rate in Borexino and MSW oscillation parameters*, Physics Letters B, Volume 707, Issue 1, 16 January 2012, Pages 22-26, ISSN 0370-2693.
- [65] R.S. Raghavan, J.W. Mitchell, E.A. Chandross, B.G. Cortez, *Design concepts for BOREX*, 1988.
- [66] <http://www.lngs.infn.it/>
- [67] LVD, M. Aglietta et al., Phys. Atom. Nucl. 66, 123 (2003), hep-ex/0202006.
- [68] G. 't Hooft, Phys. Lett. 37B (1971) 195.
- [69] M. G. Giammarchi, S. Bonetti and E. Resconi, *Neutrino oscillation simulation, neutrino fluxes and neutrino scattering in the Borexino Monte Carlo*, Borexino Internal report, October 1997.
- [70] John N. Bahcall, Marc Kamionkowski, and Alberto Sirlin, *Solar neutrinos: radiative corrections in neutrino-electron scattering experiments*, Physical Review D, 51, 6146-6158 (June 1, 1995); astro-ph/9502003.
- [71] A. Ianni, D. Montanino, F.L. Villante, *How to observe ^8B solar neutrinos in liquid scintillator detectors*, Phys. Lett. B627 (2005) 38.
- [72] J. F. Beacom, W. M. Farr, and P. Vogel, Phys. Rev. D66, 033001 (2002), hep-ph/0205220.
- [73] M. Fukugita and T. Yanagida, *Physics of Neutrinos* (Springer, Berlin, 2003).
- [74] Steve Hardy, *Measuring the ^7Be Neutrino Flux From the Sun: Calibration of the Borexino Solar Neutrino Detector*, Phd thesis, Virginia Polytechnic Institute and State University, 2010.
- [75] K. McCarty, *The Borexino Nylon Film and the Third Counting Test Facility*, PhD thesis, Princeton University, 2006.
- [76] N. Rossi and F. Lombardi, *Dynamic Fiducial Volume and Exposure (Updates)*, Borexino meeting, December 2, 2011.
- [77] Szymon M, on behalf of the ^7Be Seasonal, and the Stability WG, *Inner Vessel Position Reconstruction*, Internal note, November 30, 2011.
- [78] D. D'Angelo, *Towards the detection of low energy solar neutrinos in Borexino: Data Read-out, Data Reconstruction and Background Identification*, PhD Thesis, Technische Universität München, Germany, 2005.
- [79] M. Wurm, Ph.D. thesis, Technische Universität München (2009).
- [80] G. Bellini et al. (Borexino Collaboration), *Muon and Cosmogenic Neutron Detection in Borexino*, Jour. Instrum., JINST 6:P05005 (2011).

- [81] H. O. Back, *Internal radioactive source calibration of the Borexino solar neutrino detector*, PhD thesis, Virginia Tech, 2004.
- [82] G. Ranucci, et al., *A sampling board optimized for pulse shape discrimination in liquid scintillator applications*, IEEE Trans. Nucl. Sci. 51 4 (2004); pp. 1784-1790.
- [83] J.B. Birks, *Scintillations from organic crystals: Specific fluorescence and relative response to different radiations*, Proc. Phys. Soc. A 64 (1951), pp. 874-877
- [84] J.B. Birks, *The Theory and Practice of Scintillation Counting*, Pergamon Press (1964).
- [85] V.I. Tretyak, *Semi-empirical calculation of quenching factors for ions in scintillators*, Astropart. Phys. 33 (2010).
- [86] M. Pallavicini et al. (Borexino Steering Committee), *Update on Borexino Purification Campaign*, Borexino internal note, 2010.
- [87] C. Arpesella et al., *Direct Measurement of the Be-7 Solar Neutrino Flux with 192 Days of Borexino Data*, Phys. Rev. Lett., vol. 101, p. 091302, 2008, astro-ph/0805.3843.
- [88] C.M. Lederer, V.S. Shirley (Eds.), *Table of Isotopes*, Wiley Interscience, NY (1978)
- [89] M. Shapiro, *Cosmic Radiation in Contemporary Astrophysics*, Reidel Publishing House (1986).
- [90] Dunai Tibor J., *Cosmogenic Nuclides: Principles, Concepts and Applications in the Earth Surface Sciences*, Cambridge University Press (2010) ISBN: 0521873800, pp. 1-198
- [91] K. Nakamura et al. (Particle Data Group), J. Phys. G 37 075021 (2010).
- [92] M. Ambrosio et al., *Measurement of the energy spectrum of underground muons at Gran Sasso with a transition radiation detector*, Astropart. Phys., 10:11, 1999.
- [93] M. Ambrosio et al. (MACRO collaboration), *Vertical muon intensity measured with MACRO at the Gran Sasso Laboratory*, Phys. Rev. D 52 (1995)
- [94] M. Selvi (LVD collaboration), *Analysis of the seasonal modulation of the cosmic muon flux in the LVD detector during 2001-2008*, Proceedings of the 31st ICRC, Lodz, Poland, July 2009 (2009).
- [95] M. Buizza Avanzini (Borexino Collaboration), *Experimental evidence of electron neutrino oscillations and validation of MSW-LMA model with Borexino*, Prog. Part. Nucl. Phys. 66, 412 (2011).
- [96] G. L. Fogli, E. Lisi, A. Marrone, A. Palazzo, and A. M. Rotunno, Phys. Rev. Lett. 101, 141801 (2008).
- [97] V. Barger, D. Marfatia and K. Whisnant, Phys. Lett. B 617, 78 (2005).
- [98] J.N. Bahcall, A.M. Serenelli, and S. Basu, Astrophys. J. Suppl. 165, 400 (2006).

- [99] Q.R. Ahmad et al. (SNO Collaboration), *Phys. Rev. Lett.* 87, 071301 (2001); B. Aharmim et al. (SNO Collaboration), *Phys. Rev. C* 75, 045502 (2007); B. Aharmim et al. (SNO Collaboration), *Phys. Rev. C* 81, 055504 (2010).
- [100] F. Mantovani et al., *Antineutrinos from Earth: A reference model and its uncertainties*, *Phys. Rev. D* 69 013001 (2004); arXiv:hep-ph/0309013v2
- [101] T. Araki, et al., KamLAND Collaboration, *Phys. Rev. Lett.* 94 (2005) 081801.
- [102] T. Adam et al. (The OPERA Collaboration), *Measurement of the neutrino velocity with the OPERA detector in the CNGS beam*, arXiv:1109.4897v1 [hep-ex] (2011).
- [103] G. Alimonti et al., *The Borexino detector at the Laboratori Nazionali del Gran Sasso*, *Nucl. Inst. Meth. A*, 600,568, 2009.
- [104] https://bxweb.lngs.infn.it/docs/FlashAdcs/FWFD-manual_v1.1.1.pdf
- [105] <http://root.cern.ch/>.
- [106] The Borexino Collaboration, G. Alimonti, et al., *Science and technology of Borexino: a real-time detector for low energy solar neutrinos*, *Astropart. Phys.* 16 (2002) 205.
- [107] O. SMirnov, *Report on the Borexino data analysis*, Borexino Internal Report (2007).
- [108] pep working group, Report to DVC on pep analysis, Talk at Borexino meeting.
- [109] The Borexino Collaboration, C. Arpesella, et al., *Measurements of extremely low radioactivity levels in BOREXINO*, *Astropart. Phys.* 18 (2002) 1.
- [110] Y.Koshio, B.Cacianiga, A.Razeto, *The study of the position reconstruction*, Internal Borexino Note.
- [111] O. Smirnov, P. Lombardi, and G. Ranucci, *Precision measurements of time characteristics of the 8" ETL9351 series photomultiplier*, *Instr. and Exper. Techn.*, vol. 47, no. 1, pp. 69-79, 2004.
- [112] E. Gatti and F. Martini, *A new linear method of discrimination between elementary particles in scintillation counters*, in *Proceedings of the Conference on Nuclear Electronics*, p. 265, IAEA, 1962.
- [113] B. Caccianiga et al., *GENEB: GEneration of NEutrino and Background*, Borexino Internal Report, October 1997
- [114] W.R. Nelson, H. Hirayama, and D.W.O. Rogers, *The EGS4 code system*, SLAC-265 UC-32 (1985), pp. 1-398
- [115] <http://www-nds.iaea.org/>

- [116] Y.Suvorov, *The Geo-neutrino signal in Borexino*, Phd Thesis, UNIVERSITÀ DEGLI STUDI DI MILANO, 2009.
- [117] L. Cadonati, Ph.D. thesis, Princeton University (2001).
- [118] A. Derbin, Y. Suvorov, S. Zavatarelli, October 29, 2009, *The study of the registered Charge and the Gatti parameter vs the $^{241}\text{Am} - ^9\text{B}$ neutron source position*, Internal Note
- [119] J.N.Bahcall, *Neutrino Astrophysics*, Cambridge University Press, 1989.
- [120] M.Fukugita, *Astrophysical Neutrinos and Nuclear Physics*, in Lectures given at the 103rd Enrico Fermi Summer School, 1987 (North-Holland, Amsterdam, 1989) p. 331
- [121] M.Koshihara, *Phys. Rep.* 220, 229 (1992).
- [122] J.N.Bahcall and R.K.Ulrich, *Rev. Mod. Phys.* 60, 297 (1988).
- [123] J. Arafune, M. Fukugita, Y. Kohyama, and K. Kubodera, ^{13}C as a solar neutrino detector, *Phys. Lett. B* 217, 186 (1989).
- [124] M. Fukugita, Y. Kohyama, K. Kubodera, and T. Kuramoto, *Reaction cross sections for $\nu + ^{13}\text{C} \rightarrow e^- + ^{13}\text{N}$ and $\nu^{13}\text{C} \rightarrow \nu^{13}\text{C}^*$ for low energy neutrinos*, *Phys. Rev. C* 41, 1359 (1990).
- [125] K. Kubodera and S. Nozawa, *NEUTRINO-NUCLEUS REACTIONS*, *Int. J. Mod. Phys. E* 3, 101 (1994).
- [126] R. Davis Proc. Seventh Workshop on Grand unification, Toyama, 1986 World Scientific, Singapore (1987).
- [127] J.N. Bahcall and R. Davis, *Essays in nuclear astrophysics*, Cambridge U.P, Cambridge (1982).
- [128] G. Friedlander, BNL report BNL50879, Proc. Informal Conf. on Status and future of solar neutrino research (1978).
- [129] M. Koshihara, Proc. Workshop on Grand unified theories and cosmology, KEK report 84-12, KEK, Tsukuba, Japan, 1983 (1984). K. Hirata et al., . UT-ICEPP-87-04, (1987) University of Tokyo preprint.
- [130] G. Aardsma et al.. *Phys. Lett. B*, 194 (1987), p. 321.
- [131] M. Aglietta et al.. *Nuovo Cimento*, 9C (1986), p. 185.
- [132] R.S. Raghaven, S. Pakvasa and B.A. Brown. *Phys. Rev. Lett.*, 57 (1986), p. 1801.
- [133] Homestake Collaborations, B. T. Cleveland et al., *Astrophys. J.* 496, 505 (1998).
- [134] W. Hampel et al., Gallex Collaboration, *Phys. Lett. B* 447, 127 (1999).
- [135] M. Altmann et al., GNO Collaboration, *Phys. Lett. B* 490, 16 (2000).

- [136] J. N. Abdurashitov et al., SAGE Collaboration, *J. Exp. Theor. Phys.* 95 181 (2002).
- [137] K. S. Hirata et al., Kamiokande Collaboration, *Phys. Rev. Lett.* 65, 1297 (1990).
- [138] S. Fukuda et al., Super-Kamiokande Collaboration, *Phys. Rev. Lett.* 86, 5651 (2001).
- [139] Q. R. Ahmad et al., SNO Collaboration, *Phys. Rev. Lett.* 89, 011301 (2002).
- [140] T. Araki et al., KamLAND Collaboration, *Phys. Rev. Lett.* 94, 081801 (2005).
- [141] talk by F. von Feilitzsch at CuTAPP workshop, *Current Topics in Astroparticle Physics*, (Ringberg, Germany, 2005). Slides available at the conference home page, www.mppmu.mpg.de/common/seminar/conf/conf2005/cutapp/
- [142] A. Arima, K. Shimizu, W. Bentz and H. Hyuga, *Adv. Nucl. Phys.* 18, 1 (1987), [SPIRES]; I. S. Towner, *Phys. Rep.* 155, 263 (1987), [CAS].
- [143] B. A. Brown and B. H. Wildenthal, *At. Data Nucl. Data Tables* 33, 347 (1985) [CAS].
- [144] A. Ianni, Talk at HA ν SE: HAMBURG neutrinos from Supernova Explosions, *Supernova Neutrino with Liquid Scintillators with a closer look at ν -p interaction channel*, Hamburg, July 2011
- [145] H. Fujimura et al., *Phys. Rev. C* 69 064327 (2004).
- [146] J. N. Bahcall, *Solar neutrino cross sections and nuclear beta decay*, *Phys.Rev.*135,B137-B146,1964
- [147] John N. Bahcall and E. Lisi, D. E. Alburger, L. De Braekeleer, S. J. Freedman, J. Napolitano, *Standard neutrino spectrum from 8B decay*, *Phys. Rev. C*, 54, 1 (1996).
- [148] Tables of the 8B spectrum can be found at the J.N. Bahcall, home page, <http://www.sns.ias.edu/jnb/>, see *Neutrino Software and Data*.
- [149] J.N. Bahcall, E. Lisi, D.E. Alburger, L. De Braekeleer, S.J. Freedman, and J. Napolitano, *Standard Neutrino Spectrum from 8B decay*, *Phys. Rev. C.*, 54, 411-422
- [150] G. L. Fogli, E. Lisi, A. Marrone, A. Palazzo and A. M. Rotunno, arXiv:0806.2649 (2008).
- [151] S. Abe et al. (KamLAND Collaboration) *Measurement of the 8B solar neutrino flux with the KamLAND liquid scintillator detector*, *Phys. Rev. C* 84, 035804 (2011).
- [152] T. Hagner, R. von Hentig, B. Heisinger, L. Oberauer, S. Schonert, F. von Feilitzsch, and E. Nolte, *Muon-induced production of radioactive isotopes in scintillation detectors*, *Astroparticle Physics*, vol. 14, no. 1, pp. 33-47, 2000.
- [153] Galbiati, C. et al, *Cosmogenic ^{11}C production and sensitivity of organic scintillator detectors to pep and CNO neutrinos*, *Phys. Rev. C* 71, 055805 (2005)

- [154] T. Luu and C. Haggmann, *Neutron Production by Muon Spallation I: Theory*, <https://e-reports-ext.llnl.gov/pdf/340911.pdf> (2006).
- [155] S. Abe et al., *Study of the Production of Radioactive Isotopes through Cosmic Muon Spallation in KamLAND*, 2009, hep-ex/0907.0066.
- [156] R. N. Saldanha, ^{11}C subtraction in Borexino, Presentation given at Borexino collaboration meeting, 2008.
- [157] K. Fomenko, Private communication, 2011.
- [158] *^7Be Cuts Committee - Minutes of Meetings, Borexino*, Oct. 18
- [159] M.B. Avanzini, *The ^8B Solar Neutrino Analysis in Borexino and Simulations of Muon Interaction Products in Borexino and Double Chooz*, Phd Thesis, (2011).
- [160] Y.Koshio, B.Caccianiga, LNGS analysis group, *Position reconstruction and determination of the fiducial volume*, Internal note, October 24, 2010.
- [161] Borexino Monte Carlo code, in preparation.
- [162] M.Crouch, in Proc. 20th Int. Cosmic Rays Conf. (Moscow) 6, 165 (1987).
- [163] Yu.M.Andreew, V.I. Gurentzov and I.M.Kogai, in Proc. 20th Int. Cosmic Rays Conf. (Moscow) 6, 200 (1987).
- [164] M. Aglietta et al. (LVD collaboration), *Astropart. Phys.* 3, 311 (1995).
- [165] Ch.Berger et al. (Frejus collaboration), *Phys. Rev. D* 40, 2163 (1989).
- [166] M. Yao et al., COSMIC RAYS,24, *Journal of Physics G* 33, 1 (2006), available on the PDG WWW pages (URL: <http://pdg.lbl.gov/>).
- [167] Davide D'Angelo, Livia Ludhova, Quirin Meindl, Michael Wurm, *Cosmic Backgrounds in BOREXINO*, January 20, 2010, Internal note.
- [168] F.Gatti et al., *Nucl.Instr.andMeth.*A370(1996)609.
- [169] F.Elisei et al., *Nucl.Instr.andMeth.*A400(1997)53.
- [170] G. Alimonti et al. (Borexino collaboration), *Light propagation in a large volume liquid scintillator*, *Nucl. Inst. Meth A* 440 (2000), pp. 360-371

Acknowledgements

I want to express my gratitude to everybody who supported and encouraged me during this wonderful period of my scientific career. This work would have never been accomplished without their great help. I dedicate my thesis to them and to all the people with whom I shared something in these years, be it small or big. Everybody is part of my path:

⊗ First of all to my family: I thank my parents for the support that they gave me, without whom I would not have been able to complete my PhD, and of course, for the nice drawings. I also thank my headstrong big brother Francesco, even for the “..Little Mole digs digs”, but you know..he is an engineer...

⊗ To Yura, for being here and always present.

⊗ To Aldo Ianni, Francesco Villante and Daniele Montanino..my advisors and my referee. I thank Aldo for giving me the opportunity to work at LNGS and to participate in the Borexino experiment, where I was able to work in an international collaboration, thus gaining invaluable experience and knowledge. In particular I thank Aldo and Daniele for the patience in reading and correcting my thesis, for the useful advices and comments.

⊗ To Sergio Petrera, my PhD tutor.

⊗ To Davide Franco. I am infinitely grateful to him, who made a special contribution to my thesis. Thanks a lot Davide for your patience!

⊗ To Alessandro, a good guide through the obscure meander of informatics and programming, although sometimes a little bit hermetic and hard to gain.

⊗ To Prof. GianPaolo Bellini, a special thanks for his attention to me and for organizing the very interesting school in Varenna.

⊗ To Igor Machulin, for his invaluable help on Monte Carlo simulations.

⊗ To my office mate Paolo, for all the informatics helps and tips, and also for tolerating the sauna-office.

⊗ To Nicola and Francesco both as friend and colleagues, for helping me in many occasions, reading my stuff and giving me advices.

⊗ To Vincenzo, but just a bit!

⊗ To the american group: Alvaro, Amanda, Richard, Pablo and Szymon. I appreciate and will always appreciate the time spent together both in LNGS and outside.

⊗ To all the Gran Sasso people: Gyorgy, Paolo, Michele, Giuseppe, Stefano, Augusto, Andrea, Massimo, Peppino, Corrado. Nice group and nice people! In between them I also thanks the emigrant Stefano D. A particular thank to Kirill for his help on the fit.

- ⊗ To Meggy and Davide D., two dear people that I always enjoy meeting. Thanks to Davide who first introduced me to Echidna.
- ⊗ To all the “crucchi” group that made me change my opinion on germans: Michi, Daniel, Timo, Jurgen, Quirin and Werner, ... yes, Werner is in between the germans.
- ⊗ To all the people of the Borexino collaboration. It is a very nice and expert collaboration, and I have learned so much listening to all the presentations and discussions at meetings, and reading all the papers written. I also had a great time together on shifts and also in restaurants.
- ⊗ To my dearest friend in Parma, even though now we share only a few days a year, I carry them in my hearth with all the moments full of magic and wonder: Giulio, Elena, Marketto, Robbi.
- ⊗ To Alessandro, for coming to see me often in these years in Abruzzo during his many trips up and down for Italy.
- ⊗ To Gianmarco and Ana Amelia, with which I began my adventure in abruzzo.
- ⊗ To Michela and Katia for not forgetting me even if I am far away.
- ⊗ To Gianluca Gabriella and Diego.
- ⊗ Last but not least, to the Gran Sasso mountains.

